



**IAEA**

International Atomic Energy Agency

**IAEA TECDOC SERIES**

**No. 2090**

# Coated Particle Fuels for High Temperature Gas Cooled Small Modular Reactors

Progress in Design, Manufacturing, Experimentation, Modelling  
and Analysis Technologies

COATED PARTICLE FUELS  
FOR HIGH TEMPERATURE GAS COOLED  
SMALL MODULAR REACTORS

The following States are Members of the International Atomic Energy Agency:

AFGHANISTAN	GEORGIA	PAKISTAN
ALBANIA	GERMANY	PALAU
ALGERIA	GHANA	PANAMA
ANGOLA	GREECE	PAPUA NEW GUINEA
ANTIGUA AND BARBUDA	GRENADA	PARAGUAY
ARGENTINA	GUATEMALA	PERU
ARMENIA	GUINEA	PHILIPPINES
AUSTRALIA	GUYANA	POLAND
AUSTRIA	HAITI	PORTUGAL
AZERBAIJAN	HOLY SEE	QATAR
BAHAMAS, THE	HONDURAS	REPUBLIC OF MOLDOVA
BAHRAIN	HUNGARY	ROMANIA
BANGLADESH	ICELAND	RUSSIAN FEDERATION
BARBADOS	INDIA	RWANDA
BELARUS	INDONESIA	SAINT KITTS AND NEVIS
BELGIUM	IRAN, ISLAMIC REPUBLIC OF	SAINT LUCIA
BELIZE	IRAQ	SAINT VINCENT AND
BENIN	IRELAND	THE GRENADINES
BOLIVIA, PLURINATIONAL	ISRAEL	SAMOA
STATE OF	ITALY	SAN MARINO
BOSNIA AND HERZEGOVINA	JAMAICA	SAUDI ARABIA
BOTSWANA	JAPAN	SENEGAL
BRAZIL	JORDAN	SERBIA
BRUNEI DARUSSALAM	KAZAKHSTAN	SEYCHELLES
BULGARIA	KENYA	SIERRA LEONE
BURKINA FASO	KOREA, REPUBLIC OF	SINGAPORE
BURUNDI	KUWAIT	SLOVAKIA
CABO VERDE	KYRGYZSTAN	SLOVENIA
CAMBODIA	LAO PEOPLE'S DEMOCRATIC	SOMALIA
CAMEROON	REPUBLIC	SOUTH AFRICA
CANADA	LATVIA	SPAIN
CENTRAL AFRICAN	LEBANON	SRI LANKA
REPUBLIC	LESOTHO	SUDAN
CHAD	LIBERIA	SWEDEN
CHILE	LIBYA	SWITZERLAND
CHINA	LIECHTENSTEIN	SYRIAN ARAB REPUBLIC
COLOMBIA	LITHUANIA	TAJIKISTAN
COMOROS	LUXEMBOURG	THAILAND
CONGO	MADAGASCAR	TOGO
COOK ISLANDS	MALAWI	TONGA
COSTA RICA	MALAYSIA	TRINIDAD AND TOBAGO
CÔTE D'IVOIRE	MALI	TUNISIA
CROATIA	MALTA	TÜRKİYE
CUBA	MARSHALL ISLANDS	TURKMENISTAN
CYPRUS	MAURITANIA	UGANDA
CZECH REPUBLIC	MAURITIUS	UKRAINE
DEMOCRATIC REPUBLIC	MEXICO	UNITED ARAB EMIRATES
OF THE CONGO	MONACO	UNITED KINGDOM OF
DENMARK	MONGOLIA	GREAT BRITAIN AND
DJIBOUTI	MONTENEGRO	NORTHERN IRELAND
DOMINICA	MOROCCO	UNITED REPUBLIC OF TANZANIA
DOMINICAN REPUBLIC	MOZAMBIQUE	UNITED STATES OF AMERICA
ECUADOR	MYANMAR	URUGUAY
EGYPT	NAMIBIA	UZBEKISTAN
EL SALVADOR	NEPAL	VANUATU
ERITREA	NETHERLANDS,	VENEZUELA, BOLIVARIAN
ESTONIA	KINGDOM OF THE	REPUBLIC OF
ESWATINI	NEW ZEALAND	VIET NAM
ETHIOPIA	NICARAGUA	YEMEN
FIJI	NIGER	ZAMBIA
FINLAND	NIGERIA	ZIMBABWE
FRANCE	NORTH MACEDONIA	
GABON	NORWAY	
GAMBIA, THE	OMAN	

The Agency's Statute was approved on 23 October 1956 by the Conference on the Statute of the IAEA held at United Nations Headquarters, New York; it entered into force on 29 July 1957. The Headquarters of the Agency are situated in Vienna. Its principal objective is "to accelerate and enlarge the contribution of atomic energy to peace, health and prosperity throughout the world".

IAEA-TECDOC-2090

# COATED PARTICLE FUELS FOR HIGH TEMPERATURE GAS COOLED SMALL MODULAR REACTORS

PROGRESS IN DESIGN, MANUFACTURING,  
EXPERIMENTATION, MODELLING  
AND ANALYSIS TECHNOLOGIES

INTERNATIONAL ATOMIC ENERGY AGENCY  
VIENNA, 2025

## COPYRIGHT NOTICE

All IAEA scientific and technical publications are protected by the terms of the Universal Copyright Convention as adopted in 1952 (Geneva) and as revised in 1971 (Paris). The copyright has since been extended by the World Intellectual Property Organization (Geneva) to include electronic and virtual intellectual property. Permission may be required to use whole or parts of texts contained in IAEA publications in printed or electronic form. Please see [www.iaea.org/publications/rights-and-permissions](http://www.iaea.org/publications/rights-and-permissions) for more details. Enquiries may be addressed to:

Publishing Section  
International Atomic Energy Agency  
Vienna International Centre  
PO Box 100  
1400 Vienna, Austria  
tel.: +43 1 2600 22529 or 22530  
email: [sales.publications@iaea.org](mailto:sales.publications@iaea.org)  
[www.iaea.org/publications](http://www.iaea.org/publications)

For further information on this publication, please contact:

Nuclear Fuel Cycle and Materials Section  
International Atomic Energy Agency  
Vienna International Centre  
PO Box 100  
1400 Vienna, Austria  
Email: [Official.Mail@iaea.org](mailto:Official.Mail@iaea.org)

© IAEA, 2025  
Printed by the IAEA in Austria  
May 2025  
<https://doi.org/10.61092/iaea.zyya-k9sd>

### IAEA Library Cataloguing in Publication Data

Names: International Atomic Energy Agency.  
Title: Coated particle fuels for high temperature gas cooled small modular reactors : progress in design, manufacturing, experimentation, modelling and analysis technologies / International Atomic Energy Agency.  
Description: Vienna : International Atomic Energy Agency, 2025. | Series: IAEA TECDOC series, ISSN 1011-4289 ; no. 2090 | Includes bibliographical references.  
Identifiers: IAEAL 25-01758 | ISBN 978-92-0-107625-0 (paperback : alk. paper) | ISBN 978-92-0-107525-3 (pdf)  
Subjects: LCSH: Nuclear reactors — Design and construction. | Nuclear reactors — Technological innovations. | Nuclear fuels. | Gas cooled reactors.

## FOREWORD

The high temperature gas cooled reactor (HTGR) concept is considered a promising nuclear reactor technology owing to its inherent safety and operational features. A typical example of a design feature unique to the HTGR core that imparts inherent safety to the system is the inert, single-phase coolant (helium gas) coupled with a high temperature, high heat capacity moderator (graphite), which can provide a longer time to respond to core heat-up accidents. With the potential of the HTGR to supply high temperature process heat, many other applications such as hydrogen production in addition to electricity generation are also viable.

Significant efforts have been made by several Member States to develop HTGRs for process heat, hydrogen production and electricity generation. With the feature of enhanced safety and modularity, HTGRs have recently been identified as a potentially viable small modular reactor (SMR) technology line. These reactors are primarily fuelled by tristructural isotropic (TRISO) coated particles. The main advantage of TRISO fuel is its capability to withstand extreme conditions like high temperature and prolonged irradiation.

Research programmes have been pursued in these Member States on the development of coated particle fuel technology including fuel design, manufacture, characterization, irradiation behaviour, accident tests and simulations of fuel behaviour.

The international experts who participated in the Consultancy Meeting on the Design, Fabrication and Operation of Small and Medium Sized or Modular Reactor Fuels, held in 2020, identified the need for a comprehensive review of HTGR particle fuel technologies (e.g. design, fabrication, characterization, irradiation performance, performance modelling) to support the development of high temperature gas cooled SMRs. This publication is intended to provide up-to-date information on coated particle fuel technologies to be used as a baseline reference to support the development and deployment of TRISO fuel technologies for HTGR type SMRs.

The IAEA is grateful to all those who actively contributed to the preparation of this publication. The IAEA officers responsible for this publication were K. Sim and A. Khaperskaia of the Division of Nuclear Fuel Cycle and Waste Technology.

## EDITORIAL NOTE

*This publication has been prepared from the original material as submitted by the contributors and has not been edited by the editorial staff of the IAEA. The views expressed remain the responsibility of the contributors and do not necessarily represent the views of the IAEA or its Member States.*

*Guidance and recommendations provided here in relation to identified good practices represent expert opinion but are not made on the basis of a consensus of all Member States.*

*Neither the IAEA nor its Member States assume any responsibility for consequences which may arise from the use of this publication. This publication does not address questions of responsibility, legal or otherwise, for acts or omissions on the part of any person.*

*The use of particular designations of countries or territories does not imply any judgement by the publisher, the IAEA, as to the legal status of such countries or territories, of their authorities and institutions or of the delimitation of their boundaries.*

*The mention of names of specific companies or products (whether or not indicated as registered) does not imply any intention to infringe proprietary rights, nor should it be construed as an endorsement or recommendation on the part of the IAEA.*

*The authors are responsible for having obtained the necessary permission for the IAEA to reproduce, translate or use material from sources already protected by copyrights.*

*The IAEA has no responsibility for the persistence or accuracy of URLs for external or third party Internet web sites referred to in this publication and does not guarantee that any content on such web sites is, or will remain, accurate or appropriate.*

## CONTENTS

1.	INTRODUCTION .....	1
1.1.	BACKGROUND .....	1
1.2.	OBJECTIVE .....	2
1.3.	SCOPE.....	2
1.4.	STRUCTURE .....	3
2.	DESIGN DESCRIPTION AND DESIGN REQUIREMENTS.....	4
2.1.	GENERAL DESCRIPTION OF COATED PARTICLES AND FUEL ELEMENTS .....	4
2.2.	DESIGN BASES .....	5
2.3.	DESIGN CONSIDERATIONS .....	6
2.3.1.	Kernel.....	6
2.3.2.	Buffer layer .....	10
2.3.3.	Inner pyrocarbon layer.....	12
2.3.4.	SiC layer .....	19
2.3.5.	Outer pyrocarbon layer .....	20
2.3.6.	Fuel element (spherical pebble or cylindrical compact).....	21
2.4.	SUMMARY AND DISCUSSION .....	22
3.	UPDATES IN MEMBER STATES .....	23
3.1.	CANADA .....	23
3.2.	CHINA.....	24
3.3.	REPUBLIC OF KOREA .....	26
4.	COATED PARTICLE FUEL MANUFACTURING.....	29
4.1.	FUEL KERNEL MANUFACTURING .....	29
4.1.1.	Powder metallurgical process .....	29
4.1.2.	Sol-gel process .....	29
4.1.3.	Gel precipitation process for UO <sub>2</sub> kernels .....	30
4.2.	CERAMIC COATINGS BY FLUIDIZED BED CHEMICAL VAPOUR DEPOSITION.....	35
4.3.	FABRICATION OF SPHERICAL FUEL ELEMENTS.....	38
4.3.1.	Preparation of resonated graphitic matrix powder.....	39
4.3.2.	Overcoating of the TRISO particles .....	41
4.3.3.	Moulding and pressing of fuel spheres with TRISO particle .....	42
4.4.	FABRICATION OF COMPACT FUEL ELEMENTS .....	43
4.5.	SUMMARY AND DISCUSSION .....	43
5.	QUALITY CONTROL FOR FUEL PARTICLE CHARACTERIZATION .....	44
5.1.	QUALITY CONTROL METHODS .....	44
5.1.1.	Particle size measurement.....	47
5.1.2.	Kernel, buffer and coating layer density and thickness measurement .....	47

5.1.3.	Anisotropy measurement .....	47
5.1.4.	Phase contrast radiography .....	48
5.1.5.	Burn-leach testing .....	49
5.1.6.	Fuel elements .....	49
5.2.	QUALITY CONTROL RESULTS .....	50
5.2.1.	UO <sub>2</sub> kernel results .....	52
5.2.2.	Coated particle results.....	53
5.2.3.	Fuel elements .....	55
5.3.	SUMMARY AND DISCUSSION .....	56
6.	IRRADIATION TESTS, HEATING TESTS AND POST IRRADIATION EXAMINATIONS.....	57
6.1.	TESTS CONDUCTED BEFORE THE EARLY 2000S .....	57
6.1.1.	Spherical pebbles .....	57
6.1.2.	Cylindrical compacts .....	61
6.1.3.	Loose TRISO particle fuels .....	62
6.2.	PROGRESS ON TESTS SINCE THE EARLY 2000S.....	62
6.2.1.	Spherical pebbles .....	62
6.2.2.	Cylindrical compacts .....	87
6.2.3.	Loose TRISO particle fuels .....	114
6.2.4.	Overall comparison of available irradiations in terms of fission gas release .....	114
6.3.	REQUIREMENTS FOR FUTURE IRRADIATION TESTS .....	114
6.4.	SUMMARY AND DISCUSSION .....	117
7.	FUEL PERFORMANCE ASSESSMENTS .....	118
7.1.	FISSION PRODUCTS .....	118
7.1.1.	Fission product yields and inventory .....	118
7.1.2.	Fuel chemistry.....	118
7.1.3.	Chemical state and location of fission products in a TRISO particle fuel .....	122
7.1.4.	Fission product transport .....	137
7.1.5.	Fission product release.....	147
7.2.	EFFECT OF FABRICATION DIFFERENCES ON FUEL PERFORMANCE.....	153
7.2.1.	Pyrocarbon anisotropy and density.....	153
7.2.2.	Nature of the IPyC-SiC interface.....	154
7.2.3.	SiC microstructure .....	154
7.3.	TENSILE STRESSES IN SiC LAYER AND FUEL FAILURES.....	155
7.4.	PARAMETERS AFFECTING FUEL PERFORMANCE .....	157
7.5.	FUEL FAILURE MECHANISMS.....	158
7.5.1.	Overpressure .....	160
7.5.2.	Inner pyrocarbon layer related issues leading to SiC failure .....	160
7.5.3.	Outer pyrocarbon layer related issues leading to SiC failure .....	163
7.5.4.	Factors directly leading to SiC failures.....	164
7.5.5.	Kernel-coating mechanical interaction .....	168
7.5.6.	As-manufactured defects .....	169
7.5.7.	Failure mechanisms during accidents .....	169
7.6.	PARAMETERS AFFECTING PARTICLE PERFORMANCE DURING NORMAL OPERATING CONDITIONS.....	169

7.6.1.	Kernel.....	169
7.6.2.	Buffer layer .....	170
7.6.3.	Inner pyrocarbon layer.....	171
7.6.4.	Silicon carbide layer .....	171
7.6.5.	Outer pyrocarbon layer .....	172
7.6.6.	Fuel element.....	172
7.6.7.	Summary .....	173
7.7.	FUEL FAILURES DURING NORMAL OPERATIONS .....	174
7.7.1.	German fuel .....	174
7.7.2.	Chinese fuel .....	174
7.7.3.	US fuel .....	175
7.7.4.	Japanese fuel.....	177
7.7.5.	Summary.....	179
7.8.	FUEL FAILURES UNDER ACCIDENT CONDITIONS.....	180
7.8.1.	Summary of parameters of high importance identified for accident conditions.....	194
7.8.2.	Fuel failures under accident conditions (corresponding to core heat up) .....	198
7.8.3.	Fuel failures under accident conditions (corresponding to reactivity insertion accident).....	202
8.	FUEL MODELLING AND CODE DEVELOPMENTS .....	204
8.1.	MODELLING OF COATED PARTICLE FUEL PERFORMANCE ..	204
8.1.1.	Fuel burnup and depletion .....	204
8.1.2.	Pressure build-up in a coated particle .....	204
8.1.3.	Failure of pressure-bearing layers.....	205
8.1.4.	Kernel migration .....	206
8.1.5.	Fission product attack .....	207
8.1.6.	Thermal decomposition .....	208
8.1.7.	Failure analysis for a batch of particles .....	208
8.1.8.	Fission product releases from a coated particle .....	209
8.1.9.	Fission product releases into the coolant .....	211
8.2.	DEVELOPMENT OF COATED PARTICLE FUEL PERFORMANCE ANALYSIS CODES .....	215
8.3.	SUMMARY AND DISCUSSION .....	228
	REFERENCES.....	229
	ANNEX I.....	241
	ANNEX II. ....	245
	LIST OF ABBREVIATIONS .....	253
	CONTRIBUTORS TO DRAFTING AND REVIEW .....	257



# 1. INTRODUCTION

## 1.1. BACKGROUND

High temperature gas cooled reactor technology has the following operational and safety distinctive characteristics compared to light water reactors (LWRs):

- Higher thermal efficiencies due to higher operating temperatures;
- Limited fuel temperature after a loss-of-coolant accident (LOCA) due to lower power-density and higher heat-capacity core;
- No release of explosive hydrogen gas under accident conditions due to the absence of Zr and water;
- Capability of on-power refuelling (depending on design).

The HTGR technology has evolved over several decades through the development of several designs. The historical path of the HTGR technology can be summarized as follows [1]:

- Deployment of early Gas Cooled Reactors (GCRs), which was characterized by graphite moderator and CO<sub>2</sub> gas coolant. Examples included Magnox reactors and Advanced Gas Cooled Reactors (AGRs) in UK, the Uranium Naturel Graphite Gaz reactor in France and GCRs in Italy, Japan and Spain;
- Deployment of HTGR prototype plants, which was demonstrated by UK's Dragon reactor, German Arbeitsgemeinschaft Versuchs Reaktor (AVR) and US Peach Bottom 1;
- Deployment of HTGR demonstration plants, which was demonstrated by Fort St. Vrain GCR in US, and Thorium High Temperature Reactor 300 (THTR-300) in Germany;
- Development of large HTGR steam cycle plants, which was demonstrated by German High Temperature Reactor HTR-500, Russian VG-400, and US HTGR steam cycle plants;
- Development of modular HTGR steam cycle plants, which was demonstrated by HTR-Module and HTR-100 in Germany, Russian VGR, Modular HTGR (MHTGR) in US, High Temperature Test Reactor (HTTR) in Japan, and HTR-10 and HTR-PM in China;
- Development of Gas Turbine-Modular Helium Reactor (GT-MHR). Examples included Pebble Bed Modular Reactor (PBMR) developed in South Africa, GTHTR-300 in Japan and ACACIA in Netherlands;

Two types of HTGRs exist: pebble bed and prismatic types. The pebble bed type contains pebble shape fuel elements in a cylindrical pressure vessel. The prismatic type contains cylindrical compacts as fuel elements inserted in the hexagonal graphite blocks in a cylindrical pressure vessel. Each spherical pebble or cylindrical compact contains thousands of coated particles.

Significant efforts have been made by several Member States to develop HTGRs for process heat, hydrogen production and electricity generation. Currently designed HTGRs have been considered as SMRs with significantly enhanced safety features compared to older large HTGR designs and modularity. (Annex I lists high temperature gas cooled SMRs and also advanced HTGR-type reactors.)

These high temperature gas cooled SMRs are characterized with the following features:

- Small to medium reactor power ranging from 100<sup>1</sup> to 300 MWe;

---

<sup>1</sup> Power of demonstration plants (HTR-10, HTTR-30) were lower than 100 MWe.

- Modularity<sup>2</sup> to target the economics of serial production with shorter construction time;
- Use of tri-structural isotropic (TRISO) particle fuel.

From fuel performance aspects, power density, burnup and fast neutron fluence are important operating parameters to be taken into account to ensure the safe and reliable operation of the fuel in a reactor. High power density can lead to high operating temperature and consequently can increase the probability to be at the risk of fuel failure and undesirable release of fission products at extended burnups during operation.

The main advantage of TRISO fuel is its capability to withstand extreme conditions like high temperature and prolonged irradiation. The components of TRISO fuel such as multiple protective layers, a fissile kernel, a buffer layer and a silicon carbide layer have been refined significantly for showing structural integrity, fission product retention and mechanical strength under irradiation. The fuel kernel of TRISO particles consists of uranium dioxide (UO<sub>2</sub>), uranium carbide (UC), or uranium oxycarbide is the primary source of fission energy. The buffer carbon layer absorbs fission gases and mitigates the mechanical stresses caused by kernel swelling. By enhancing the porosity and thickness, fission gas retention capacity has been improved without deteriorating the structural integrity. The inner and outer pyrolytic carbon layers (IPyC & OPyC) provide structural support, fission gas barrier, and protect the silicon carbide the layer, the main barrier for metallic fission products. Its excellent characteristics showing improved strength, thermal conductivity, and radiation resistance make it an essential element of TRISO fuel.

Research programmes on TRISO particle fuel development have been pursued in several Member States focusing on design, fabrication, characterization, in-reactor behaviour and its prediction, accident tests and simulation under normal operating and accident conditions.

Earlier IAEA publications [2–5] documented available results of such research programmes on TRISO particle fuel up to 2010.

## 1.2. OBJECTIVE

The main objective of the publication is to provide an up-to-date compilation of information on technological progress in design, manufacturing, experimentation, modelling, and analysis technologies for HTGR coated particle fuels, and to identify the major challenges and prospects for use of these coated particle fuels in high temperature gas cooled SMRs.

## 1.3. SCOPE

This publication addresses:

- General description of major design features along with design bases of coated particle fuels;
- Overall information on fuel manufacturing technology;
- Overall information on fuel particle characterization methods, quality assurance and quality control;
- Overview on irradiation tests and annealing tests;
- Irradiation performance, fission product release under accident conditions, and failure mechanisms;
- Capabilities of fuel performance analysis codes.

---

<sup>2</sup> The term ‘modularity’ refers to the ability to fabricate major components of the nuclear steam supply system in a factory environment and ship to the point of use.

## 1.4. STRUCTURE

The rationales and purpose of developing this publication are described above in this section.

Major design characteristics of TRISO particle fuel are described in Section 2 along with design bases.

R&D activities are underway in some Member States to set up manufacturing process for TRISO particle fuel and to develop advanced coated particle fuel (e.g. fully ceramic microencapsulated fuel). The status of such R&Ds is described in Section 3.

The manufacturing processes used to produce TRISO particle fuel and related production quality control practices are described in Section 4 and Section 5, respectively.

There have been a number of irradiation tests and post-irradiation heating tests conducted on coated particle fuels since 1970s. Important tests are summarized in Section 6 with a description of highlighted post-irradiation examination (PIE) results. Key phenomena affecting the in-reactor performance of coated particle fuel, observed from these irradiation and heating tests, are discussed in Section 7, with respect to fuel failure mechanisms.

Fuel modelling and computer codes for predicting the thermal-mechanical behaviour of TRISO particle fuel in the reactor are described in Section 8. International benchmarking exercises of fuel performance analysis codes are briefly described.

Annexes contain useful supplemental information:

- Annex I provides a list of high temperature gas cooled SMRs and also advanced HTGR-type reactors;
- Annex II provides the design specifications of TRISO particle fuels developed by various fuel vendors or developers.

## 2. DESIGN DESCRIPTION AND DESIGN REQUIREMENTS

### 2.1. GENERAL DESCRIPTION OF COATED PARTICLES AND FUEL ELEMENTS

The essential component of HTGR fuel is the TRISO particle. A TRISO particle contains a ceramic kernel of fuel materials, surrounded by four coating layers that function collectively as an effective fission product barrier. These TRISO coatings begin with a low density, porous, non-load bearing carbon layer (i.e. buffer layer) that surrounds the fuel kernel. The buffer layer is surrounded by three load-bearing composite layers that consist of two high density, isotropic pyrocarbon (PyC) layers (i.e. the inner PyC (IPyC) and outer PyC (OPyC)), and a very dense silicon carbide (SiC) layer in between. These load-bearing composite layers are intended to withstand the pressure of the generated fission products and to form an essentially leak-tight barrier to fission product release.

The TRISO particles are embedded in a matrix made of special grade graphite in the form of spheres for a pebble bed HTGR or in the form of cylindrical compacts to be loaded into the hexagonal blocks in a prismatic HTGR (see Fig. 1).

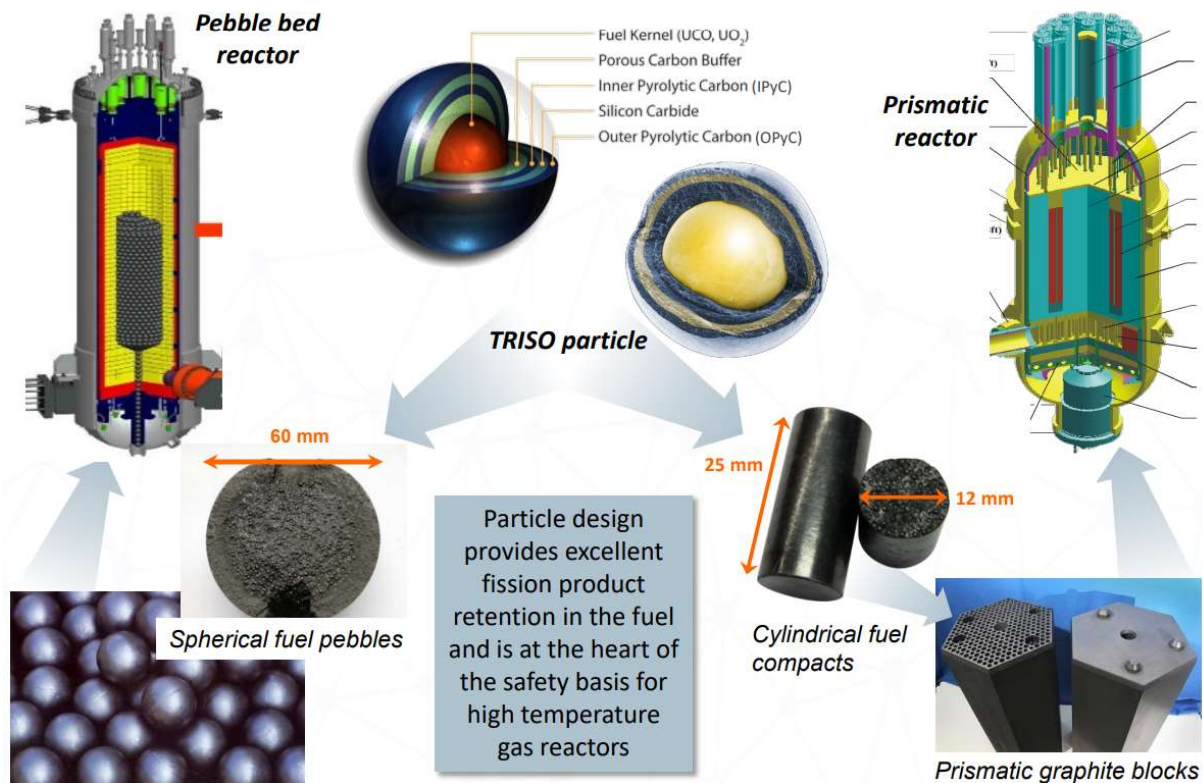


FIG. 1. TRISO particle in a pebble and in a compact made from special grade graphite matrix (reproduced from Ref. [6], courtesy of Idaho National Laboratory (INL)).

Figure 2 shows the cross-sectional view of a TRISO particle with the description of the intended role of each layer. In the figure, some typical values are shown, though values may vary from one design to another. For example, while the kernel diameter varies between 350 to 500  $\mu\text{m}$  in the US, German and Chinese designs, it is 600  $\mu\text{m}$  in the Japanese HTTR design where an annular fuel compact design is adopted.

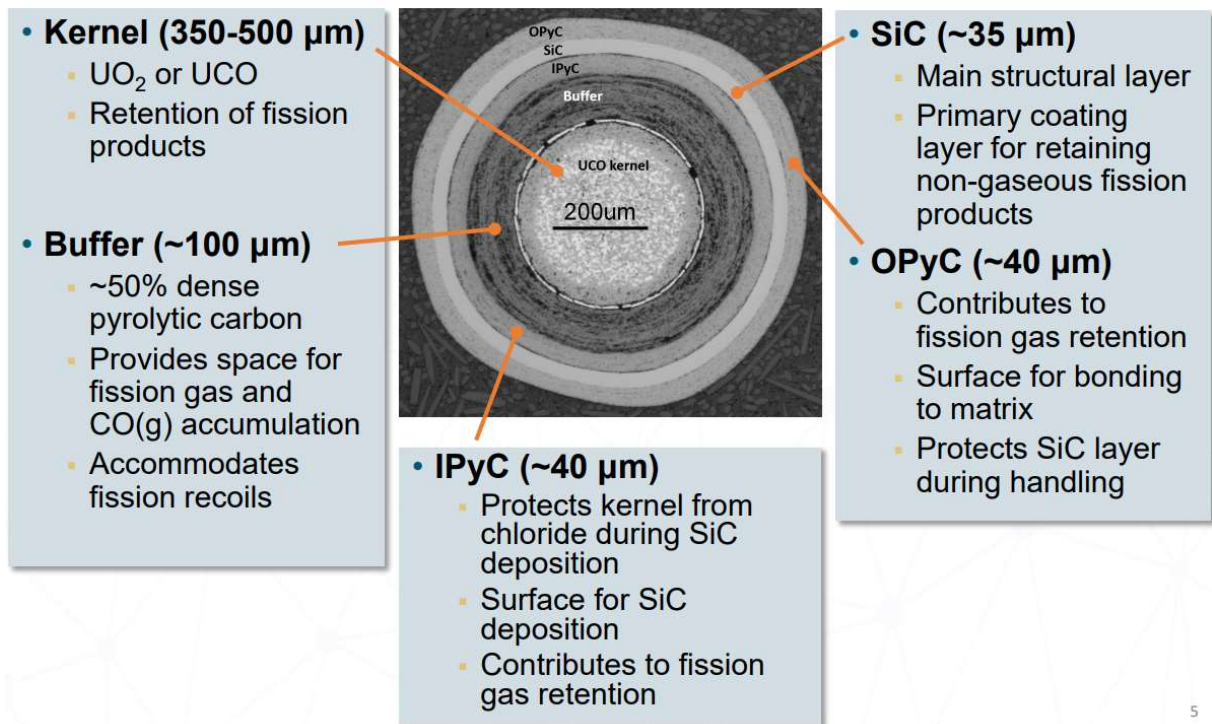


FIG. 2. Cross-sectional view of a TRISO particle fuel with typical dimensions (reproduced from Ref. [6], courtesy of INL).

## 2.2. DESIGN BASES

According to the IAEA Safety Standard, Specific Design Requirements SSR-2/1 (Rev. 1) [7], the fuel and reactor core are required to be designed based on the concept of defence in depth, to fulfil the fundamental reactor safety functions. The fundamental safety functions as they apply specifically to the design of the reactor core are:

- Control of reactivity;
- Removal of heat from the reactor core;
- Confinement of radioactive material.

In order to achieve the fundamental safety function (c) above, the fuel is designed and manufactured to minimize the release of fission products from the fuel, and together with other means, such as purification systems, the radionuclide activity in the coolant is maintained ‘as low as reasonably achievable (ALARA)’.

Defective TRISO particles may be produced during the fabrication process or in the reactor during normal operation (e.g. a missing layer due to the flaw in the quality assurance of the manufacturing process can produce a defect in the particle during normal operation). A rigorous quality assurance and quality control approach is applied to the manufacturing process to ensure that the manufactured fuel quality specifications are met.

To ensure good performance of TRISO particle fuel, all mechanisms that result in the degradation of the collective fission product barrier (that is, the fuel kernel, the TRISO coating of particles and the matrix surrounding these particles in a spherical fuel pebble or a cylindrical fuel compact) need to be examined.

Design limits<sup>3</sup> or acceptance criteria<sup>4</sup> are established to prevent significant degradation of these fission product barriers. (See Ref. [9] for some examples of design limits or acceptance criteria used for TRISO particle fuel.)

The design of the fuel ensures that a sufficient margin exists to the design limits (or acceptance criteria) to prevent any failure of the collective fission product barrier of the fuel. This necessitates design and safety analysis tools based on the fundamental understanding of damage/failure mechanisms and supporting experiments.

## 2.3. DESIGN CONSIDERATIONS

In this section, design considerations for determining critical parameters of the different components of the coated particle fuel are described. Fuel design specifications developed by various vendors or developers are described in Annex II for information.

### 2.3.1. Kernel

A variety of fissile and fertile kernels including ThC<sub>2</sub>, ThO<sub>2</sub>, PuO<sub>2</sub>, (Th,U)O<sub>2</sub>, UC<sub>2</sub>, UO<sub>2</sub>, UCO [10] and UN [11] have been fabricated and tested; among these, UO<sub>2</sub> and UCO (a two-phase mixture of UO<sub>2</sub> and UC<sub>2</sub>) are the fissile materials that are most commonly considered for recent reactor designs. Much experience has been gained with UO<sub>2</sub> kernels.

UCO kernels were originally proposed to better control CO gas production and thereby mitigate its negative impacts on fuel performance [12]. A significant amount of performance data has been collected in the US in the last two decades [13]. This fuel type is considered, in particular, for applications where fuel will experience relatively high burnup (10–20% fissions per initial metal atoms (FIMA)<sup>5</sup>) and high temperatures (i.e. ~1200°C).

The two phases, UC<sub>2</sub> and UO<sub>2</sub>, interact in the following way [14]:

- As oxygen is liberated from fissioning, it first oxidizes the UC<sub>2</sub> and rare earth elements (e.g. Sm, La, Nd, Pr, Ce, Y) because they have the greatest affinity for oxygen;
- Once UC<sub>2</sub> and rare earth elements are oxidized, oxygen is available for some of the elements with less affinity, such as Sr, Eu, Zr, and Ba, which formed originally carbides from the liberated carbon from UC<sub>2</sub>;
- Finally, only at the end of life, there is enough oxygen for CO production;

The goal is to balance this final CO production point (e.g. by defining the burnup accordingly or at the end of life).

---

<sup>3</sup> The term ‘design limits’ is used in SSR-2/1 (Rev.1) [7]: In Requirement 15, it is stated that “a set of design limits consistent with the key physical parameters for each item important to annealing for the nuclear power plant shall be specified for all operational states and for accident conditions”.

<sup>4</sup> The term ‘acceptance criteria’ is defined in the IAEA Safety Glossary [8] as “Specified bounds on the value of a functional indicator or condition indicator used to assess the ability of a structure, system or component to perform its design function”.

<sup>5</sup> FIMA stands for fissions per initial metal atom. Depending on the neutron energy spectrum and the proportions of fast fissions in <sup>238</sup>U and in <sup>235</sup>U/<sup>239</sup>Pu/<sup>241</sup>U, the conversion factor ranges from 9.38 to 9.75 GWd/tU per 1% FIMA, and a mid-range value of 9.5 GWd/tU/FIMA is often used.

For the fuel utilizing TRISO particle with High Assay Low Enriched Uranium (HALEU), we may assume that the conversion factor from FIMA to GWd/tU established for LWR fuel with up to 5 wt.% enrichment for the thermal energy spectrum corresponding to LWR type of reactors are applicable to thermal gas cooled reactor fuel.

At low to moderate burnups (e.g. 10% FIMA) under normal operating conditions, the kernel can retain ~50% of total fission products generated. Gas retention of the kernel diminishes with burnup and is often assumed to be nil for accidents [14].

Several issues have been identified with the production of CO, which is associated with an increase in the oxygen potential in the fuel kernel (by fissioning the U in UO<sub>2</sub>) and subsequent reaction with the carbon buffer layer:

- Increase of pressure in the particle due to CO (see Section 2.3.1.1);
- Corrosion of the SiC layer by CO;
- ‘Amoeba effect’ or the kernel migration (see section 2.3.1.2).

### 2.3.1.1. CO pressure

The fission products, carbon and uranium, all compete for the liberated oxygen from UO<sub>2</sub> (due to fissioning) in this closed system, and the system oxygen potential determines which elements are oxidized for a limited amount of oxygen. The carbon buffer layer can react with the liberated oxygen from UO<sub>2</sub> to form CO. CO production can increase the particle pressure and hence its failure likelihood. Furthermore, in the presence of a thermal gradient, CO can cause kernel migration.

Another reason for the control of the oxygen potential is to ensure that the rare earth elements are oxidized and thus immobilized in the kernel, preventing migration to the SiC layer and reaction with it.

Consequently, the oxygen potential is controlled either by limiting burnup or by tailoring the kernel composition. For the latter, UCO kernels has been developed and employed since the 1970s [14].

In pure UO<sub>2</sub> fuel the oxygen potential increases as a function of burnup and results in the production of CO, which in turn increases the pressure in the particle. The effect of burnup and temperature on the CO pressure is described in [14] and is represented in Table 1.

TABLE 1. EFFECT OF BURNUP AND TEMPERATURE ON CO PRESSURE

UO <sub>2</sub> burnup	Oxygen potential (kcal/mol)	T(K)/(°C)	P <sub>co</sub> (atm)
Low (< 10% FIMA)	-100	1300 / 1027	1
		1600 / 1327	5
High (> 10% FIMA)	-75	1300 / 1027	580
		1600 / 1327	1300

To prevent overpressure failure of the SiC, a simple calculation was carried out using the stress equation [14] to define an allowable particle internal pressure as:

$$\sigma = \frac{rP}{2t} \rightarrow P_{max} = \frac{UTS_{SiC}2t}{r} \approx 80 \text{ MPa} \quad (1)$$

where  $P_{max}$  includes all the pressure that is applied by fission gases Xe and Kr, and CO;  $UTS_{SiC}$  is the ultimate tensile strength of SiC and it is 350 MPa;  $t$  is the SiC thickness and it is 35 μm;  $r$  is the SiC layer radius and it is 310 μm.

It is noted that the krypton and xenon pressures depend on burnup. This equation simply sets a limit (for designers) for internal pressure to avoid overpressurization of the SiC layer, and the result will be dependent on particle dimensions and burnup, which has an impact on the fission gas inventory.

To avoid the problems associated with CO production, several approaches are considered:

- Making a sub-stoichiometric kernel and thus limiting the amount of oxygen available for CO production. This is possible with plutonium, but not with uranium [14];
- Including a ‘getter’ material (e.g. ZrC) in or near the kernel to absorb the released oxygen and make it unavailable for CO production, though it involves greater complexity in particle production [14,15];
- Making a two-phase kernel consisting of both carbide and oxide phases, which is known as UCO [14,15];
- Reducing the kernel size; reducing kernel size as enrichment/burnup increases will reduce CO and fission gas pressures;
- Replacing the SiC layer with ZrC. ZrC was indicated [15] to have great potential/performance capability as a coating for particle fuel, based on some testing.

### 2.3.1.2. Amoeba effect – Carbon transportation from the hot side to the cool side

In the presence of a temperature gradient, carbon transfers from one side of the kernel to another, known as ‘Amoeba’ effect (see Fig. 3). This effect can also be observed in UC<sub>2</sub>, though it is particularly important for UO<sub>2</sub>. The net effect of this carbon transport is the gradual movement of the kernel in the direction of increasing temperature so that the kernel moves toward the SiC layer and it may damage the layer. Particle failure is assumed to occur when the kernel touches the SiC layer.

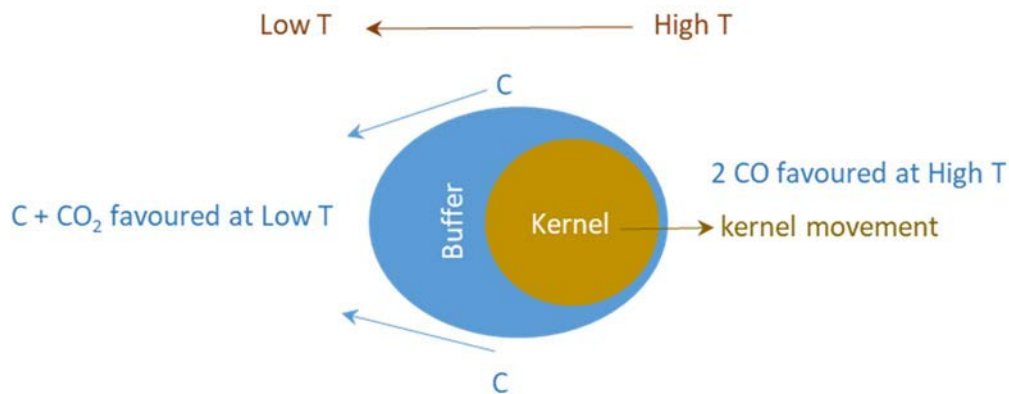


FIG. 3. Illustration of the amoeba effect.

The kernel migration/movement,  $\Delta x$  in meters, can be calculated [14] as:

$$\Delta x = KMC \frac{1}{T^2} \frac{dT}{dx} t \quad (2)$$

where  $t$  is time in seconds,  $T$  is the temperature in Kelvin, and  $KMC$  is the kernel migration coefficient in m<sup>2</sup>K/s. Typical  $KMC$  values at 1300 K are [14]:

- LEU (low enriched uranium) UCO:  $9 \times 10^{-13}$  m<sup>2</sup> K/s;
- LEU UO<sub>2</sub>:  $6 \times 10^{-11}$  m<sup>2</sup> K/s;
- UC<sub>2</sub>:  $9 \times 10^{-13}$  m<sup>2</sup> K/s.

The amoeba effect has been identified to be a concern for the fuels using  $UC_2$  and  $UO_2$  kernels in large (1000 MWe) HTGR designs [14]. For the reactor systems with low power and low burnup below  $\sim 10\%$  FIMA, the amoeba effect may not be of significant concern for  $UO_2$  fuel kernel [14]. Since CO production is minimized in the UCO kernel and solid-state carbon transport through the UCO is very low, it is expected that kernels with UCO will significantly reduce the amoeba effect.

### 2.3.1.3. Asphericity

In a study to investigate the impact of various particle properties on calculated failure probability [16], it is stated that “aspherical particles can generate tensile stresses in the SiC layer and cause failure”. The failure probability of SiC layer for deviations from particle sphericity (indicated as ‘aspect ratio’) is shown in Fig. 4 [16]. The probability of failure increases with increasing aspect ratio (or asphericity), where 1 indicates perfect spherical shape. Then, the cumulative failure fraction was calculated by numerical integration of the SiC failure (due to asphericity) probability curve shown in Fig. 4.

On the cumulative failure fraction curve, the point at which the particle becomes increasingly susceptible to failure is determined as the critical limit [16]. For the aspect ratios varying between 1.0 and 1.24, of the value 1.06 was determined as the critical limit for SiC failure due to particle asphericity [16], above which the failure probability increases significantly.

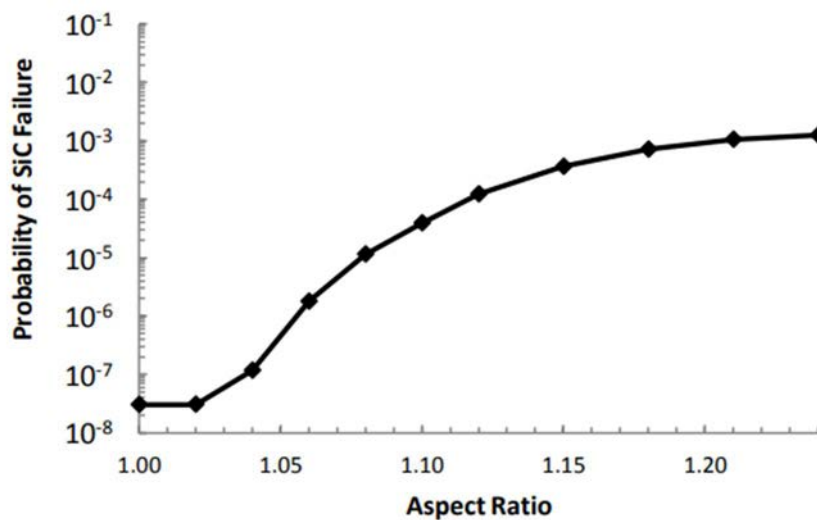


FIG. 4. Probability of SiC failure due to particle asphericity (reproduced from Ref. [16], courtesy of INL).

### 2.3.1.4. Kernel design parameters

Specifications for kernels are somewhat different from LWR fuel pellets. For example, for TRISO particle kernels there is less concern with grain structure or size and pores. Important kernel design parameters and their rationales are described in Ref. [14] and are represented in Table 2 (based on the information in Ref. [14]).

TABLE 2. KERNEL DESIGN PARAMETERS

Kernel design parameters	Rationale
Diameter	Diameter affects the power generation and hence generation of fission products.
Density	Density affects the amount of fissile material available in the particle as well as the degree to which the kernel can retain fission products (at least at lower burnup). In addition, it affects the kernel reactivity with chlorine during the SiC coating process.
Sphericity	Sphericity affects the coating uniformity (stress distribution in coating layers). Significant deviations from sphericity can result in high local stress in the coating layers. It is desirable to have a round kernel or a kernel with little deviations from sphericity.
Stoichiometry for UO <sub>2</sub> : uranium to oxygen ratio	Stoichiometry in UO <sub>2</sub> kernel affects the CO production, resulting in higher pressures in the particle and kernel migration. Hypo-stoichiometry (i.e., oxygen to metal ratio O/M < 2) may be preferable to decrease the C-O reaction, but it is difficult to achieve hypo-stoichiometry in UO <sub>2</sub> .
Stoichiometry for UCO: uranium to oxygen ratio and uranium to carbon ratio	Stoichiometry in UCO kernel affects CO production and oxidation of rare earths (e.g. Sm, La, Nd, Pr, Ce, Y), which is directly related to the retention of rare earth elements in the kernel.
Purity	Impurities may affect the chemical (i.e., reactions) and nuclear (i.e., neutron absorber, poison) behaviour of the fuel
Enrichment	Enrichment affects the power density, burnup, and radiotoxicity in the spent fuel.

### 2.3.2. Buffer layer

As the first layer surrounding the kernel, the thickness and the density of the buffer layer plays an important role in the attenuation of fission product recoil and in the accommodation of gases. In the majority of current TRISO particle designs, the thickness of the buffer layer is 100  $\mu\text{m}$ , and the density is approximately 50% theoretical density (TD). In case of LWR fuel, high energetic fission products are slowed down and stopped by dense UO<sub>2</sub> in the range of 10  $\mu\text{m}$ . However, in low-density materials, such as carbon, the range of the recoils can be longer. The buffer layer captures fission-produced recoils originating on the surface of the kernel and shields the IPyC from recoil damage. This indicates that it is important to have a thicker buffer layer. While a denser carbon layer may be preferable to slow down and stop the fission-produced recoils in a shorter distance, low-density carbon is desirable for the buffer layer to accommodate gases, serving as a gas plenum or void volume. This discussion supports thicker and low-density buffer layer to have a better control on particle pressure. On the other hand, a thinner buffer layer is also taken into account from heat transfer aspect: the thermal conductivity of the buffer is not as high as the other coatings and there is a more substantial temperature drop across this layer. Therefore, the buffer layer thickness is optimized for gas pressure and heat transfer. Finally, the buffer layer can serve as a sacrificial layer, as it can distort to accommodate kernel swelling. Important buffer layer design parameters and their rationales are described in [14] and summarized in Table 3 (based on the information in Ref. [14]).

TABLE 3. BUFFER LAYER DESIGN PARAMETERS

Buffer layer design parameters	Rationale
Thickness	Both thickness and density affect: 1) Void volume available for gases – low density and thicker layer may be preferable to accommodate gases; 2) Fission product recoil attenuation – thicker and high-density layer may be preferable to reduce the fission product attenuation range; 3) Flexibility for distortion to accommodate kernel swelling – thicker and low-density layer may be preferable to accommodate kernel swelling.
Density	Heat transfer is also affected by the density and the thickness of the buffer layer. Denser and thinner layer may be preferable for a better heat transfer. Overall, density and thickness need to be optimized for better gas retention and heat transfer.

With the increase of the buffer thickness, the free volume for storing fission gas increases. As a result, pressure becomes lower and stress in the SiC layer becomes lower. Probability of SiC layer failure decreases with increasing layer thickness (as shown in Fig. 5).

A lower critical limit of 50  $\mu\text{m}$  for the buffer layer thickness was determined for SiC failure, below which the failure probability increases significantly. Note that the cited study [16] was based on a nominal particle design with a 425  $\mu\text{m}$  diameter UCO kernel with 15.5%  $^{235}\text{U}$  enrichment and a peak burnup of 16% FIMA.

Different particle designs and operating conditions will produce unique results with regard to coating layer optimization. The intent is to demonstrate that such analysis can be applied to optimize the parameters of interest (e.g. layer thickness) for a given layer for TRISO particles that would be employed under different conditions.

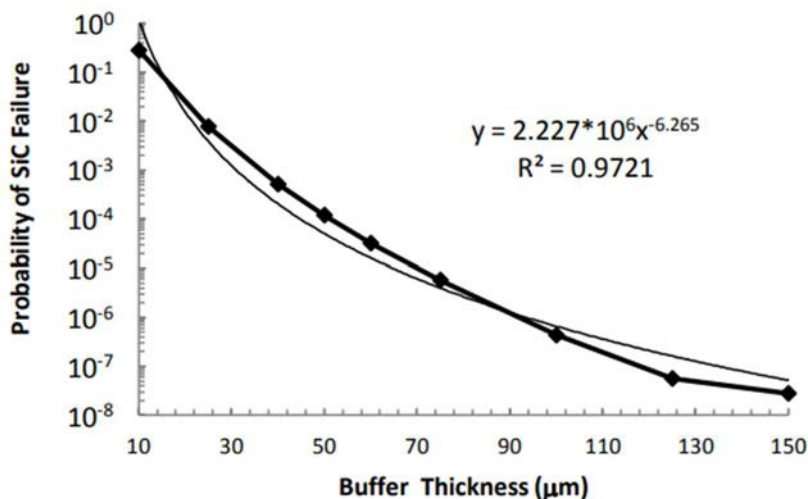


FIG. 5. Probability of SiC failure due to buffer layer thickness (reproduced from Ref. [16], courtesy of INL).

### 2.3.3. Inner pyrocarbon layer

The high density inner pyrocarbon layer (IPyC) is deposited on the buffer layer and provides a smooth surface for SiC deposition. It is the layer that protects both the kernel and SiC layer. In the absence of the inner pyrocarbon layer, during the SiC deposition process, liberated chlorine (in the form of hydrochloric acid, HCl) from the process would easily migrate to the kernel through the buffer layer and react with uranium, producing volatile chlorides. In this case, it would be highly likely that these chlorides would transport the uranium out of the kernel and contaminate the coatings [14]. Consequently, uranium fissioning would occur outside the kernel in the contaminated layers resulting in increase of fission product transport and releases.

The IPyC is an effective layer for gas retention and delays the transport of fission products to the SiC layer. The IPyC thickness influences stress in the IPyC layer and thus its propensity to fail: the failure probability increases as the IPyC layer thickness increases [16]. This is due to the increase in pyrocarbon material causing an increase in shrinkage early in irradiation, increasing the tensile stress in the IPyC layer and resulting in a higher IPyC cracking probability, which in turn can cause localized stress concentrations in the SiC layer [16].

An analysis of the effect of IPyC thickness on particle failure probability [16] was performed to determine the critical value for the IPyC layer thickness. As the IPyC layer thickness increases, the probability of SiC layer failure increases as shown in Fig. 6. An upper critical limit of 52  $\mu\text{m}$  for the IPyC layer thickness was determined for SiC failure, above which the failure probability increases significantly. It is noted that the study was performed under a specific condition, but similar analysis can be applied to optimize the parameters of interest (e.g. layer thickness).

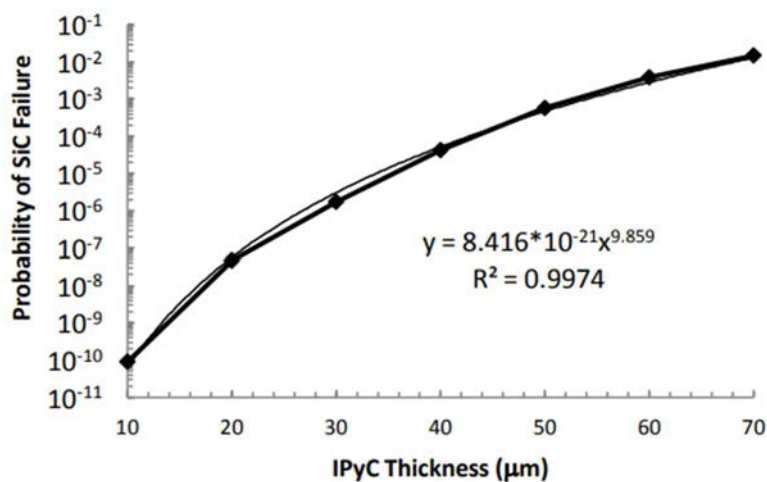


FIG. 6. Probability of SiC failure due to IPyC layer thickness (reproduced from Ref. [16], courtesy of INL).

IPyC density determines dimensional change and thus determines IPyC failure probability [16]. The failure probability decreases with increasing IPyC density, as shown in Fig. 7. An upper<sup>6</sup> critical limit of 2.0  $\text{g}/\text{cm}^3$  for the IPyC layer density was determined for SiC failure.

---

<sup>6</sup> It was not clarified in Ref. [16] why 2.0  $\text{g}/\text{cm}^3$  was chosen to be the upper limit and there is no information on failure probabilities beyond 2.0  $\text{g}/\text{cm}^3$ ; however, the attainable density of 2.0  $\text{g}/\text{cm}^3$  for pyrocarbon can be interpreted as both the upper and lower limit because, practically, higher densities cannot be achieved and the probability of failure is the lowest for 2.0  $\text{g}/\text{cm}^3$ .

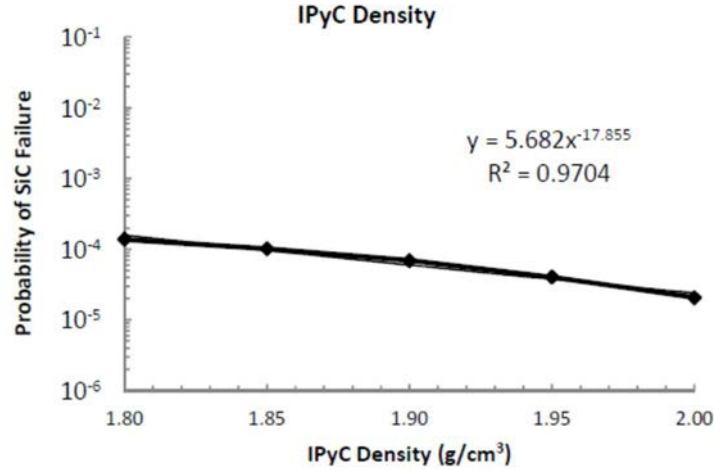


FIG. 7. Probability of SiC failure due to IPyC layer density (reproduced from Ref. [16], courtesy of INL).

High density pyrolytic carbon behaves similarly with a polycrystalline material. The properties of each crystallite are inherently anisotropic, as represented by, for example, thermal expansion and fast neutron induced shrinkage. For macroscopic graphite samples, macroscopic material anisotropy is defined by Bacon Anisotropy Factor (BAF) that can be measured by X-ray diffraction [4]. (Note that because of the very small dimensions of the coated particle layers, normal X-ray diffraction is not effective.) It is noted from [4] that “The intensity of reflected and polarized light differs depending on the orientation of the polarization direction relative to the crystallographic axes of the graphite crystal. Measurement of the ratio of the reflected intensities of a light beam, polarized first along one direction and then perpendicular to that direction, will yield an Optical Anisotropy Factor (OAF). It can be shown that this OAF can be related in a consistent way to the BAF, which in turn relates to actual expected anisotropy and fuel performance”. In addition, an advanced ellipsometry technique, developed by Oak Ridge National Laboratory (ORNL) and called the Two-Modulator Generalized Ellipsometry Microscope, was applied to the measurement of pyrocarbon anisotropy in TRISO particle fuels, determining the polarization effect on light reflected out of a polished pyrocarbon cross-section [4].

BAF was also described using the coefficient of thermal expansion (CTE) [17]:

$$BAF = \frac{\alpha_{AG}}{\alpha_{WG}} \quad (3)$$

or [18]

$$BAF = \frac{\alpha_X}{\alpha_Z} \quad (4)$$

where  $\alpha$  is CTE; subscripts, AG, WG indicate against grain, with grain; X and Z are the X axis and Z axis (of two orthogonal sample axes), respectively. It is indicated in Ref. [17] that “BAF is usually quoted at ~400°C”. In Ref. [18], the BAF obtained using CTE data was correlated with BAF estimated by measuring the graphite texture using transmission X-ray diffraction (XRD), as

$$BAF_{CTE} = BAF_{XRD} = \frac{\bar{\alpha}_X}{\bar{\alpha}_Z} = \frac{1}{2} \frac{\int_0^{\frac{\pi}{2}} I(f) \cdot \sin^3 f \cdot df}{\int_0^{\frac{\pi}{2}} I(f) \cdot \cos^2 f \cdot \sin f \cdot df} \quad (5)$$

where  $\alpha_Z$  is the constant stress estimate for CTE of the polycrystalline graphite at 400°C in the Z direction, where Z is the symmetry axis;  $\alpha_X$  is the constant stress estimate for CTE of the polycrystalline graphite at 400°C in the X direction, where X is one of the other two orthogonal axes;  $I(\phi)$  is the density of [002] plane normal per unit solid angle about the angle  $\phi$ ;  $\phi$  is the angle between the [002] normal and the sample horizontal during transmission XRD measurement, in this case the WG direction.  $I(\phi)$  describes the proportion of crystallites oriented at a given angle to Z, the sample symmetry axis.

It is indicated in Ref. [14]: “Good irradiation behaviour requires that the pyrocarbon layer exhibit similar dimensional changes in the longitudinal and latitudinal directions for the fast fluence of interest. That is, it is desired that the carbon layer material and physical properties be anisotropic. This can be achieved by ensuring that the deposited carbon has a random rather than a preferred macroscopic crystal orientation. A measurement of anisotropy is known as the BAF. A BAF of 1 is completely isotropic, greater than 1 implies increasing crystal orientation. Some argue that a BAF of less than about 1.05 is necessary for good irradiation performance, with a BAF in the range of 1.02–1.05 as the desired target.”

The shrinkage and swelling behaviour of the PyC layers is a function of BAF and determined by the fabrication process of the layers. The dimensional change in the radial and tangential directions are equal for an isotropic material [19]. When the PyC is considered slightly anisotropic ( $BAF > 1.0$ ), less shrinkage of the PyC in the radial direction is expected in the early stages of irradiation [20]. It is also indicated in Ref. [19] that, at some point during the irradiation, the shrinkage in the radial direction changes to swelling. Therefore, the dimensional change behaviour in the tangential direction becomes more important than that in the radial direction.

Based on BAF measurements on TRISO particles based on ThO<sub>2</sub> and fabricated by General Atomics in the US, the degree of crystallite anisotropy in IPyC layers ( $1.065 < BAF < 1.098$ ) was observed to be greater than anisotropy in OPyC layers ( $1.018 < BAF < 1.036$ ) [21]. The relatively large IPyC BAF values were thought to be caused by the exposure of IPyC layer to coating temperatures of 1550 to 1650°C during SiC deposition [21]. This hypothesis was tested by measuring BAF at the bi-structure isotropic (or BISO) stage (i.e., kernel + buffer layer + pyrocarbon) for specimens heat-treated at different temperatures, and was shown that BAF increases with increasing temperature, but when the sample was held at a constant temperature for a long period of time, a decrease in BAF was observed. The results indicate that higher temperatures cause larger deviations from isotropy, and longer hold times result in smaller crystallite anisotropy values (Table 4, based on data from Ref. [21]).

TABLE 4. HEAT TREATMENT OF BISO FOR THE EFFECT OF TEMPERATURE ON BAF

Thermal Treatment	BAF
As-coated through IPyC stage (1300–1400°C)	1.051
1 h at 1550°C	1.088
2 h at 1550°C	1.086
3 h at 1550°C	1.082
3 h at 1550°C + ½ h at 1650°C	1.087
½ h at 1850°C	1.112

In a computational analysis of TRISO fuel behaviour, it was demonstrated in Ref. [16] that anisotropy is critical to determining the magnitude of the dimensional change and the SiC failure probability due to stress concentration in the layer caused by an irradiation-induced shrinkage crack in the IPyC layer. However, based on the analysis results (see Fig. 7 for the probability of the SiC layer failure), there was little change in the failure probability when BAF was varied between 1.0 and 1.16, though an upper critical limit of 1.09 was determined. The lack of response was attributed to the uncertainties in the material properties, especially irradiation-induced creep.

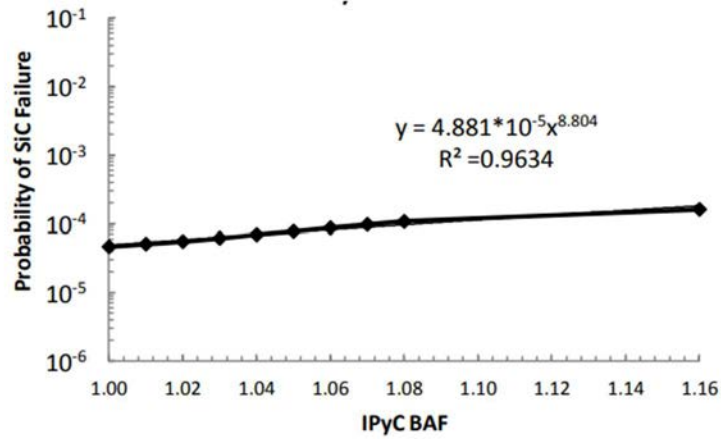


FIG. 8. Probability of SiC failure due to IPyC BAF (reproduced from Ref. [16], courtesy of INL).

Another sensitivity analysis was performed by using three different BAF values (i.e., 1.0, 1.03 and 1.06), resulting in three different PyC irradiation-induced dimensional change rates for the radial and tangential directions [19]. When it is considered as isotropic (BAF=1), the dimensional changes in the radial and tangential directions are the same as shown in Fig. 9. The effect of BAF on PyC dimensional changes is the largest at the largest BAF value considered and it increases with increasing fast fluence (or burnup for a constant power). Figure 9 shows that the difference in dimensional change values in the radial and tangential directions increases with increasing BAF value and with increasing fast fluence, though for BAF above 1.03 in the radial direction, the PyC dimensional change makes a minimum with fast fluence [19].

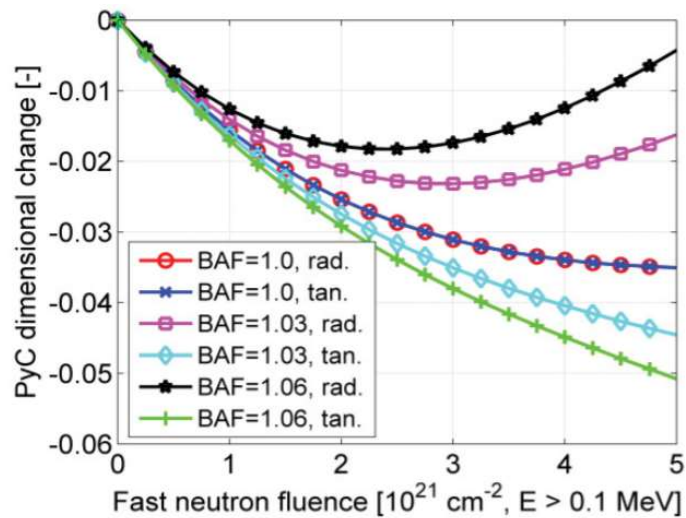


FIG. 9. Irradiation-induced dimensional change as a function of the fast fluence ( $E > 0.1$  MeV) for three different BAF values (reproduced from Ref. [19], courtesy of INL).

Figure 10 shows the stress levels in IPyC, SiC and OPyC coating layers for three different BAF values (i.e., 1.0, 1.03 and 1.06). The stress in the SiC layer is especially sensitive to the dimensional change of

the PyC, in particular at high fast fluences (or high burnups for a constant power), while the maximum stress of the IPyC or OPyC is relatively insensitive.

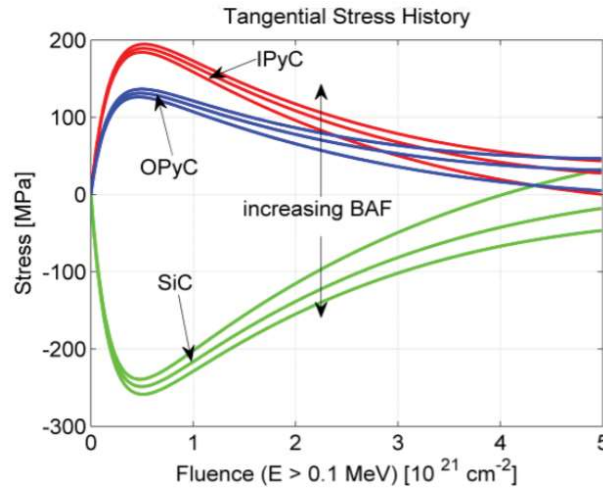


FIG. 10. Stresses in the IPyC, SiC, OPyC coating layers as a function of the fast fluence ( $E > 0.1$  MeV) for three different BAF values (1.00, 1.03, 1.06) (reproduced from Ref. [19], courtesy of INL).

Figure 11 shows the effect of BAF on elastic modulus as a function of irradiation, or fast neutron fluence,  $f$  ( $\times 10^{25}$  n/m<sup>2</sup>,  $E > 0.18$  MeV): the elastic modulus in the radial direction is the highest for isotropic (BAF=1.0) PyC (for the BAF values ranging between 1.0 and 1.2), and it decreases with increasing BAF value, while in the tangential direction, it is the lowest for BAF=1.0 and it increases with increasing BAF [22].

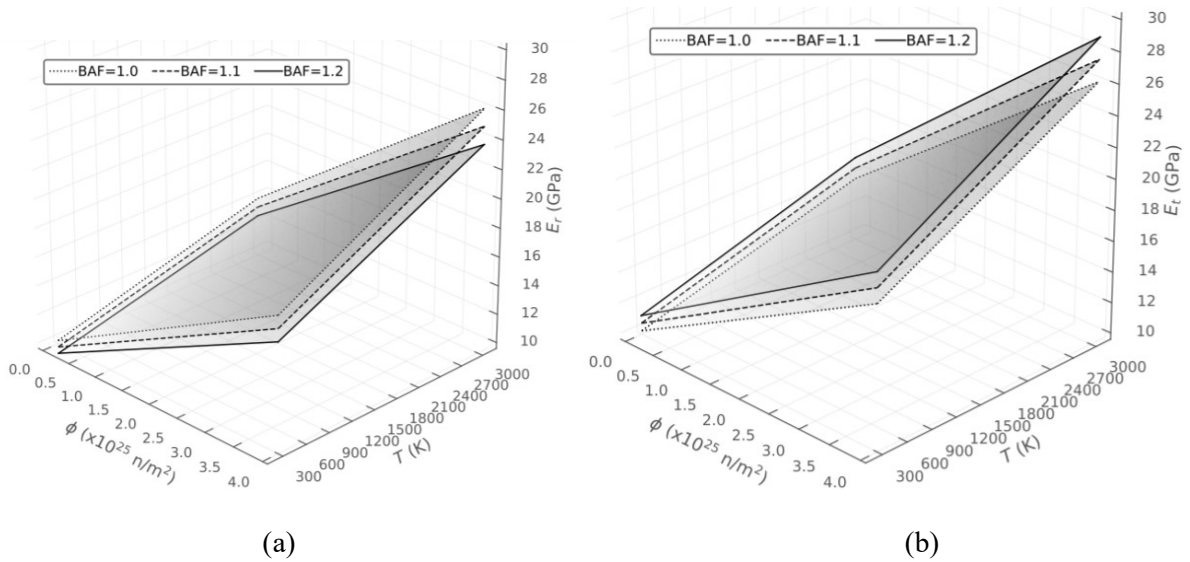


FIG. 11. Effect of BAF on PyC elastic modulus: (a) Radial, (b) Tangential (reproduced from Ref. [22], courtesy of INL).

Figure 12 shows the effect of BAF on CTE  $\alpha$ :  $\alpha$  increases in the radial direction with increasing BAF, whereas it decreases in the tangential direction with increasing BAF [22].

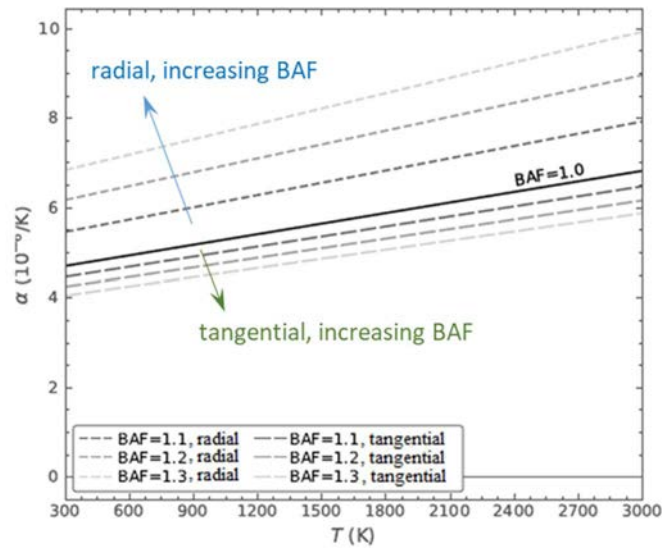


FIG. 12. Effect of BAF on CTE  $\alpha$  (reproduced from Ref. [22], courtesy of INL).

Figure 13 shows the effect of BAF on irradiation strain as a function of irradiation, or fast neutron fluence,  $\phi$  ( $\times 10^{25}$  n/m<sup>2</sup>,  $E > 0.18$  MeV) [22]: The eigenstrain increases with increasing BAF in the radial direction, while it is decreasing in the tangential direction. The effect of irradiation on eigenstrain in both directions (i.e., radial and tangential) is more pronounced at the highest temperature (i.e., 1350°C) and at the highest BAF (i.e., 1.25).

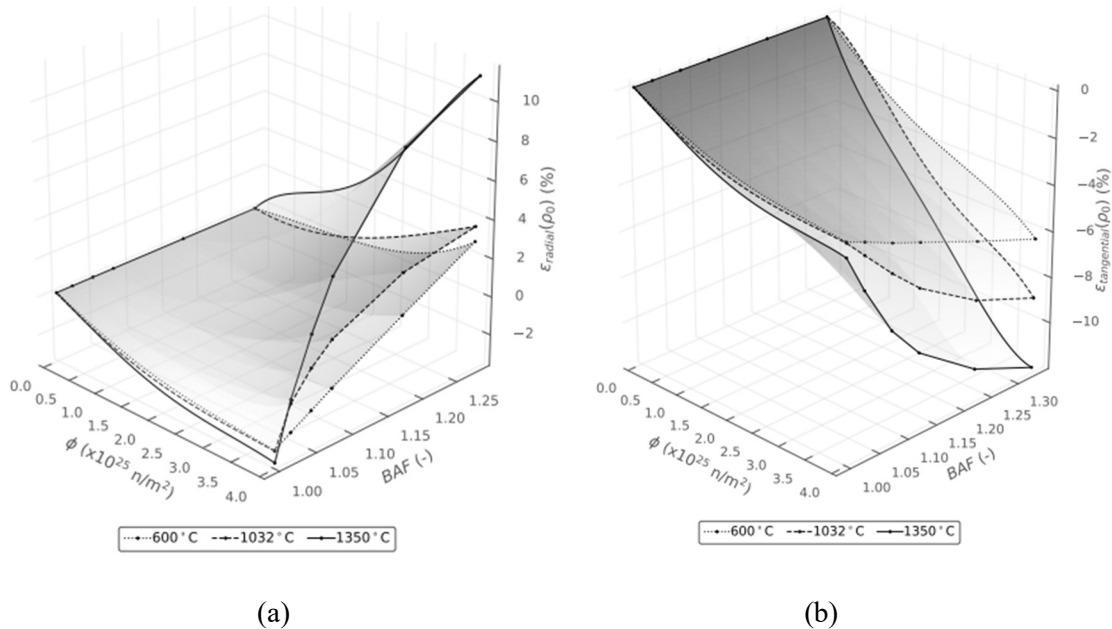


FIG. 13. Effect of BAF on PyC irradiation strain at  $\rho_0 = 1.96\text{g/cm}^3$ : (a) Radial, (b) Tangential (reproduced from Ref. [22], courtesy of INL).

BAF is presumed to accelerate radial swelling and tangential shrinkage with fast neutron fluence in a fairly but not completely constant volume, as shown in Fig. 14, where ‘Iso Vol’ indicates isotropic

volume changes and ‘Vol’ indicates anisotropic volume changes. At BAF=1.16, dimensional change in the radial direction switched from shrinkage to swelling at the fast neutron fluence of  $5 \times 10^{25} \text{ n/m}^2$ , whereas the same behaviour for BAF=1.036 was observed at a higher fast neutron fluence (i.e.,  $10 \times 10^{25} \text{ n/m}^2$ ).

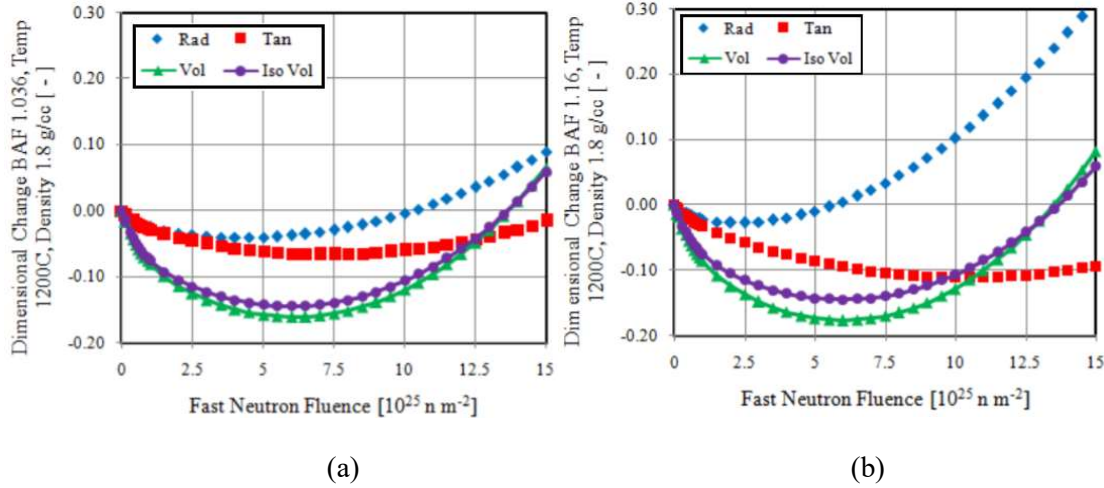


FIG. 14. Effect of BAF on dimensional and volume changes at 1200 °C: (a) BAF=1.036, (b) BAF=1.16 (reproduced from ref. [23], courtesy of INL).

The following material and physical properties were identified for IPyC design, though the requirements for some of them may conflict with the requirements of the others:

- Density;
- Permeability and anisotropy:
  - Permeability (i.e., chlorine transport to the kernel during SiC layer coating) tends to be less with a higher BAF, but BAF with a value ranging between 1.02 and 1.05 is desirable for good irradiation performance [14]. Therefore, these permeability and anisotropy need to be optimized for irradiation stability and controlling coating contamination by chlorine reactivity in the kernel;
  - Increased IPyC thickness would not resolve the permeability problem since thicker IPyC can cause higher irradiation induced stresses, leading to higher failure probabilities of the particle.
- Creep and shrinkage:
  - The IPyC layer (influenced also by BAF) shrinks due to the fast flux, but it is also relieved by IPyC creep [14]. The tangential stresses in the IPyC and OPyC layers provide radial stress components on the SiC, thereby affecting the tangential stress in that layer [24]. Cracks (or debonding) in the IPyC can cause locally high tensile stresses in the SiC layer if the between layer bond is strong [14]. Such cracks can also provide a passage for CO to oxidize the SiC at high temperatures. Therefore, dimensional stability is important as cracking can lead to particle failure [14]. During irradiation both PyC layers shrink, compressing the SiC coating (see Fig. 15) and counteracting the hoop stresses created in it by the internal gas pressure [25]. These compressive stresses have to not be so large that the tangential stresses in the PyC layers exceed the fracture stress. In addition, the radial stress between the IPyC and SiC layers have to not be so large that debonding between the two occurs. This requires that these two layers are to be approximately isotropic [25].
- Strength.

The IPyC design parameters of interest to the fuel design to avoid failures are described in Ref. [14], and they are shown in Table 5 (based on information from Ref. [14]).

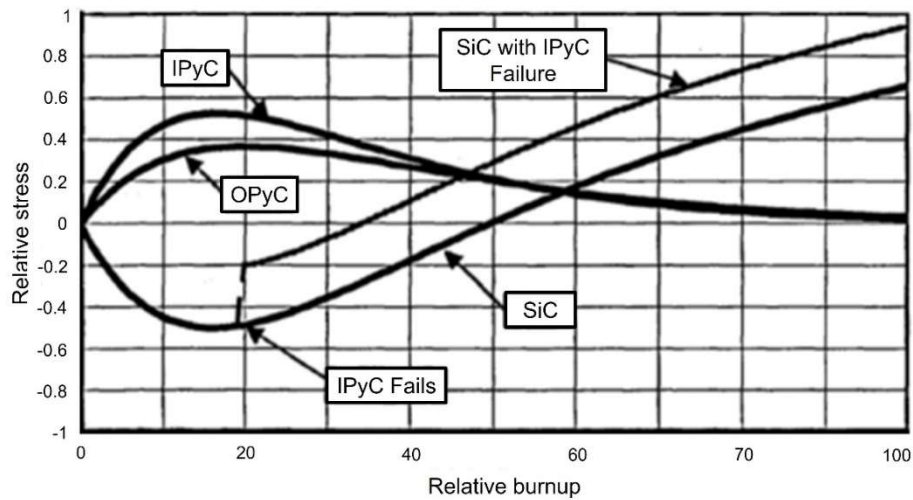


FIG. 15 Qualitative stresses in coated particle layers (reproduced from Ref. [25], courtesy of IAEA).

TABLE 5. IPYC DESIGN PARAMETERS

IPyC design parameters	Rationale
Thickness	Thickness affects structural properties of the IPyC, gas retention, and control of possible hydrochloric acid attack of kernel during fabrication.
Density	Density indirectly determines material properties.
Anisotropy	The irradiation stability of the layer is determined by the crystalline structure.

#### 2.3.4. SiC layer

SiC layer is considered as the main barrier against release of fission products, including metallic fission products - serving as an impermeable layer, and gases - serving as a pressure vessel. It is dimensionally stable under irradiation and shows significant tensile strength.

Strains between the pyrocarbon layers and the SiC layer can result in SiC layer failure. Stresses are caused in the PyC layers by gas pressure and irradiation induced shrinkage, and in the SiC layer by gas pressure and the relative stress distributions between the layers [14]. It is desirable for pyrocarbon layers to keep the SiC in compression as long as possible. However, the stress distributions will change upon the failure of pyrocarbon layers, and the stress in the SiC layer will change from compression to tension even at low burnups.

Under normal operating conditions, it is expected that SiC layer retains all fission products, though silver is an exception, having a high release rate above 1100°C. At higher temperatures (>1250°C) palladium is of concern to diffuse and attack the SiC layer as it is not retained in the kernel like lanthanide elements, which form oxides that are well retained in the kernel. Therefore, this behaviour sets a limit on the normal operating temperatures (< 1300°C) [14]. At accident temperatures, above 1800°C, fission products release quickly. Above ~2000°C, thermal decomposition of SiC is a dominant failure

mechanism. However, even at 1600°C, formation of porosities was observed, indicating the decomposition of SiC [14]. Therefore, the conditions are set such that the SiC layer is kept in compression during most of the irradiation and the operating (and accident) temperatures are limited to control SiC layer corrosion and decomposition.

A computational analysis was performed to determine the critical value for the SiC thickness. It was determined that the failure probability increases as the thickness decreases (see Fig. 16 for the probability of the SiC layer failure), which is attributed to less structural material to retain the fission gas pressure and subsequent increase in tangential stress in the layer. The analysis indicated a lower critical limit of 20 μm for the SiC layer thickness, for the thickness values varying between 10 and 60 μm.

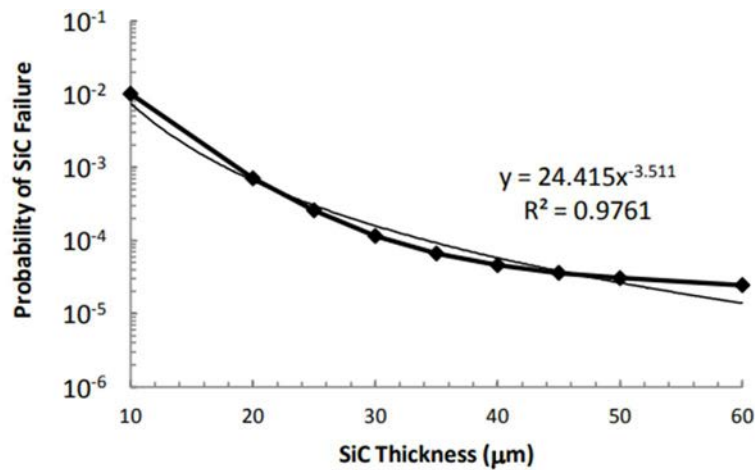


FIG. 16. Probability of SiC failure due to SiC layer thickness (reproduced from Ref. [16], courtesy of INL).

The SiC parameters of particular interest to the fuel design to avoid failures are described in Ref. [14], and they are represented in Table 6 (based on information from Ref. [14]).

TABLE 6. SiC DESIGN PARAMETERS

SiC design parameters	Rationale
Thickness	Thickness affects the strength of the layer. Uniform distribution of the thickness is desirable.
Density	Density determines material properties. It is desirable to have a high density SiC with small grains.
Fraction with defective SiC layers	Initially defective particles affect in-reactor performance and fabrication cost.

### 2.3.5. Outer pyrocarbon layer

The OPyC is the last layer, serving as a cushion to protect the SiC layer from mechanical damage during handling, and binding the particle to the matrix. It has similar requirements as discussed for IPyC layer.

Permeability of the OPyC has been identified to be important due to the potential intrusion of matrix material into the pores of the coating [14]. An OPyC layer that is too permeable would result in coating

failure due to the strong bond formed between the OPyC and the fuel element matrix material, and differential shrinkage of these materials from irradiation exposure.

The computational analysis performed in Ref. [16] determined that calculated particle failure rates were insensitive to the OPyC BAF or density. Therefore, no critical limits for these properties were determined in that study.

Similar to the IPyC design parameters, the OPyC design parameters are listed in Table 7, based on information described in Ref. [14]. Originally, density and anisotropy were thought to be important, though the importance was deemed not significant in a separate study [16]; these parameters are kept in Table 7 because a separate experimental study can be performed to confirm either of the statements.

TABLE 7. OPYC DESIGN PARAMETERS

OPyC design parameters	Rationale
Thickness	Thickness affects the strength of the OPyC and gas retention in the case where SiC layer fails.
Density	Density indirectly determines material properties.
Anisotropy	The irradiation stability of the layer is determined by the crystalline structure.

### 2.3.6. Fuel element (spherical pebble or cylindrical compact)

While fabricating fuel elements, pressure is applied to compact the fuel. Consequently, cracks can form in the layers of the TRISO particle due to direct particle-to-particle contact. In order to avoid particle-to-particle interaction, particles are overcoated with matrix material before they are pressed to fabricate fuel elements. The thickness of the overcoating will vary considerably depending on the desired particle volumetric packing fraction in the final fuel element, though a typical value would be in the range of 200  $\mu\text{m}$ .

The compacted fuel elements, either in the form of spherical pebbles or cylindrical compacts stabilizing the particles in the matrix (so that particles cannot move), allow the fuel to be handled without damage to the particles and provide a medium for heat transfer from particles to the coolant.

Traditionally, graphite matrix-based spherical fuel pebbles are used in a pebble bed reactor, and graphite matrix-based cylindrical fuel compacts are used in hexagonal blocks in a prismatic reactor. However SiC-based matrix fuel elements, called fully ceramic microencapsulated (FCM), have been proposed to be used in SMRs and some micro-modular reactors (MMRs). The FCM fuel consists of TRISO particles in a SiC matrix, offering the following potential advantages over a graphite matrix, which were taken from Ref. [26]:

- “Improved irradiation stability;
- Incorporation of yet another effective barrier to fission product release;
- Environmental stability under operating (steady state) and transient conditions as well as long-term storage;
- Proliferation resistance.”

The high thermal conductivity of SiC may allow thermal conductivity of the FCM fuel to be comparable to that of traditional graphite-matrix fuel.

Power of a fuel element depends on the number of coated particles in the fuel element (i.e. more particles are desirable for higher power); however, too many particles (or heavy fuel particle loading) in the fuel

matrix will result in damaging the particles during the fabrication of the element. In addition, inhomogeneous distribution of particles will result in peculiar power distribution in the element, creating hot spots in the element, which may eventually lead to the fuel element failure. Design parameters related to the fuel element are described in [14] and represented in Table 8, based on the information from Ref. [14].

TABLE 8. FUEL ELEMENT DESIGN PARAMETERS

<b>Fuel element design parameters</b>	<b>Rationale</b>
Matrix material (i.e. graphite, SiC)	Matrix material contributes to the fuel element properties, such as thermal conductivity.
Particle packing fraction (particle load)	Particle packing fraction determines not only the power that can be extracted from the fuel element, but also impacts the likelihood of particle damage during fabrication; the higher the particle packing fraction, the higher the power and higher the possibility of damaged particles.
Particle distribution in the fuel element	Inhomogeneous particle distribution within fuel elements can result in hot spots.
Particle overcoating	Another layer on TRISO particles is applied in particular for pebble bed spherical fuels. This layer provides a particle-to-particle spacing function.
Fuel free zone	A fuel-free zone, surrounding the fuelled core that contains the TRISO particles, provides a protective shell at the periphery of the fuelled core in an element. This is typically used in spherical fuel pebbles, which will experience continual pebble-to-pebble contact and abrasion during their operational lifetime in a pebble-bed reactor core; however, it is also considered for cylindrical fuel elements.
Unconfined heavy metal outside SiC layer	It is undesirable to have the fuel elements contaminated with heavy metals (outside the particle), which will increase the release of fission products into the coolant.

#### 2.4. SUMMARY AND DISCUSSION

Design bases for determining the dimensions and specifications of coated particle fuel components (i.e. kernel and coating layers) are well understood. Taking into account the current practice that fuel design limits or acceptance criteria form the basis for margin assessment to ensure the good performance and safe operation of fuels in LWRs, a similar approach needs to be taken for coated particle fuels for HTGRs. Hence, a complete list of design limits or criteria needs to be developed.

### 3. UPDATES IN MEMBER STATES

A survey during the Technical Meeting on the Design, Fabrication and Irradiation Behaviour of Small Modular Reactor Fuels, held virtually from 18 to 22 October 2021 indicated that more than 10 countries consider high temperature gas cooled SMRs for prospects in their energy planning. Some countries are also interested in developing FCM<sup>7</sup> fuel with intention to use in LWRs<sup>7</sup> or MMRs.

In this section, R&D activities in some Member States are described to set up a domestic manufacturing capability for TRISO particle fuel and to develop advanced coated particle fuel, i.e. FCM fuel.

#### 3.1. CANADA

Four vendors have expressed their interest in building HTGRs in collaboration/partnership with the Canadian nuclear industry or the government. These include:

- Ultra Safe Nuclear Corporation (USNC) – MMR-5/MMR-10: 5-10 MWe;
- U-Battery Canada Ltd. – U Battery HTGR: 4 MWe (project started pending as of 2022);
- X-Energy LLC – Xe-100 HTGR: 80 MWe;
- StarCore Nuclear – StarCore Module HTGR: 10 MWe.

In addition, other activities related to coated particle fuel have also been pursued. One example is the joint research between Canadian Nuclear Laboratories (CNL) and USNC on FCM fuel in support of MMRs. The research project has explored manufacturing process for FCM fuel.

The first concept of FCM fuel developed by USNC is based on layered structure (see Fig. 17). One layer consists of SiC crust, which is pressed SiC powder, a TRISO plane, and a SiC lid. Once one layer is complete, the layer is pressed again. At CNL, the first fabrication trials were made using a surrogate material of ZrO<sub>2</sub> in the kernel instead of UO<sub>2</sub> or UCO. The matrix material was nano-sized SiC powder.

Figure 18 shows the sintered FCM fuel with surrogate kernels. Several analyses for characterization of the fuel were performed, using:

- X-Ray Computed Tomography with which it is possible to identify defective particles as a result of manufacturing, how densely packed the particles are inside the fuel form, and how close the particles are to the edges;
- Particle Size Analyser that is used to measure the average TRISO particle diameter;
- Optical Microscopy/Analytical Software that is used to determine the size, shape and distribution of TRISO particles in the FCM;
- Dilatometer that is used to determine the SiC thermal expansion;
- Differential Scanning Calorimeter that is used to determine the SiC matrix melting point, heat capacity and phase diagrams;
- Laser Flash Apparatus that is used to determine the SiC matrix specific heat capacity, thermal diffusivity – currently not on irradiated fuel;
- Pycnometer to determine the density of TRISO particles.

---

Compared to the conventional TRISO particle fuel, the FCM fuel is characterized by the use of a large diameter kernel containing an increased density of uranium, SiC matrix and the cladding made of advanced steel, SiC clad or refractory alloys. When coupled with SiC cladding, FCM fuel eliminates zirconium altogether and is expected to drastically reduce hydrogen generation during a beyond-design basis accident.

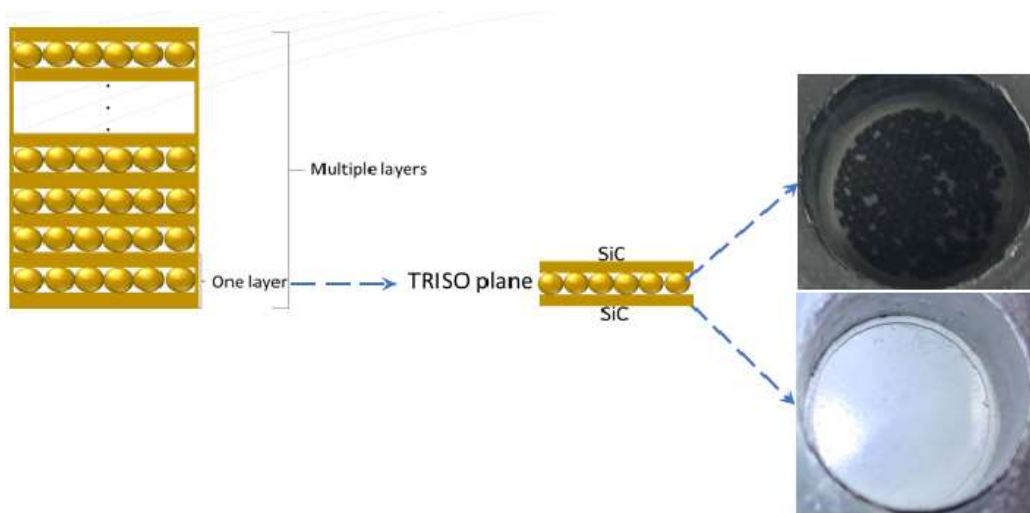


FIG. 17. Layered structured of fully ceramic microencapsulated fuel concept and one layer of the layered structure (courtesy of CNL).



FIG. 18. Sintered FCM fuel with surrogate kernels (courtesy of CNL).

### 3.2. CHINA

Coated particle fuel has been developed in China since the 1970s, in several stages (see Fig. 19).

In the first stage, from the 1970s to 1986, the principles of coated particle fuel fabrication were developed, including the sol-gel method for the kernel, the fluidized bed chemical vapour deposition (CVD) for coated particles, and the module press for the fuel sphere. The principal research work was accelerated by the international cooperation with Jülich Research Centre (FZJ), Germany.

In the second stage, from 1986 to 2003, coated particle fuel was developed for the HTR-10. Based on the research work, the HTR-10 reactor project was approved by the government and constructed in the Institute of Nuclear and New Energy Technology (INET) located in Tsinghua University. Comprehensive coated particle fuel fabrication technology was developed, including examination

methods, quality control, and quality assurance. A lab scale manufacturing line was established in INET, which manufactured 23 000 spheres for the first loading of HTR-10 including the irradiation test.

In the third stage (2003-2012), large scale manufacture technology of coated particle fuel was developed for HTR-PM. From 2006 to 2016, based on the development of HTR-10, the HTR-PM project was approved, and the coated particle fuel was developed. A prototype manufacturing line with the capability of producing 100 000 spheres in one year was established in INET based on the lab scale process.

Meanwhile, the fuel fabrication technology was transferred to China Nuclear North Fuel Company and an industrial manufacturing line was designed and constructed based on the prototype manufacturing line in INET, with a capability of producing 300 000 spheres per year. This manufacturing line produced the first loading for the HTR-PM. By the end of 2019, a total of 860 000 spheres were fabricated for HTR-PM. The first batch of fuel was loaded in the HTR-PM in 2021, which allowed the HTR-PM to reach the criticality that year.

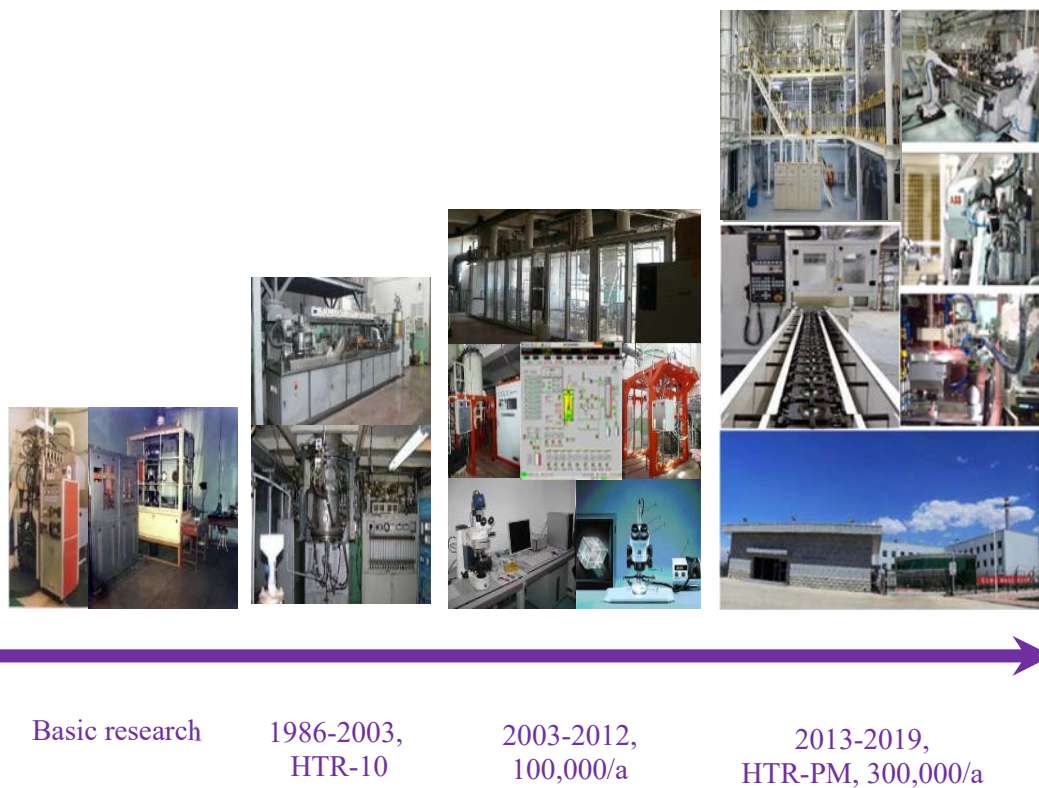


FIG. 19. The development map of coated particle fuel in China (courtesy of Tsinghua University).

Now the coated particle fuel technology development is in the next stage, which includes the design for a large-scale industrial manufacturing line with the capability of producing more than 3 000 000 spheres per year. This fuel manufacturing capability is intended to support the deployment of the HTR-PM600 reactor.

In addition, a new type of coated particle with new fuel kernels and new coating layers is being developed for the application of coated particle fuel in SMRs. The new coated particle fuel includes new kernels such as UCO, UN, and a new coating layer of ZrC.

### 3.3. REPUBLIC OF KOREA

In 2019, the Korean government announced its plan to foster a hydrogen related industry such as hydrogen-powered vehicles and hydrogen fuel cells. Hydrogen demand by 2040 is expected to reach 5.26 million tonnes per year. Under this circumstance, VHTR technology has been considered as one potential option for 'green' technologies for the production of hydrogen gas.

An intensive R&D programme to develop important technologies required for VHTR has been launched, which focuses on design and analysis technologies, thermal fluid experiments, TRISO fuel, high temperature materials database, and high temperature heat application.

The Korea Atomic Energy Research Institute (KAERI) has successfully established a manufacturing process for TRISO particle fuel at the laboratory scale (20~30 g UO<sub>2</sub>/batch). During this development, KAERI made progress in kernel fabrication, TRISO coating, overcoating, and compaction of the coated fuel particles using graphite powder. Figure 20 shows kernel fabrication equipment installed at KAERI.



*FIG. 20. Kernel fabrication system at KAERI (courtesy of KAERI).*

KAERI uses gel supported precipitation for the fabrication of spherical UO<sub>2</sub> kernels. Associated process parameters have been determined as appropriate.

KAERI uses fluidized bed-chemical vapour deposition (FB-CVD) technology for TRISO coating (Fig. 21) with a capacity of 20~30 g/batch scale.



FIG. 21. TRISO coating system (courtesy of KAERI).

KAERI's TRISO fuel has been irradiated at the HANARO material test reactor, followed by PIE of the irradiated fuel.

Research and development for advanced coated particle fuel technology has been undertaken at KAERI, which includes UCO kernel fabrication and ZrC/SiC double layer coatings. As regards UCO kernel fabrication, a process to dissolve the carbon powder in the viscous solution using an ultrasonic and mechanical blending method has been established.

As regards ZrC coating,  $ZrCl_4$  powder as a Zr source was vaporized in the sublimation system equipped with a screw feeding system. A lab-scale ZrC coating process capable of controlling the stoichiometry of ZrC was established using FB-CVD. The high temperature stability of ZrC/SiC double layers was confirmed by measuring microstructural changes (composition and grain size) and mechanical properties (elastic modulus and hardness) after heat treatment.

TRISO-SiC-composite fuel, widely called FCM fuel, was conceptualized as an accident tolerant fuel for LWRs. Through the Korea-US International Nuclear Energy Research Initiative, the feasibility of LEU FCM replacement fuel for current LWRs was investigated. Using enriched UN kernels with a higher TRISO particle volume fraction was suggested to meet uranium loading and fuel cycle length of LWRs.

As a promising processing method other than hot-pressing and spark-plasma sintering, non-pressurized sintering was applied to fabricate FCM fuels. A new quaternary additive system of  $AlN-Y_2O_3-Sc_2O_3-MgO$  was chosen to make SiC matrix densified at as low as  $1850^\circ C$  without applied pressure. FCM fuels with  $> 35$  vol.% TRISO particles were fabricated. Thermal conductivity of the FCM pellets was measured as a function of TRISO particle content (see Fig. 22).

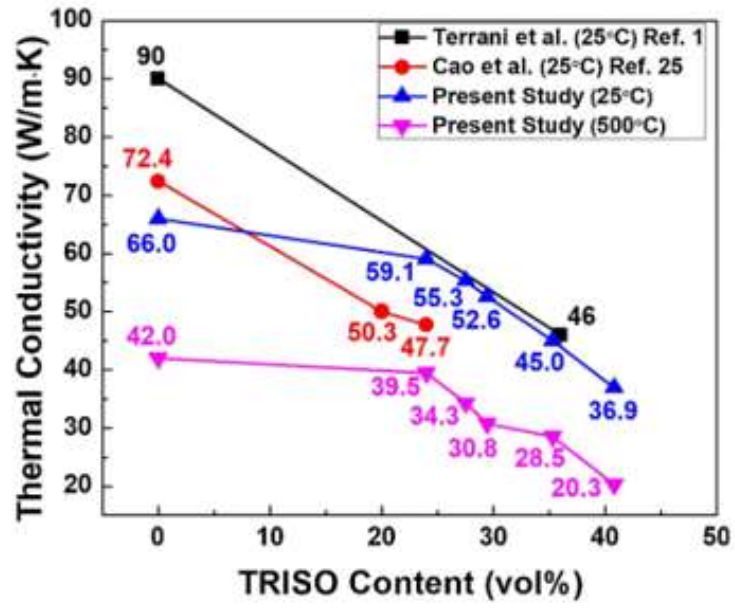


FIG. 22. Thermal conductivity of non-pressurized sintered FCM pellet characterization (courtesy of KAERI).

## 4. COATED PARTICLE FUEL MANUFACTURING

Coated particle fuel manufacturing technology has been developed for over 60 years. The technology includes the fuel kernel, coated particle and the pebble or compact manufacture, and the associated examination methods. This section provides an overview of coated particle fuel fabrication technology together with advancements made.

### 4.1. FUEL KERNEL MANUFACTURING

Fuel kernel manufacture has two processes: the powder metallurgical process and the sol-gel process.

#### 4.1.1. Powder metallurgical process

The powder metallurgical process, known as the 'dry route process' is widely used in LWR fuel manufacturing. The first fuel charges of the AVR, Peach-Bottom and Dragon reactors were made from carbide kernels produced by such a powder metallurgical process.  $\text{UO}_2$  or  $\text{U}_3\text{O}_8$ , alone or mixed with  $\text{ThO}_2$ , is granulated to form green particles (carbon powder and a binder are added during this process). The green particles embedded in graphite powder form kernels of  $\text{UC}_2$  or  $(\text{Th,U})\text{C}_2$  at a temperature above  $2500^\circ\text{C}$  [27,28]. After sieving, these kernels become suitable for coating. Oxides in the form of  $\text{UO}_2$  or  $(\text{Th,U})\text{O}_2$  are formed by burning off the carbon in air. Following sintering at  $1600^\circ\text{C}$  in hydrogen environment, porous kernels (e.g. with 90% theoretical density) are produced. Note that liquid processes (refer to [29–37]) are necessary for producing dense kernels. Some of aqueous processes are described in the subsequent sections.

#### 4.1.2. Sol-gel process

The sol-gel process known as the wet process is widely used in kernel manufacturing for coated particles. There are two primary ways of making spherical kernels by wet route procedures: external gelation (or gel precipitation) - where the gelation proceeds from the outside, and internal gelation - where the gelation proceeds from the inside.

Figure 23 shows the external gelation sol-gel process, represented based on information from Ref. [38]. A sol is prepared using  $\text{UO}_2(\text{NO}_3)_2$ , polyvinyl alcohol, and other additives. Then, the sol is dropped into a liquid from small nozzles to form microspheres. The sol contains small crystallites (~5 nm) of an oxide of the fuel; it is possible for oxides to obtain high densities after the sintering at  $1600^\circ\text{C}$  in a reducing atmosphere with no applying pressure.

External gelation is done by extracting water from the droplet, while internal gelation is achieved by a chemical reaction inside the droplets. In the chemical reaction ammonia is formed by thermal decomposition of hexamethylenetetramine to initiate gelation. Internal gelation is fast and uniform.

As a result of the sol-gel process, spherical and high density  $(\text{Th,U})\text{O}_2$  or  $\text{UO}_2$  fuel kernels are produced with diameters of more than  $500\ \mu\text{m}$ . Carbide microspheres are formed from the mixtures of  $\text{UO}_2$  sol and carbon black through the pre-sintering process at  $1000^\circ\text{C}$  in an argon atmosphere. These  $\text{UO}_2+\text{C}$  microspheres are sintered in the graphite powder at  $1900^\circ\text{C}$  to obtain porous  $\text{UC}_2$  kernels.

The microspheres are dried and calcined at temperatures higher than  $700^\circ\text{C}$ . Highly spherical and high-density kernels of  $\text{UO}_2$  are obtained by sintering in a reducing atmosphere at  $1600^\circ\text{C}$ . Of the techniques used to synthesize UN from  $\text{UO}_2$ , carbothermic reduction is commonly used in industrial applications.

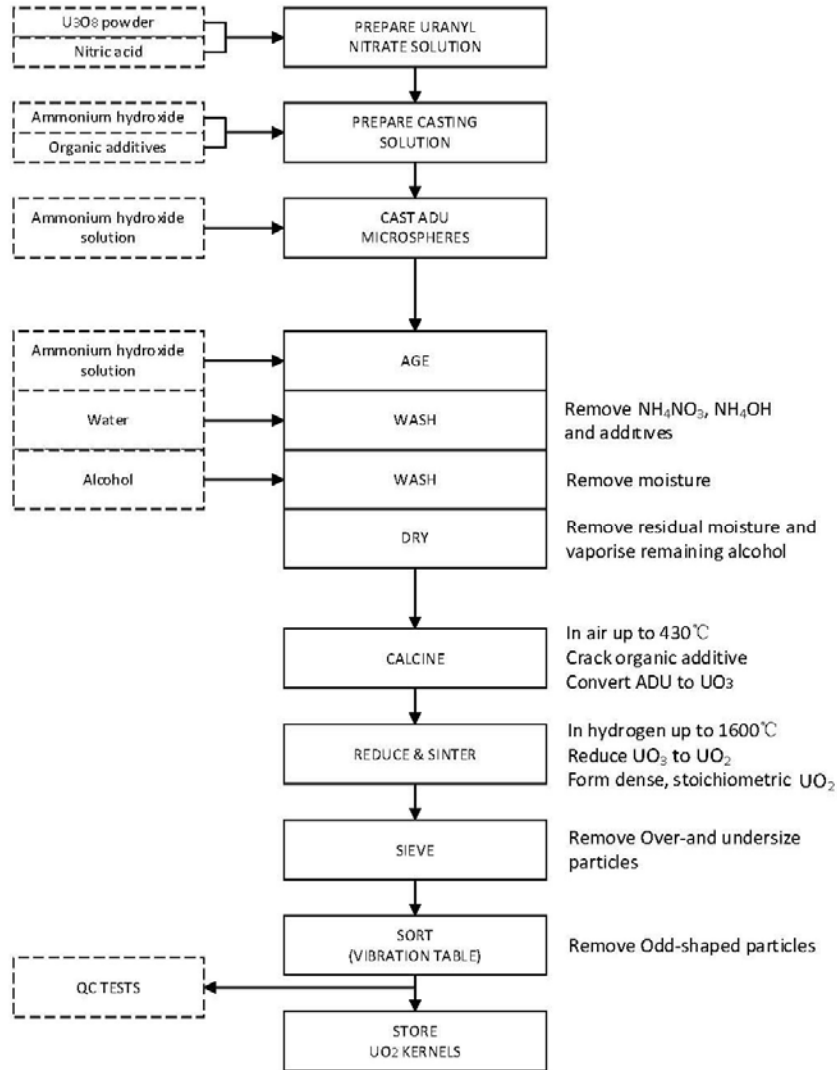


FIG. 23. Illustrative flow diagram of the external sol-gel process for kernel fabrication.

#### 4.1.3. Gel precipitation process for UO<sub>2</sub> kernels

A modified sol-gel external gelation process using a drip casting method to produce UO<sub>2</sub> microspheres was developed by NUKEM [38,39], which is also known as ‘gel precipitation’. The production of UO<sub>2</sub>, ThO<sub>2</sub> or mixed oxide kernels by this external gelation process is relatively simple due to a few process steps involved and a small volume of effluent and waste generated and is prone to automated manufacturing. The overview of this process is represented in Fig. 23. Important steps are described below:

- Prepare feed solution. U<sub>3</sub>O<sub>8</sub> powder dissolved in nitric acid to form a uranyl nitrate solution is fed:



The uranyl nitrate solution is pre-neutralized with ammonium hydroxide just prior to precipitation:



- Prepare casting solution. Small amounts of polyvinyl alcohol and tetrahydrofurfuryl alcohol are added to the pre-neutralized uranyl nitrate solution and a casting solution is prepared. By adjusting the surface tension and viscosity in this process, the formation of proper droplets is facilitated. Figure 24 illustrates the casting equipment of the gel-sol.



FIG. 24. Casting equipment of the sol-gel in INET (courtesy of Tsinghua University).

- Cast acid-deficient uranyl nitrate (ADUN) microspheres in aqueous solution. This step is performed in a glass column that is filled with the ammonium hydroxide precipitation solution. Figure 25 shows a schematic diagram of the casting process: (a) The casting solution is pneumatically supplied to the nozzles (up to five) through a silicone tube at the top of the column. A vibrator is used to shake off droplets at a rate of 100 droplets per second from the feed stream; (b) The droplets travel through air to form a spherical shape owing to surface tension; (c) Then, the microspheres pass through an ammonia atmosphere, causing it to precipitate as ammonium diuranate (ADU) in the outer layer of the microspheres, through a chemical reaction with the uranyl nitrate on the surface of the microspheres. The diameter of a cast gel sphere is about 1.8 mm.
- Age. The microspheres along with the accompanying precipitation solution are transferred from the casting column to a jacketed rotary flat tank for aging. Steam is used to heat the vessel to 80°C during ageing. The gel spheres are fully converted to solid ADU kernels, and a complete crystal growth takes place.
- Wash. The solution after ageing remains drained from the vessel. Water is used to wash the ADUN kernels in the vessel to remove the ammonium nitrate, ammonium hydroxide and tetrahydrofurfuryl alcohol. The kernels are washed again with isopropyl alcohol to remove moisture, and any remains from ammonium nitrate, ammonium hydroxide and tetrahydrofurfuryl alcohol.

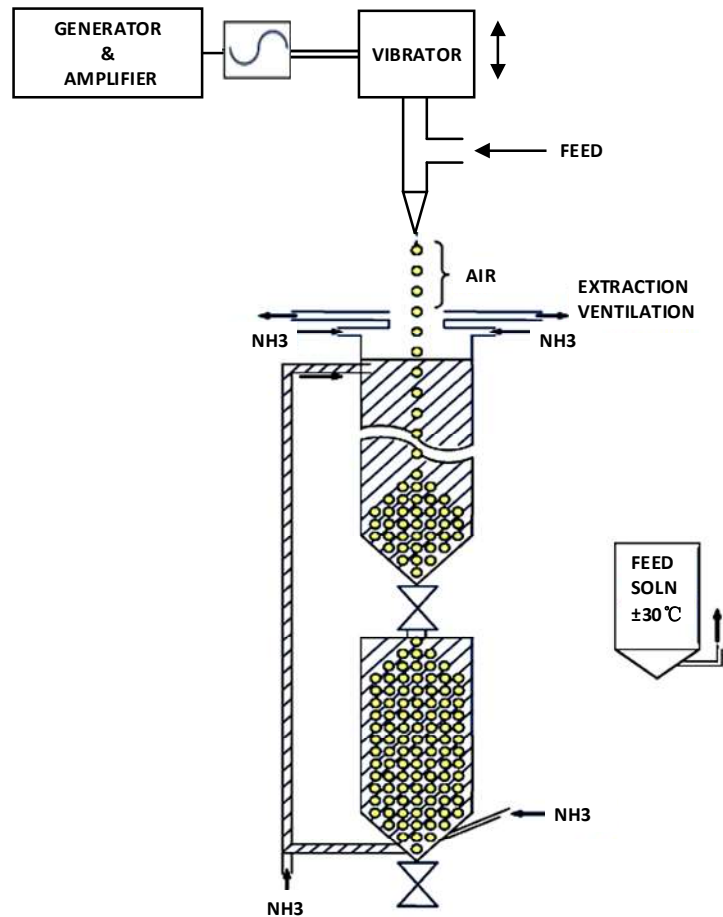


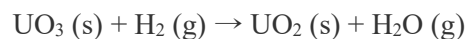
FIG. 25. Illustrative casting process for nuclear fuel kernel production (courtesy of Tsinghua University).

- Dry. The kernels are dried at 80°C under vacuum. The diameter of a dried ADU kernel becomes about 1 mm and the bulk density 1 g/cm<sup>3</sup>.
- Calcine. After drying, the ADUN kernels are calcined in air at up to 430°C. Above 400°C the ADU is converted to UO<sub>3</sub>:



The diameter of a calcined kernel becomes ~0.8 mm and the bulk density ~ 2 g/cm<sup>3</sup>.

- Reduce and sinter. After calcining, reduction and sintering processes at high temperature are followed. As a result, the remaining impurities are removed, and the kernels are densified. The process is conducted under hydrogen atmosphere and UO<sub>3</sub> is converted to UO<sub>2</sub>:



The temperature is maintained up to 1600°C so that dense and stoichiometric UO<sub>2</sub> kernels are formed with a diameter of 500 μm and a density close to the theoretical value of 10.96 g/cm<sup>3</sup>.

Figure 26 shows a composite picture of mixed oxide (Th,U)O<sub>2</sub> fuel gel spheres and kernels after various stages of processing.

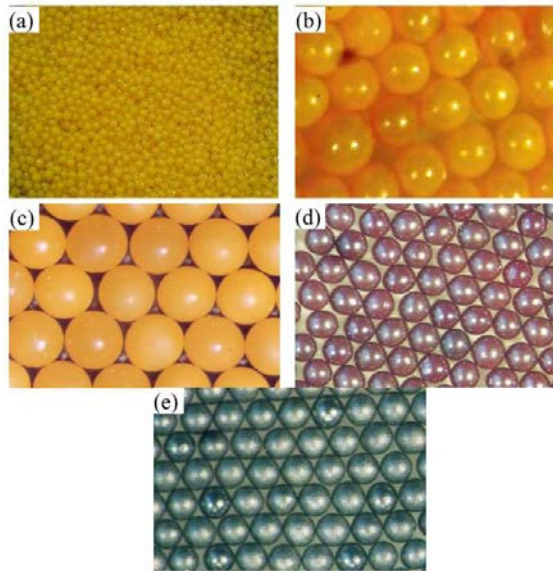


FIG. 26. Kernels in different steps: (a) casted gel particle, (b) aged particle, (c) dried particle, (d) calcined particle, and (e) reduced and sintered particle (courtesy of Tsinghua University).

- Sieve. The final production steps are sieving and sorting. Sieving is used to remove kernels of undersized and oversized.
- Sort. Kernels with odd shapes are then removed through sieving. On a vibrating sorting table that is slightly inclined, spherical kernels roll down-hill and odd-shaped particles are transported along a perpendicular direction by means of vibration and are collected for recycling.

In addition to  $\text{UO}_2$  kernels used widely in HTGR fuel, UCO, UC and UN kernels are considered for use in HTGRs and other SMRs. These kernel compositions have higher thermal conductivity and higher uranium loading fraction compared with  $\text{UO}_2$ . UCO kernels have been used in coated particles in the US for several decades, including in the Next Generation Nuclear Plant (NGNP) project. Based on the  $\text{UO}_2$  kernel manufacturing process, UCO, UC and UN kernel manufacturing technologies are being developed. Figures 27 and 28 show flowsheets of the internal gelation and kernel conversion processes for UC and the UN kernels. Now the new process is under testing to some manufacture scale.

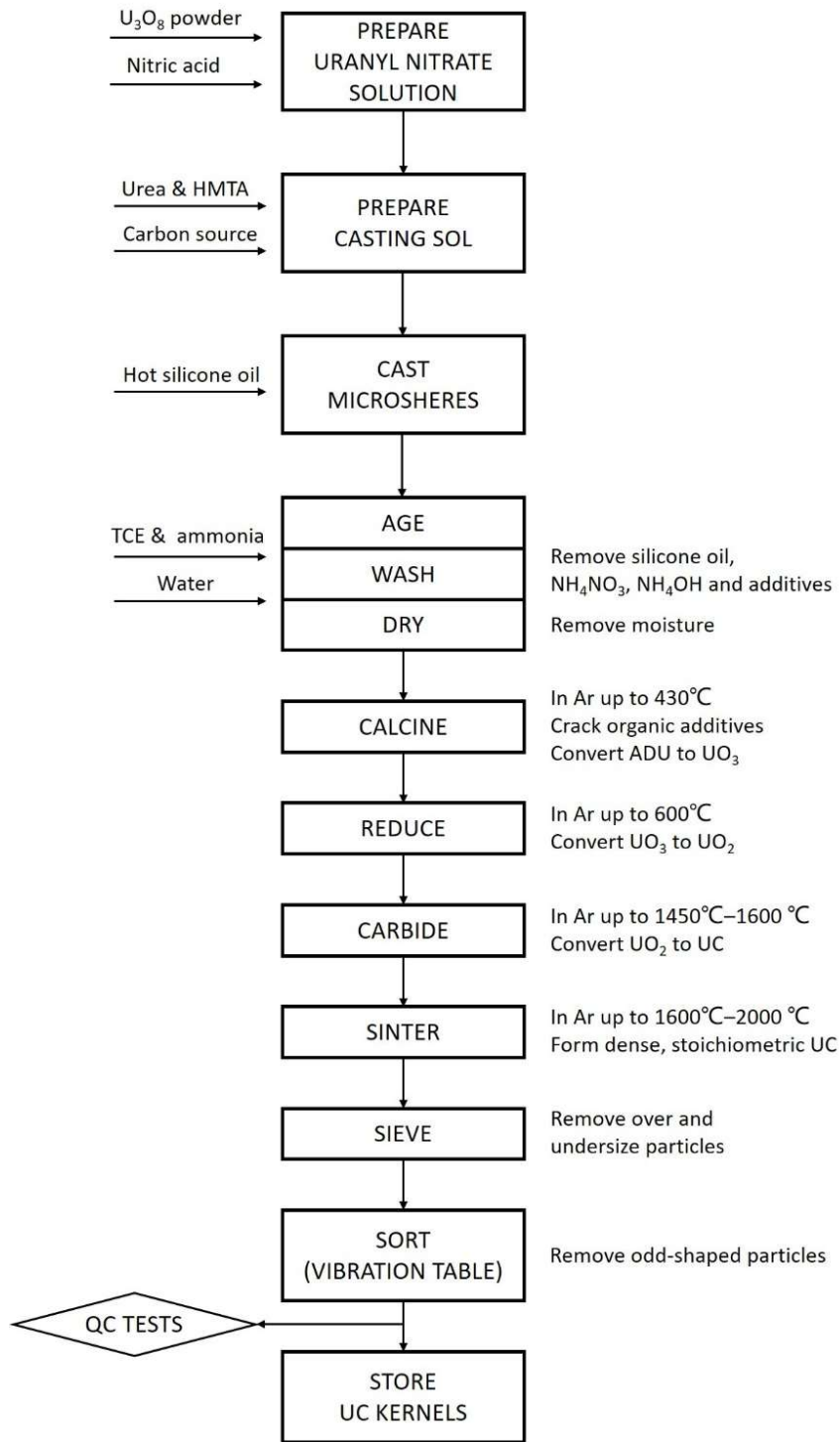


FIG. 27. Illustrative flowsheet for UC kernel fabrication by the sol-gel process (courtesy of Tsinghua University).

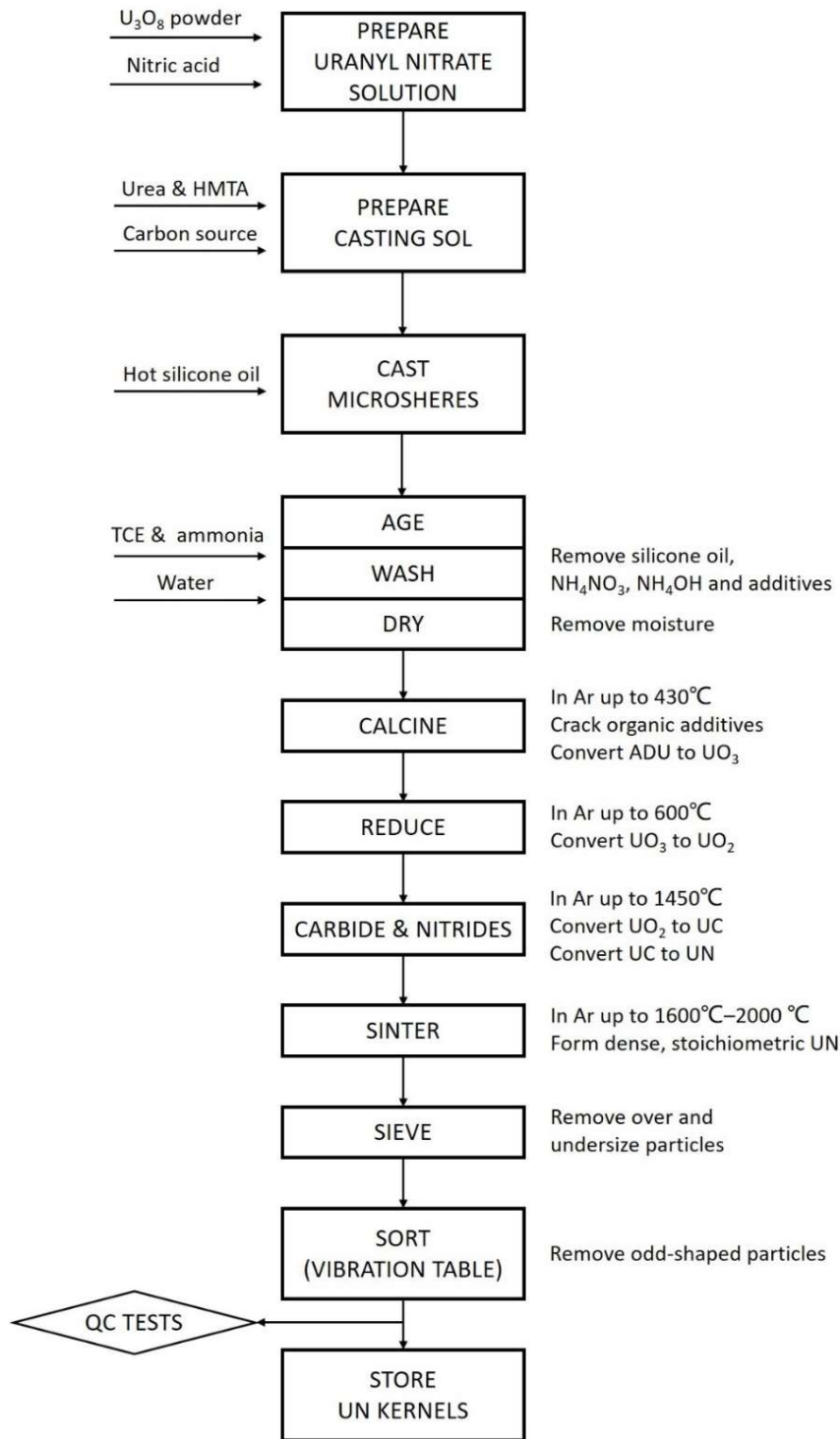


FIG. 28. Illustrative flowsheet for UN kernel fabrication by the sol-gel process (courtesy of Tsinghua University).

#### 4.2. CERAMIC COATINGS BY FLUIDIZED BED CHEMICAL VAPOUR DEPOSITION

The sequence of ceramic coating layers is specific to coated particle fuel: since it is primarily responsible for guaranteeing intact fuel, the design, material selection and processing methods of the layers is

immensely important. But this also makes the fuel largely independent of fuel chemistry in the kernel and provides a wide range of burnup and temperature with intact fuel.

In the manufacturing of TRISO particles, spherical fuel kernels are coated with multiple layers of PyC and an additional layer of SiC. Each layer is deposited by the FB-CVD method. Flowing gases are fed into a bed of kernels in a reaction chamber in a high temperature furnace to suspend the kernels so that they form a fluidized bed. The coating gases thermally decompose at temperatures from 1200°C to 1600°C and deposit their constituent materials onto the surface of the particles.

The low-density buffer layer of pyrolytic carbon is obtained by the decomposition of acetylene ( $C_2H_2$ ) at temperatures from 1200 to 1400°C, whilst the dense pyrolytic layers are obtained by the decomposition of a mixture of ethyne and propene ( $C_3H_6$ ) at temperatures from 1300 to 1400°C. The deposition rate of the dense pyrolytic layers is lower than that of the buffer layer.

The SiC layer is also obtained by a CVD process that includes the decomposition of methyl trichlorosilane ( $CH_3SiCl_3$ ) with  $H_2$  at 1500–1650°C. The deposition rate is correlated with the SiC density, which is very important for the permeability of fissions products.

In the fabrication of the TRISO coating layers, it was noticed that coating temperature was the main parameter affecting the content of free silicon, density, crystallite size, and microstructure [39–44].

The temperature range in which stoichiometric SiC is produced depends on gas flow rates, coater characteristics and particle loading. Deposition at lower temperatures results in the co-deposition of excess silicon and the formation of some porosity, and hence is avoided. Note that the grain size grows considerably with thickness in the coating production, and also affects the retention of fission products as well as the mechanical properties of ceramic materials. Some new technologies have been developed to make fine SiC grain sizes. The crushing strength of SiC coated particles decreases with increasing coating temperature and the strength is correlated with grain size. Xu and co-workers at the Tsinghua University studied coating temperature effect on various parameters of SiC layer such [45] as the microstructure, density, strength and elastic modulus, and concluded that strength and elastic modulus reached the highest values at 1500–1550°C. This is in full agreement with the original DRAGON studies of the 1960s and early 1970s [46,47]. Ref. [43] shows the lower SiC deposition temperatures may be used.

Fuel particle concepts using ZrC as a substitute or in combination with SiC have been studied to a considerable degree since the 1970s. The major advantage of ZrC over SiC is its ability to withstand temperatures in the 2000–2400°C range. However, in modern modular HTGRs the peak fuel temperature is limited by design to  $\leq 1600^\circ C$  and ZrC may be no longer interesting as an alternative particle coating, particularly in view of the substantial development effort that would be needed to achieve similar quality as SiC particles.

A potential benefit of ZrC is an increased resistance to chemical corrosion caused by fission products, particularly by Pd. Some coated particles with ZrC layers have been shown to survive irradiation at elevated temperatures higher than those with SiC. Some results reveal that particles with a thin ZrC coating on the kernel serve as an oxygen absorber, thereby preventing kernel migration through coatings. ZrC may retain caesium and possibly silver better than SiC. However, the retention of certain fission products by SiC is better than by ZrC. In particular,  $^{106}Ru$  has been found to have higher diffusion rates in ZrC than in SiC, and because Pd has not been found concentrated at the inner surface of ZrC layers, there is concern that it could migrate through the coating.

The correlation of coating structure with its irradiation stability has been studied over decades. Different microstructure and density of PyC or SiC coatings can be obtained depending on the concentration of the hydrocarbon or silane coating gases and the temperature of their decomposition (pyrolysis). Figure 29 illustrates a schematic of the CVD process for depositing PyC and SiC coatings.

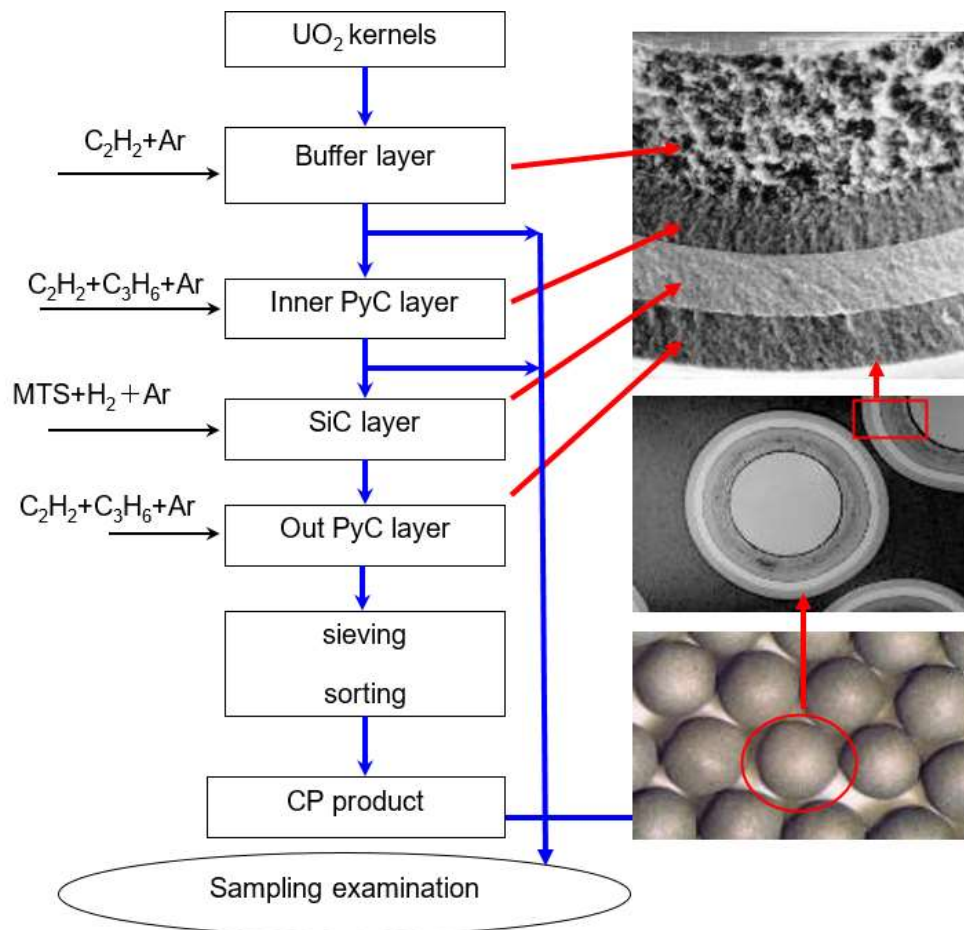


FIG. 29. Illustrative schematic of the deposition of PyC and SiC coatings on dense spherical  $UO_2$  fuel kernels by the CVD process; MTS = methyltrichlorosilane, CP = coated particle (courtesy of Tsinghua University).

A schematic of a typical fluidized bed coating furnace with a so-called ‘spouting nozzle’ [48] is shown in Fig. 30 and the spouted bed principle [48] in Fig. 31.

The fluidized bed coating furnace is a vertically installed, cylindrical stainless-steel vessel and is double-walled with insulation and water cooled. In the centre of this vessel, a graphite resistance heating furnace is mounted which contains a graphite particle-bed tube in which the fuel kernels are fluidized and coated. Various hydrocarbons or silane-coating gases are added to the carrier gas (usually argon gas), responsible for fluidizing the particle-bed, depending on the targeted structure and density of the coating. The temperature for coating remains in the range  $1200\text{--}1600^\circ\text{C}$ , depending on the nature of the coatings. PyC-coated particles were produced at Battelle with a fluidized bed as early as 1959 [49,50].

The process for ZrC layer fabrication is very like the process of a SiC coating layer, but using  $ZrCl_4$  or  $ZrBr_4$  as the precursor for the source of Zr, and ethyne or propene as the source of C.

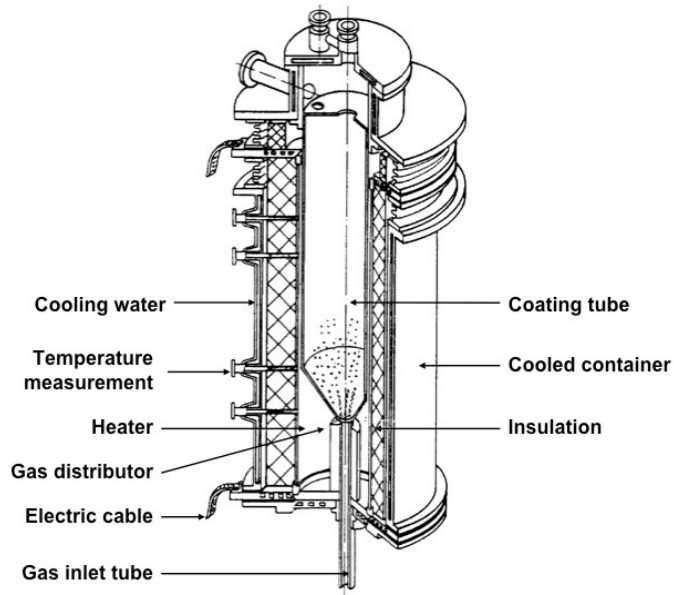


FIG. 30. Typical conical coater with spouted bed (courtesy of IAEA).

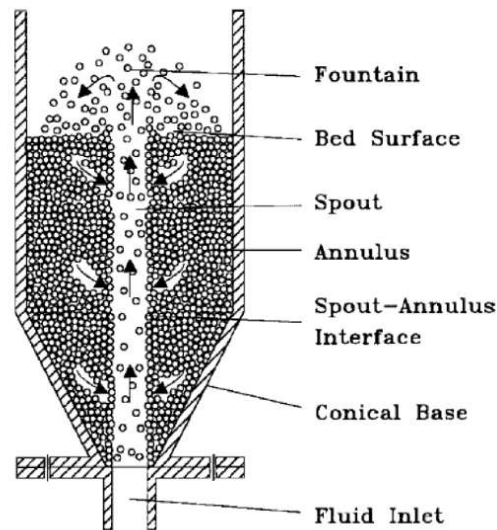


FIG. 31. Principle of the spouted bed characterized by low pressure drop, excellent heat transfer, and good mass transfer (courtesy of IAEA).

#### 4.3. FABRICATION OF SPHERICAL FUEL ELEMENTS

The fabrication process for HTGR spherical fuel elements (pebbles) includes mainly the following steps as described in Ref. [51,52]:

- “Resonated graphitic matrix powder preparation;

- Overcoating of particles;
- Pre-moulding of fuel zone;
- High-pressure isostatic pressing of the complete fuel element;
- Machining;
- Carbonization at 800°C;
- Final heat treatment at 1900–1950°C.”

These processes are illustrated in Fig. 32.

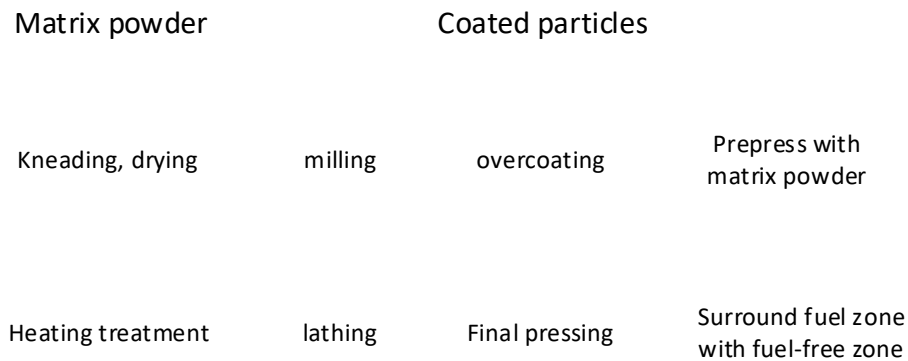


FIG. 32. Illustrative flow chart of processes involved in spherical fuel element fabrication (courtesy of Tsinghua University).

#### 4.3.1. Preparation of resonated graphitic matrix powder

Graphitic matrix is important for the properties of spherical fuel, because more than 90% wt. of the spherical fuel is composed of the graphitic matrix, as shown in Fig. 33, which is based on HTR-10 fuel with 5 g U per pebble loading.

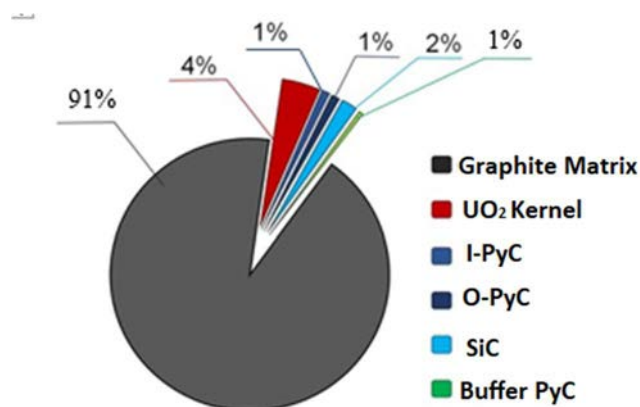


FIG. 33. The weight composition of the spherical fuel (with 5 g U loading of HTR-10 fuel) (courtesy of Tsinghua University).

Table 9 represents differences in composition and fabrication conditions employed by two types of matrix graphite, A3-3 and A3-27, developed for spherical fuel element production by NUKEM [53]. Both types of matrix graphite comprise ~64% natural graphite, ~16% electro-graphite powders, and ~20% phenol resin binder. The primary difference between both types is related to binder.

TABLE 9. COMPOSITION AND FABRICATION PARAMETERS OF GRAPHITE MATRIX MATERIALS USED IN SPHERICAL FUEL ELEMENT FABRICATION

Materials and fabrication	Standard matrix, A3-3	Matrix with synthesized resin, A3-27
Composition of raw materials:		
— Natural graphite	64 wt.%	62.4 wt.%
— Petroleum coke graphite	16 wt.%	15.6 wt.%
— Resin binder	20 wt.%	22.0 wt.%
Binder	Phenolic resin Prefabricated from phenol and formaldehyde	Synthesized resin 2 Synthesized from phenol and hexamethylenetetramine formation
Moulding method	Quasi-isostatic cold moulding	
High temperature treatment:		
— Fuel elements	1800 or 1950°C	1950°C
— Fuel-free matrix spheres	1800°C	1950°C
	<ul style="list-style-type: none"> <li>• For AVR fuel elements: A3-3 and A3-27</li> <li>• For THTR fuel element production: A3-3.</li> </ul>	

The manufacturing process for the graphitic matrix powder is as follows, as described in Ref. [53]:

- “Natural graphite and electro-graphite powders are mixed in a four-to-one ratio in a conical mixer. Depending on the type of matrix required, either A3-3 or A3-27, the binder materials are added in a different manner and the binder is synthesized differently:
  - Standard A3-3 matrix: a phenolic resin is dissolved in alcohol (methanol) to form the binder in a separate process step, added to the natural- and electro-graphite powders and then the mixture homogenized. This mixture is then fed into a kneading machine;
  - A3-27 matrix: all of the raw materials, including the natural- and electro-graphite powders, are warm-mixed together with the binder components—phenol and hexa methylene tetramine—at a temperature of ~130°C where the binder synthesized. This process eliminates the need for kneading and steps 3 and 4 below.
- The paste-like mixture is extruded through a punched screen creating strings that are cut into small pieces.
- These small pieces are placed in drying trays which are heated to approximately 100°C.
- The graphitic mass is then transferred into a hopper that feeds a hammer mill used to grind the material into powder of the desired grain size.
- The dried graphitic mass is transferred into a hopper that feeds a hammer mill used to grind the material into powder of the desired grain size.
- The milled powder is homogenized and ready for pressing.”

The two resin binders show differences in terms of the binder type and cross-linking. As described in Ref. [53], “the phenolic resin binder used for the standard A3-3 matrix graphite is thermoplastic and the polymers are cross-linked primarily two dimensionally. In the A3-27 matrix material, the binder synthesized from phenol and hexamethylenetetramine is duoplastic and the polymers are cross-linked primarily three dimensionally. Thus, the binder cokes formed from the resin binders during the carbonization and heat treatment processes are of different structure.”

The material properties of the two fuel matrix types are described in Ref. [53] and are represented in Table 10. As described in Ref. [53], “a comparison of the test data on the standard A3-3 matrix shows

an improvement in the corrosion rate with the higher 1950°C heat-treatment compared to the lower 1800°C heat-treatment data. The falling strength in the drop and tumble test and the corrosion rate for the A3-27 matrix material are significantly better than those of the standard A3-3 at the higher heat-treatment temperature of 1950°C.”

TABLE 10. MATERIAL PROPERTIES OF GRAPHITE MATRIX USED IN SPHERE FABRICATION

Material property	Standard matrix A3-3		Matrix w. synth. Resin A3-27
	1800°C	1950°C	1950°C
	Older AVR fuel elements	AVR fuel elements THTR prod.	AVR fuel elements
Young's modulus (kN/cm <sup>2</sup> )			
— Parallel*	1020	1000	1070
— Perpendicular*	991	970	1020
Geometrical density (g/cm <sup>3</sup> )	1.70	1.73	1.74
Coefficient of linear thermal expansion (10 <sup>-6</sup> /K), 20-500°C	2.80	2.89	2.43
— Parallel	2.92	3.45	2.69
— Perpendicular			
Quotient of coefficient of thermal expansion (ration of 'perpendicular' over 'parallel')	1.07	1.19	1.11
Thermal conductivity @ room temperature (W/cm/K)			
— Parallel	0.59	0.70	0.69
— Perpendicular	0.63	0.63	0.64
Thermal conductivity @ 1000°C (W/cm/K)			
— Parallel	0.38	0.41	0.44
— Perpendicular	0.38	0.37	0.39
Spec. electrical resistance (10 <sup>-3</sup> Ω.cm)			
— Parallel	1.56	1.46	1.43
— Perpendicular	1.60	1.48	1.48
Falling strength (number of falls to fracture), fall of a tests sphere from a height of 4 m onto A3-3 spheres	521	437	652
Corrosion rate (mg/cm <sup>2</sup> /h), @ 1000°C in He of 1 bar with 1 vol.% H <sub>2</sub> O (10 h)	1.19	0.97	0.73

\* Parallel and perpendicular to the equatorial plane of the matrix sphere.

#### 4.3.2. Overcoating of the TRISO particles

The overcoating of the TRISO particles takes place in a rotating drum as illustrated in Fig. 34. The overcoating is intended to prevent direct contact between particles that may cause the cracking of coating layers during sphere formation. The overcoating is of ~200 μm thickness on the rigid TRISO coated particles. It has the same composition with the graphite matrix. As described in Ref. [53], “the dry graphitic matrix material and a solvent are added simultaneously into the rotating drum in order to maximize adherence and obtain a uniform thickness. The moist overcoated particles are then dried at 80–90°C to remove any of the remaining solvent. The dried overcoated particles are sieved to select the proper sized particles within the range of 1.1 mm and 1.5 mm and are once again sorted on an inclined vibrating table to remove odd shaped, twin, or non-spherical overcoated particles.”



(a)

(b)

FIG. 34. (a) An old, manual overcoating drum and (b) a new, automated overcoating facility located at the INET, Tsinghua university (courtesy of Tsinghua University).

#### 4.3.3. Moulding and pressing of fuel spheres with TRISO particle

Silicon rubber moulds are used to manufacture the fuel spheres by means of quasi-isostatic pressing at room temperature. The pressing operation first includes pre-pressing operation such as taking overcoated TRISO particles together with graphite matrix powder and moulding them to form the internal fuelled spherical zone, ~50 mm diameter. Then the fuel-free shell of ~5 mm thickness is formed by adding additional matrix material around the fuelled core using a final high pressure moulding process. Figure 35 shows the sphere pressing line of the HTR-PM fuel manufacture, Baotou, China.

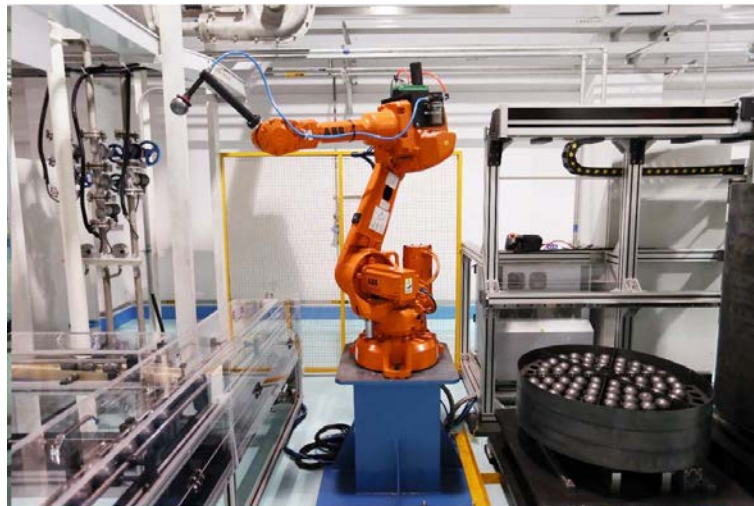


FIG. 35. Moulding and pressing lines for green fuel sphere at the HTR-PM fuel manufacture line, Baotou, China (courtesy of Tsinghua University).

The sphere moulding and pressing process consists of the following steps:

- Firstly, combine overcoated particles with matrix graphite powder and form the fuel zone. As described in Ref. [53],
  - “The matrix graphite powder volume is carefully controlled along with the overcoated particle volume and the mixture is homogenized. The homogenized mixture is injected into the pre-pressing mould and pressed at 5 MPa pressure;
  - The pressed fuel zone spheres are then transferred into the final mould. The lower half of the final mould contains matrix graphite powder. The fuel zone sphere is placed into the centre of the bottom mould and the second half of the mould is placed on top. More matrix material is added through a feeder tube to completely fill the internal annulus between fuel zone sphere and top final mould. Final pressing process is performed at 300 MPa pressure.”
- Secondly, carbonization.
  - After pressing, the green fuel spheres are transported to the carbonization equipment and are heated to 800°C in an inert argon atmosphere furnace to carbonize the phenolic resin binder to provide strength. During this process, the phenolic resin pyrolyzes to carbon materials, which form the matrix strength. Volatile gases are evolved from the sphere at this stage.
- Thirdly, lathing the elements. As described in Ref. [53],
  - “After carbonization, the fuel spheres are transported to the lathing equipment, where they are machined in a two-step process to obtain uniform spheres with specified dimensions.”
- At last, high temperature annealing.
  - The annealing process is conducted in a vacuum at a temperature between 1800–1950°C for one hour with the intention of eliminating residual impurities in the matrix graphite. A higher temperature (1950°C) is preferred to improve corrosion resistance and mechanical strength. Following a cool down phase, the spherical elements are inspected.

#### 4.4. FABRICATION OF COMPACT FUEL ELEMENTS

Fuel compacts are fabricated in cylindrical forms and loaded into the graphite blocks of prismatic HTGR. Solid fuel compacts are mostly used except for Japanese design where annular fuel compact is adopted. Fuel compacts are fabricated in a way generally similar to spherical fuel elements.

Resinated graphite matrix powder is prepared by mixing natural graphite powder, synthetic graphite powder, and resin binder. TRISO particles are overcoated with resinated graphite powder. The overcoating prevents particle-to-particle contact. The coated particles are warm pressed to form cylindrical compacts. Sometimes unfuelled end caps are introduced at both ends of a fuel compact to reduce the likelihood of damage to TRISO particles during compaction and handling. The green compacts are subjected to heat treatments. The resin is carbonized in the range of 800–950°C in an inert nitrogen atmosphere. A subsequent sintering process is made to form compacts and eliminate gaseous impurities by baking at 1650–1950°C under vacuum condition. Cylindrical compacts are typically fabricated to net shape meeting the product specification during this process and are not machined.

#### 4.5. SUMMARY AND DISCUSSION

Technologies for fabricating coated particle fuels have been developed for around half century continued by several countries, which includes the sol-gel technology for the kernel manufacture of UO<sub>2</sub>, UCO and other kinds of Uranium compounds, the fluidized bed chemical vapour deposition technology for the coated fuel particles, and the press technology for both sphere fuel and compact.

Adaption of new technologies, such as additive manufacturing technology, may facilitate a large-scale industrial manufacturing line.

## 5. QUALITY CONTROL FOR FUEL PARTICLE CHARACTERIZATION

### 5.1. QUALITY CONTROL METHODS

In the fuel qualification, quality characteristics are specified and then proven by examinations. The quality characteristics examined for coated particle fuel and associated testing methods are represented in Table 11, based on data from Ref. [54].

TABLE 11. CHARACTERIZATION METHODS FOR HTGR FUEL INCLUDING KERNEL, COATED PARTICLE AND THE SPHERICAL FUEL

Inspection item	Method	Sampling rate
Starting and raw materials		
Compression density of graphite powder	Density measurement under defined load	Powder in forging die
Rebound of graphite powder	Measurement of height difference of powder column during and after load	Powder in forging die
Spec. electric resistance of graphite powder	Measurement of voltage drop along powder column	Powder in forging die
Impurities in graphite powder	Chemical analysis after incineration, emission and absorption spectrometry, photometry, fluorimetry	Representative quantity
Impurities in uranyl nitrate solution	Chemical analysis after incineration, emission and absorption spectrometry, photometry, fluorimetry	Representative quantity
Isotope composition	Mass spectrometry with regards to $^{234}\text{U}$ , $^{235}\text{U}$ , $^{238}\text{U}$	Representative quantity
Fuel kernel		
Heavy metal loading	Transfer of kernels into a stoichiometrically well-defined state and chemical analysis	
Oxygen to metal ratio (O/M)	Potential controlled coulometry	
Isotope composition	Mass spectrometry with regards to $^{234}\text{U}$ , $^{235}\text{U}$ , $^{238}\text{U}$	
Carbon content	Oxidation of kernels and chemical analysis of $\text{CO}_2$	
Oxygen content (UCO)	Hot extraction of oxygen, transfer into $\text{CO}$ , chemical analysis of $\text{CO}$ , infrared spectrometry	
Dopant material content	Spectral photometry, atom absorption spectrometry	
Diameter	Optical imaging with particle size analyser, X ray micro-radiography	
Sphericity	Counting of fraction of odd-shaped particles, multiple measurement of maximum and minimum diameter, micro-radiography, stereomicroscopy	
Density	Optical particle size analyser or V-slot to measure mean diameter. Mercury pycnometer or air pycnometer to measure volume	Larger number of kernels
Structure	Measurement of reflection on defined lattice planes, X ray with Debye-Scherrer goniometer	Ground kernels
Sieve fraction	100% sieving with DIN sieves	
Weight	Weight of counted number of kernel and determine mean weight	
Impurities	Spectral photometry, atom absorption spectrometry	
Coated fuel particle Diameter	Optical particle size analyser	

TABLE 11. CHARACTERIZATION METHODS FOR HTGR FUEL INCLUDING KERNEL, COATED PARTICLE AND THE SPHERICAL FUEL

Layer thickness	X ray projection micro-radiography (only OPyC and SiC), X ray contact microradiography, microscopy analysis of ceramographic sections, optical particle size analyser, fluid pycnometer (in case of discontinuous coating of single layers at a time)	
Density	Weight of counted number of particles and determine mean weight	
Density of highly dense layers	Liquid density gradient column with calibration bodies; Gas pycnometer	Volume of ~50 g
OAF, BAF	Ceramographic sections exposed to polarized light. OAF is ratio of reflected light intensity vertically to deposition direction over reflected light intensity in deposition direction. Correlation between OAF and BAF.	
Growth features, size, and distribution	Etching of ceramographic sections by wet oxidation, plasma oxidation, or ion bombardment, scanning electron microscopy (SEM), transmission electron microscopy (TEM)	SEM on fractured coating, TEM on thinned coating specimens
Polygonity of layers	X ray diffraction, stereomicroscope, measurement of layer thickness in 300–900 position	
Heavy metal content	Grinding of particles and transfer into distinct compounds of U by oxidation, quantitative chemical analysis of U	
Surface contamination	Leaching of particles with HNO <sub>3</sub> , quantitative chemical analysis of U	
Defective SiC layers	Burn-leach method	
Heavy metal migration	Micro-radiography, visual inspection of buffer layer	
Tightness of IPyC	Micro-radiography, visual inspection of buffer and IPyC layers after leaching with HNO <sub>3</sub> compared to before	Samples taken after IPyC coating process
Micro-porosity	Determination of fractions of layer, fibre, mosaic components in PyC by X ray small-angle diffraction	Fragments of PyC layers
Pore structure	Quantitative image analysis and determination of pore size distribution	
Ultimate tensile strength of SiC and PyC	Determination of fracture load by crushing between sapphire plates, hemispherical bursting, ring compression test	Single SiC or PyC rings prepared from layers, single SiC half shells
Micro-hardness	Vickers or Brinell hardness	
Young's modulus: PyC, SiC	Crushing between sapphire plates and recording stress-strain curve	PyC or SiC specimens
<b>Fuel sphere</b>		
Matrix density	Dimension and weight measurements	Matrix specimens 5 mm × 5 mm × 35 mm
Thermal expansion coefficient and anisotropy	Measurement of temperature and dimensional change with dilatometer; Anisotropy is ratio of coefficient (parallel) to coefficient (vertical)	Matrix specimens 5 mm × 5 mm × 35 mm
Dynamic elasticity modulus	Elastomat or frequency generator $E = 4 \times f^2 \times l^2 \times \rho$ where f = resonance frequency, l = length, ρ = density.	Matrix specimens 5 mm <sup>3</sup> × 5 mm <sup>3</sup> × 35 mm <sup>3</sup>
Bending strength	3-point test on bending device $\sigma = (F_m \times l) / W$ where F <sub>m</sub> = fracture strength, l = support span, W = resistance momentum	Matrix specimens 5 mm × 5 mm × 35 mm

TABLE 11. CHARACTERIZATION METHODS FOR HTGR FUEL INCLUDING KERNEL, COATED PARTICLE AND THE SPHERICAL FUEL

Compressive strength	$\sigma = F_c/Q$ where $F_c$ = crushing strength, $Q$ = cross section of specimen.	Matrix specimens 5 mm × 5 mm × 35 mm
Tensile strength	$\sigma = F_t/Q$ where $F_t$ =breaking force, $Q$ = cross section of specimen.	Matrix specimens 8 mm diameter × 30 mm.
Specific electrical resistance	$R = (U \times Q) / (I \times l)$ where $U$ = voltage drop, $Q$ = cross section, $I$ = electric current, $l$ = length.	Matrix specimens 5 mm × 5 mm × 35 mm
Thermal conductivity @ room temperature	Direct measurement	Matrix specimens 5 mm × 5 mm × 35 mm
Thermal conductivity @ 40°C	Thermo-conductometer after Schröder setting a stationary temperature difference by means of the boiling temperatures of two liquids and measuring the time required for the vaporization of a certain quantity of liquid, comparison with calibration standard	Matrix specimens 5 mm × 5 mm × 35 mm
Thermal conductivity @ 1000°C	Radial flux method $\lambda = (Q \times \ln(r_2/r_1)) / (2 \times l \times \Delta T)$ where $Q$ = power of central heater, $r_1$ , $r_2$ = distances of thermocouple (TC) from specimen axis, $l$ = active length of specimen, $\Delta T$ = temperature difference between TC Modified Kohlrausch procedure by setting an almost parabolic axial temperature profile with maximum in specimen centre and small drop to the sides (< 10°)	Matrix specimens 40 mm diameter × 25 mm  Matrix specimens 6 mm diameter × 32 mm with axial bore hole of 1 mm diameter
Impurities, ash contents, B equivalent	Spectral photometer, atomic absorption spectrometry	20–50 g of matrix material
Number of falls	Falls onto pebble bed of the same spheres until fracture	Sphere
Fracture load	Direct measurement	Sphere
Corrosion velocity	Determination of mass loss after 10 h heating @ 900°C or 1000°C in flowing helium at 0.1 MPa and 1% steam: Corrosion velocity $K = \Delta m / (F \times t)$ where $\Delta m$ = mass loss, $F$ = sphere surface, $t$ = time	Sphere
Fuel-free zone	Examination of particle-free shell by X ray and visual inspection	Sphere
Abrasion	Determination of mass loss in mg/h in abrasion drum	Sphere
Surface appearance	Visual inspection	Sphere
Released heavy metal (matrix contamination)	Electrolytic deconsolidation of matrix material with HNO <sub>3</sub> and quantitative chemical analysis of U in electrolyte and leach solution	Sphere
Defective SiC layers	Burning of spheres in muffle furnace and leaching of uranium	Sphere
Heavy metal content	Burning of spheres in muffle furnace, destruction of SiC layers	
Pore size distribution	Quantitative image analysis or determination of pore radius by mercury porosimeter: $P \times r = 2 \times s \times \cos q$ , where $P$ = pressure, $r$ = pore radius, $s$ = surface tension, $q$ = border angle between specimen and mercury	

### **5.1.1. Particle size measurement**

The size (diameter) of the kernel and the particle is measured by using the automated optical particle size analyser (PSA). It can measure at a rate of about 50 particles per second maximum, depending on the feed rate [55]. The sphericity of the kernel and the coated particle is determined by passing through one particle in the light beam many times at randomly changed positions. The PSA can also be used in the optical image analysis of a photograph of many particles on a tray.

### **5.1.2. Kernel, buffer and coating layer density and thickness measurement**

Density significantly affects the retention of fission gases, thermomechanical properties and irradiation behaviour in reactor. Densities of SiC and pyrolytic carbon can be measured with the sink-float method [56] by gradient density columns. In a column, two miscible liquids are mixed and a uniform density gradient is developed. Representative test samples are extracted from the coater after the layer is completed. Pieces of that layer are broken, sink and settled in the column. The column is calibrated by using standards of known density.

This method is not applicable to  $\text{UO}_2$  kernels whose density is high and not applicable to the porous buffer layer because of the possibility of liquid infiltration. For these components, volume can be measured using the PSA or a mercury porosimeter.

The sample's mass is determined prior to its passage through the PSA. Subsequently, the cumulative volume of all kernels within the sample is divided by the sample mass to derive the mean 'apparent' density of the kernels. Following a similar methodology, the density of the buffer layer is determined, taking into account the subtraction of the mean kernel volume from the mean total volume and employing the corresponding mass values. To ascertain the real or 'theoretical' density, assuming a specimen devoid of internal voids, the specimen is crushed into powder using particles of approximately 1  $\mu\text{m}$  in size. A pycnometer is then utilized to measure the volume of the powder. The total porosity is subsequently calculated as 1 minus the ratio of apparent density to theoretical density.

Mercury porosimetry involves surrounding each kernel or buffer-coated particle in a sample with mercury within a container of known volume such that the weight of mercury displaced by the sample defines the envelope volume of the sample. This provides a more accurate measurement of volume compared with the PSA method, especially in the case of non-spherical particles.

A technique for measuring layer thickness involves X-ray micro-radiography, providing robust statistical data on the inherent variation in layer thickness across a substantial number of particles (100–200). In this method, a monolayer of particles is placed directly on a high-resolution photographic film and subjected to X-ray exposure. The analysis of layer thickness on the film is performed using a transmission light microscope and standard image processing software. Alternatively, another approach involves optical image analysis of a monolayer of particles that has been polished to the midplane.

### **5.1.3. Anisotropy measurement**

High density pyrocarbon is a polycrystalline graphitic material and therefore has anisotropic material properties, such as thermal expansion and fast neutron induced shrinkage. The material should be as isotropic as possible to allow uniform heat conduction and minimize dimensional changes under irradiation.

The BAF, outlined in Equations (3) and (4) in section 2.3.3, serves as a direct measure of the anisotropy in macroscopic material. This factor is primarily defined by the coefficients of thermal expansion at 400°C in parallel and perpendicular directions to the preferred orientation. However, obtaining BAF measurements on coated fuel particles is challenging. To overcome this, it becomes necessary to deposit pyrolytic carbon on graphite, producing small disk-type specimens.

Given the non-uniform structure of pyrolytic carbon on spherical particles, an optical method leveraging the bi-reflection of crystalline graphite can be employed. This involves directing a beam of linear polarized light through the equatorial area of the coated particle onto a ceramographic cut.

The procedures for the fabrication and quality control of spherical fuel elements based on the experience of the Institute of Nuclear and New Energy Technologies, Tsinghua University, Beijing, China are shown in Fig. 36 [57].

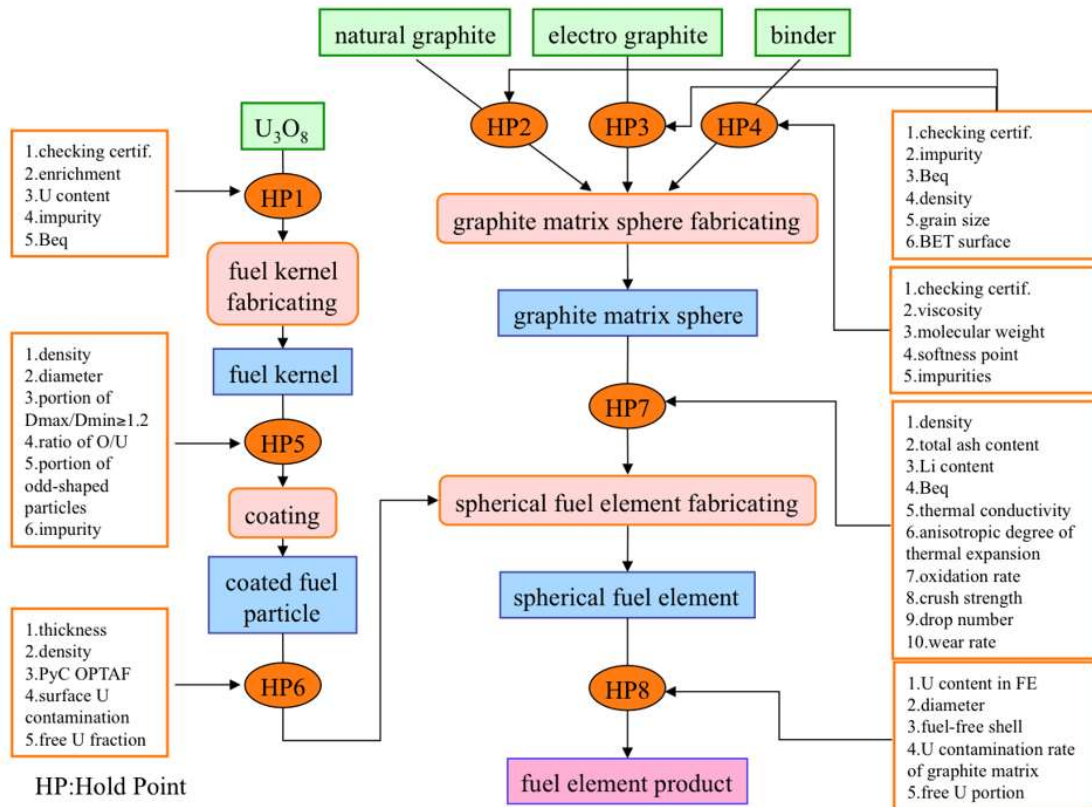


FIG. 36. Fabrication process and quality control diagram for modern TRISO fuel; FE = fuel element, Beq = activity, OPTAF = Optical Anisotropy Factor (courtesy of Tsinghua University).

#### 5.1.4. Phase contrast radiography

Phase contrast radiography is an emerging non-destructive testing method where X-ray radiation from a monochromatic synchrotron or a microfocus source is passed through the TRISO coated microspheres for obtaining the image of various coating layers. This technique is best suited for the detection of boundaries between various coating layers. The boundaries between buffer layer, IPyC layer, SiC layer and the OPyC layer can be clearly distinguished by employing this technique. Using appropriate image analysis software like contrast enhancement or edge enhancement, the thickness of the various coatings can also be measured with good accuracy. Additionally, the uniformity of coating and the shape of the coated layers can also be evaluated.

Phase contrast radiography has been developed at KAERI where they have acquired images with very good contrast using  $ZrO_2$  simulated TRISO particles with a microfocus X-ray source and digital imaging

system [58]. From the acquired images the coating thickness was non-destructively measured using proper calibration. AREVA has developed an X-ray technique that enables the non-destructive control of both the geometry and density of coating layers, replacing the previously employed destructive methods [59,60]. This technique has been explored in the Bhabha Atomic Research Centre (BARC), India to study the pyrocarbon coating on surrogate  $ZrO_2$  kernels as part of the Compact High Temperature Reactor programme in India [61]. This information thus obtained may be used for optimization of the various parameters of the deposition process during TRISO coating development. The phase contrast radiography technique using thermal neutrons instead of X-rays is also being explored at BARC. The interference between neutrons that have been scattered and those transmitted without scatter has been employed to get a contrasting image on neutron detectors. At thermal energies, phase shifts of  $2\pi$  can occur after passing through only a few tenths of  $\mu m$  for many materials. This work is in the preliminary stage at present.

Such new promising techniques for the time being developed only at laboratory level and is required to be industrialized. Though this technique is non-destructive, non-contaminating and yielded comparable results to those obtained with other methods like ceramography, it may find difficult to integrate into a production line. However, this technique may be useful for benchmarking the coating thickness measurement during the coating process development stage.

#### **5.1.5. Burn-leach testing**

A crucial technique for quality assurance is burn-leach testing, particularly in the examination of coated particle fuel for HTGRs. In a 'burn-and-leach' test, the graphite within the sample (which may be loose coated particles, fuel spheres, fuel compacts, or coupons) undergoes combustion in a chamber at 800–850°C in air until reaching the SiC layer, maintaining a constant weight (typically around 90 hours for a fuel sphere). The remaining ash and particles are then treated with a nitric acid solution at ~90°C, and the dissolved uranium content is analysed.

Due to the corrosion-resistant nature of the SiC layer, the uranium detected in the solution comprises both the natural uranium content of the matrix material and the uranium content of particles with a defective SiC layer. Additionally, particles with incomplete coating can be identified. Test results are presented as the ratio of measured free uranium to the inserted uranium, denoted as  $U_{free}/U_{total}$ . The detection limit typically reaches a level of  $(1-3)\times 10^{-6}$ , depending on the uranium content of the sample. This is significantly lower than the uranium content of a single defective coated particle. In a fuel element containing approximately 1 g of  $^{235}U$  per sphere and 0.07 mg per particle, the content of one defective particle corresponds to a  $U_{free}/U_{total}$  value of  $7\times 10^{-5}$ .

#### **5.1.6. Fuel elements**

Sphere fuel (pebble) will be recycling in the pebble-bed reactor, which has some additional requirements in some properties, such as the fall test, the abrasion test and the free fuel zone examination.

The free-fall drop test is a special requirement for the pebble fuel. During the fall test, the sphere fuel usually represented by graphite ball which was fabricated used the same materials and the same process, the graphite ball will be dropped from 4 m height onto the pebble bed composed of the same spheres. Usually, the test cycle will continue more than 50 times for each graphite ball, or until the graphite ball fractures. After fall test, every graphite ball should be checked, and also the graphite balls in the pebble bed.

Abrasion is another special requirement for the sphere fuel, due to the sphere fuel movement in the reactor. The abrasion test is conducted in the special designed abrasion drum, usually the fuel is represented by the graphite ball. The abrasion drum is designed to simulate the sphere fuel move path, both abrasion between fuels in the reactor, and the abrasion between the fuels and the metal pipes, which used to upload and download the fuels out of the reactor. The graphite balls were put into the drum, and the drum rotate at a designed speed. After 100 h, the graphite balls will be checked. And the total ash

will be collected and weighted, the mass loss is the determination of the abrasion properties. The detection mass loss limit is typically at a level of 6.0 mg/h per ball, but usually the test results is less than 2.0 mg/h per ball.

As mentioned above, the sphere fuel moves in the reactor from the top to the bottom and recycle in the handing pipe out of the reactor. The fuel free zone of the sphere fuel is designed for the protection of the coated particles in the fuel zone when the sphere fuel cycles. The free fuel zone is examined by X-ray method while the sphere fuel makes a complete rotation to find the coated particles out of the fuel zone. The free fuel zone is designed with a 5 mm thickness. All the sphere fuels should be examined after manufactured.

## 5.2. QUALITY CONTROL RESULTS

There exists a well-defined set of criteria for contemporary high-quality nuclear fuel, encompassing stringent standards for minimal levels of heavy metal contamination, prevention of manufacture-induced particle defects during the fuel body and fuel element production, mitigation of irradiation/accident-induced particle failures, and restrictions on fission product release from intact particles [62,63].

While the design of HTGRs remains flexible, incorporating configurations for prismatic and spherical fuel elements, there is a global consensus on the characteristics of high-quality fuel. This typically involves a 500  $\mu\text{m}$  diameter  $\text{UO}_2$  kernel enveloped by a substantial sacrificial buffer layer, succeeded by a dense inner pyrocarbon layer, a high-quality silicon carbide layer with close to theoretical density, and another dense outer pyrocarbon layer.

The development and manufacturing details of  $\text{UO}_2$  TRISO fuel elements in Germany are described in [64] and are represented in Tables 12 and 13. Good performance has been demonstrated both under operational conditions to 12% FIMA and more and under accident conditions to a maximum 1600°C.

TABLE 12. DEVELOPMENT OF THE LOW ENRICHE UO<sub>2</sub> TRISO FUEL ELEMENTS IN GERMANY

Characteristic	Before 1985 production			After 1985 production	
	1981-83	1981	1983	1985-87	1988
Year of manufacture	1981-83	1981	1983	1985-87	1988
Designation	AVR 19	LEU Phase 1	AVR 21-1	AVR 21-2	Proof Test Phase 2
Matrix material	A3-27	A3-27	A3-27	A3-3	A3-3
Irradiation tests	GLE 3	HFR-K3 FRJ2-K13 HFR-P4 SL-P1 FRJ2-P27 FRJ2-P28	GLE 4 FRJ2-K15	GLE 4/2  HFR-EU1 HFR-EU1bis	HFR-K5 HFR-K6
No. of spheres manufactured	24 600	100	20 500	14 000	200
Number of fuel element lots (1)	14	-	11	8	-
Number of coating batches	65	1	54	29	8
Coating batch size (kg)	5	5	3	3	5
Coated particle batch designation	HT232-245	EUO 2308	HT354-383	HT385-393 HT395-404 HT406-423	EUO 2358-2365
Number of kernel sets	5	1	2	5	1

TABLE 13. MANUFACTURING DETAILS OF LEU UO<sub>2</sub> TRISO FUEL IN GERMANY

Characteristic	Before 1985 production			After 1985 production		Typical modern specs
	AVR 19	LEU Phase 1	AVR 21	AVR 21-2	Proof test Phase 2	
Kernel diameter (µm)	500	497	501	502	508	500
Kernel density (g/cm <sup>3</sup> )	10.80	10.81	10.85	10.86	10.72	> 10.4
Coating thickness (µm)						
- Buffer	93	94	92	94	102	95
- IPyC	38	41	38	41	39	40
- SiC	35	36	33	36	36	35
- OPyC	40	40	41	40	38	40
Coating density (g/cm <sup>3</sup> )						
- Buffer	1.01	1.00	1.01	1.0	1.02	< 1.05
- IPyC	1.86	~1.9	1.9	1.87	1.92	1.9
- SiC	3.19	3.20	3.20	3.20	3.20	≥ 3.18
- OPyC	1.89	1.88	1.88	1.87	1.92	1.9
Loading						
Heavy metal (g/fuel element)	10	10	6	6	9.4	9
<sup>235</sup> U (g/fuel element)	1	1	1	1	1	0.86
Enrichment (% <sup>235</sup> U)	9.82	9.82	16.76	16.76/ 16.67	10.6	9.6
Number of particles/fuel element	16 400	16 400	9560	9560	14 580	14 440
Free uranium fraction (10 <sup>-6</sup> )	50.7	35	43.2	7.8	13.5	< 60

### 5.2.1. UO<sub>2</sub> kernel results

The fuel kernel, in a spherical form, comprises stoichiometric uranium dioxide (UO<sub>2</sub>). This kernel functions as a partial barrier, effectively immobilizing a significant portion of fission products and slowing down the diffusive release of others. Consequently, this mechanism significantly diminishes the release of radionuclides from the particle, as a considerable portion undergoes radioactive decay before being released from the kernel.

Table 14 represents the quality control results from the latest large scale AVR fuel manufacture type GLE-4/2 (reload 21-2) from December 1985 to August 1987 [65,66].

TABLE 14. SIMPLIFIED QUALITY CONTROL DATA FROM KERNEL MANUFACTURE OF THE AVR 21-2 FUEL WITH ~ 17% ENRICHMENT

Property	Test frequency	Specification	Lot number				
			#4	#5	#6	#7	#8
Sieve fraction (μm)	100%	450–560					
Kernel diameter (μm)	1000 kernels per lot	(480 ≤ d ≤ 520) 90	502 ± 1	500 ± 1	501 ± 1	501 ± 1	507 ± 1
		(d > 600) 95/95	T <sub>U</sub> <sup>(1)</sup> = 520	T <sub>U</sub> = 519	T <sub>U</sub> = 520	T <sub>U</sub> = 521	T <sub>U</sub> = 522
Sphericity ≤ 1.2	800 kernels	≤ 11	0	1	0	0	0
Sphericity ≤ 1.5	800 kernels	≤ 3	0	0	0	0	1
Other shapes	800 kernels	≤ 3	0	0	1	1	1
Density (g/cm <sup>3</sup> )	1 determination per lot	mean ≥ 10.4	10.81	10.85	10.90	10.89	10.89
Stoichiometry	1 determination per lot	O/U ≤ 2.015	2.00	2.00	2.01	2.00	2.01
Equivalent boron content (ppm)	1 sphere per lot	≤ 2	0.64	0.54	0.60	0.54	0.59

(1) T<sub>U</sub> = one-sided 95% confidence/ 95% coverage upper limit.

In manufacturing processes, there are two types of tests and specifications:

- Comprehensive non-destructive inspection tests are conducted on 100% of the fuel kernels. Techniques such as sieving and other methods are employed to ensure that diameters fall within the range of 450 to 560 μm;
- Sampling tests are also implemented, where a portion of the product undergoes testing. All destructive tests fall under the category of sampling, representing a subset of the overall production.

For sampling tests, sampling statistics has been employed to deal with variations of properties. For the kernel diameter, the one-sided 95% confidence/ 95% coverage upper limit  $T_U$  is correlated with mean value  $m$  and standard deviation  $\sigma$ , as it follows:

$$T_U = m + K_U \sigma \quad (6)$$

where  $K_U$  is displayed as function of sample size  $n$  (see Fig. 37);  $K_U$  serves as the multiplying factor applied to the standard deviation to define an upper tolerance limit in production; the ' $K_U$  95/95' values are calculated using the non-central t-distribution, as detailed in Ref. [67].

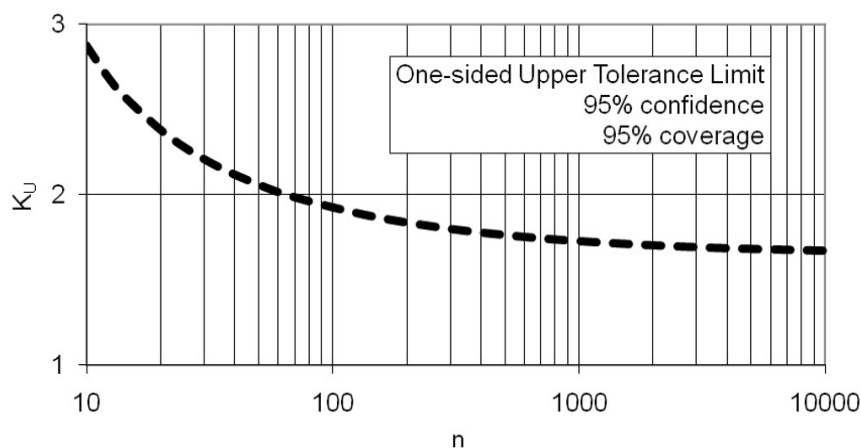


FIG. 37. Factor  $K_U$  as a function of sample size  $n$  for covering a one-sided upper 95% of the cases with 95% confidence (e.g.  $K_U = 1.727$  for  $n=1000$ ).

This correlation allows for the derivation of standard deviations for kernel diameters, a crucial parameter in model calculations predicting the irradiation performance of coated particles. In the case of the AVR 21-2 fuel, the model would incorporate kernels with a diameter of  $502.2 \pm 10.6 \mu\text{m}$ , taking into account the specified standard deviation. This information is vital for accurate and comprehensive assessments of irradiation behaviour based on the specified kernel size and its associated variability.

### 5.2.2. Coated particle results

The first layer in contact with the kernel is the buffer layer deposited from  $\text{C}_2\text{H}_2$ . Temperature and other conditions in the fluidized bed are adjusted to produce a porous layer with approximately 50% of theoretical density  $2.2 \text{ g/cm}^3$ .

The buffer layer serves a dual purpose in coated particles. Firstly, it provides void volume for gaseous fission products, preventing undue pressure build-up within the particle. Additionally, it mechanically decouples the kernel from the inner pyrocarbon layer, accommodating kernel swelling and minimizing stress accumulation in the outer coating layers during irradiation. The buffer layer also acts as a shield, absorbing energetic fission products recoiling from the kernel surface and protecting the inner pyrocarbon layers.

The inner layer of high-density, isotropic IPyC is deposited from a mixture of  $\text{C}_3\text{H}_6$  and  $\text{C}_2\text{H}_2$ , boasting an average density of around  $1.9 \text{ g/cm}^3$ . As the first load-bearing barrier, the IPyC layer mitigates pressure exerted by fission products within the fuel kernel and buffer layer, thus reducing the stress on SiC. During irradiation, the IPyC and OPyC layers initially shrink, potentially expanding again with sufficiently high fast neutron dose levels. The interaction between the high-density pyrocarbon layers and the SiC layer is crucial for maintaining compression on the SiC layer during irradiation.

While an intact IPyC layer forms an effective barrier against fission gases and iodine, its permeability increases at higher temperatures, allowing passage of palladium, caesium, silver, and strontium. SiC, deposited from methyl trichlorosilane  $\text{Si}(\text{CH}_3)\text{Cl}_3$  under specific conditions, attains a density of  $3.20 \text{ g/cm}^3$ , slightly below the theoretical density of  $\beta$  SiC with a 3C structure ( $3.216 \text{ g/cm}^3$ ).

At elevated temperatures, the ability of the IPyC and OPyC layers to contain caesium, silver, and strontium diminishes. The SiC layer plays a critical role in preventing the release of these metallic fission products into the graphite matrix and subsequently into the reactor helium stream. Thus, the SiC layer acts as the primary retention barrier for metallic fission products in the coated particle.

With a numerical property like the coating layer thickness with mean  $m$  and the standard deviation  $\sigma$ , the upper tolerance limit  $T_u$  is given by:

$$T_u = m + k\sigma \quad (7)$$

The lower tolerance limit  $T_l$  is given by:

$$T_l = m - k\sigma \quad (8)$$

where:

$$k = \sqrt{\frac{(n-1)\left(1+\frac{1}{n}\right)z_{(1-p)/2}^2}{\chi_{\gamma,n-1}^2}} \quad (9)$$

$\chi_{\gamma,n-1}^2$  represents the critical value of the  $\chi^2$  distribution with  $(n - 1)$  degrees of freedom, indicating the threshold beyond which this distribution is exceeded with a probability of  $\gamma$ ; and  $z_{(1-p)/2}$  represents the critical value of the standard normal distribution that is exceeded with a probability of  $(1 - p)/2$ . This value is often utilized in statistical analyses to establish confidence intervals or significance levels. The  $k$  values data as a function of sample size are shown in Fig. 38.

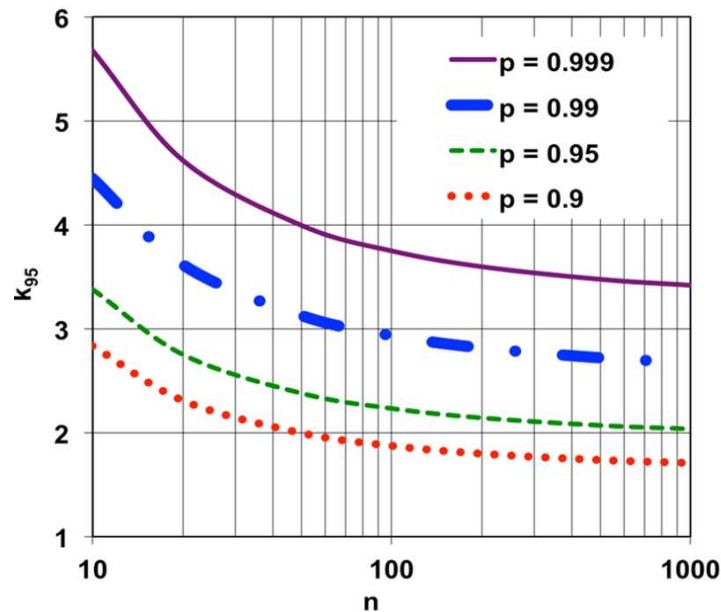


FIG. 38.  $K$ -value for two-sided tolerance limits in the case of a two-sided 95% confidence for 99.9%, 99%, 95% and 90% coverage (or proportion)  $p$  as a function of sample size  $n$  (courtesy of Tsinghua University).

From this, the necessary particle data with standard deviation as required for modelling purposes are derived. A summary is given in Ref. [68]. These data are used in mechanical performance benchmark calculation of the IAEA Coordinated Research Programme #6 on Advances in HTGR Fuel Technology [5]. Table 15 represents these data.

TABLE 15. GERMAN LEU PARTICLE DATA DERIVED FROM MANUFACTURER'S QUALITY CONTROL DATA

Test	HFR-K3 with fuel from AVR GLE3	FRJ2-K15 with fuel from AVR GLE4	HFR-EU1 with fuel from AVR GLE4/2
Coating batch number	EUO 2308	HT 354-383	HT 385-393 HT 395-404 HT 406-423
Kernel composition	LEU UO <sub>2</sub>	LEU UO <sub>2</sub>	LEU UO <sub>2</sub>
Enrichment (U-235 wt.%)	9.82	16.76	16.76/16.67
Kernel diameter (µm)	497 ± 14.1	501 ± 10.8	502.2 ± 10.6
Buffer layer thickness (µm)	94 ± 10.3	92 ± 14.3	94.3 ± 13.0
IPyC layer thickness (µm)	41 ± 4.0	38 ± 3.4	40.6 ± 3.7
SiC layer thickness (µm)	36 ± 1.7	33 ± 1.9	35.9 ± 2.2
OPyC layer thickness (µm)	40 ± 2.2	41 ± 3.8	39.8 ± 3.3
Kernel density (g/cm <sup>3</sup> )	10.81	10.85	10.86
Buffer density (g/cm <sup>3</sup> )	1.00	1.013	1.012
IPyC density (g/cm <sup>3</sup> )	1.9	1.9	1.87
SiC density (g/cm <sup>3</sup> )	3.20	3.20	3.20
OPyC density (g/cm <sup>3</sup> )	1.88	1.88	1.87
IPyC anisotropy BAF	1.053	1.029	1.02
OPyC anisotropy BAF	1.019	1.020	1.02

### 5.2.3. Fuel elements

In the pre-1985 category, particle overcoating was carried out manually, while in the post-1985 category, an automated process was implemented using a specifically designed mixer operated by a robot. This transition to automation significantly enhanced fuel quality, as illustrated in Table 16 (from [69]).

To create a fuel sphere, overcoated particles, along with matrix material, are pressed into a 50 mm diameter inner sphere, accommodating between 9000 and 17,000 coated particles. Subsequently, this inner fuel sphere is encased within a protective layer of A3 matrix material, measuring 5 mm in thickness. The outer layer is formed through an isostatic pressing process and precision machining to achieve the final dimensions.

TABLE 16. GERMAN AVR 21-2 (GLE-4/2) BURN-LEACH DATA

Number of particle defects in sphere (see Note)	Lot number							
	#1	#2	#3	#4	#5	#6	#7	#8
#1	0	0	0	0	0	0	0	0
#2	0	0	0	1	0	0	0	0
#3	0	0	0	0	0	0	0	0
#4	0	0	0	0	0	2	0	0
#5	0	0	0	0	0	0	0	0
Total number of defective particles in 5 spheres	0	0	0	1	0	2	0	0
Defect fraction (expected level) =	$\frac{1 \times 1 + 1 \times 2 + 0 \times 3 + \dots}{5 \times 8 \times 9560} = \frac{3}{382400} = 7.8 \times 10^{-6}$							
Defect fraction (upper 95% conf. limit) =	$2.0 \times 10^{-5}$							

Note: Evaluation of defect fraction (mean= expected and one-sided upper 95% confidence limit).

Only 8,740 fuel elements from the 14,000 spheres of the GLE-4/2 production were inserted as reload AVR 21-2 in October 1987, because no further fuel was needed due to AVR shutdown on 31 December 1988. Some of the remaining elements underwent further investigations including the insertion of five spheres into the HFR-EU1bis irradiation test and three spheres into the HFR-EU1 irradiation test [69].

Results shown in Table 17 represent a record low level in terms of particle defects during HTGR fuel manufacture. This is due to improved tabling of kernels, coated particles and overcoated particles in the selection of spherical shapes and also due to advances in the design and operation of the overcoating drum in producing a perfected product for the cold isostatic pressing of spheres. Selected data from overcoating runs are shown in Table 17.

TABLE 17. SELECTED RESULTS FROM AVR 21-2 OVERCOATING RUNS

<b>Overcoating charge</b>	<b>TU208</b>	<b>TU209</b>	<b>TU210</b>	<b>TU212</b>	<b>TU213</b>	<b>TU214</b>	<b>Mean</b>
Diameter of overcoated particles (µm)	1327	1306	1279	1319	1308	1332	1312
Diameter of particles (µm) after removal of overcoating	917	915	913	915	917	916	916
Overcoating density (g/cm <sup>3</sup> )	1.60	1.59	1.61	1.57	1.59	Not measured	
Overcoating thickness (µm)	205	195.5	183	202	195.5	208	198
Observations in 1500 overcoated particles:							
Missing overcoating	0	0	0	0	0	0	
Partial overcoating	0	0	0	0	0	0	
Overcoating < 50 µm	0	0	0	0	0	0	
Twins	0	0	0	0	0	0	
Overcoated graphite lumps	0	1	0	0	0	1	
Odd shapes	0	0	0	0	0	0	

The compact fuel is designed and used in the HTTR in Japan, and in the NGNP in US. In the production of HTTR fuel, a total of 4770 fuel rods were manufactured using the fuel kernel, coated fuel particle, and fuel compaction processes. Subsequently, in December 1997, these fuel rods were assembled into 150 fuel elements within the reactor building. NFI developed the measurement equipment for the coated layer thickness of a coated fuel particle and the uranium content of a fuel compact. The uranium content examination method is leach-burn-leach, which is similar for both sphere fuel and compact fuel. The leach-burn-leach process is described in Section 5.1.5. The initial loading fuel met the design specifications completely. The fuel compacts exhibited an average bare uranium fraction of  $2 \times 10^{-6}$  and a SiC defective fraction of  $8 \times 10^{-5}$ , both in accordance with the specified criteria [67].

### 5.3. SUMMARY AND DISCUSSION

The quality assurance/quality control system for the TRISO coated particle fuel was also established based on the examination methods. The industrial scale manufacture technology established in some countries can provide the high quality TRISO coated fuel particle needed for SMRs deployment using this type of fuel.

## 6. IRRADIATION TESTS, HEATING TESTS AND POST IRRADIATION EXAMINATIONS

A number of irradiation tests, post-irradiation annealing tests at elevated temperatures and follow-up PIEs have been conducted on coated particle fuels in several countries. These irradiation tests were done in operating HTGRs or in various material test reactors where gas loop techniques enable to detect failed coated particles. Typical irradiation conditions were of normal operation in a wide range of burnup, temperature and fast fluence.

### 6.1. TESTS CONDUCTED BEFORE THE EARLY 2000S

#### 6.1.1. Spherical pebbles

##### 6.1.1.1. Irradiation tests

Table 18 shows irradiation tests performed with spherical pebbles up to the early 2000s. These irradiations were found from various sources such as [3–5,70–74]. The information includes fuel types, irradiation time in full power days (FPDs), fast fluence, burnup, operating temperature, and the fractional release of  $^{85m}\text{Kr}$  (i.e., the ratio of release (R) to birth (B) of  $^{85m}\text{Kr}$ ). All test elements in Table 18 remained intact as described in Ref. [3], which reveals that spherical pebbles can withstand normal operating conditions in the reactor that covers burnup to 14% FIMA and higher operating temperatures than 1000°C.

##### 6.1.1.2. Heating tests

Heating tests on irradiated coated particle fuel at elevated temperature are performed to simulate accident conditions of HTGRs. For a small HTGR, the maximum temperature during a LOCA with complete depressurization is estimated to slightly exceed 1600°C for around 30 h, as shown in Fig. 39 [3].

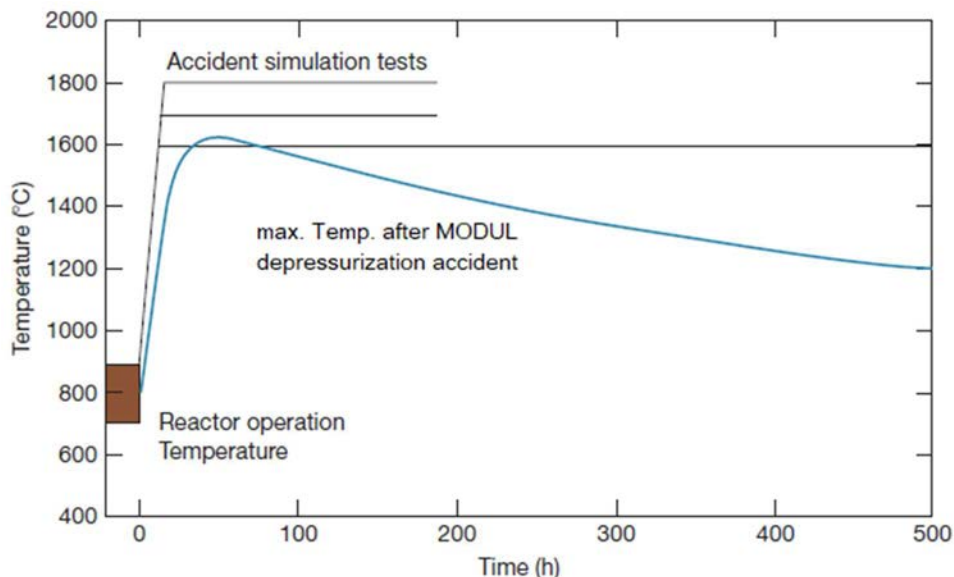


FIG. 39. Temperature evolution during a loss-of-coolant accident in a small HTR, and in heating tests to simulate the accident (taken from Ref. [3], courtesy of IAEA).

TABLE 18. IRRADIATIONS OF SPHERICAL PEBBLES CONDUCTED BEFORE THE EARLY 2000s

Test reactor	Experiment ID	No. of specimen and fuel type (mm)	Country	Irradiation time (FPDs)	Fast fluence ( $10^{21}$ n/cm <sup>2</sup> , E>0.10 MeV)	Burnup (% FIMA)	Operating temp. (°C)	Defective SiC layer fraction (U/U-total)	BOL <sup>85m</sup> Kr R/B EOL <sup>85m</sup> Kr R/B	Reference
R2 (Studsvik, Sweden)	R2-K12	4 spheres (dia. 59.9, fuel zone 47) HEU (Th,U)O <sub>2</sub> TRISO	Germany	28 Nov. 1978 – 12 Feb. 1980 (308)	5.6, 6.9	11.1, 12.4	Centre; 1100, 1280 Surface; 950, 1120	< 1×10 <sup>-5</sup>	3.9×10 <sup>-9</sup> , 4.6×10 <sup>-9</sup> 3.0×10 <sup>-7</sup> , 2.0×10 <sup>-7</sup>	[70]
R2 (Studsvik, Sweden)	R2-K13	2 spheres (dia. 59.77, fuel zone 47) HEU (Th,U)O <sub>2</sub> TRISO	Germany (12 compacts, USA)	22 Apr. 1980 – 19 Sep. 1982 (517)	8.5, 6.8	10.2, 9.8	Centre; 1170, 980 Surface; 960, 750	< 5×10 <sup>-6</sup>	2.2×10 <sup>-9</sup> , 1.5×10 <sup>-9</sup> 7.0×10 <sup>-8</sup> , 5.0×10 <sup>-8</sup>	[3,70]
BR2 (Mol, Belgium)	BR2-P25	12 small spheres (spherical fuel zone 20 mm in graphite compact; dia. 26.58-27.74, height 29.87-30.03) HEU (Th,U)O <sub>2</sub> TRISO	Germany	30 Oct. 1978 – 19 Sep. 1981 (350)	62-8.1	13.9-15.6	Centre; 1070 Surface; 1010	< 1×10 <sup>-5</sup>	2×10 <sup>-7</sup> 1×10 <sup>-6</sup>	[70]
HFR (Petten, Netherlands)	HFR-P4	12 small spheres (spherical fuel zone 20 mm in graphite compact; dia. 23-29, height 32) LEU UO <sub>2</sub> TRISO	Germany	10 Jun. 1982 – 28 Nov. 1983 (350)	8.0 (peak)	14.7, 14.9, 14.0 (max.)	940, 945, 1075 (max) 915, 920, 1050 (min.)	< 1×10 <sup>-6</sup>	3.5×10 <sup>-9</sup> , -, 3.6×10 <sup>-8</sup> 8×10 <sup>-9</sup> , 8×10 <sup>-9</sup> , 8×10 <sup>-9</sup>	[3,5,70,74]
Siloë (Grenoble, France)	SL-P1	12 small spheres (spherical fuel zone 20 mm in graphite compact; dia. 30.1, height 30.8) LEU UO <sub>2</sub> TRISO	Germany	24 Jun. 1982 – 23 Dec. 1983 (330)	5.0-6.8	8.6-11.3	743-794 (compact mean temp.)	< 1×10 <sup>-6</sup>	5.8×10 <sup>-7</sup> 1.2×10 <sup>-6</sup>	[3,5,70]

TABLE 18. IRRADIATIONS OF SPHERICAL PEBBLES CONDUCTED BEFORE THE EARLY 2000s (CONT)

Test reactor	Experiment ID	No. of specimen and fuel type (mm)	Country	Irradiation time (FPDs)	Fast fluence ( $10^{21}$ n/cm <sup>2</sup> , E>0.10 MeV)	Burnup (% FIMA)	Operating temp. (°C)	Defective SiC layer fraction (U/U-total)	BOL <sup>85m</sup> Kr R/B EOL <sup>85m</sup> Kr R/B	Reference
HFR (Petten, Netherlands)	HFR-K3	4 spheres (dia. 59.89, fuel zone 47) LEU UO <sub>2</sub> TRISO	Germany	15 Apr. 1982 – 5 Dec. 1983 (359)	4.0, 5.8, 5.9, 4.9	7.5, 10.0, 10.6, 9.0	Centre; 1200, 920, 920, 1220 Surface; 1020, 700, 700, 1020	< 4×10 <sup>-5</sup>	1×10 <sup>-9</sup> , 9×10 <sup>-10</sup> , 9×10 <sup>-10</sup> , 2×10 <sup>-9</sup> 2×10 <sup>-7</sup> , 1×10 <sup>-7</sup> , 1×10 <sup>-7</sup> , 3×10 <sup>-7</sup>	[3,5,70,71]
HFR (Petten, Netherlands)	HFR-K4	2 spheres LEU UO <sub>2</sub> TRISO	Germany	- (667)	10.0	13	Centre; 1250	-	-	[70,71]
DIDO (Jülich, German)	FRJ2-K13	4 spheres (dia. 59.89, fuel zone 47) LEU UO <sub>2</sub> TRISO	Germany	24 Jun. 1982 – 12 Dec. 1984 (396)	0.2, 0.2, 0.2, 0.2	7.5, 8.0, 7.9, 7.6	Centre; 1125, 1150, 1150, 1120 Surface; 985, 990, 990, 980	4×10 <sup>-5</sup>	2×10 <sup>-9</sup> , 2×10 <sup>-10</sup> , 8×10 <sup>-10</sup> , 8×10 <sup>-10</sup> 2×10 <sup>-8</sup> , 2×10 <sup>-8</sup> , 7×10 <sup>-9</sup> , 7×10 <sup>-9</sup>	[3,5,70]
DIDO (Jülich, German)	FRJ2-K15	3 spheres (dia. 60.04, fuel zone 47) LEU UO <sub>2</sub> TRISO	Germany	4 Sep. 1986 – 20 May 1990 (590)	0.2, 0.2, 0.1	14.1, 15.3, 14.7	Centre; 970, 1150, 990 Surface; 800, 980, 800	< 5×10 <sup>-5</sup>	2×10 <sup>-10</sup> , 2.47×10 <sup>-10</sup> , 2.0×10 <sup>-10</sup> 1×10 <sup>-8</sup> , 5×10 <sup>-9</sup> , 3.0×10 <sup>-9</sup>	[3,5,70]
HFR (Petten, Netherlands)	HFR-K6	4 spheres (dia. 60, fuel zone 47) LEU UO <sub>2</sub> TRISO	Germany	21 Jun. 1990 – 8 April 1993 (634)	3.2, <4.8, 4.8, <4.8	7.2, 9.3, 9.7, 9.2	Centre; 800 (1/3 of a cycle), 1000 (2/3 of a cycle)	-	EOL ≤ 3×10 <sup>-7</sup>	[5,70]
HFR (Petten, Netherlands)	HFR-K5	4 spheres (dia. 60, fuel zone 47) LEU UO <sub>2</sub> TRISO	Germany	8 Jan. 1991 – 16 May 1994 (564)	2.9, <4.3, 4.3, <4.3	6.7, 8.8, 9.1, 8.7	Centre; 800 (1/3 of a cycle), 1000 (2/3 of a cycle)	-	EOL ≤ 3×10 <sup>-7</sup>	[5,70]
IVV-2M (Zarechny, Russia)	Vostok-1~6 (6; long term irradi.)	4 spheres/each LEU UO <sub>2</sub> TRISO	Russia	1982-1989 (208-283)	0.4-2.2 (E>0.1 MeV)	8.8-21.5	900-1400; irradiation temp. (1600 shortly)	-	at 1000°C ≤ 1×10 <sup>-6</sup> at 1200°C 1×10 <sup>-5</sup> at 1400°C ≤ 1×10 <sup>-5</sup>	[3,5]
MR (Moscow, Russia)	PG-100 (KVG-1~5)	Spheres	Russia	56-637	0.075-2.3 (E>0.2 MeV)	1.5-18	440-1350; irradiation temp.	-	-	[3]

TABLE 18. IRRADIATIONS OF SPHERICAL PEBBLES CONDUCTED BEFORE THE EARLY 2000s (CONT)

Test reactor	Experiment ID	No. of specimen and fuel type (mm)	Country	Irradiation time (FPDs)	Fast fluence ( $10^{21}$ n/cm <sup>2</sup> , E>0.10 MeV)	Burnup (% FIMA)	Operating temp. (°C)	Defective SiC layer fraction (U/U-total)	BOL <sup>85m</sup> Kr R/B EOL <sup>85m</sup> Kr R/B	Reference
VVR-C (Obnisk, Russia)	Cashtan-1~ - 4	Spheres 0.5-1.5% LEU UO <sub>2</sub> TRISO	Russia	393-1370	0.22-0.57 (E>0.2 MeV)	6.8-41	1000-1700; irradiation temp.	-	-	[3]
RBT-6 (Dimitrovgrad, Russia)	Udar	Spheres 21-45% LEU UO <sub>2</sub> TRISO	Russia	-	0.1 (E>0.18 MeV)	1.0	300 (up to 2000 cycles) (1200 max.); irradiation temp.	-	-	[3,4]
RBT-6 (Dimitrovgrad, Russia)	BKS	Sphere prototype (10 mm dia.)	Russia	-	2.0-5.1	4.5-11	1250-1400; irradiation temp.	-	-	[5]
RBT-6 (Dimitrovgrad, Russia)	RBT	Spheres	Russia	-	1.6-2.1	10-12	1250-1400; irradiation temp.	-	-	[5]

Heating tests at 1600–1800°C were performed with spherical pebbles containing 16,400 particles. Details of some of these tests are described in Ref. [3] and are summarized in Table 19.

TABLE 19. RESULTS OF POST-IRRADIATION HEATING TESTS WITH PEBBLES

Fuel element UO <sub>2</sub> TRISO	Burnup [% FIMA]	Fast fluence [10 <sup>25</sup> /m <sup>2</sup> 	Heating test		No. of failed particles <sup>(2)</sup>		Fractional release				
			Temp. [°C]	Time [h]	Manuf.	Heating	Kr-85	Sr-90	Ag- 110m	Cs-134	Cs-137
AVR 71/22	3.5	0.9	1600	500	-	-	4.0·10 <sup>-7</sup>	5.3·10 <sup>-6</sup>	9.0·10 <sup>-4</sup>	6.9·10 <sup>-5</sup>	2.0·10 <sup>-5</sup>
HFR- K3/1	7.7	3.9	1600	500	-	-	1.8·10 <sup>-6</sup>	1.8·10 <sup>-7</sup>	2.7·10 <sup>-2</sup>	1.3·10 <sup>-4</sup>	1.1·10 <sup>-4</sup>
FRJ2- K13/2	8.0	0.1	1600	138 (160)	-	-	6.4·10 <sup>-7</sup>	3.3·10 <sup>-7</sup>	2.8·10 <sup>-3</sup>	1.0·10 <sup>-4</sup>	3.9·10 <sup>-5</sup>
AVR 82/20	8.6	2.4	1600	100	-	-	1.5·10 <sup>-7</sup>	3.8·10 <sup>-6</sup>	4.4·10 <sup>-3</sup>	1.2·10 <sup>-4</sup>	6.2·10 <sup>-5</sup>
AVR 82/9	8.9	2.5	1600	500	-	-	5.3·10 <sup>-7</sup>	8.3·10 <sup>-5</sup>	1.9·10 <sup>-2</sup>	5.9·10 <sup>-4</sup>	7.6·10 <sup>-4</sup>
AVR 89/13	9.1	2.6	1620 <sup>(1)</sup> 1620 <sup>(1)</sup>	≈ 10 ≈ 10	-	-	2.0·10 <sup>-7</sup> 1.3·10 <sup>-9</sup>	(3) (3)	8.3·10 <sup>-4</sup> 1.5·10 <sup>-2</sup>	1.3·10 <sup>-5</sup> 1.6·10 <sup>-6</sup>	1.1·10 <sup>-5</sup> 1.4·10 <sup>-6</sup>
AVR 85/18	9.2	2.6	1620 <sup>(1)</sup>	≈ 10	-	-	1.4·10 <sup>-7</sup>	(3)	6.5·10 <sup>-3</sup>	1.0·10 <sup>-5</sup>	1.3·10 <sup>-5</sup>
AVR 90/5	9.2	2.7	1620 <sup>(1)</sup> 1620 <sup>(1)</sup>	≈ 10 ≈ 10	-	-	1.9·10 <sup>-7</sup> 6.6·10 <sup>-9</sup>	(3) (3)	1.1·10 <sup>-3</sup> 9.0·10 <sup>-4</sup>	7.7·10 <sup>-6</sup> 3.5·10 <sup>-6</sup>	9.0·10 <sup>-6</sup> 3.3·10 <sup>-6</sup>
AVR 90/2	9.3	2.7	1620 <sup>(1)</sup>	≈ 10	1	2	1.0·10 <sup>-4</sup>	(3)	3.7·10 <sup>-2</sup>	5.0·10 <sup>-5</sup>	4.6·10 <sup>-5</sup>
AVR 90/20	9.8	2.9	1620 <sup>(1)</sup>	≈ 10	2	3	2.4·10 <sup>-4</sup>	(3)	7.6·10 <sup>-2</sup>	5.6·10 <sup>-6</sup>	6.5·10 <sup>-6</sup>
AVR 91/31	9.0	2.6	1700 <sup>(1)</sup>	≈ 10	2	18	1.2·10 <sup>-3</sup>	(3)	6.2·10 <sup>-1</sup>	3.7·10 <sup>-3</sup>	2.4·10 <sup>-3</sup>
AVR 74/11	6.2	1.6	1700	185	1	-	3.0·10 <sup>-5</sup>	7.2·10 <sup>-6</sup>	4.8·10 <sup>-2</sup>	8.4·10 <sup>-5</sup>	7.6·10 <sup>-5</sup>
FRJ2- K13/4	7.6	0.1	1600 1800	138 100	-	2	3.0·10 <sup>-7</sup> 7.2·10 <sup>-5</sup>	2.0·10 <sup>-8</sup> 1.4·10 <sup>-3</sup>	4.5·10 <sup>-4</sup> 5.3·10 <sup>-1</sup>	5.7·10 <sup>-6</sup> 9.7·10 <sup>-3</sup>	2.5·10 <sup>-6</sup> 9.9·10 <sup>-3</sup>
AVR 88/33	8.5	2.3	1600 1800	50 20	-	-	1.0·10 <sup>-7</sup> 1.8·10 <sup>-4</sup>	8.4·10 <sup>-6</sup> 2.3·10 <sup>-4</sup>	1.2·10 <sup>-3</sup> 2.1·10 <sup>-1</sup>	1.1·10 <sup>-4</sup> 4.4·10 <sup>-4</sup>	1.2·10 <sup>-4</sup> 4.6·10 <sup>-4</sup>
AVR 88/15	8.7	2.4	1600 1800	50 20	-	≈ 4	6.3·10 <sup>-8</sup> 2.9·10 <sup>-4</sup>	(3) 1.1·10 <sup>-2</sup>	9.1·10 <sup>-3</sup> 8.1·10 <sup>-1</sup>	8.8·10 <sup>-6</sup> 1.3·10 <sup>-2</sup>	1.2·10 <sup>-5</sup> 1.4·10 <sup>-2</sup>
AVR 76/18	7.1	1.9	1800	200	-	≈ 3	1.2·10 <sup>-4</sup>	6.6·10 <sup>-2</sup>	6.2·10 <sup>-1</sup>	5.3·10 <sup>-2</sup>	4.5·10 <sup>-2</sup>
AVR 88/41	7.6	2.0	1800	24	-	-	2.4·10 <sup>-7</sup>	1.2·10 <sup>-4</sup>	7.7·10 <sup>-2</sup>	1.4·10 <sup>-4</sup>	1.5·10 <sup>-4</sup>
HFR- K3/3	10.2	6.0	1800	100	-	≈ 12	6.5·10 <sup>-4</sup>	1.5·10 <sup>-3</sup>	6.7·10 <sup>-1</sup>	6.4·10 <sup>-2</sup>	5.9·10 <sup>-2</sup>

(1) Simulation calculated core heat up curve.  
(2) Out of 16,400 particles.  
(3) Not measured.

## 6.1.2. Cylindrical compacts

### 6.1.2.1. Irradiation tests

Table 20 shows irradiation tests performed with cylindrical compacts up to the early 2000s. These irradiations were collected from various references such as Refs. [3, 71-82]. The information includes fuel types, irradiation time in FPDs, fast fluence, burnup, operating temperature, and the fraction releases (i.e., the ratio of release (R) to birth (B) of <sup>85m</sup>Kr). The irradiation results showed the good performance

of cylindrical compacts under normal operating conditions with a peak burnup to about 27% FIMA and to high operating temperature, e.g. 1000°C.

#### 6.1.2.2. Heating tests

Heating tests at 1600–1800°C were performed with cylindrical compacts containing 1600 particles. Details of these tests are described in Refs. [3,70] and are summarized in Table 21.

Two experiments, HRB-17 and HRB-18 were also conducted with Highly Enriched Uranium (HEU) TRISO UCO unbonded, irradiated particles at the ORNL [83]. Eighty particles each were heated at 1400 and 1600°C for 300 and 100 h, respectively. Four experiments with HRB-22 fuel were also reported [3,70,80].

Post-irradiation heating tests at temperatures up to 1500°C for long durations were performed to accelerate the diffusional release of fission gas atoms from various fuel types including UO<sub>2</sub>, UC<sub>2</sub>, UCO, UO<sub>2</sub>\*(1), and UO<sub>2</sub>\*(2) fuel particles irradiated at the HRB-15B capsule installed in the High Flux Isotope Reactor (HFIR) [70,84]. Note that in the UO<sub>2</sub>\*(1) fuel the kernel was enveloped by a ZrC layer, which replaced the graphite buffer. In contrast, the UO<sub>2</sub>\*(2) fuel featured a buffer layer surrounding the kernel that included dispersed ZrC.

The distribution of fission product releases among particles within the fuel batches indicated that the release of caesium from the UO<sub>2</sub> fuel particles was from two of the ten UO<sub>2</sub> particles and from only one of the ten UC<sub>2</sub> particle [70] (see Table 22).

#### 6.1.3. Loose TRISO particle fuels

Irradiation tests of loose coated particle fuels were also carried out in various material test reactors to support the design of coated particle fuels. The historical irradiation testing, conducted in variety of material test reactors in Germany, USA, Japan, and Russia, of loose coated particle fuels is summarized in Table 23 which contains information on fuel types, irradiation time (in FPDs), fast fluence, burnup, irradiation temperature, and <sup>85m</sup>Kr R/B.

### 6.2. PROGRESS ON TESTS SINCE THE EARLY 2000S

Since the early 2000s, VHTR, one of the advanced reactor systems, has been paid attention, and irradiation tests have been conducted to qualify TRISO coated particle fuels under such conditions. In this section, progress of such irradiation tests since the early 2000s is described.

#### 6.2.1. Spherical pebbles

Table 24 shows irradiations of spherical pebbles performed since the early 2000s.

##### 6.2.1.1. HFR-EU1bis irradiation experiment

The irradiation experiment HFR-EU1bis [5,69,86] was intended to demonstrate a low failure fraction of coated particles under normal operating condition, with specific objectives of (1) successfully operating at increased central temperature of 1250°C (in comparison with 1000–1200°C in earlier irradiation tests), (2) successfully operating at burnups nearing 16%<sup>8</sup>, and (3) affirming low failure fraction at demanding conditions such as increased temperature, burnup and neutron fluence conditions.

---

<sup>8</sup> The target value was double the license limit of the HTR-Module. Due to a neutronics data processing error, the experiment could not continue beyond 11.07% FIMA.

TABLE 20. IRRADIATIONS OF COMPACTS CONDUCTED BEFORE THE EARLY 2000s

Reactor	Experiment ID	No. of specimen and fuel type (mm)	Country	Irradiation time (FPDs)	Fast fluence ( $10^{21}$ n/cm <sup>2</sup> , E>0.18 MeV)	Burnup (%FIMA)	Operating temp. (°C)	Defective SiC layer fraction (U/U-total)	BOL <sup>85m</sup> Kr R/B EOL <sup>85m</sup> Kr R/B	Reference
GETR (GE(Pleasanton), USA)	F-30	13 compacts (dia. 12.45, length 18.54 & 49.28); Cell 1,3,4,5 HEU (Th,U)C <sub>2</sub> TRISO and ThC <sub>2</sub> TRISO	USA	15 May 1972 – 5 Apr 1994 (269)	8, 11.5, 9.5, 12	15, 20, 18, 12 (fissile) 3, 5, 4, 1.5 (fertile)	1100, 1120, 1100, 1200 (time ave. peak temp. (TAPT))	< 5×10 <sup>-4</sup> – 1.5×10 <sup>-3</sup> (fissile particles) 3×10 <sup>-4</sup> – 1.0×10 <sup>-3</sup> (fertile particles)	2×10 <sup>-6</sup> , 8×10 <sup>-7</sup> , 7×10 <sup>-7</sup> , 2×10 <sup>-6</sup> 8×10 <sup>-6</sup> , 1×10 <sup>-5</sup> , 2×10 <sup>-5</sup> , 2×10 <sup>-5</sup>	[70]
HFIR (ORNL, USA)	HRB-4	6 compacts (dia. 12.4, length 25.4) LEU WAR UC <sub>2</sub> TRISO and ThO <sub>2</sub> BISO	USA	8 Oct. 1972 – 26 Jun. 1972 (244)	10.5 (peak)	27.7 (peak fissile) 13.4 (peak fertile)	1250 (peak)	-	1.4×10 <sup>-5</sup> 3.2×10 <sup>-4</sup>	[70]
HFIR (ORNL, USA)	HRB-5	6 compacts (dia. 12.4, length 25.4) LEU WAR UC <sub>2</sub> TRISO and ThO <sub>2</sub> BISO	USA	8 Oct. 1972 – 3 Feb. 1973 (107)	4.7 (peak)	15.7 (peak fissile) 4.3 (peak fertile)	1250 (peak)	-	3×10 <sup>-6</sup> 1×10 <sup>-4</sup>	[70]
HFIR (ORNL, USA)	HRB-6	6 compacts (dia. 12.4, length 25.4) HEU (Th,U)C <sub>2</sub> TRISO and ThO <sub>2</sub> BISO	USA	27 Feb. 1973 – 8 Sep. 1973 (183)	7.9 (peak)	26.6 (peak fissile) 9.3 (peak fertile)	1100 (peak)	< 5×10 <sup>-4</sup>	5.0×10 <sup>-7</sup> (min.) 2.7×10 <sup>-4</sup> (max.)	[70]

TABLE 20. IRRADIATIONS OF COMPACTS CONDCUTED BEFORE THE EARLY 2000s (CONT)

Reactor	Experiment ID	No. of specimen and fuel type (mm)	Country	Irradiation time (FPDs)	Fast fluence ( $10^{21}\text{n/cm}^2$ , $E>0.18\text{ MeV}$ )	Burnup (%FIMA)	Operating temp. ( $^{\circ}\text{C}$ )	Defective SiC layer fraction (U/U-total)	BOL $^{85\text{m}}\text{Kr}$ R/B EOL $^{85\text{m}}\text{Kr}$ R/B	Reference
ORR (ORNL, USA)	OF-2	16 compacts (dia. 15.75, height 25.4) 48 compacts (dia. 15.75 OD, 3.30 ID, height 12.70) 24 compacts (dia. 15.75, height 50.8) WAR UCO UC <sub>2</sub> (Th,U)O <sub>2</sub> TRISO and ThO <sub>2</sub> BISO	USA	21 Jun. 1975 – 1 Aug. 1976 (352)	5.86-8.91 1.94-8.36	75.9-79.6 50.0-795.	1350 (max.)	-	$2\times 10^{-5}$ , $1\times 10^{-4}$ $1\times 10^{-4}$ , $5\times 10^{-6}$	[70]
HFIR (ORNL, USA)	HRB-14	20 compacts (dia. 12.5, height 9.52) LEU UCO UO <sub>2</sub> (Th,U)O <sub>2</sub> TRISO and ThO <sub>2</sub> BISO	USA	20 May 1978 – 4 Jan. 1979 (214)	8.3 (peak)	28.6 (peak fissile) 8.5 (peak fertile)	1190 (max.), 895 (min.)	$7.0\times 10^{-7}$ – $1.3\times 10^{-4}$ (fertile particles)	$3.8\times 10^{-7}$ (min.) $3.0\times 10^{-4}$ (max.)	[3],[70]
R2 (Studvik, Sweden)	R2-K13	12 compacts (dia. 12.52, height 25.4) LEU UCO TRISO and ThO <sub>2</sub> TRISO	USA (2 spheres, Germany)	22 Apr. 1980 – 19 Sep. 1982 (517)	7.8, 7.4 (peak)	22.5, 22.1 (peak fissile) 7.8, 7.4 (peak fertile)	1190, 985 (ave.)	$1.9\times 10^{-4}$ – $4.4\times 10^{-4}$ (fissile particles) $< 2\times 10^{-6}$ – $1.6\times 10^{-5}$ (fertile particles)	$1\times 10^{-5}$ , $2\times 10^{-7}$ $8\times 10^{-5}$ , $8\times 10^{-6}$	[3],[70]
HFIR (ORNL, USA)	HRB-15A	20 compacts (dia. 12.52, 3 compacts; height 9.53, 17 compacts; 19.05) LEU UCO UC <sub>2</sub> UO <sub>2</sub> TRISO and ZrC-TRISO and ThO <sub>2</sub> TRISO and Si-BISO	USA	26 Jul. 1980 – 29 Jan. 1981 (174)	6.5 (peak)	29.0 (peak fissile) 6.4 (peak fertile)	1150 (ave.)	$1.4\times 10^{-5}$ – $7.4\times 10^{-2}$ (fissile particles) $6.7\times 10^{-5}$ – $1.4\times 10^{-3}$ (fertile particles)	$6.96\times 10^{-6}$ $3.76\times 10^{-4}$	[3],[70]
	HRB-15B	LEU UCO UC <sub>2</sub> UO <sub>2</sub> TRISO			6.6	27	815–1000			[3]

TABLE 20. IRRADIATIONS OF COMPACTS CONDUCUTED BEFORE THE EARLY 2000s (CONT)

Reactor	Experiment ID	No. of specimen and fuel type (mm)	Country	Irradiation time (FPDs)	Fast fluence ( $10^{21}$ n/cm <sup>2</sup> , E>0.18 MeV)	Burnup (%FIMA)	Operating temp. (°C)	Defective SiC layer fraction (U/U-total)	BOL <sup>85m</sup> Kr R/B EOL <sup>85m</sup> Kr R/B	Reference
HFIR (ORNL, USA)	HRB-16	18 compacts (dia. 12.54, height 18.70) LEU UCO UC <sub>2</sub> UO <sub>2</sub> (Th,U)O <sub>2</sub> TRISO and ZrC-TRISO and ThC <sub>2</sub> ThO <sub>2</sub> TRISO and BISO	USA	21 Jun. 1981 – 23 Dec. 1981 (170)	6.3 (peak)	28.7 (peak fissile) 6.1 (peak fertile)	1150 (ave.)	4.6×10 <sup>-7</sup> – 4.4×10 <sup>-4</sup> (fissile particles) 1.6×10 <sup>-5</sup> , 5.0×10 <sup>-4</sup> (fertile particles)	2.44×10 <sup>-5</sup> 2.08×10 <sup>-4</sup>	[3],[70]
	HRB-17, -18	18 compacts (dia. 12.54, height 18.70) LEU UCO UC <sub>2</sub> TRISO				4.3-4.6	25	700–1000		
DIDO (Jülich, German)	FRJ2-P27	9 compacts (dia. 27.9–28.03, height 29) LEU UO <sub>2</sub> TRISO	Germany	17 Feb. 1984 – 10 Feb. 1985 (232)	1.4, 1.7, 1.3 1.5–2 (E>0.10 MeV)	7.6, 8.0, 7.6	Centre; 1080, 1320, 1130 Surface; 880, 1220, 1080	< 3×10 <sup>-6</sup>	1.0×10 <sup>-6</sup> , 8.6×10 <sup>-7</sup> , 2.0×10 <sup>-8</sup>	[3],[70]
	FRJ2-P28				1.5–2	11–13	950–1150			1.6×10 <sup>-6</sup> , 1.0×10 <sup>-5</sup> , 1.2×10 <sup>-7</sup>
HFR (Petten, Netherlands)	HFR-B1	36 fuel rods LEU UCO and ThO <sub>2</sub> TRISO	Germany USA	Apr. 1987 – Jul. 1989 (445)	6.5 (E>0.10 MeV)	19	1470	-	EOL 4.1×10 <sup>-3</sup> (10% failed particles)	[3],[71]
HFIR (ORNL, USA)	HRB-21	24 compacts (dia. 12.27–12.51, height 49.13–49.35) LEU UCO and ThO <sub>2</sub> TRISO-P	USA	20 Jun. 1991 – 21 Nov. 1991 (105)	3.5 (peak)	22 (peak)	950 (ave.), 1300 (peak)	≤5.4×10 <sup>-6</sup> (fissile particles) 1.7×10 <sup>-5</sup> (fertile particles)	1×10 <sup>-8</sup> 2×10 <sup>-4</sup>	[70]
HFIR (ORNL, USA)	NPR-1	16 compacts (dia. 12.43, height 49.42)	USA	25 Jul. 1991 – 29 May 1992 (170)	3.75 (peak)	79 (peak)	974 (ave.), 1240 (peak)	3×10 <sup>-6</sup>	1×10 <sup>-8</sup> 3×10 <sup>-4</sup>	[5],[70],[72]

TABLE 20. IRRADIATIONS OF COMPACTS CONDUCUTED BEFORE THE EARLY 2000s (CONT)

Reactor	Experiment ID	No. of specimen and fuel type (mm)	Country	Irradiation time (FPDs)	Fast fluence ( $10^{21}\text{n/cm}^2$ , $E>0.18\text{ MeV}$ )	Burnup (%FIMA)	Operating temp. ( $^{\circ}\text{C}$ )	Defective SiC layer fraction (U/U-total)	BOL $^{85\text{m}}\text{Kr R/B}$ EOL $^{85\text{m}}\text{Kr R/B}$	Reference
		HEU UCO TRISO-P								
HFIR (ORNL, USA)	NPR-2	16 compacts (dia. 12.43, height 49.42) HEU UCO TRISO-P	USA	28 Aug. 1991 – 29 May 1991 (172)	3.75 (peak)	79 (peak)	753 (ave.), 1030 (peak)	$3\times 10^{-6}$	$5\times 10^{-9}$ $6\times 10^{-5}$	[5],[70],[72]
ATR (INL, USA)	NPR-1A	20 compacts (dia. 12.37-12.50, height 49.33) HEU UCO TRISO-P	USA	2 Oct. 1991 – 3 Jan. 1992 (64)	2.1 (peak)	64 (peak)	977 (ave.), 1220 (peak)	$3\times 10^{-6}$	$4\times 10^{-9}$ $1.8\times 10^{-5}$	[5],[70],[72]
JMTR (Oarai, Japan)	OGL-1 1 <sup>st</sup> (TRISO)	54 compacts (OD 24, ID 8, height 40) LEU $\text{UO}_2$ TRISO	Japan	JMTR cycle 39–40 Feb. 1977 – May 1977 (39)	0.12 (max.) ( $E>0.1\text{ MeV}$ )	0.08 (min.) 0.62 (max.)	1380 (time ave. max. temp.) (calculated by STPDSP-2) (max.-min. 1356–897)	-	ave. $3.7\times 10^{-7}$	[5],[73–76]
JMTR (Oarai, Japan)	OGL-1 2 <sup>nd</sup> (TRISO)	60 compacts (OD 24, ID 8, height 36) LEU $\text{UO}_2$ TRISO	Japan	JMTR cycle 42–45 Dec. 1977 – Feb 1979 (71.6)	0.20 (max.) ( $E>0.1\text{ MeV}$ )	0.12 (min.) 1.0 (max.)	1430 (time ave. max. temp.) (calculated by STPDSP-2) (max.-min. 1425–935)	-	ave. $7.3\times 10^{-7}$	[5],[73–76]
JMTR (Oarai, Japan)	OGL-1 3 <sup>rd</sup> (TRISO)	20 compacts (OD 36, ID 18, height 36) LEU $\text{UO}_2$ TRISO	Japan	JMTR cycle 46–47 Mar. 1979 – Jul. 1979 (40.7)	0.09 (max.) ( $E>0.1\text{ MeV}$ )	0.08 (min.) 0.45 (max.)	1320 (time ave. max. temp.) (calculated by STPDSP-2) (max.-min. 1355–965)	-	ave. $3.1\times 10^{-5}$	[5],[73–76]
JMTR (Oarai, Japan)	OGL-1 4 <sup>th</sup> (TRISO)	60 compacts (OD 24, ID 8, height	Japan	JMTR cycle 48–51	0.23 (max.) ( $E>0.1\text{ MeV}$ )	0.22 (min.) 1.96(max.)	1340 (time ave. max. temp.)	-	ave. $5.9\times 10^{-7}$	[5],[73–76]

TABLE 20. IRRADIATIONS OF COMPACTS CONDUCUTED BEFORE THE EARLY 2000s (CONT)

Reactor	Experiment ID	No. of specimen and fuel type (mm)	Country	Irradiation time (FPDs)	Fast fluence ( $10^{21}$ n/cm <sup>2</sup> , E>0.1 MeV)	Burnup (%FIMA)	Operating temp. (°C)	Defective SiC layer fraction (U/U-total)	BOL <sup>85m</sup> Kr R/B EOL <sup>85m</sup> Kr R/B	Reference
		36) LEU UO <sub>2</sub> TRISO		Nov. 1979 – Jun. 1980 (78.0)			(calculated by STPDSP-2) (max.-min. 1470–873)			
JMTR (Oarai, Japan)	OGL-1 5 <sup>th</sup> (TRISO)	60 compacts LEU UO <sub>2</sub> TRISO	Japan	JMTR cycle 52–58 Dec. 1980–Apr. 1983 (142.3)	0.38 (max.) (E>0.1 MeV)	3.3 (max.)	1350 (time ave. max. temp.) (calculated by STPDSP-2)	-	-	[5],[73],[76]
JMTR (Oarai, Japan)	OGL-1 6 <sup>th</sup> (TRISO)	20 compacts LEU UO <sub>2</sub> TRISO	Japan	JMTR cycle 59 (21.9)	0.04 (max.) (E>0.1 MeV)	0.4 (max.)	-/1480×280 (°C×h; transient, (calculated by STPDSP-2))	1×10 <sup>-3</sup>	- 1.5×10 <sup>-6</sup>	[3],[5],[73],[77],[78]
JMTR (Oarai, Japan)	OGL-1 7 <sup>th</sup> (TRISO)	60 compacts LEU UO <sub>2</sub> TRISO	Japan	JMTR cycle 61,61,63 (58.0)	0.16 (max.) (E>0.1 MeV)	1.4 (max.)	1380 (time ave. max. temp.) (calculated by STPDSP-2)	3.0×10 <sup>-3</sup> 5.8×10 <sup>-3</sup>	- 4.0×10 <sup>-7</sup>	[3],[5],[73],[77],[78]
JMTR (Oarai, Japan)	OGL-1 8 <sup>th</sup> (TRISO)	20 compacts LEU UO <sub>2</sub> TRISO	Japan	JMTR cycle 64–66 (53.8)	0.12 (max.) (E>0.1 MeV)	1.0 (max.)	1390 (time ave. max. temp.) (calculated by STPDSP-2)	4.6×10 <sup>-4</sup> 4.8×10 <sup>-4</sup>	- 1.1×10 <sup>-7</sup>	[3],[5],[73],[77],[78]
JMTR (Oarai, Japan)	OGL-1 9 <sup>th</sup> (TRISO)	20 compacts LEU UO <sub>2</sub> TRISO	Japan	JMTR cycle 67–73 (145.5)	0.28 (max.) (E>0.1 MeV)	2.7 (max.)	1340 (time ave. max. temp.) (calculated by STPDSP-2)	3.9×10 <sup>-3</sup>	-	[5],[73],[77],[78]
JMTR (Oarai, Japan)	OGL-1 10 <sup>th</sup> (TRISO)	20 compacts LEU UO <sub>2</sub> TRISO	Japan	JMTR cycle 74–79 May 1986 – Jun. 1987 (130.2)	0.24 (max.) (E>0.1 MeV)	2.8 (max.)	1330 (time ave. max. temp.)/ 1500×95 (°C×h; transient) (calculated by STPDSP-2)	9.5×10 <sup>-4</sup> 5.4×10 <sup>-4</sup>	- 3.2×10 <sup>-6</sup>	[3],[5],[73],[77],[78]

TABLE 20. IRRADIATIONS OF COMPACTS CONDCUTED BEFORE THE EARLY 2000s (CONT)

Reactor	Experiment ID	No. of specimen and fuel type (mm)	Country	Irradiation time (FPDs)	Fast fluence ( $10^{21}$ n/cm <sup>2</sup> , E>0.18 MeV)	Burnup (%FIMA)	Operating temp. (°C)	Defective SiC layer fraction (U/U-total)	BOL <sup>85m</sup> Kr R/B EOL <sup>85m</sup> Kr R/B	Reference
JMTR (Oarai, Japan)	OGL-1 11 <sup>th</sup> (TRISO)	54 compacts LEU UO <sub>2</sub> TRISO	Japan	JMTR cycle 80–82 Feb. 1988 – Jul. 1988 (62.3)	0.17 (max.) (E>0.1 MeV)	1.6 (max.) (calculated by STPDSP-2)	1350 (time ave. max. temp.)	$1.1 \times 10^{-3}$ $7.5 \times 10^{-4}$	-	[5],[73],[77],[78]
JMTR (Oarai, Japan)	OGL-1 12 <sup>th</sup> (TRISO)	19 compacts (OD 26, ID 10, height 39) LEU UO <sub>2</sub> TRISO	Japan	JMTR cycle 83–91 Oct. 1988 – Jun. 1990 (195.0)	0.31 (max.) (E>0.1 MeV)	3.9 (max.) (calculated by STPDSP-2)	1340 (time ave. max. temp.)	$3.6 \times 10^{-4}$ $5.4 \times 10^{-4}$	- $3.2 \times 10^{-6}$	[3],[5],[73],[77],[78]
JMTR (Oarai, Japan)	OGL-1 13 <sup>th</sup> (TRISO)	19 compacts (OD 26, ID 10, height 39) LEU UO <sub>2</sub> TRISO	Japan	JMTR cycle 92–102 (243.0)	0.49 (max.) (E>0.1 MeV)	3.7 (max.)	1340 (time ave. max. temp.)/ 1500×30.5 (°C×h; transient)	$3.9 \times 10^{-6}$	- $6.8 \times 10^{-8}$	[3],[5],[73]
JMTR (Oarai, Japan)	OGL-1 14 <sup>th</sup> (TRISO)	19 compacts (OD 26, ID 10, height 39) LEU UO <sub>2</sub> TRISO	Japan	JMTR cycle 103–106 (73.0)	0.07-0.12 0.14 (max.) (E>0.1 MeV)	0.73-1.17 1.2 (max.)	1160, 1339 (max.) 1122, 1305 (ave.) 1350 (time ave. max. temp.)/1500×47 (°C×h; transient)	$6.1 \times 10^{-5}$	BOL ave. $4.1 \times 10^{-5}$ EOL ave. $1.0 \times 10^{-4}$	[3],[5],[70],[73]
JMTR (Oarai, Japan)	OGL-1 15 <sup>th</sup> (TRISO)	19 compacts (OD 26, ID 10, height 39) LEU UO <sub>2</sub> TRISO	Japan	JMTR cycle 107–115 (217.8)	0.44 (max.) (E>0.1 MeV)	3.1 (max.)	1345 (time ave. max. temp.)	$5.1 \times 10^{-6}$	- $3.8 \times 10^{-7}$	[3],[5],[73]
JMTR (Oarai, Japan)	79F-1A	5 compacts (smaller than those for HTTR)	Japan		0.027 (E>0.1 MeV)	0.5	normal 1197 transient 1510			[79]
JMTR (Oarai, Japan)	80F-5A	5 compacts (smaller than those for HTTR)	Japan		0.097 (E>0.1 MeV)	1.0	normal 1236 transient 1520			[79]

TABLE 20. IRRADIATIONS OF COMPACTS CONDUCUTED BEFORE THE EARLY 2000s (CONT)

Reactor	Experiment ID	No. of specimen and fuel type (mm)	Country	Irradiation time (FPDs)	Fast fluence ( $10^{21}$ n/cm <sup>2</sup> , E>0.1 MeV)	Burnup (%FIMA)	Operating temp. (°C)	Defective SiC layer fraction (U/U-total)	BOL <sup>85m</sup> Kr R/B EOL <sup>85m</sup> Kr R/B	Reference
JMTR (Oarai, Japan)	83F-2A	5 compacts (smaller than those for HTTR)	Japan		0.012 (E>0.1 MeV)	1.2	normal 1373 transient 2000			[79]
JMTR (Oarai, Japan)	91F-1A	2 compacts (OD 26, ID 10, height 39) LEU UO <sub>2</sub> TRISO	Japan	(~360)	6.0, 4.6 (E>0.1 MeV)	9.6, 7.9	1120, 1340			[70]
JMTR (Oarai, Japan)	94F-9A (TRISO)	2 compacts (OD 26, ID 10, height 39) LEU UO <sub>2</sub> TRISO	Japan	(~360)	3.1, 2.3 (E>0.1 MeV)	7.0, 5.5	1120, 1190 (max.)	-	-	[5],[70]
HFIR (ORNL, USA)	HRB-22	12 compacts (OD 26.03-26.07, ID 10.00-10.02, height 38.95-39.09) HEU UO <sub>2</sub> TRISO	Japan	10 Apr. 1994 – 22 Aug. 1994 (88)	1.3–2.8 (E>0.1 MeV)	4.1-6.7	821–1071 (ave.), 898–1156 (max.)	-	$1.0 \times 10^{-6}$ $3.0 \times 10^{-6}$	[5],[70],[74],[80],[81]
JMTR (Oarai, Japan)	78F-4A (ZrC layer)	Compacts (OD 18, ID 8, height 18) LEU UO <sub>2</sub> TRISO	Japan	81.2	2.2 (E>0.1 MeV)	4.0	1100	-	-	[82]
JMTR (Oarai, Japan)	80F-4A (ZrC layer)	Compact (OD 18, ID 8, height 18) LEU UO <sub>2</sub> TRISO	Japan	79.9	1.2 (E>0.1 MeV)	1.5	900	-	<sup>88</sup> Kr R/B at ~900°C $2 \times 10^{-7} - 4 \times 10^{-7}$	[82]
JMTR (Oarai, Japan)	88-3A (ZrC layer)	Compact (OD 24, ID 8, height 36) LEU UO <sub>2</sub> TRISO	Japan	99.9	0.9 (E>0.1 MeV)	4.5	1400–1650	-	-	[82]
JRR-2 (Oarai, Japan)	ICF-26H (ZrC layer)	Compact (OD 18, ID 8, height 18) LEU UO <sub>2</sub> TRISO	Japan	134.7	1.0 (E>0.1 MeV)	1.8	1400–1500			[74],[82]

TABLE 20. IRRADIATIONS OF COMPACTS CONDCUTED BEFORE THE EARLY 2000s (CONT)

Reactor	Experiment ID	No. of specimen and fuel type (mm)	Country	Irradiation time (FPDs)	Fast fluence ( $10^{21}$ n/cm <sup>2</sup> , E>0.18 MeV)	Burnup (%FIMA)	Operating temp. (°C)	Defective SiC layer fraction (U/U-total)	BOL <sup>85m</sup> Kr R/B EOL <sup>85m</sup> Kr R/B	Reference
IVV-2M (Zarechny, Russia)	MT-2	6–8 pellets	Russia	1982–1989 (63, 167, 333)	0.21–2.7 (E>0.1 MeV)	1.4–14	1100–1950; irradiation temp.	-	-	[3],[5]
IVV-2M (Zarechny, Russia)	MTI	6–8 pellets	Russia	1982–1989 (~221)	0.6–2.0 (E>0.1 MeV)	4–12	1400; irradiation temp.	-	-	[3],[5]
IVV-2M (Zarechny, Russia)	MT-3	6–8 compacts	Russia	1982–1989 (129)	1.5–2.3 (E>0.1 MeV)	11–17	750–1400; irradiation temp.	-	-	[3],[5]
MR (Moscow, Russia)	ASU-8	1 compact	Russia	-	0.7–2.7 (E>0.1 MeV)	5–15.3	1000–1300; irradiation temp.	-	-	[5]
SM-2 (Dimitrovgrad, Russia)	Carat-2~6	Pellets 0.7–45% LEU UO <sub>2</sub> TRISO	Russia	-	0.75–2.2 (E>0.1 MeV)	3–24	800–1700; irradiation temp.	-	-	[3],[5]

TABLE 21. RESULTS OF POST-IRRADIATION HEATING TESTS WITH FUEL COMPACTS AT 1600-1800°C

Fuel compact	Irradiation conditions			Heating test		Fractional release			
	Burnup (% FIMA)	Fast fluence ( $10^{25} \text{ n m}^{-2}$ )	Temperature (°C)	Temperature (°C)	Duration (h)	$^{85}\text{Kr}$	$^{90}\text{Sr}$	$^{134}\text{Cs}$	$^{137}\text{Cs}$
SL-P1/6	10.7	6.7	790–800	1600	304	$7.3 \times 10^{-7}$	$4.3 \times 10^{-5}$	$7.5 \times 10^{-4}$	$3.9 \times 10^{-4}$
HFR-P4/1/12	11.1	5.5	900–940	1600	304	$5.4 \times 10^{-7}$	$6.0 \times 10^{-6}$	$3.0 \times 10^{-4}$	$2.6 \times 10^{-4}$
HFR-P4/1/8	13.8	7.2	900–940	1600	304	$5.4 \times 10^{-5}$	$1.5 \times 10^{-4}$	$1.5 \times 10^{-3}$	$2.0 \times 10^{-3}$
HFR-P4/2/8/	13.8	7.2	900–945	1600	304	$8.1 \times 10^{-5}$	$1.1 \times 10^{-4}$	$1.5 \times 10^{-3}$	$1.4 \times 10^{-3}$
HFR-P4/3/7	13.9	7.5	1050–1075	1600	304	$9.9 \times 10^{-4}$	$2.4 \times 10^{-4}$	$3.5 \times 10^{-3}$	$3.9 \times 10^{-3}$
SL-P1/10	10.3	6.0	790–800	1700	304	$9.1 \times 10^{-5}$	$2.1 \times 10^{-2}$	$9.3 \times 10^{-2}$	$1.0 \times 10^{-1}$
SL-P1/9	10.7	6.3	790–800	1700	304	$3.7 \times 10^{-5}$	$5.8 \times 10^{-2}$	$1.3 \times 10^{-1}$	$9.8 \times 10^{-2}$
HFR-P4/3/12	9.9/12.0	5.5	1050–1075	1800	279	$1.0 \times 10^{-3}$	Not measured	$5.2 \times 10^{-1}$	$5.2 \times 10^{-1}$

TABLE 22. DISTRIBUTION OF FISSION PRODUCT RELEASE WITHIN PARTICLE BATCHES DURING POST IRRADIATION ANNEALING

Annealing temperature (°C)	TRISO particle type <sup>a</sup>	Release breakdown from the ten particles within a test batch for:			
		$^{134}\text{Cs}$ $^{137}\text{Cs}$	$^{110\text{m}}\text{Ag}$	$^{154}\text{Eu}$	$^{144}\text{Ce}$
1500	UC <sub>2</sub> with laminar SiC	9 : 0% 1 : 99% 10 : 12%	1 : 0% 1 : 50% 85%<2<95% 6 : 100% 10 : 82%	15%<5<25% 45%<3<55% 2 : 100% 10 : 46%	12%<3<18% 18%<3<25% 70%<3<80% 1 : 99% 10 : 45%
1500	UO <sub>2</sub> with columnar SiC	8 : 0% 2 : 99% 10 : 24%	10 : 100%	Uniform release of 16%	10 : 0%
1500	UC <sub>0.4</sub> O <sub>1.6</sub> with laminar SiC	10 : 0%	7 : 0% 10%<3<20% 10 : 3%	Uniform release of 37%	10 : 1% <sup>b</sup>
1500	UC <sub>2</sub> <sup>*</sup> (2) with laminar SiC	10 : 0%	7 : 0% 70%<3<80% 10 : 27%	2 : 0% 0%<5<10% 15%<3<25%	10 : 0%
1350	UC <sub>0.4</sub> O <sub>1.6</sub> with laminar SiC	10 : 0%	10 : 0%	Uniform release of 23%	10 : 0%
1350	UC <sub>2</sub> <sup>*</sup> (2) with laminar SiC	10 : 0%	7 : 0% 45%<3<55% 10 : 19%	10 : 4% <sup>b</sup>	10 : 0%
1200	UC <sub>0.4</sub> O <sub>1.6</sub> with laminar SiC	10 : 0%	10 : 0%	Uniform release of 6%	10 : 0%
1200	UC <sub>2</sub> <sup>*</sup> (2) with laminar SiC	10 : 0%	10 : 2% <sup>b</sup>	10 : 0%	10 : 0%

According to Ref. [70].

<sup>a</sup> “There was zero release within about ±5% as determined from individual particle counting before and after annealing for all isotopes from each of the ten particles in all test combinations not listed, that is, UC<sub>2</sub><sup>\*</sup>(1) at all temperatures, and UC<sub>2</sub>, UO<sub>2</sub>, and UC<sub>0.4</sub>O<sub>1.6</sub> at 1350 and 1200°C. As no release on collectors was detected at the 0.01% level from the combined ten particles within each of these test batches, it can be assumed that release from any one of these particles was certainly <0.01% and was probably not more than 0.001%.

<sup>b</sup> These total releases from ten particles were too small and too uniformly distributed among particles to allow the determinations of individual release values.”

TABLE 23. IRRADIATIONS OF LOOSE COATED PARTICLE FUELS BEFORE THE EARLY 2000s

Reactor	Experiment ID	No. of specimen and fuel type (mm)	Country	Irradiation time (FPD)	Fast fluence ( $10^{21}n\cdot cm^{-2}$ , $E>0.18$ MeV)	Burnup (%FIMA)	Operating temp. ( $^{\circ}C$ )	Defective SiC layer fraction (U/U-total)	BOL $^{85m}Kr$ R/B EOL $^{85m}Kr$ R/B	Ref.
HFR (Petten, Netherlands)	HFR-P5	116 coupons LEU UO <sub>2</sub> TRISO	Germany	(142)	5.5 ( $E>0.10$ MeV)	7.2	Centre; 1730	-	EOL $1.1\times 10^{-4}$ (amoeba effect)	[70],[71]
GETR (GE(Pleasanton), USA)	F-30	Loose particles; Cell 2 & 5 HEU (Th,U)C <sub>2</sub> TRISO and ThC <sub>2</sub> TRISO	USA	15 May 1972 – 5 Apr 1994 (269)	10.5, 12	19, 12 (fissile) 4.5, 1.5 (fertile)	1100, 1200 (time ave. peak temp.; TAPT)	$< 5\times 10^{-4}$ – $1.5\times 10^{-3}$ (fissile particles) $3\times 10^{-4}$ – $1.0\times 10^{-3}$ (fertile particles)	$7\times 10^{-7}$ , $2\times 10^{-6}$ $1\times 10^{-4}$ , $2\times 10^{-5}$	[70]
HFIR (ORNL, USA)	HRB-15B	184 particle trays (OD 22.3-23.6, ID 11.1) 116 loose particles/tray LEU UCO UC <sub>2</sub> UO <sub>2</sub> TRISO	USA	6 Jul. 1978 – 4 Jan. 1979 (169)	6.6 ( $E>0.10$ MeV)	26.7 (peak fissile) 6.0 (peak fertile)	Centre; 815–915 (time ave. temp.)	-	$2.9\times 10^{-8}$ $5.1\times 10^{-6}$	[70]
DIDO (Jülich, Germany)	FRJ2-P27	2 coupons (dia. 29, height 2.2, fuel annulus dia. 23, 34 particles/coupon) LEU UO <sub>2</sub> TRISO	Germany	17 Feb. 1984 – 10 Feb. 1985 (232)	1.4, 1.7, 1.3 ( $E>0.10$ MeV)	7.6, 8.0, 7.6	Centre; 1080, 1320, 1130 Surface; 880, 1220, 1080	$< 3\times 10^{-6}$	$1.0\times 10^{-6}$ , $8.6\times 10^{-7}$ , $2.0\times 10^{-8}$ $1.6\times 10^{-6}$ , $1.0\times 10^{-5}$ , $1.2\times 10^{-7}$	[5],[70]
HFIR (ORNL, USA)	HRB-16 HRB-17, -18	27 loose particle trays (110 particles/tray, 2 particles/holes) LEU UCO UC <sub>2</sub> UO <sub>2</sub> (Th,U)O <sub>2</sub> TRISO and ZrC-TRISO and ThC <sub>2</sub> ThO <sub>2</sub> TRISO and BISO	USA	21 Jun. 1981 – 23 Dec. 1981 (170)	6.3 (peak)	28.7 (peak fissile) 6.1 (peak fertile)	1150 (peak)	$4.6\times 10^{-7}$ – $4.4\times 10^{-4}$ (fissile particles) $1.6\times 10^{-5}$ , $5.0\times 10^{-4}$ (fertile particles)	$2.44\times 10^{-5}$ $2.08\times 10^{-4}$	[3],[70]

TABLE 23. IRRADIATIONS OF LOOSE COATED PARTICLE FUELS BEFORE THE EARLY 2000s (CONT)

Reactor	Experiment ID	No. of specimen and fuel type (mm)	Country	Irradiation time (FPD)	Fast fluence ( $10^{21}n \cdot cm^{-2}$ , $E > 0.18$ MeV)	Burnup (%FIMA)	Operating temp. (°C)	Defective SiC layer fraction (U/U-total)	BOL $^{85m}Kr$ R/B EOL $^{85m}Kr$ R/B	Ref.
HFIR (ORNL, USA)	HRB-21	24 encapsulates piggyback specimens (absorptivity specimens or loose fuel particles) LEU UCO and ThO <sub>2</sub> TRISO-P	USA	20 Jun. 1991 – 21 Nov. 1991 (105)	3.5 (peak)	22 (peak)	950 (ave.), 1300 (peak)	$\leq 5.4 \times 10^{-6}$ (fissile particles) $1.7 \times 10^{-5}$ (fertile particles)	$1 \times 10^{-8}$ $2 \times 10^{-4}$	[70]
HFIR (ORNL, USA)	NPR-1	12 encapsulates piggyback specimens (loose fuel particles) HEU UCO TRISO-P	USA	25 Jul. 1991 – 29 May 1992 (170)	3.75 (peak)	79 (peak)	974 (ave.), 1240 (peak)	$3 \times 10^{-6}$	$1 \times 10^{-8}$ $5 \times 10^{-9}$	[70],[72]
HFIR (ORNL, USA)	NPR-2	16 encapsulates piggyback specimens (loose fuel particles) HEU UCO TRISO-P	USA	28 Aug. 1991 – 29 May 1991 (172)	3.75 (peak)	79 (peak)	753 (ave.), 1030 (peak)	$3 \times 10^{-6}$	$3 \times 10^{-4}$ $6 \times 10^{-5}$	[70],[72]
JRR-2 (Oarai, Japan)	VOF-8H (ZrC layer)	Loose particles in graphite disk	Japan	156.4	<0.1	1.6	1370 (15°C/min; temp. gradient)			[85]
JRR-2 (Oarai, Japan)	VOF-14H (ZrC layer)	Loose particles in graphite disk	Japan	138.7	<0.1	1.6	1600 (15°C/min; temp. gradient))			[85]
JRR-2 (Oarai, Japan)	ICF-51H	Loose particles in graphite disk	Japan	142.6	-	2.1–2.3	1318-1363(ave.) (1173-1471; min. –max.)			[3],[82]
MR (Moscow, Russia)	ASU-8	Loose coated particles Fuel coupons (5250–7500)	Russia	-	0.7-2.2 (E>0.1 MeV)	5–15.3	1000–1300; irradiation temp	-	-	[5]
RBT-6 (Dimitrovgrad, Russia)	BKS	Loose coated particles Fuel coupons	Russia	-	2.0-5.1 (E>0.1 MeV)	4.5–11	1250–1400; irradiation temp	-	-	[5]

TABLE 24. IRRADIATIONS OF SPHERICAL PEBBLES PERFORMED SINCE THE EARLY 2000s

Reactor	Experiment ID	No. of specimen and fuel type (mm)	Country	Irradiation time (FPDs)	Fast fluence ( $10^{21} \text{ n} \cdot \text{cm}^{-2}$ , $E > 0.18 \text{ MeV}$ )	Burnup (%FIMA)	Operating temp. ( $^{\circ}\text{C}$ )	Defective SiC layer fraction (U/U-total)	BOL $^{85\text{m}}\text{Kr}$ R/B EOL $^{85\text{m}}\text{Kr}$ R/B	Ref.
IVV-2M (Russia)	(HTR-10 fuel)	4 spheres (dia. 60.2, fuel zone dia. 50) LEU $\text{UO}_2$ TRISO	China	Jul. 2000 – Feb. 2003	1.10, 1.31, 1.30, 1.06 ( $E > 0.10 \text{ MeV}$ )	11.9, 13.1, 11.6 (10.4, 11.4, 10.9, 10.1)	1000 $\pm$ 50 (centre temp.) 1200 (max.) at 4.7% FIMA 1250 (max.) at 12% FIMA	-	EOL $10^{-6-8} \times 10^{-5}$	[5],[70],[87–89]
HFR (Petten, Netherlands)	HFR-EU1bis	5 spheres (dia. 60.2, fuel zone dia. 50, AVR) LEU $\text{UO}_2$ TRISO	Germany	9 Sep. 2004 – 18 Oct. 2005 (249.9)	3.0–4.0 (peak)	9–11 (max.)	1200 (max.), 900 (min.)	-	$1.0 \times 10^{-6}$ $4.0 \times 10^{-6}$	[5],[69],[70]
HFR (Petten, Netherlands)	HFR-EU1 (AVR & HTR-10 fuel)	3 spheres (dia. 60.2, fuel zone dia. 50, AVR) 2 spheres (dia. 60, fuel zone dia. 50, INET) LEU $\text{UO}_2$ TRISO	Germany China	29 Sep. 2006 – 24 Feb. 2008 (332.8)	3.7 (peak)	9–11 (max.)	1000 (max.), 800 (min.)	-	$1.0 \times 10^{-8}$ , $1.0 \times 10^{-8}$ $4.0 \times 10^{-8}$ , $1.4 \times 10^{-7}$	[4],[70],[88]
HFR (Petten, Netherlands)	(HTR-PM fuel)	5 spheres for HTR-PM LEU $\text{UO}_2$ TRISO	China	8 Sep. 2012 – 30 Dec. 2014 (355)	3.79–4.95	11.1–13.7 (estimated) >12.3	1050 $\pm$ 50 (centre temp.) 1023, 1040, 1020, 1017, 1067 (ave. central temp.)	-	$2.4-3.3 \times 10^{-9}$ Fig. 10 in Ref. 13	[5],[12],[90–92]

Table 25 shows specifications of the spherical pebbles irradiated for HFR-EU1bis experiment [88]. Burnup measurements on the HFR-EU1bis spheres were measured and described in Refs. [69,70], which is shown in Table 26 [88].

TABLE 25. NOMINAL CHARACTERISTIC DATA OF AVR GLE-4/2 PEBBLES

Coated particle	AVR
Particle batch	HT 384-393
Kernel composition	UO <sub>2</sub>
Kernel diameter (μm)	502
Enrichment ( <sup>235</sup> U wt.%)	16.76
Coat thicknesses (μm)	
Buffer	92
Inner PyC	40
SiC	35
Outer PyC	40
Particle diameter (μm)	916
Pebble	
Heavy metal loading (g/pebble)	6.0
<sup>235</sup> U content (g/pebble)	1.00 ± 1%
Number of coated particles per pebble	9560
Volume packing fraction (%)	6.2
Free U fraction (U/U <sub>tot</sub> )	7.8 · 10 <sup>-6</sup>
Matrix graphite grade	A3-3
Matrix density (kg/m <sup>3</sup> )	1750
Temperature at final heat treatment (°C)	1900

TABLE 26. MEASURED CS-137 ACTIVITIES, CORRECTED FOR DECAY TO END OF IRRADIATION, RESULTING BURNUP AND NEUTRON FLUENCE

Pebble	<sup>137</sup> Cs (Bq)	<sup>137</sup> Cs (Bq) at EOI	Burnup (% FIMA)	Thermal fluence (n/m <sup>2</sup> , E<0.638 eV)	Fast fluence (n/m <sup>2</sup> , E>0.1 MeV)
HFR-EU1bis/1 (top)	6.19 × 10 <sup>10</sup>	6.48 × 10 <sup>10</sup>	9.34%	1.34 × 10 <sup>25</sup>	2.41 × 10 <sup>25</sup>
HFR-EU1bis/2	N/A due to destructive PIE				
HFR-EU1bis/3	7.34 × 10 <sup>10</sup>	7.68 × 10 <sup>10</sup>	11.07%	1.59 × 10 <sup>25</sup>	2.86 × 10 <sup>25</sup>
HFR-EU1bis/4	7.34 × 10 <sup>10</sup>	7.69 × 10 <sup>10</sup>	11.07%	1.59 × 10 <sup>25</sup>	2.86 × 10 <sup>25</sup>
HFR-EU1bis/5 (bottom)	6.43 × 10 <sup>10</sup>	6.73 × 10 <sup>10</sup>	9.70%	1.40 × 10 <sup>25</sup>	2.51 × 10 <sup>25</sup>

Some observations of interest from post-irradiation examinations are noted below:

- Gamma scanning of the pebbles showed inhomogeneities in the distribution of coated particles within the pebbles.
- Visual inspection of the pebbles confirmed the absence of corrosion phenomena through their shiny surface.
- High porosity and a significant number of metallic inclusions were generated due to irradiation in the kernel [93,94]. These porosities in the UO<sub>2</sub> kernel were more biased at the colder side of the particle from outer region of the pebble. Other particles showed no such bias and evenly distributed pores and metallic inclusions.

- It is noted from Ref. [94] that “larger metallic islands and larger porosity are observed within kernels from particles at the centre of the fuel pebble compared to kernels from particles from the outer region of the fuel pebble”. As also described in Ref. [95], “the presence of the larger metallic islands in the centre of the pebbles is in agreement with the observation on other fuels (e.g. LWR fuel) where it is also observed that the higher temperature (in transient conditions, for example) and thus the larger thermal diffusion coefficient increases the size of these precipitates”.
- As described in Ref. [96], “The network of intergranular porosities created in outer particles is to be only partially interconnected. In the fuel particles located in the centre of the pebble, larger porosities are observed compared to outer fuel particles. The pores on the cold side of the particles at the outer radius of the pebble fuel zone have a more irregular shape than the pores in the kernel bulk. Additionally, the UO<sub>2</sub> structure at the cold side of these kernels is different: there are hardly any grain boundaries visible, and metallic islands do not occur. This could indicate displacement of UO<sub>2</sub> from the kernels to the cold side, leaving irregular pores as a result. However, such UO<sub>2</sub> migration should be associated with the amoeba-effect (carbon migration), but for the particles considered it was clear that the kernels remained in the centre of the coating, and the buffer layer remained of uniform thickness”. From this point of view, the particles irradiated in this test showed a very different aspect from that shown in Ref. [96] that is described in such a manner that “an example of very extensive amoeba attack was identified on a UO<sub>2</sub> TRISO particle after irradiation conditions rather similar to an irradiated German TRISO fuel (9% FIMA at 1373 K, 207 days). The difference in behaviour could be assumed to be linked to the difference of enrichment (9% versus 17% <sup>235</sup>U here). In less enriched fuel, a significant fraction of the fissions occurs via plutonium leading to release of a larger amount of oxygen and greater CO + CO<sub>2</sub> internal pressure.”
- As additional information obtained from electron probe microanalyses (EPMA) [94]:
  - At room temperature, xenon either adhered to the buffer layer or presented within enclosed pores beneath the pyrolytic carbon. This supported a significant release of xenon from the kernel, and also was consistent with the report in Ref. [96].
  - While caesium was primarily detected in the buffer layer, its presence in the kernel was minimal, potentially originating from xenon decay.
  - Ruthenium was very largely contained within the metallic islands in the kernel, but some ruthenium was also found in the coatings. Palladium was distinguished as a small trace near the IPyC/SiC interface, but palladium was not present in the metallic inclusions.
  - Important observations were (1) palladium had accumulated near the IPyC/SiC, but not at the SiC layer (no Pd attack was observed), and (2) most caesium was found in the buffer layer (not in the other coating layers). The latter observation coincides with the presence of xenon in the buffer [5]. More evaluation and interpretation can be referred to Refs. [86,94].

Palladium is characterized with its high vapour pressure and affinity with variety of fission products to form inter-metallic compounds or mixed phases with volatile fission products [97]. For the outer-pebble zone samples, palladium is more clearly distinguished, albeit on the cold side of the sample, confirming similar observation presented in Ref. [96].

Comparison of destructive PIEs on samples taken from the centre and outside of the fuel zone of the pebble revealed a more deterioration of the SiC coatings in the central zone. The central zone sample showed apparent break-out of the SiC coating and the outer zone sample no cracking of the SiC coating [5].

Four spherical pebbles (HFR-EU1bis/1, HFR-EU1bis/3, HFR-EU1bis/4, and HFR-EU1bis/5) irradiated at the High Flux Reactor (HFR) in Petten for the HFR-EU1bis irradiation campaign were transported to JRC-ITU for PIEs and heating tests at the KÜFA facility.

Fractional release of fission products during the heating tests on these pebbles are described in Ref. [98] and are represented in Figs. 40 and 41. From these figures, the following observations were made [99]:

- During reactor normal operation, simulation of both  $^{134}\text{Cs}$  and  $^{137}\text{Cs}$  fractional release remained below  $10^{-4}$ ;
- HFR-EU1bis/5 showed the highest release of Cs among the entire series due to high temperature ( $1800^{\circ}\text{C}$ ) and rapid cycling of temperature. (Note that HFR-EU1bis/5 was exposed to extended heating phases at temperatures of  $1800^{\circ}\text{C}$  as well as rapid temperature transients to  $1800^{\circ}\text{C}$ );
- HFR-EU1bis/4 yielded a release around  $10^{-2}$  after extensive accident testing at  $1700^{\circ}\text{C}$ . The release was similar to the release from HFR-EU1bis/5 which was subjected to more extreme heating conditions, which might be attributed to an unfavourable operation of the test equipment for HFR-EU1bis/4.

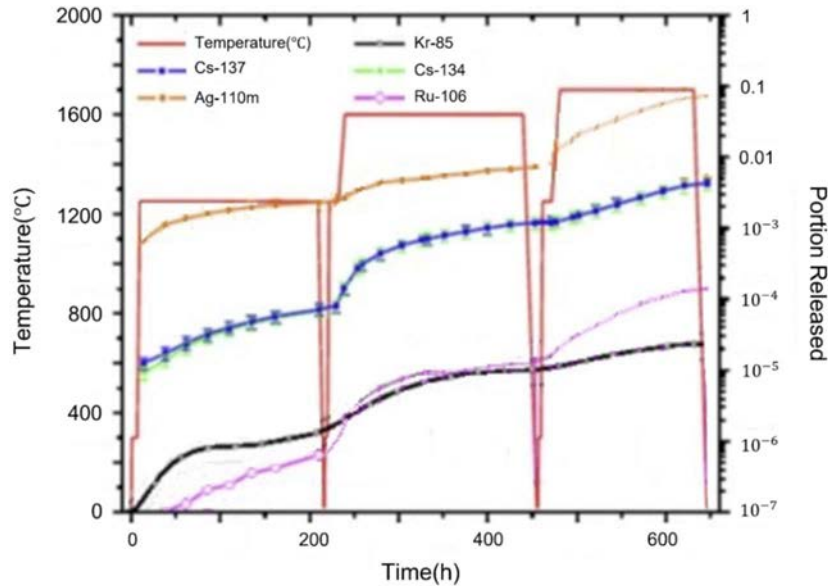


FIG. 40. Fractional release of various fission products during KÜFA test on HFR-EU1bis/1 through 15.

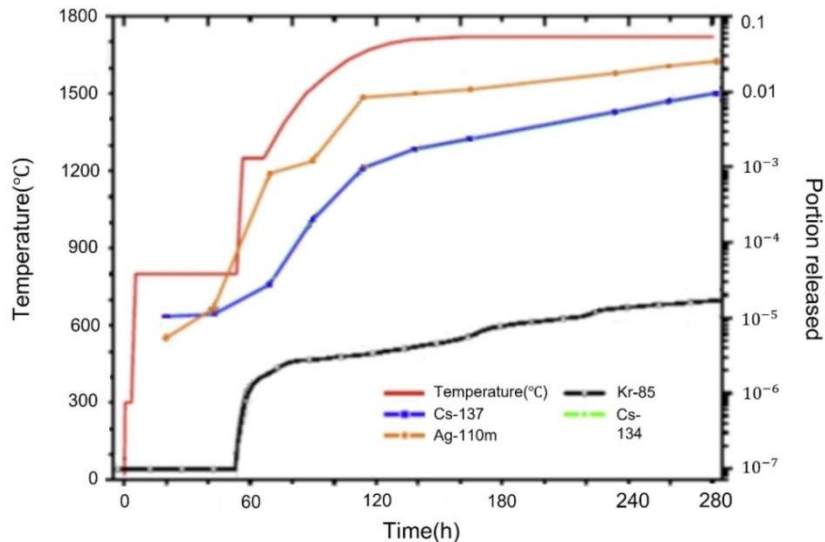


FIG. 41. Fractional release of various fission products during KÜFA test on HFR-EU1bis/4 and 5.

#### 6.2.1.2. HFR-EU1 irradiation experiment

The irradiation experiment HFR-EU1 [5,88] was conducted with three spherical pebbles, each containing 9500 particles in the Petten HFR reactor. It aimed at exploring the possibility for high power and high burnup operation of the German AVR pebbles and of newly developed fuel for VHTR.

Figure 42 shows the schematic configuration of the test rig.

Table 27 shows specifications of test pebbles. Three AVR pebbles were produced by Hochtemperaturreaktor-Brennelement GmbH (HOBEG), Germany and two by INET, China.

Conditions for the irradiation test are described in Ref. [100] and are represented in Table 28 [100]. During the irradiation, fission gas releases were measured through sweep loop facility. Detailed information on irradiation conditions, facilities and test pebbles can be found from [5,88,100].

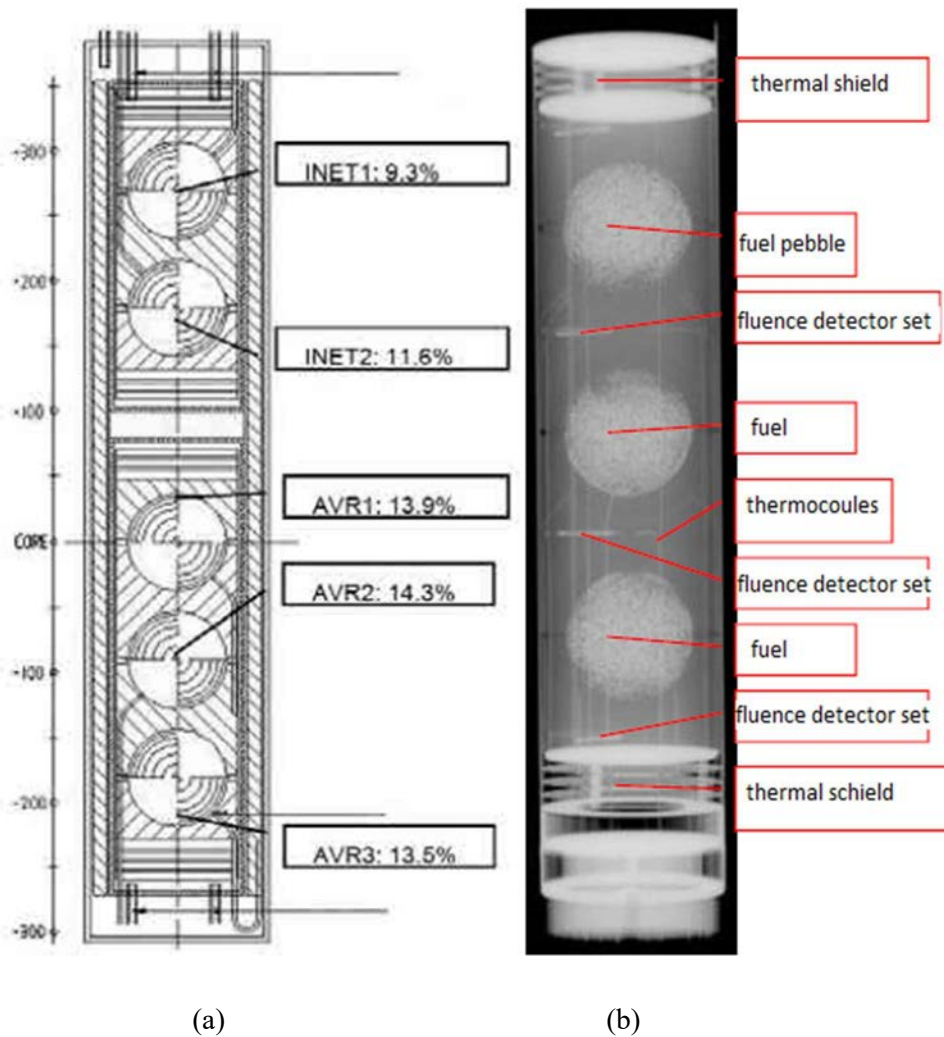


FIG. 42 (a) Cross-section of the HFR-EU1 sample holder with upper Capsule 1 containing two Chinese spheres and lower Capsule 2 containing three German spheres; (b) pre-irradiation X ray of German capsule, Capsule 2.

TABLE 27. NOMINAL CHARACTERISTICS OF INET AND AVR GLE-4 PEBBLES OF HFR-EU1 IRRADIATION

	INET	AVR
<b>Coated particle</b>		
Particle batch	V000802	HT384-393
Kernel composition	UO <sub>2</sub>	UO <sub>2</sub>
Kernel diameter (μm)	490.3	502
Enrichment ( <sup>235</sup> U wt.%)	17.08	16.76
Coat thicknesses (μm)		
Buffer	97	92
Inner PyC	7.42	40
SiC	37.8	35
Outer PyC	40.8	40
Particle diameter (μm)	926.9	916
<b>Pebble</b>		
Heavy metal loading (g/pebble)	5.02	6.0
<sup>235</sup> U content (g/pebble)	0.858	1.00 ± 1%
Number of coated particles per pebble	8500	9560
Volume packing fraction (%)	5.0	6.2
Free U fraction (U/U <sub>tot</sub> )	2.3×10 <sup>-7</sup>	7.8×10 <sup>-6</sup>
Matrix graphite grade	A3-3	A3-3
Matrix density (kg/m <sup>3</sup> )	1760	1750
Temperature at final heat treatment (°C)	1900	1900

TABLE 28 HFR-EU1 IRRADIATION EXPERIMENT

	HFR-EU1
Pebble number and type	2 INET + 3 AVR
Start	30.09.2006
End	19.02.2010
Duration (EFPD)	445
Burnup (% FIMA)	11–14
Temperature (°C)	900 (INET) – 950 (AVR)
R/B at end of irradiation (based on <sup>85m</sup> Kr release)	Approx. 5.5×10 <sup>-8</sup> (INET) Approx. 1.6×10 <sup>-7</sup> (AVR)

Figure 43 shows the fractional release of fission products at end of irradiation [5]. The fractional release in Fig. 43 was approximately  $2.5 \times 10^{-7}$  based on <sup>85m</sup>Kr for AVR fuel [5,88] and was at least two orders lower than the fractional release that could come out in theoretical maximum from a single particle in the capsule (approximately  $2.8 \times 10^{-4}$  for the AVR capsule). Also note that HFR-EU1bis experiment showed a higher fractional release of approximately  $4 \times 10^{-6}$  [69,101].

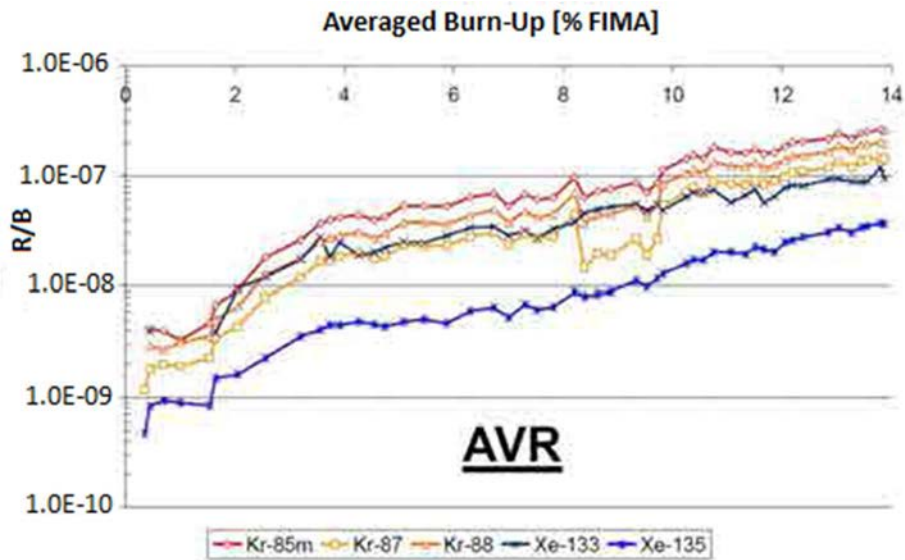


FIG. 43. R/B vs. burnup for AVR pebbles (reproduced from Ref. [5], courtesy of IAEA).

Figure 44 shows the fractional release of fission products from INET pebbles as a function of burnup [5]. The fractional release of  $^{85\text{m}}\text{Kr}$  at the end of irradiation was approximately  $8 \times 10^{-8}$ , which was lower than those from the earlier experiments HFR-K5 and HFR-K6 ( $5 \times 10^{-7}$ ) and HFR-EU1bis experiment (approximately  $4 \times 10^{-6}$ ) [69,101].

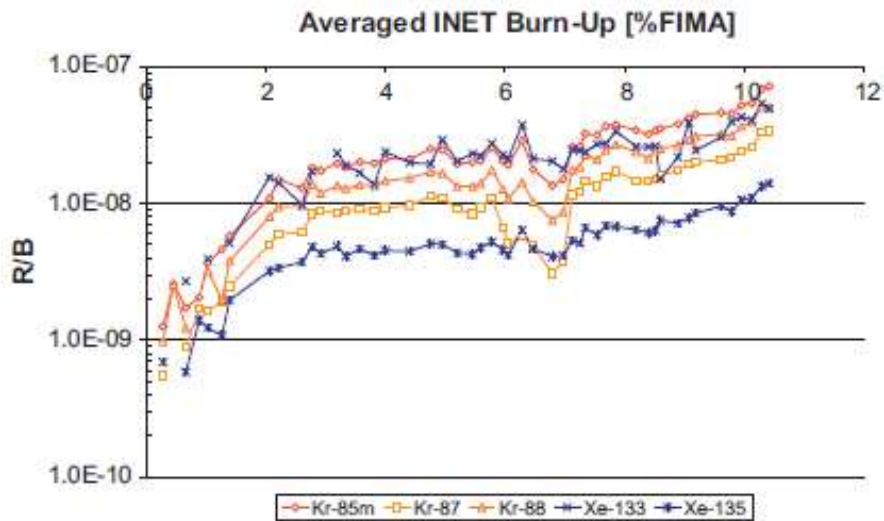


FIG. 44. R/B vs. burnup for INET pebbles (reproduced from Ref. [5], courtesy of IAEA).

### 6.2.1.3. HTR-10 fuel irradiation at HFR

The HTR-10 fuel was irradiated at the IVV-2M reactor during 2000–2003 [87]. Five capsules were contained in the irradiation rig. These capsules were numbered 1 through 5 from top to bottom. Each capsule contained:

- Capsule 1: 13,500 loose particles plus 60 samples of matrix graphite;
- Capsule 2: a spherical pebble (identification no: SFE5);
- Capsule 3: a spherical pebble (identification no: SFE12);
- Capsule 4: a spherical pebble (identification no: SFE8);
- Capsule 5: a spherical pebble (identification no: SFE7).

Table 29 [102] represents specifications of test pebbles. Note that test pebbles SFE5 and SFE7 were taken from batch 1 and test pebbles SFE8 and SFE12 from batch 2. Irradiation conditions are described in Refs [87,102] and are summarized in Table 30.

TABLE 29. MAIN CHARACTERISTICS OF THE HTR-10 PEBBLES

Batch no.	1 <sup>c</sup>	2 <sup>d</sup>
UO <sub>2</sub> kernel		
Enrichment (%)	17	17
Diameter (μm)	500.9	497.0
Density (g/cm <sup>3</sup> )	10.81	10.90
Sphericity (D <sub>max</sub> /D <sub>min</sub> )	1.04	1.06
O/U ratio	2.00	2.00
B equivalent (μg/g)	0.49	0.90
Coated fuel particle		
Buffer PyC layer thickness (μm)	91.0	96.0
IPyC layer thickness (μm)	48.1	44.7
SiC layer thickness (μm)	35.0	36.6
OPyC layer thickness (μm)	41.6	42.1
Buffer PyC layer density (g/cm <sup>3</sup> )	1.02	1.05
IPyC layer density (g/cm <sup>3</sup> )	1.84	1.84
SiC layer density (g/cm <sup>3</sup> )	3.20	3.20
OPyC layer density (g/cm <sup>3</sup> )	1.90	1.84
IPyC layer OPTAF <sup>a</sup>	1.03	1.02
OPyC layer OPTAF	1.03	1.03
Fuel ball		
Density (g/cm <sup>3</sup> )	1.73	1.72
Total ash (μg/g)	91.0	94.5
Li content (μg/g)	<0.01	<0.02
B equivalent (μg/g)	1.14	0.87
Corrosion rate (He with 1% H <sub>2</sub> O, 1000°C, 10 h) (mg/cm <sup>2</sup> h)	1.0	1.2
Erosion rate (μg/g)	3.0	3.0
Number of drops (4 m in height)	375	>200
Breaking loading (KN)	23.9	22.0
Thermal conductivity (1000°C) [W/cm·K]	29.5	30.8
CTE <sup>b</sup> anisotropy (α <sub>1</sub> / α <sub>l</sub> )	1.1	1.1
U loading (g)	5.00	4.98
U contamination	1.1×10 <sup>-6</sup>	7.6×10 <sup>-7</sup>
U <sub>free</sub> /U <sub>total</sub>	1.4×10 <sup>-4</sup>	2.3×10 <sup>-4</sup>

<sup>a</sup> Optical anisotropy factor.

<sup>b</sup> Coefficient of thermal expansion.

<sup>c</sup> Test pebbles SFE5 and SFE7 were taken from batch 1.

<sup>d</sup> Test pebbles SFE8 and SFE12 were taken from batch 2.

\* Information taken from Ref. [102].

TABLE 30. HTR-10 TEST FUEL IRRADIATION DATA

Start date	July 2000			
End date	February 2003			
Irradiation temperature (°C)	1000±50			
Capsule number	2	3	4	5
Fuel batch number/sphere ID	1/SFE5	2/SFE12	2/SFE8	1/SFE7
Burnup (% FIMA)	10.4	11.4	10.9	10.1
Fast neutron fluence (10 <sup>25</sup> n/m <sup>2</sup> ) <sup>a</sup>	1.10	1.31	1.30	1.06
EOL <sup>85m</sup> Kr R/B <sup>b</sup>	1.7×10 <sup>-5</sup>	6.7×10 <sup>-7</sup>	Not measured	7.8×10 <sup>-6</sup>
Capsule notes		In-pile heat-up test to 1200 and 1250°C for 200 h each	Capsule failed after 3.9% FIMA	In-pile heat-up test above 1600°C at end of irradiation

<sup>a</sup> Cut-off energy for fast neutron fluence not specified.

<sup>b</sup> The tabulated end of life (EOL) R/B for capsule 5 was measured at the end of the irradiation test phase and prior to the start of the high-temperature heat-up test.

Figure 45 shows the levels of fractional release (R/B ratio) of <sup>135</sup>Xe from four irradiated pebbles as a function of the burnup [5]. From Fig. 45, it can be noted [87]:

- Overall, the R/B values did not show significant increases and varied with only small fluctuations at temperatures of ~1000°C during irradiation. This implies that most likely irradiation-induced failures of the coated particles can be eliminated during normal operation.
- The high R/B levels were mainly attributed to the high failure fractions of fuel particles easily encountered in the early stage of fuel particles fabrication. The measured amount of the average tramp uranium from the four pebbles indicated the failures of some particles during fabrication.

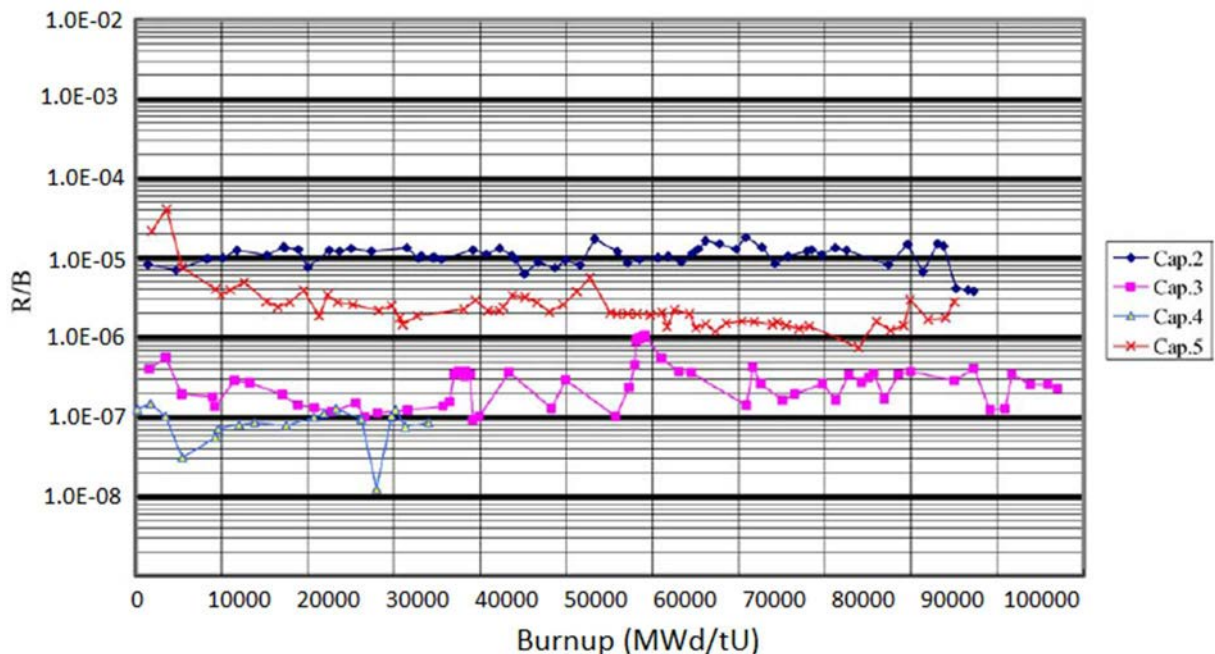


FIG. 45. R/B of <sup>135</sup>Xe of four irradiated fuel elements as a function of the burnup (reproduced from Ref. [5], courtesy of IAEA).

Table 31 demonstrates irradiation induced deformation of pebbles [89]; see dimensional changes of test pebbles (SFE5, SFE12 and SFE7) after the irradiation [89].

TABLE 31. NEUTRON-INDUCED DIAMETER CHANGE OF THE FUEL ELEMENTS AT 1000°C

Fuel element	Fast neutron fluence (E>0.1 MeV)/(10 <sup>21</sup> cm <sup>-2</sup> )	Before irradiation (mm)	After irradiation (mm)	Relative change (%)
Parallel to equatorial plane of fuel sphere	SFE5	1.10	60.03	-0.68
	SFE12	1.31	60.04	-0.62
	SFE7	1.06	60.06	-0.67
Perpendicular to equatorial of fuel sphere	SFE5	1.10	59.90	-0.70
	SFE12	1.31	60.06	-0.73
	SFE7	1.06	60.10	-0.72

During the irradiation, Capsule 4 failed due to a chemical reaction of the matrix graphite contained in test pebble SFE8 with impurities ingressed through the helium loop, e.g. oxygen of ingressed air. Due to the heat released from this chemical reaction, thermocouple was damaged, and the integrity of the graphite matrix was lost. This reaction caused the matrix graphite of the test pebble SFE8 to form a graphite powder agglomerate which was unbreakable during PIE. The loss of integrity of Capsule 4 resulted in the failure of all particles embedded in the pebble SFE8.

Figure 46 shows the fission gas release of SFE8 in Capsule 4, indicating a massive failure of coated particles [5].

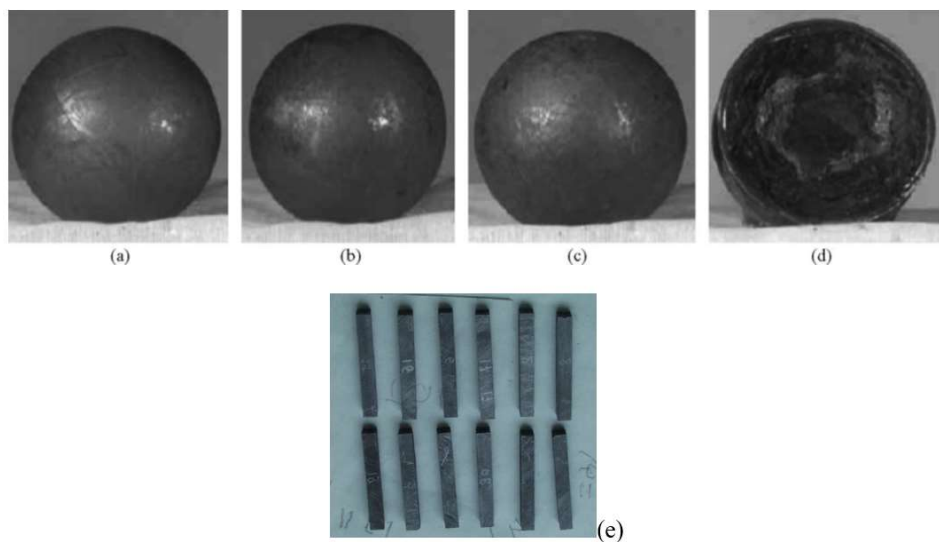


FIG. 46. Appearance of irradiated fuel elements in (a) Capsule 2; (b) Capsule 3; (c) Capsule 5; (d) Capsule 4; and in (e) matrix graphite specimens (courtesy of IAEA).

The microstructure of the well-coated particles was examined both before and after irradiation, extracted from Capsule 2. Remarkably, the PyC and SiC layers in these particles remained fully intact. No

observable cracks or other radiation-induced defects were noted in these layers. The buffer layers retained an adequate thickness, and there was no evidence of damage in the IPyC layers, which could have potentially resulted from fission fragments.

The temperature of test pebble SFE12 in Capsule 3 was increased from 1050 to 1200°C and then up to 1250°C, which resulted in an increase of fission gas release. When the temperature returned to 1050°C, the R/B ratio was restored to its initial level.

Failures during irradiation were determined by using the criterion of activity ratio between caesium ( $^{134}\text{Cs}$  or  $^{137}\text{Cs}$ ) and  $^{144}\text{Ce}$ . The activity ratio indicates the ratio of activities between a volatile fission product and a non-volatile fission product. The boiling point of Cs is 678°C, and Ce 3470°C. During the high temperature irradiations, Cs escaped much more readily from a defective coating than Ce. If the activity ratio between Cs and Ce from a particle is less than  $A_{mean} - 3\sigma$  (where  $A_{mean}$  is the mean average of the activity ratios and  $\sigma$  standard deviation), this particle is considered failed.

A total of 2,014 particles from the fragmented pebble SFE12 were scrutinized using the specified criteria, resulting in the identification of one failed particle among the 2,014 examined. Ceramographic sections, ranging from 200 to 400 coated particles, were meticulously prepared within a hot cell. A detailed examination of these sections using an optical microscope revealed that the PyC and SiC layers in these particles remained unaltered. No cracks, exfoliation, or other irradiation-induced defects were evident in these layers. There were no signs of corrosive impact from fission products on the SiC layer. Notably, the buffer layer maintained an ample thickness, and no damages were observed in the subsequent IPyC layer, as well as in the SiC and OPyC layers.

As stated earlier, test pebble SFE7 contained in Capsule 5 showed a significant number of failures of particles during the in-pile heating test. Test pebble SFE7 was disintegrated by electrolysis to obtain loose coated particles for the examination of failed particles. By examining the activity ratio of  $^{134}\text{Cs}$  to  $^{144}\text{Ce}$ , 127 coated fuel particles were determined to have failed, amounting to a failure fraction of approximately 6%. Such massive failures were believed to have caused by the operation at higher temperatures than 1600°C, from PIE results. Cracked layers that were most likely caused by the very high heating temperature and the resultant high stress.

#### *6.2.1.4. HTR-PM fuel irradiation at HFR*

To validate the manufactured fuel for the HTR-PM, an in-pile irradiation test was conducted. INET produced ten HTR fuel pebbles, which were subsequently delivered to NRG for irradiation at HFR in 2012. These HTR fuel pebbles are composed of a moulded graphite matrix with a diameter of 60 mm, encompassing coated particles within an inner zone of 52 mm diameter. The fuel-free shell surrounding this inner zone is more than 4 mm in thickness. Table 32 shows the specification of HTR-PM pebbles [91].

To create a cylindrical structure housing approximately 60,000 TRISO particles, a stack of five fuel pebbles was enveloped in graphite half-shells. This assembly was then enclosed within a stainless-steel containment, serving as the initial barrier for the fuel pebbles. Within this containment, 24 thermocouples were placed near the pebbles and in the graphite half-shells for temperature measurements. Additionally, continuous gas flow was maintained within the containment to enable online measurements of fission gas release.

The irradiation plan aimed to achieve burnup levels exceeding 12.3% FIMA with central temperatures of  $1050 \pm 50^\circ\text{C}$  for the upper four pebbles. This extended over a duration of 355 full power irradiation days. Neutronics calculations indicated total fast fluence levels ranging between  $3.79$  and  $4.95 \times 10^{25}$  n/m<sup>2</sup> ( $E > 0.1$  MeV). The estimated burnup was 11.1% FIMA for Pebble 5 and between 12.6 and 13.7% FIMA for the remaining pebbles. Central temperatures consistently hovered around the specified target boundaries of  $1050 \pm 50^\circ\text{C}$ .

TABLE 32. NOMINAL CHARACTERISTIC DATA OF INET PEBBLES

<b>Pebble properties</b>	
Particle batch	1
Kernel composition	UO <sub>2</sub>
Kernel diameter (μm)	500
Enrichment (U-235 wt.%)	17
Thickness of coatings (μm):	
Low density graphite (buffer)	95
Inner high-density Pyrolytic	40
Carbon or "PyC"	35
High density SiC	40
Outer high density PyC	
Particle diameter (μm)	920
Pebble	
Heavy metal loading (g/pebble)	7
U-235 content (g/pebble)	1.19
Number of coated particles (-)	
per pebble	12,000
Matrix graphite grade (-)	A3-3
Matrix density (g/cm <sup>3</sup> )	1.75
Temperature at final heat treatment (°C)	1900

All five spheres underwent irradiation in a single test rig, with online fission gas measurements capturing cumulative releases from the entire set. Remarkably, R/B ratios remained very low ( $(2.4-3.3) \times 10^{-9}$  at the end of irradiation), consistently below the calculated value ( $1.1 \times 10^{-7}$ ) for <sup>85m</sup>Kr from a single failed particle. This outcome strongly suggested the absence of manufacturing defects and the absence of in-pile particle failures.

From PIEs, the dimensional shrinkage in all 5 pebbles was found in the range between 0.88% and 1.25% [92].

Burnups were determined based on measured activities of <sup>137</sup>Cs [92] and are represented in Table 33.

TABLE 33. CS-137 ACTIVITY AT EOI AND CALCULATED BURNUP OF FUEL ELEMENTS FOR HTR-PM

<b>Fuel element</b>	<b>Cs-137 activity at EOI (Bq)</b>	<b>Calculated burnup (%FIMA)</b>
HTR-PM 1	$9.27 \times 10^{10}$	11.64
HTR-PM 2	$9.97 \times 10^{10}$	12.53
HTR-PM 3	$1.01 \times 10^{11}$	12.66
HTR-PM 4	$9.47 \times 10^{10}$	11.89
HTR-PM 5	$8.05 \times 10^{10}$	10.11

Heating tests were carried out with three irradiated pebbles (HTR-PM 1, 2 and 4) in the KüFA facility. Figure 47 shows the temperature histories and measured fractional releases during the heating test with HTR-PM 1 [102].

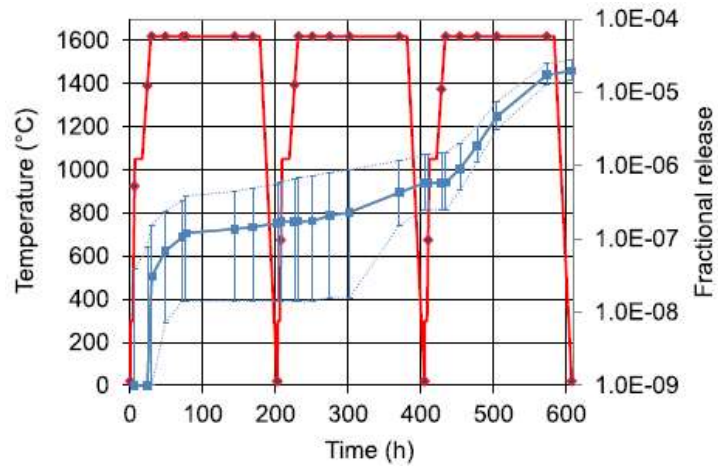


FIG. 47. HTR-PM 1 heating programme (red) and fractional release of Cs-137 (blue) (courtesy of INL).

Figure 48 shows the temperature histories and measured fractional releases during the heating test with HTR-PM 4 [102].

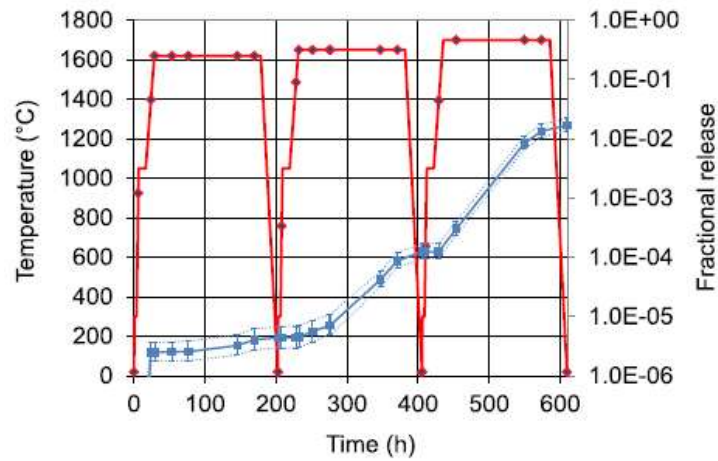


FIG. 48. HTR-PM 4 heating programme (red) and fractional release of Cs-137 (blue) (courtesy of INL).

Figures 49 and 50 show the temperature histories and measured fractional releases during the heating test with HTR-PM 2 [102].

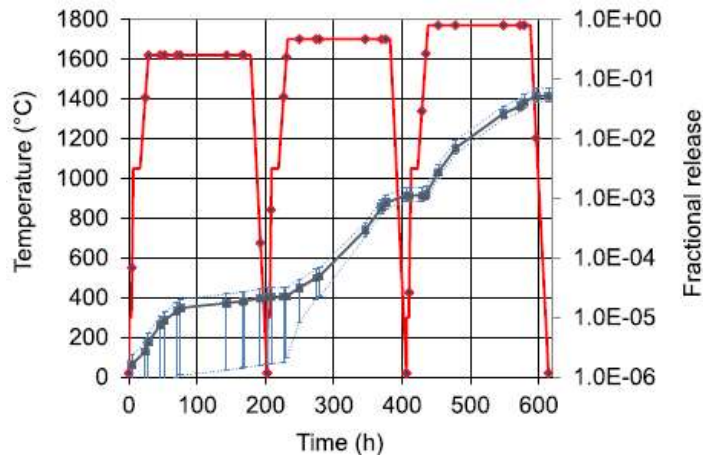


FIG. 49. HTR-PM 2 heating programme (red) and fractional release of Cs-134 (blue) and Cs-137 (grey) (courtesy of INL).

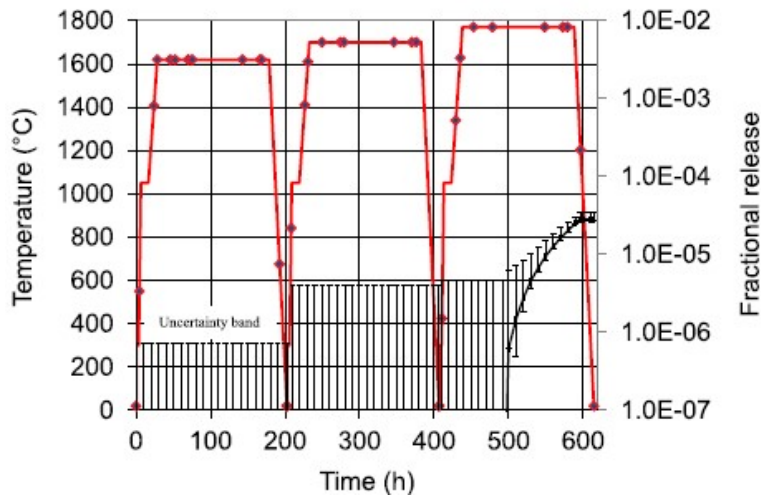


FIG. 50. HTR-PM 2 Kr-85 fractional release plus uncertainty (courtesy of INL).

### 6.2.2. Cylindrical compacts

Irradiations of cylindrical compacts have been pursued since the early 2000s mainly for the qualification of coated particle fuels for use in VHTRs. Table 34 represents relevant information.

In the United States, the Advanced Gas Reactor (AGR) Fuel Development and Qualification Program was initiated to qualify coated particle fuels within an operational range that encompasses both pebble bed and prismatic reactors. The objective was to develop a fuel form capable of withstanding peak fuel temperatures averaging 1250°C and achieving high burnups ranging from 150 to 200 GWd/tHM or 16.4 to 21.8% FIMA. UCO was chosen as the fissile kernel for this program due to its ability to restrict carbon monoxide (CO) production and prevent kernel migration under irradiation. These factors were deemed potential life-limiting issues for traditional UO<sub>2</sub> TRISO fuels when operating at elevated temperatures (~1250°C) and extended burnup, characteristic of a prismatic HTGR.

Four irradiation tests have been performed at the Advanced Test Reactor (ATR) at INL (AGR-1, AGR-2, AGR-3/4, and AGR-5/6/7; see Table 34 for irradiation experiment details). PIE including high-

temperature annealing tests of compacts from the AGR-1 experiment followed. PIE including annealing tests of AGR-2, AGR-3/4 and AGR-5/6/7 are planned.

The AGR program has already been described in the literature [4,5,12,70,103–106], and is not described in detail here. The progress and results of irradiation testing, PIE, and annealing testing for each AGR experiment are briefly described in the following sections.

#### 6.2.2.1. AGR-1 irradiation experiment

Figure 51 [110] shows a schematic diagram of the AGR-1 irradiation rig.

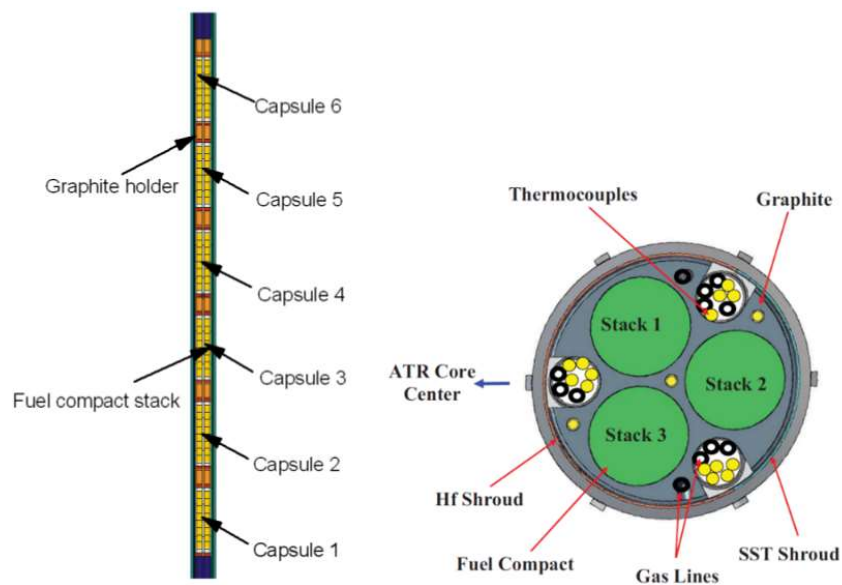


FIG. 51. Axial and radial cut schematics of the AGR-1 capsule (courtesy of INL).

The experiment used coated particle and fuel compacts fabricated at the laboratory scale at ORNL. One of the goals of the experiment was to explore the impact of coating microstructure and properties on fuel performance by including several different types of TRISO-coated particles. There were six separate capsules, each containing 12 fuel compacts. The baseline fuel underwent irradiation in Capsules 6 and 3, Variant 1 in Capsule 5, Variant 2 in Capsule 2, and Variant 3 in Capsules 1 and 4.

TABLE 34. IRRADIATIONS OF CYLINDRICAL COMPACTS SINCE THE EARLY 2000s

Reactor	Experiment ID	No. of specimen and fuel type (mm)	Country	Irradiation time (FPDs)	Fast fluence ( $10^{21}n\cdot cm^{-2}$ , $E>0.18$ MeV)	Burnup (%FIMA)	Operating temp. (°C)	Defective SiC layer fraction (U/U-total)	BOL $^{85m}Kr$ R/B EOL $^{85m}Kr$ R/B	Reference
ATR (INL, USA)	AGR-1	UCO; 72 compacts (dia. 12.34–12.36, height 25.0-25.3) LEU UCO TRISO	USA	24 Dec. 2006 – 30 Oct. 2009 (621)	3.2, 3.8, 4.1, 4.0, 3.7, 3.0 (peak)	17.5, 18.9, 19.5, 19.3, 18.3, 16.2 (max.)	1136, 1118, 1118, 1180, 1152, 1117 (time-ave. peak Temp.) 1029, 991, 980, 1041, 1005, 980 (time-ave. vol.-ave. temp.)	$< 4 \times 10^{-5}$	$8 \times 10^{-8}$ , $1 \times 10^{-8}$ , $6 \times 10^{-9}$ , $9.0 \times 10^{-9}$ , $1 \times 10^{-8}$ , $1 \times 10^{-8}$  $9 \times 10^{-8}$ , $4 \times 10^{-8}$ , $1 \times 10^{-8}$ , $5 \times 10^{-8}$ , $2 \times 10^{-7}$ , $1 \times 10^{-7}$	[5],[12],[70], [107–108]
ATR (INL, USA)	AGR-2 included French compacts and South Africa compacts	UCO; 36 compacts UO <sub>2</sub> ; 12 compacts LEU UCO and UO <sub>2</sub> TRISO	USA France South Africa	Jun. 2010– Nov. 2013 (560)	3.47 (UCO) 3.05–3.53 (UO <sub>2</sub> )	7.3–13.2 (UCO) 9.0–10.7 (UO <sub>2</sub> )	1080–1360 (UCO) 1072–1105 (UO <sub>2</sub> ) (time-ave. peak temp.)		$\sim 10^{-6}$ (UCO) $\sim 10^{-7}$ (UO <sub>2</sub> ) (3 cycle irradiation)	[12],[82], [103],[108]
ATR (INL, USA)	AGR-3/4 (designed to fail (DTF) fraction; $1 \times 10^{-2}$ )	UCO; 48 compacts 20 DTF particles/ compacts LEU UCO TRISO	USA	Dec. 2011 – Apr. 2014 (370)	1.19–532	4.9–15.3	845–1276 (time-ave. peak temp.)		$10^{-4} \sim 10^{-3}$	[12],[103]
ATR (INL, USA)	AGR-5/6/7	194 compacts LEU UCO TRISO	USA	Feb. 2018 – Jul. 2020 (~500)	1.5–4.0	7.4–18.6 (ave. $\geq 6$ )	AGR-5/6; 750-1350 (time-ave. peak temp.) AGR-7; 1350-1550 (time-ave. peak temp.)			[12],[103]
HANARO (KAERI, Republic of Korea)	12F-01K	14 compacts (dia. 8.0, height 10.0) LEU UO <sub>2</sub> TRISO	Republic of Korea	Aug. 2013–Mar. 2014 (132)	0.3	3.81 (max.)	1083 (calculated max.)	-	-	[5],[109]

A brief description of the coating property variations in these fuel types is given below [56]:

- Baseline fuel — Due to its outstanding irradiation performance, the coating process conditions employed in the fabrication of the historical German fuel were selected as the initial basis for the baseline fuel. Subsequent parametric studies fine-tuned these conditions, specifically tailored to the coater utilized for coating AGR-1 fuel. The goal was to generate coatings deemed most likely to exhibit successful performance during the AGR-1 irradiation, as well as in PIE and annealing testing. These adjustments were informed by assessments of the relative performance of previously irradiated TRISO fuels [10].
- Variant 1 — The temperature for coating the IPyC was elevated compared to the baseline process. This adjustment was anticipated to potentially improve the irradiation dimensional stability of the pyrocarbon, albeit with a potential trade-off of increased uranium dispersion due to higher permeability. The IPyC layer exhibited a slightly lower density than the baseline, and the anisotropy of the IPyC layer was also marginally reduced.
- Variant 2 — The IPyC coating gas fraction was increased relative to the baseline process for this variant. This change was expected to possibly reduce permeability, which could decrease uranium dispersion, but possibly at the expense of higher anisotropy reducing the irradiation dimensional stability of the pyrocarbon. The IPyC layer density was slightly higher than the baseline density and the IPyC anisotropy was also slightly higher after 1800°C heat treatment of the compacts.
- Variant 3 — The carrier gas composition for the SiC layer deposition was changed from hydrogen to an argon-hydrogen mixture. The introduction of the argon diluent resulted in more re-nucleation during SiC deposition and the optimal deposition temperature was lowered. This lower temperature was expected to possibly reduce SiC defects resulting from uranium dispersion, and the SiC microstructure had significantly finer and more equiaxed grains than in the other fuel types above [111], which could impact irradiation performance.

Tables 35, 36 and 37 represent properties of kernel, particles and compacts, respectively, taken from Refs. [110, 113].

TABLE 35. SELECTED PROPERTIES FOR AGR-1 KERNEL LOT G73D-20-69302

<b>Kernel property</b>	<b>Specified range for mean value</b>	<b>Actual mean value ± population standard deviation</b>
Diameter (μm)	350±10	349.7 ± 9.0
Density (kg/m <sup>3</sup> )	≥ 10.4	10.924 ± 0.0015
U-235 enrichment (wt %)	19.80±0.10	19.736 ± 0.047
Carbon/uranium (atomic ratio)	0.50±0.20	0.3253 ± 0.0028
Oxygen/uranium (atomic ratio)	1.50±0.20	1.3613 ± 0.0064
(Carbon + oxygen)/uranium (atomic ratio)	Not specified	1.6850 ± 0.0093
Total uranium (wt. %)	Not specified	90.059 ± 0.086
Sulfur impurity (ppm – wt.)	Not specified	608
All other impurities	Various	Below minimum detection limits and within specification

TABLE 36. SELECTED PROPERTIES FOR AGR-1 COATED PARTICLE COMPOSITES

Property	Specified range for mean	Actual mean value $\pm$ Population standard deviation			
		Baseline	Variants 1	Variants 2	Variants 3
Buffer thickness ( $\mu\text{m}$ )	100 $\pm$ 15	103.5 $\pm$ 8.2	102.5 $\pm$ 7.1	102.9 $\pm$ 7.3	104.2 $\pm$ 7.8
IPyC thickness ( $\mu\text{m}$ )	40 $\pm$ 4	39.4 $\pm$ 2.3	40.5 $\pm$ 2.4	40.1 $\pm$ 2.8	38.8 $\pm$ 2.1
SiC thickness ( $\mu\text{m}$ )	35 $\pm$ 3	35.3 $\pm$ 1.3	35.7 $\pm$ 1.2	35.0 $\pm$ 1.0	35.9 $\pm$ 2.1
OPyC thickness ( $\mu\text{m}$ )	40 $\pm$ 4	41.0 $\pm$ 2.1	41.1 $\pm$ 2.4	39.8 $\pm$ 2.1	39.3 $\pm$ 2.1
Buffer density ( $\text{Mg}/\text{m}^3$ )	0.95 $\pm$ 0.15	1.10 $\pm$ 0.04	1.10 $\pm$ 0.04	1.10 $\pm$ 0.04	1.10 $\pm$ 0.04
IPyC density ( $\text{Mg}/\text{m}^3$ )	1.90 $\pm$ 0.05	1.904 $\pm$ 0.014	1.853 $\pm$ 0.012	1.912 $\pm$ 0.015	1.904 $\pm$ 0.013
SiC density ( $\text{Mg}/\text{m}^3$ )	Not specified	3.208 $\pm$ 0.003	3.206 $\pm$ 0.002	3.207 $\pm$ 0.002	3.205 $\pm$ 0.001
OPyC density ( $\text{Mg}/\text{m}^3$ )	1.90 $\pm$ 0.05	1.907 $\pm$ 0.008	1.898 $\pm$ 0.009	1.901 $\pm$ 0.008	1.911 $\pm$ 0.008
IPyC anisotropy <sup>(a)</sup> (BAF <sub>o</sub> ) and diattenuation <sup>(b,c)</sup>	Not specified	1.022 $\pm$ 0.002 (0.0074 $\pm$ 0.0007)	1.014 $\pm$ 0.001 (0.0047 $\pm$ 0.0005)	1.023 $\pm$ 0.002 (0.0075 $\pm$ 0.0006)	1.029 $\pm$ 0.002 (0.0098 $\pm$ 0.0007)
OPyC anisotropy (BAF <sub>o</sub> ) and diattenuation <sup>(b,c)</sup>	Not specified	1.019 $\pm$ 0.003 (0.0063 $\pm$ 0.0009)	1.013 $\pm$ 0.002 (0.0044 $\pm$ 0.0006)	1.018 $\pm$ 0.001 (0.0059 $\pm$ 0.0004)	1.021 $\pm$ 0.003 (0.0071 $\pm$ 0.0008)
IPyC anisotropy (BAF <sub>o</sub> ) and diattenuation post compact anneal <sup>(b,c)</sup>	Not specified	1.033 $\pm$ 0.004 (0.0109 $\pm$ 0.0013)	1.021 $\pm$ 0.003 (0.0071 $\pm$ 0.0006)	1.036 $\pm$ 0.001 (0.0121 $\pm$ 0.0004)	1.034 $\pm$ 0.003 (0.0114 $\pm$ 0.0009)
OPyC anisotropy (BAF <sub>o</sub> ) and diattenuation post compact anneal <sup>(b,c)</sup>	Not specified	1.033 $\pm$ 0.003 (0.0111 $\pm$ 0.0009)	1.030 $\pm$ 0.003 (0.0100 $\pm$ 0.0011)	1.029 $\pm$ 0.004 (0.0097 $\pm$ 0.0013)	1.036 $\pm$ 0.002 (0.0120 $\pm$ 0.0007)
Sphericity (aspect ratio)	Mean not specified <sup>(d)</sup>	1.054 $\pm$ 0.019	1.056 $\pm$ 0.019	1.053 $\pm$ 0.019	1.055 $\pm$ 0.018
Particle diameter <sup>(e)</sup> ( $\mu\text{m}$ )	Mean not specified	800 $\pm$ 14	804 $\pm$ 13	798 $\pm$ 14	795 $\pm$ 15
Particle mass (g)	Mean not specified	7.27 $\cdot$ 10 <sup>-4</sup>	7.33 $\cdot$ 10 <sup>-4</sup>	7.24 $\cdot$ 10 <sup>-4</sup>	7.26 $\cdot$ 10 <sup>-4</sup>

(a) Specification does not apply to Variants 1 and 2.

(b) The first number is the equivalent-BAF<sub>o</sub>, defined as 1+3N, where N is the diattenuation. This value was discarded in favour of the optical anisotropy factor (OAF = [1+N]/[1-N]) in later AGR programme irradiation experiments but is listed here because the AGR-1 fuel specification was defined in terms of equivalent-BAF<sub>o</sub>.

(c) Values in parentheses are the diattenuation (N) that was measured with the Two-Modulator Generalized Ellipsometry Microscope (2-MGEM) developed at ORNL [112].

(d) Critical region is specified such that  $\leq$  1% of the particles shall have an aspect ratio  $\geq$  1.14.

(e) Based upon mean average particle measurements, not sums of mean layer thickness.

TABLE 37. SELECTED PROPERTIES FOR AGR-1 COMPACTS

Property	Specified range for mean value	Actual mean value ± Population standard deviation			
		Baseline	Variant 1	Variant 2	Variant 3
Compact mass (g)	Not specified	5.4789	5.3371	5.3736	
Mean uranium loading (g U/compact)	0.905±0.04	0.917	0.915	0.904	0.912
Diameter <sup>(b)</sup> (mm)	12.22–12.46	12.36±0.01	12.36±0.01	12.36±0.01	12.34±0.01
Length <sup>(b)</sup> (mm)	25.02–25.40	25.066±0.080	25.066±0.030	25.077±0.065	25.227±0.037
Number of particles per compact <sup>(a)</sup>	Not specified	4154	4145	4095	4132
Particle volume packing fraction <sup>(a)</sup> (%)	Not specified	36.99	37.42	36.26	36.04
Effective overall compact density <sup>(a)</sup> (Mg/m <sup>3</sup> )	Not specified	1.822	1.771	1.786	1.854
Compact matrix density <sup>(a)</sup> (Mg/m <sup>3</sup> )	Not specified	1.297	1.219	1.256	1.344
U contamination fraction <sup>(c)</sup> (g exposed U/g U in compact)	Not specified	0	0	0	0
Defective SiC coating fraction <sup>l</sup>	Not specified	4.0×10 <sup>-5</sup>	0	2.0×10 <sup>-5</sup>	0
Defective IPyC coating fraction <sup>o</sup>	Not specified	0	0	0	0
Defective OPyC coating fract <sup>o(c)</sup>	Not specified	0	9.6×10 <sup>-4</sup>	0	0

(a) Value derived from other characterized properties.  
(b) Allowable range corresponding to upper and lower critical limits specified with no compacts exceeding the limits, which require 100% inspection of all compacts.  
(c) Values are measured fraction in each analysed sample, and are an estimate of an attribute property, not the mean of a variable property.

Figure 52 shows the diametric changes of AGR-1 compacts. The data indicate the increase of compact diameter shrinkage up to a fast fluence of approximately  $3 \times 10^{25}$  n/m<sup>2</sup>. Above  $3 \times 10^{25}$  n/m<sup>2</sup>, the observed trend shows minimal dependence on fast fluence, indicating either negligible dependence or a slight decrease in shrinkage as fast fluence increases. It is important to note that other factors, such as irradiation temperature, could potentially exert a significant influence on the overall dimensional change.

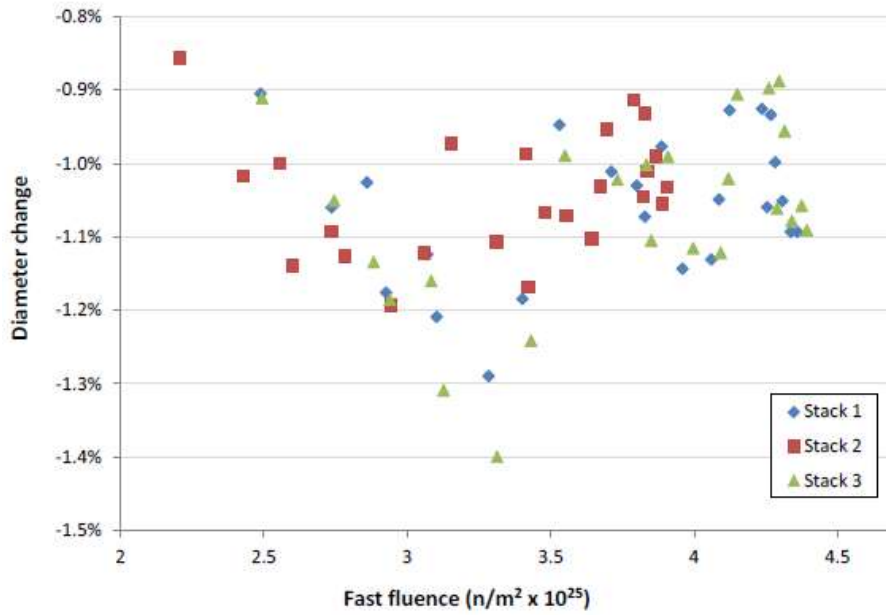


FIG. 52. Average diameter change for all AGR-1 compacts as a function of calculated fast neutron fluence ( $E > 0.18$  MeV) (courtesy of INL).

The prevalent characteristic observed was a radial gap between the buffer and IPyC layers, where the buffer underwent inward densification during irradiation, as illustrated in Fig. 53. AGR-1 buffers were initially deposited at a nominal density of  $1.1 \text{ g/cm}^3$  [110], representing 49% of the theoretical density [114]. However, Fig. 53 suggests that substantial porosity persisted post-irradiation, indicating incomplete densification. As depicted by the curved red arrow in Fig. 53 [107], the buffer and its encapsulated kernel were not securely retained within the outer TRISO shells after the buffer and IPyC layers had completely debonded. To stabilize loose buffers and kernels, fluid epoxy needed to be vacuum-impregnated (back-potted) into these gaps during grinding through the saw-damaged thickness on each mount. Failure to perform frequent back-potting posed the risk of dislodged kernels breaking into coarse abrasive fragments, potentially causing damage to the mount by notching the surface with deep scratches.

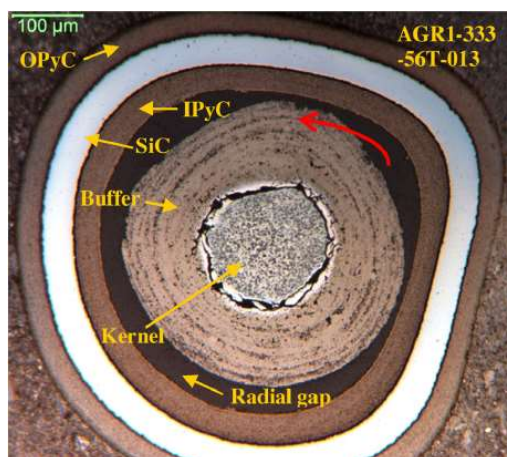


FIG. 53. Buffer and kernel that rotated before the radial gap was filled by back-potted epoxy (courtesy of INL).

The results of AGR-1 PIE and annealing testing are described in detail in Refs. [107,115–116]. The annealing test was undertaken in the FACS furnace at the INL and the Core Conduction Cooldown Test Facility at ORNL. Both systems can heat fuel specimens at temperatures up to 1800°C in inert atmospheres while monitoring the release of volatile fission products and gases.

A notable discovery was the remarkably low levels of caesium released through intact coatings, observed both during irradiation and in post-irradiation heating tests conducted at temperatures of 1800°C. It was determined that the release of caesium from a particle was predominantly linked to discrete failures in the SiC layer. In instances where the SiC layer experienced failure, a particle could release the majority of its caesium inventory. Conversely, in the absence of such failures, the release was exceptionally low, with capsule-average release from compacts (in the absence of SiC failures during irradiation) measuring less than  $3 \times 10^{-6}$ .

The primary cause of SiC failure was identified as a two-part mechanism involving (1) fracture of the IPyC layer due to densification of an adherent buffer layer, and (2) localized accumulation of palladium at the IPyC-SiC interface in the region of the IPyC fracture, leading to subsequent degradation of the SiC layer through chemical reaction with palladium. Instances of widespread chemical attack on the SiC layer by palladium were not observed in the absence of IPyC layer fracture. Four particles in the AGR-1 experiment experienced SiC layer failure during irradiation, resulting in an in-pile SiC failure fraction of  $\leq 3.1 \times 10^{-5}$  at a 95% confidence level. Importantly, no particles experienced TRISO failure (failure of all three dense coating layers) during the irradiation, yielding a particle failure fraction of  $\leq 1.1 \times 10^{-5}$  at 95% confidence.

Post-irradiation annealing test fuel performance was generally excellent. For instance, the maximum fractional releases from fuel compacts heated for 300 h at 1600°C were approximately  $2 \times 10^{-4}$  ( $^{134}\text{Cs}$ ),  $3 \times 10^{-3}$  ( $^{154}\text{Eu}$ ),  $2 \times 10^{-3}$  ( $^{90}\text{Sr}$ ), and  $4 \times 10^{-6}$  ( $^{85}\text{Kr}$ ). At 1800°C, the maximum releases for  $^{154}\text{Eu}$ ,  $^{134}\text{Cs}$ , and  $^{90}\text{Sr}$  were roughly an order of magnitude higher. In the case of  $^{134}\text{Cs}$ , release was linked to an increase in the average number of SiC failures as the test temperature rose; in the absence of SiC failures, the maximum release at 1600°C was approximately  $5 \times 10^{-6}$ . The observed  $^{85}\text{Kr}$  release at 1800°C increased due to elevated coating failure, with the maximum  $^{85}\text{Kr}$  release after 300 h at 1800°C reaching approximately  $5 \times 10^{-4}$  and being associated with TRISO failures at this extremely high test temperature. Subsequent analysis of the fuel post-annealing tests revealed that SiC failure typically followed the same mechanism observed in in-pile failures, and the localized palladium attack on the SiC layer was accelerated at higher temperatures.

The release of silver from the particles and compacts during irradiation was often notably high and primarily influenced by variations in fuel temperature, aligning with findings from previous TRISO fuel irradiation experiments. Although silver release from fuel compacts during high-temperature post-irradiation annealing tests could be substantial (reaching as high as ~30%), it typically concluded within a few hours of attaining the target test temperature. The amount of released silver was determined by the inventory available in the outer OPyC layers or compact matrix that remained at the end of the irradiation. Minimal additional silver release from particles was measured during isothermal testing lasting up to 300 h at 1600 and 1700°C. Only at a test temperature of 1800°C was clear evidence of additional silver release through intact coatings observed. Additionally, a single test indicated higher silver release at intermediate temperatures (peaking at 1150°C), warranting further investigation in future tests.

For example, as illustrated in Fig. 54 [107], silver release patterns also showed a difference between the Variant 3 compacts and the compacts with coarser-grained SiC. Transport of silver from the fine-grained SiC (Variant 3) was apparently higher at 1800°C than from the coarse-grained SiC, as additional silver release was observed after ~100 h at this temperature only for the Variant 3 specimens. Since no additional silver release was observed in the later stages of the tests from any of the fuel specimens (including Variant 3), this indicates that diffusive behaviour at 1800°C is significantly higher than at 1600°C.

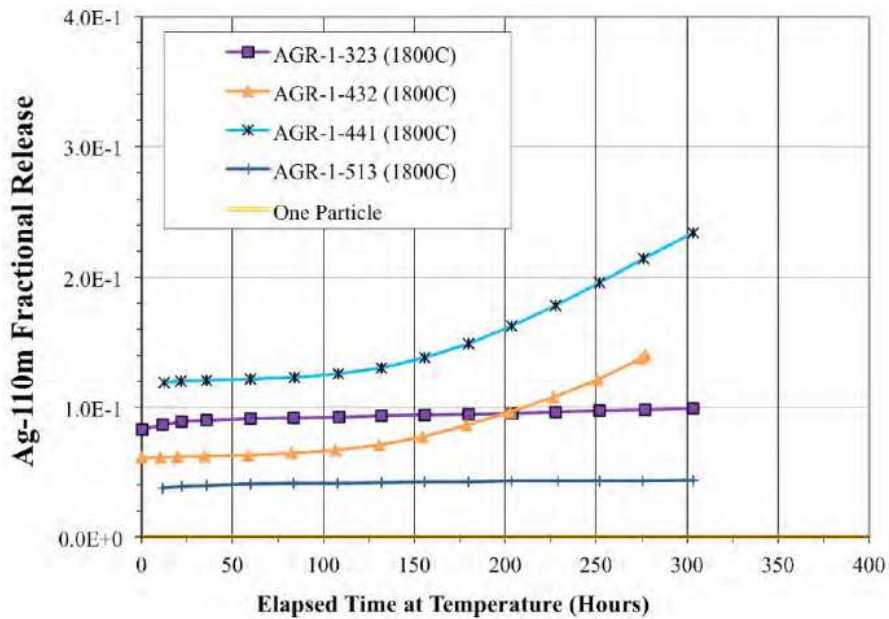


FIG. 54. Differences in silver behaviour observed between Variant 3 (compacts 4-3-2 and 4-4-1) and Baseline (Compact 3-2-3) and Variant 1 (Compact 5-1-3). (The results are qualitatively similar to the outcomes for Eu and Sr results) (courtesy of INL).

A comprehensive microanalysis of fuel particles was conducted to enhance the understanding of fission product migration under various conditions. This analysis involved conventional techniques such as optical microscopy and scanning electron microscopy, as well as more advanced methods like transmission electron microscopy and scanning transmission electron microscopy, coupled with several techniques for elemental and crystallographic analysis. In some instances, these analytical techniques were applied to irradiated TRISO fuel for the first time, allowing the analysis of fission products within the coating layer microstructures down to nanometre-length scales. For example, the particles subjected to 1600°C annealing tests and analysed by SEM (Scanning Electron Microscope) included particles from two Baseline compacts (6-4-3 and 6-2-1), two Variant 3 compacts (4-1-2 and 4-3-3), and one Variant 1 compact (5-3-3) [107].

Figure 55 [107] provides a comparison between a particle with very low silver retention ( $^{110m}\text{Ag M/C}^9 \leq 0.16$ ) and a particle with high silver retention ( $^{110m}\text{Ag M/C} = 1.12$ ) from Compact 4-1-2. The exposure to 1600°C did not alter the characteristics of the inner IPyC-SiC interface, as evidenced by the intimately stitched IPyC-SiC interface observed in the secondary electron imaging (SEI) micrographs in Fig. 55. Backscattered Electron Composition (BEC) imaging of the TRISO layers reveals the accumulation of fission products at the IPyC-SiC interface and embedded fission product clusters in the SiC layers.

The distribution and frequency of embedded fission products in the SiC layer showed a dependency on silver retention behaviour. Particles with low silver retention exhibited a greater frequency of fission product clusters distributed deeper into the SiC layer relative to high silver-retention particles. A correlation with palladium-uranium (Pd-U) and palladium (Pd) features was observed, with Pd-U features being predominant in the first 10  $\mu\text{m}$  of the SiC layer, and Pd clusters with no detectable uranium being more frequent in the outer half of the SiC layer. These observations align with the

<sup>9</sup> In some cases, individual particles taken from irradiated and heated fuel specimens were analyzed with gamma spectrometry to determine the inventory of fission products. These measured inventories were decay-corrected and compared to the calculated inventory from neutronics analysis to determine the ratio of measured to calculated (M/C) inventories. For  $^{110m}\text{Ag}$ , this provides an estimate of the level of retention in the particles. See [107] for more details.

distributions of fission product clusters in the SiC layer of as-irradiated compacts discussed in Section 3.4.2.1 of Ref. [107].

In addition to palladium and uranium, other fission products, similar to those observed in the as-irradiated particles [107], were detected by energy-dispersive X-ray spectroscopy (EDS) and were primarily located near the IPyC-SiC interface.

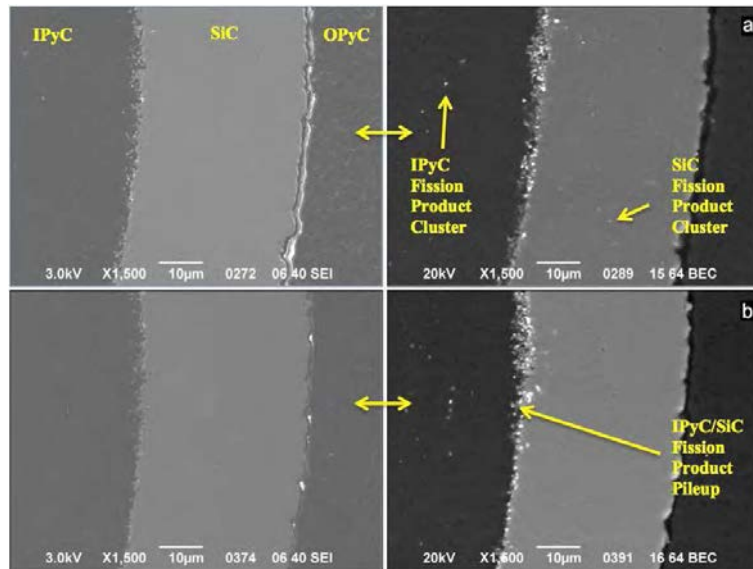


FIG. 55. SEI/BEC-paired images of Compact 4-1-2, annealed at 1600°C: (a) very low Ag retention particle ( $M/C \leq 0.16$ ) and (b) high Ag retention particle ( $M/C = 1.12$ ). Areas of bright contrast in BEC micrograph indicate isolated fission product features (courtesy of INL).

#### 6.2.2.2. AGR-2 irradiation experiment

The AGR-2 experiment was the second in the series of planned experiments designed to test TRISO-coated, LEU UCO fuel. The main objective of the AGR-2 test was to irradiate TRISO particles produced from pilot-scale coating equipment, both UCO and  $UO_2$ , to gather data on fuel performance under normal operation and accident conditions. The UCO compacts underwent a range of burnups and temperatures distributed across three capsules, while compacts containing  $UO_2$  particles from the United States, South Africa, and France were separately irradiated in three capsules [117].

The burnups and temperatures applied to the UCO compacts were representative of expected service conditions in pebble bed reactors. It is important to note that the irradiation performance of the  $UO_2$  fuel from France and South Africa has not been reported. Therefore, the following discussion focuses solely on the UCO fuel produced in the United States and irradiated in capsules 2, 5, and 6, as well as the  $UO_2$  fuel irradiated in capsule 3.

Tables 38 and 39 show properties of AGR-2 coated particles and compacts, respectively, taken from Refs. [117,118]. Table 40 describes requirements for irradiations [119].

TABLE 38. SELECTED PROPERTIES OF THE AGR-2 UCO AND UO<sub>2</sub> FUEL PARTICLES

Property	Actual mean value ± Population standard deviation	
	UCO	UO <sub>2</sub>
Kernel type		
Kernel diameter (μm)	426.7±8.8	507.7±11.9
U enrichment (wt.%)	14.029±0.026	9.600±0.010
Buffer thickness (μm)	98.9±8.4	97.7±9.9
IPyC thickness (μm)	40.4±2.5	41.9±3.2
SiC thickness (μm)	35.2±1.2	37.5±1.2
OPyC thickness (μm)	43.4±2.9	45.6±2.4
IPyC anisotropy (OAF) and diattenuation <sup>a,b</sup>	1.0236±0.0008 (0.0116±0.0004)	1.0225±0.0019 (0.0111±0.0009)
OPyC anisotropy (OAF) and diattenuation <sup>a,b</sup>	1.0177±0.0008 (0.0088±0.0004)	1.0147±0.0008 (0.0073±0.0004)
IPyC anisotropy (OAF) and diattenuation post-compact anneal <sup>a,b</sup>	1.0315±0.0033 (0.0155±0.0016)	1.0319±0.0025 (0.0157±0.0012)
OPyC anisotropy (OAF) and diattenuation post-compact anneal <sup>a,b</sup>	1.0290±0.0013 (0.0143±0.0006)	1.0246±0.0011 (0.0122±0.0005)
Particle diameter (μm)	873±23	953±28
Particle mass (mg)	1.032±0.003	1.462±0.005

a. The optical anisotropy factor (OAF) is equivalent to  $(1+N)/(1-N)$ , where N is the diattenuation.

b. Values in parentheses are the diattenuation (N) that was measured with the Two-Modulator Generalized Ellipsometry Microscope (2-MGEM) developed at ORNL [112].

TABLE 39. SELECTED PROPERTIES OF AGR-2 COMPACTS

Property	Actual mean value ± Population standard deviation	
	UCO	UO <sub>2</sub>
Compact mass (g)	6.293±0.011	6.103±0.014
Mean U loading (g U/compact)	1.257±0.03	0.993±0.006
Diameter (mm)	12.286±0.005	12.269±0.007
Length (mm)	25.141±0.017	25.134±0.018
Number of particles per compact <sup>(a)</sup>	3176	1543
Particle volume packing fraction (%)	37	23
Effective overall compact density <sup>(a)</sup> (Mg/m <sup>3</sup> )	2.11	2.05
Compact matrix density (Mg/m <sup>3</sup> )	1.589±0.005	1.677±0.006
U contamination fraction w/o exposed kernels (g leached U/g U in compact)	3.94×10 <sup>-6</sup>	9.66×10 <sup>-7</sup>

(a) Approximate calculated value derived from other characterized properties.

TABLE 40. AGR-2 FUEL IRRADIATION TEST CONDITION REQUIREMENTS

Parameter	Specification
Peak temperature for each capsule (°C)	≤1250 for the remaining capsules containing UCO fuel ≤1150 for each capsule
Time average, volume average temperature goal for each capsule (°C)	≥ime for the highest temperature UCO capsule ≥1000 for the remaining capsules containing UCO fuel ≥900 for each capsule containing UO <sub>2</sub> fuel
Minimum compact average burnup (% fissions per initial heavy metal atom)	>7 for UCO, U.S. UO <sub>2</sub> and South African UO <sub>2</sub> fuel >11 for French UO <sub>2</sub> fuel
Compact average burnup goal for majority of fuel compacts (% fissions per initial heavy metal atom)	>10 for UCO, U.S. UO <sub>2</sub> and South African UO <sub>2</sub> fuel >13 for French UO <sub>2</sub> fuel
Peak fast neutron fluence (n/m <sup>2</sup> , E>0.18 MeV)	<5×10 <sup>25</sup>
Minimum peak fast neutron fluence (n/m <sup>2</sup> , E>0.18 MeV)	>1.5×10 <sup>25</sup>
Instantaneous peak power per particle (MW/particle)	≤/pa

Actual irradiation data are shown in Tables 41 (for burnup), 42 (for fluence) and 43 (for temperature), taken from Ref. [120].

TABLE 41. MINIMUM, CAPSULE AVERAGE, AND PEAK COMPACT BURNUP (%FIMA) AT THE END OF IRRADIATION

Capsule	Minimum Compact	Capsule Average	Peak Compact	Goals
6	7.26	9.30	10.81	Burnup >7% for all compacts
5	10.07	11.68	12.88	
3	9.01	10.10	10.69	Burnup >10% <sup>(a)</sup> for the majority of compacts
2	10.80	12.17	13.15	

Thirty-six of 48 compacts (28/36 UCO and 8/12 UO<sub>2</sub>) achieved a compact burnup of at least 10%.

TABLE 42. MINIMUM, CAPSULE AVERAGE, AND PEAK COMPACT FAST FLUENCE (10<sup>25</sup> N/M<sup>2</sup>, E > 0.18 MeV) AT THE END OF IRRADIATION

Capsule	Minimum Compact	Capsule Average	Peak Compact	Goals
6	1.94	2.39	2.73	Fluence >1.5 and <5.0 for all compacts
5	2.77	3.18	3.42	
3	3.05	3.35	3.53	
2	2.88	3.25	3.47	

TABLE 43. TIME-AVERAGE (TA) MINIMUM, TIME-AVERAGE, VOLUME-AVERAGE (TAVA), AND TA PEAK TEMPERATURES (°C) AT THE END OF IRRADIATION

Capsule	TA Minimum	Capsule Average	TA Peak	Goals
6	868	1074	1183	TA peak < 1400 °C for one UCO capsule
5	923	1101	1210	TA peak < 1250 °C for other UCO capsules
3	889	1032	1105	TA peak < 1150 °C for UO <sub>2</sub> capsule
2	1034	1252	1360	TAVA > 1150 °C for one UCO capsule TAVA > 1000 °C for other UCO capsules TAVA > 900 °C for UO <sub>2</sub> capsule

In the initial three cycles of the AGR-2 irradiation (from 0 to 149 EFPD), the fission gas R/B (Release-to-Birth) ratios remained relatively low. As depicted in Fig. 56 [121] for isotopes such as <sup>85m</sup>Kr, <sup>88</sup>Kr, and <sup>138</sup>Xe, the R/B values in the UCO capsules were predominantly below 10<sup>-6</sup>. The exception was observed in the hottest Capsule 2, where the <sup>85m</sup>Kr R/B reached 2×10<sup>-6</sup>. The average <sup>85m</sup>Kr R/B values in Capsules 2, 5, and 6 were recorded as 1.3×10<sup>-6</sup>, 5×10<sup>-7</sup> and 6×10<sup>-7</sup>, respectively [120]. In the UO<sub>2</sub> capsule (Capsule 3), the R/B values during the initial three cycles consistently remained below 10<sup>-7</sup>. These values, while higher than the beginning-of-life (BOL) R/B for the AGR-1 irradiation capsules (with an average R/B of ~10<sup>-8</sup>) [122], were influenced in part by increased uranium contamination in the AGR-2 compacts compared to AGR-1 (uranium contamination in the AGR-2 compacts was ~4×10<sup>-6</sup>, compared to an average value of 3×10<sup>-7</sup> for the AGR-1 compacts).

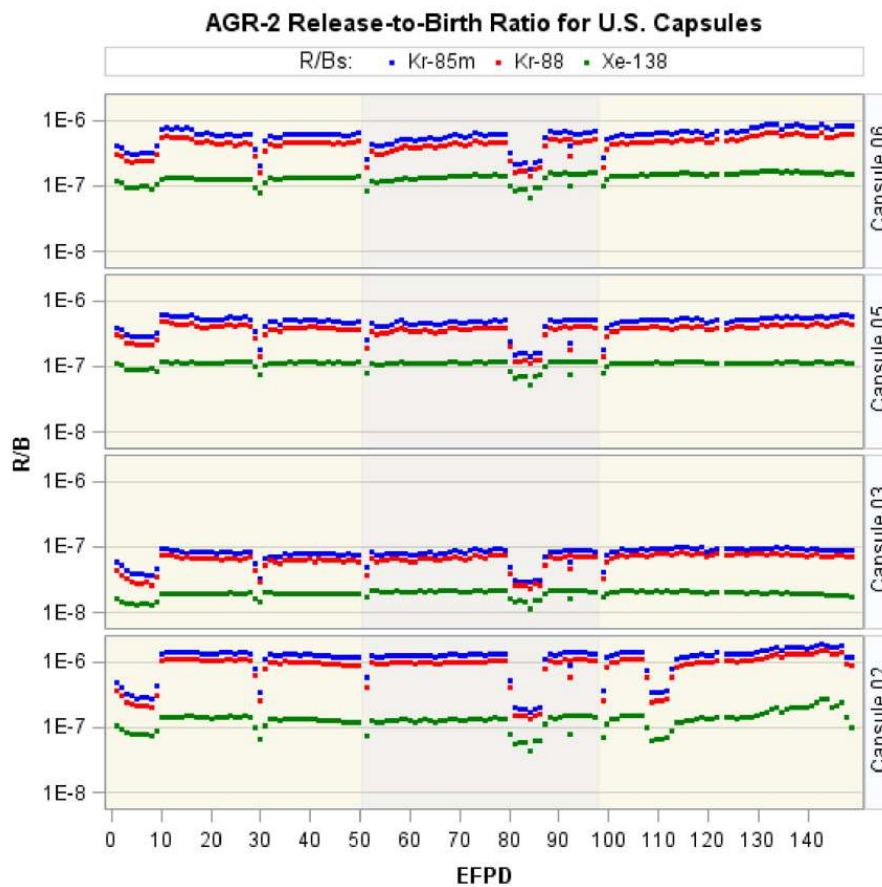


FIG. 56. R/B ratios from daily birth rates for Kr-85m, Kr-88, and Xe-138 versus time in EFPD during the initial three irradiation cycles of AGR-2 (courtesy of INL).

After the third irradiation cycle, problems with the gas lines in the capsules resulted in a loss of reliable fission gas R/B data, and therefore the EOL R/B values are not known [120]. Detailed PIE of the capsules and fuel specimens was performed to assist in determining if there were any in-pile particle failures. The results indicated that there were  $\leq 4$  UCO particle failures during the irradiation, with the uncertainty in the number arising from challenges in differentiating particles with (a) in-pile TRISO failures, (b) particles with in-pile SiC layer failures, and (c) particles with as-fabricated coating defects during the PIE process [121]. With a total of 114 000 UCO particles in the experiment, four in-pile particle failures would result in a calculated failure fraction of  $\leq 8.1 \times 10^{-5}$  at 95% confidence, while the value would be  $\leq 2.7 \times 10^{-5}$  if there were zero particle failures. No evidence of in-pile particle failure was observed for the UO<sub>2</sub> fuel in Capsule 3. With a total of 18,500 UO<sub>2</sub> TRISO particles in this capsule, this results in a calculated failure fraction of  $\leq 1.7 \times 10^{-5}$  at 95% confidence.

The major components of the AGR-2 PIE and annealing testing have been completed, and results can be found in a number of publications [108, 121, 123–134]. The in-pile behaviour and the annealing test results for the AGR-2 UCO fuel were generally consistent with previous observations from the AGR-1 fuel. Kernel and coating microstructures appeared similar to the AGR-1 fuel, with characteristic kernel porosity and a gap between the buffer and IPyC layers (Fig. 57 [135, 136]).

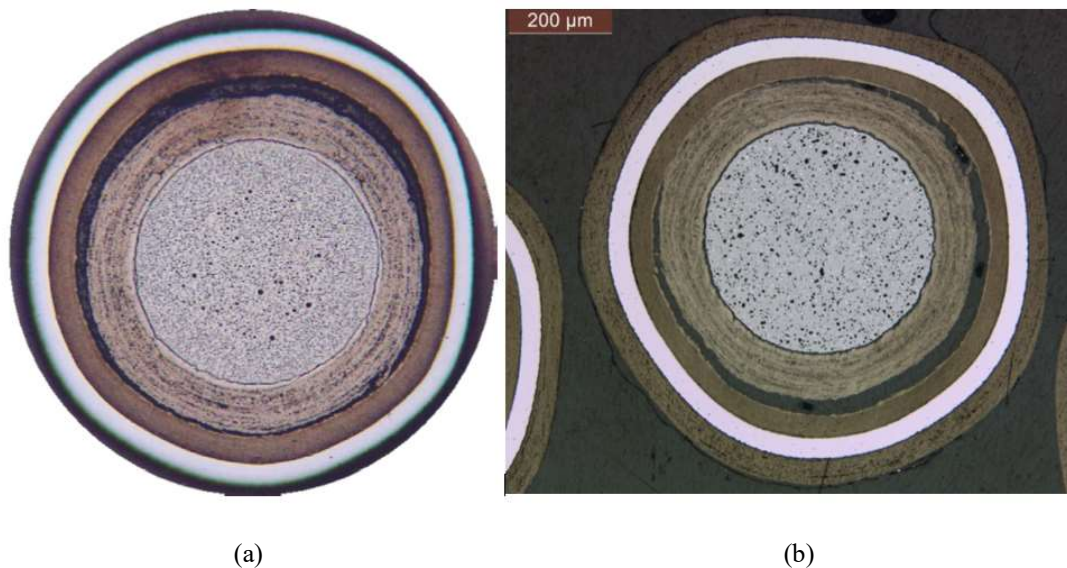


FIG. 57. Cross-section micrographs for (a) an AGR-2 UCO TRISO particle from fuel compact 5-1-3 with time-average peak temperature 1177°C and burnup 11.1% FIMA and (b) an AGR-2 UO<sub>2</sub> TRISO particle from compact 3-1-2 with time-average peak temperature 1084°C and burnup 10.7% FIMA (courtesy of INL).

Fuel compacts were annealing tested in a manner similar to the AGR-1 fuel, including a hold at the target test temperature for nominally 300 h while measuring fission product release. The AGR-2 UCO TRISO fuel exhibited performance similar to that demonstrated by the AGR-1 fuel tested previously. No particle failures were observed during 1600°C tests, and some failures occurred during 1800°C tests. The <sup>85</sup>Kr release from all fuel specimens was  $\leq 7.7 \times 10^{-6}$  at 1600°C and approximately a factor of 10 higher at 1800°C (excluding a result from a compact where a particle failed due to degradation of the SiC layer from Mo that was introduced during the fabrication process).

A notable result of the AGR-2 annealing testing was the comparison of caesium release fractions for UCO and UO<sub>2</sub> fuel. The <sup>134</sup>Cs release from the UCO fuel for all tests was  $\leq 6.2 \times 10^{-5}$  at 1600°C and  $\leq 6.7 \times 10^{-4}$  at 1800°C, indicating good retention at these extreme temperatures and very limited degradation of the SiC layers. In contrast, <sup>134</sup>Cs release from the AGR-2 UO<sub>2</sub> fuel was in the range of

approximately  $(0.2-1) \times 10^{-2}$  after 300 h at 1600°C and  $8.7 \times 10^{-2}$  after 150 h at 1700°C. This behaviour is demonstrated in Fig. 58 [108], which shows  $^{134}\text{Cs}$  release fractions for several of the AGR-2 annealing tests (note that not all AGR-2 tests are included in this figure). The caesium release from  $\text{UO}_2$  is significantly higher than UCO at 1600°C for similar test durations, and significantly higher after 150 h at 1700°C than UCO release after 300 h at 1800°C. Note that the UCO data in Fig. 58 also included fuel from Capsule 2, which had a time-average peak irradiation temperature  $\sim 250^\circ\text{C}$  higher than the  $\text{UO}_2$  fuel. Extensive detailed post-test examination of the  $\text{UO}_2$  particles indicated that the increase in caesium release throughout these tests was due to degradation of the SiC layers by reaction with  $\text{CO}(\text{g})$  generated in the particle. The result of this SiC degradation is a gradual decrease in caesium retention by the particles, with the effect accelerating with increasing test temperature [121].

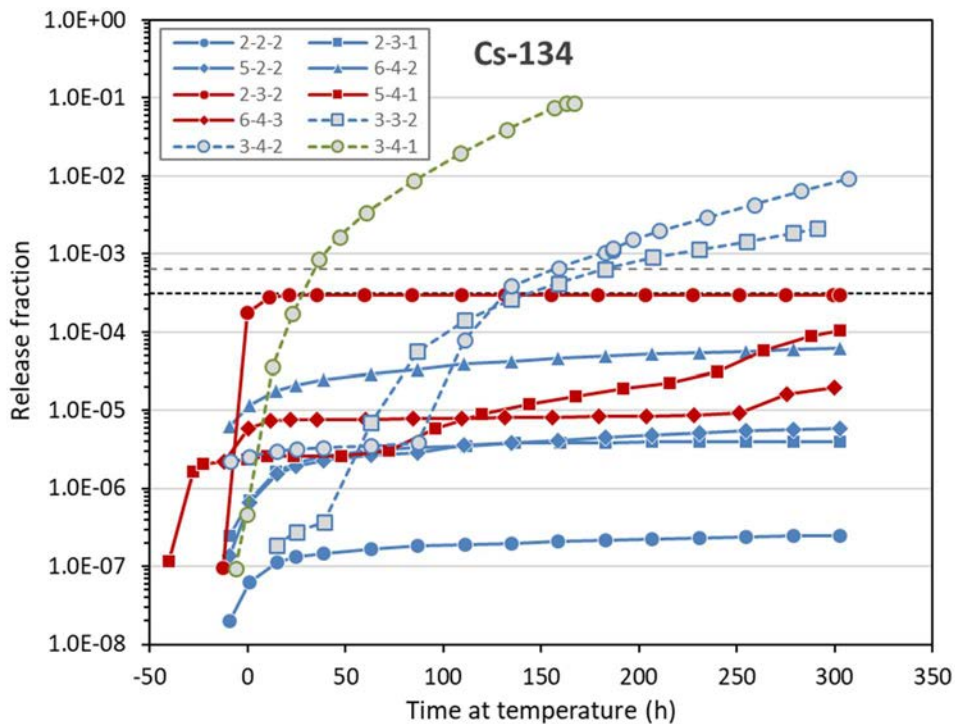


FIG. 58.  $^{134}\text{Cs}$  release from AGR-2 fuel compacts during isothermal annealing tests, plotted as a function of hold time at the target test temperature. Plot colour indicates test temperature: 1600°C (blue), 1700°C (green), or 1800°C (red).  $\text{UO}_2$  tests are indicated by dotted lines with grey-filled symbols (courtesy of INL).

Another notable result from the AGR-2 PIE and annealing tests was the impact of relatively high irradiation temperature on strontium and europium release from the fuel. The  $^{90}\text{Sr}$  release fractions from the fuel compacts in Capsules 3, 5, and 6 (time-average peak temperatures  $< 1210^\circ\text{C}$ ) were approximately  $10^{-4}$ . In contrast, Capsule 2 contained UCO fuel intentionally operated at high temperature (time-average peak fuel temperature of  $1360^\circ\text{C}$ ; see Table 40) and exhibited  $^{90}\text{Sr}$  release of  $\sim 10^{-2}$ , two orders of magnitude higher than the other capsules. Primarily due to this higher in-pile release (where most of the inventory released from the particles in-pile remains in the OPyC layer or matrix), the release of  $^{90}\text{Sr}$  from the Capsule 2 compacts after 300 h at 1600°C in post-irradiation annealing tests was appreciably higher than for the fuel in the other capsules [121]. This is demonstrated in Fig. 59, which shows  $^{90}\text{Sr}$  release fractions for several of the AGR-2 annealing tests (note that not all AGR-2 tests are included in this figure), where the higher-temperature Capsule 2 fuel is highlighted. Europium exhibited generally similar trends for in-pile and annealing test releases. Thus, an important result from the AGR-2 experiment is that while higher irradiation temperatures (up to a time-average peak of

1360°C) do not significantly impact the level of coating layer failures in UCO fuel, there is a notable increase in release of certain fission products from intact fuel particles. These impacts should be considered during HTGR core design and safety analyses.

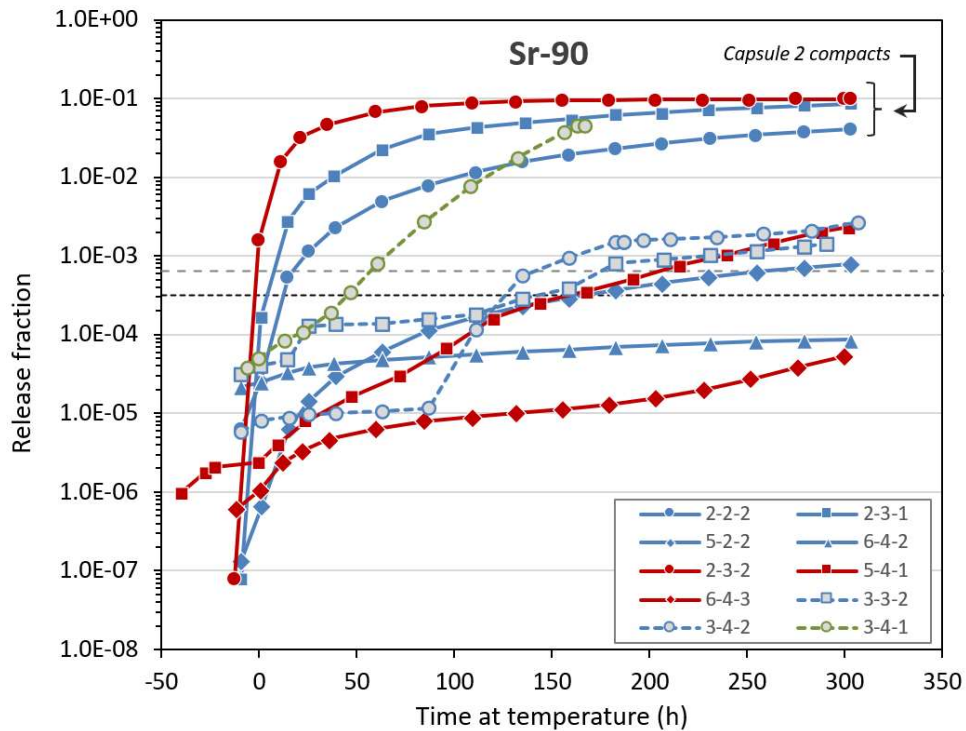
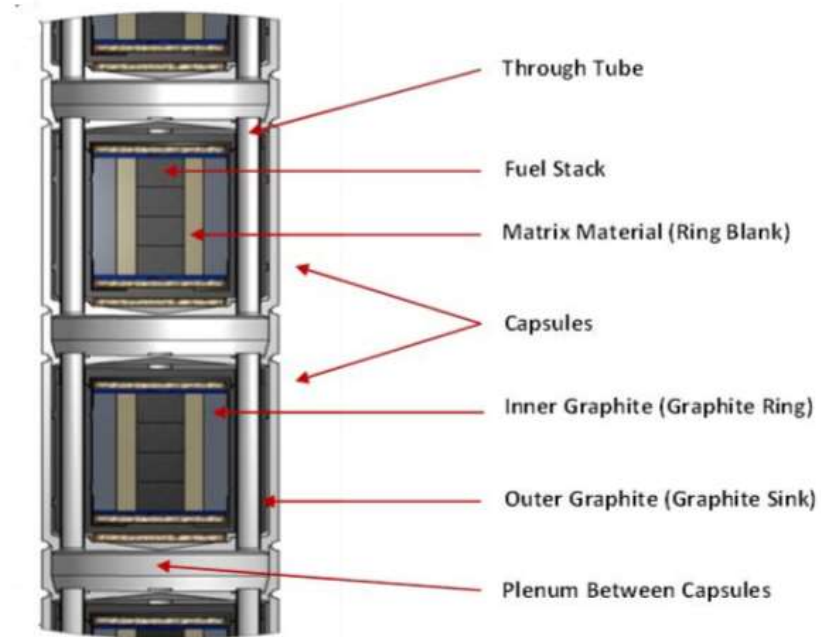


FIG. 59.  $^{90}\text{Sr}$  release from AGR-2 fuel compacts during isothermal annealing tests, plotted as a function of hold time at the target test temperature. Plot colour indicates test temperature: 1600°C (blue), 1700°C (green), or 1800°C (red).  $\text{UO}_2$  tests are indicated by dotted lines with grey-filled symbols (courtesy of EPRI).

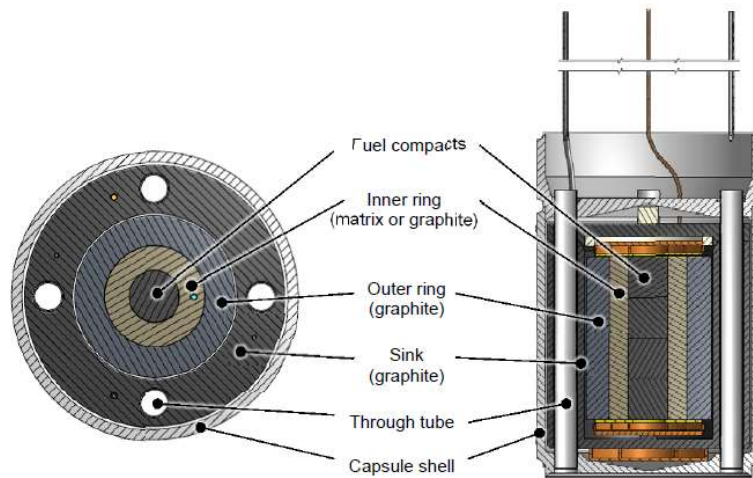
### 6.2.2.3. AGR-3/4 irradiation experiment

The AGR-3/4 irradiation experiment aimed to enhance fission product transport models and evaluate the impact of sweep gas impurities on fuel performance. This was achieved by measuring the spatial distributions of fission products within the fuel-compact matrix material and nuclear-grade graphite [137]. In addition to high-quality TRISO-coated fuel particles, each fuel compact in the experiment also contained DTF particles that would release fission products, with the objective of assessing fission product transport behaviour in core graphite and resinated graphite fuel matrix materials.

The test train comprised 12 distinct capsules, each equipped with independent control and monitoring systems (refer to Fig. 60 [137]). Within each capsule were four compacts, each measuring 12.51 mm in length and containing a mix of UCO TRISO-coated 'driver' fuel particles and UCO DTF fuel particles. The specified DTF fraction was set at  $1 \times 10^{-2}$  [137, 138].



(a)



(b)

FIG. 60. (a) Axial and (b) radial cross-sectional views of AGR-3/4 capsules (courtesy of INL).

In Fig. 61, an X-radiograph reveals a cross-sectional view along the axial centreline of an AGR-3/4 compact, with the kernels of the DTF particles highlighted by red dots [139]. The 20 DTF particles were positioned along the central axis of the compact, with some apparent clustering observed after the removal of the delivery tube. However, this minor clustering toward the bottom of the compact was not anticipated to impact the outcome of the irradiation test.

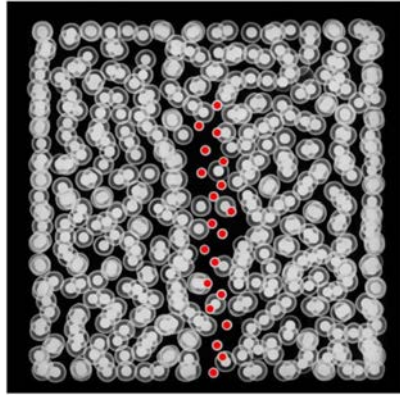


FIG. 61. X-ray radiograph of a 2.5-mm-thick section taken from the centre of an AGR-3/4 compact showing the location of 20 DTF particles (DTF kernels marked in red) (courtesy of INL).

Table 44 shows conditions for AGR-3/4 fuel test, taken from Ref. [140]. Note that with 20 DTF particles placed in each fuel compact, there were a total of 80 DTF particles in each capsule. The values in the final column of Table 44 are the best estimates for the number of DTF that failed based only on the results of fission gas measurements, but the uncertainty in this number was substantial. Thus, the deviation of these values from 80 are believed to be due to uncertainties in quantifying the particle failures based on fission gas measurements during irradiation and are not an accurate indication that some DTF particles did not fail during the irradiation. This conclusion is qualitatively supported by cross-section analysis of several irradiated AGR-3/4 compacts that included observations of the DTF particles [141].

TABLE 44. IRRADIATION DATA FOR EACH AGR-3/4 CAPSULE

Capsule	Burnup <sup>(1)</sup> (% FIMA)	Fast fluence <sup>(1)</sup> ( $\times 10^{25}$ n/m <sup>2</sup> )	Time-averaged peak temperature (°C)			End-of-life numbers of failed particles
			Fuel	Inner ring <sup>(2)</sup>	Outer ring <sup>(2)</sup>	
12	5.4	1.50	888	802	748	40
11	9.1	2.87	1280	1166	975	69
10	11.8	3.94	1249	1055	986	47
9	13.7	4.65	1083	884	721	90
8	14.5	5.08	1257	1048	945	78
7	15.0	5.27	1418	1203	1045	52
6	15.2	5.31	1133	912	728	47
5	14.9	5.19	1102	858	706	54
4	14.2	4.85	1084	882	727	76
3	12.6	4.22	1242	1050	976	96
2	10.1	3.21	1113	977	875	91
1	6.1	1.76	978	889	785	41

(1) Burnup and fast fluence are capsule-average values.

(2) Ring temperatures are the volume average for a 1-in. tall axial section centred on the fuel stack.

The R/B values for fission gases reached levels in the range of  $10^{-5}$  to  $10^{-3}$  early in the AGR-3/4 irradiation as DTF particles began to experience failure during the initial cycle. The hotter Capsule 7 exhibited a higher R/B value, reaching approximately  $3 \times 10^{-3}$  [142, 143]. To assess the impact of uncertainty in failure estimates on the release relationship with fuel temperature and decay constants,

regressions were conducted for three sets of data for the R/B per failed particle: best-estimate, maximum, and minimum failure estimates.

In Fig. 62, the R/B per failed particle for AGR-3/4 and its fitted function of reciprocal peak fuel temperature for  $^{85m}\text{Kr}$  are depicted using best-estimated (blue), maximum (red), and minimum (green) failure counts [144].

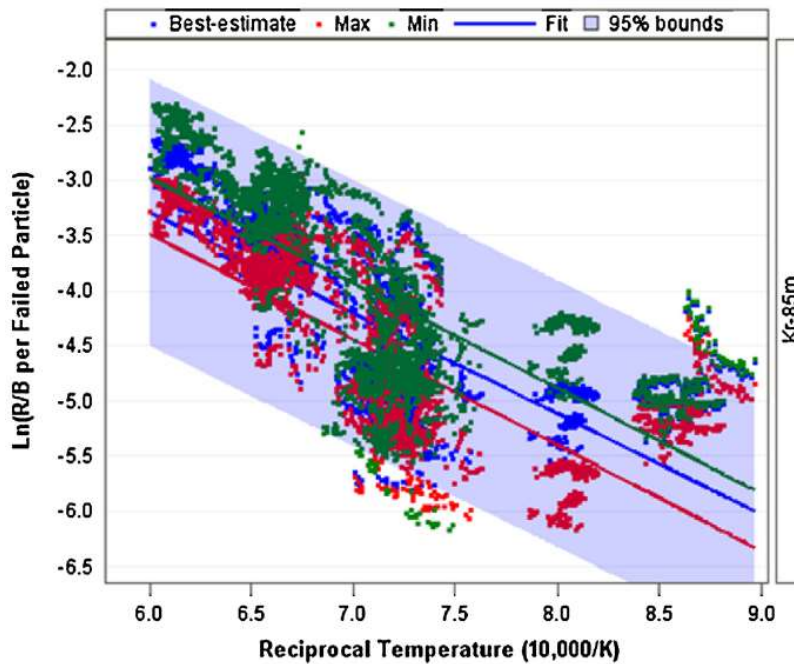


FIG. 62. AGR-3/4 R/B per failed particle and their fitted function of reciprocal peak fuel temperature for  $^{85m}\text{Kr}$  using best-estimated (blue), maximum (red) and minimum (green) failure counts (courtesy of INL).

Dimensional changes after the irradiation were also reported as summarized below (details are described in Ref. [145]):

- The diameter of all compacts was measured to decrease during irradiation, with relative changes ranging from approximately -0.5 to -2.0%;
- Most compacts showed the decrease in their length, while several compacts in Capsules 4, 5, and 7 showed a net increase in length. Relative changes ranged from approximately +0.5 to -0.9%.

PIEs on the irradiated compacts are currently ongoing, with specific objectives outlined as follows [145]:

- Assessing the migration of fission product in the matrix and graphite rings during irradiation;
- Determining the fractional inventory of fission products in fuel kernels and compact matrix at the end of irradiation;
- Investigating the transport of condensable and gaseous fission product from fuel kernels and compact matrix during heating in pure helium.

#### 6.2.2.4. AGR-5/6/7 irradiation experiment

The fourth and final irradiation in the AGR program, designated AGR-5/6/7, began in February 2018 and ended in July 2020. The AGR-5/6/7 irradiation test comprised both a fuel qualification test and a performance margin test for industrially produced UCO TRISO coated particle fuel developed under the AGR program. The primary aim of the AGR-5/6/7 irradiation experiment was to qualify UCO TRISO fuel fabricated using engineering-scale production equipment under various operating conditions, including conditions beyond normal operating parameters. Specific goals of the AGR-5/6/7 irradiation experiment were [105, 146, 147]:

- Irradiating reference design fuel containing low-enriched UCO TRISO fuel particles to support fuel qualification;
- Establishing operating margins for the fuel beyond normal operating conditions;
- Providing irradiated fuel performance data and irradiated fuel samples for PIE and safety assessments.

The AGR-5/6/7 experiment took place at the ATR at INL [146-148]. The test train included five separate capsules, each independently controlled and monitored (Fig. 63 [146]). The performance margin test, designated AGR-7, was located in the middle capsule, while the fuel qualification test, designated AGR-5/6, comprised the two bottom and two top capsules. The capsules were filled with fuel compacts containing UCO TRISO particles, using two different packing fractions (nominally 25 and 40%). Tables 45 – 47 provide properties of AGR-5/6/7 kernels (taken from Ref. [146]), particles (taken from Ref. [146, 149]) and compacts (taken from Ref. [146]), respectively.

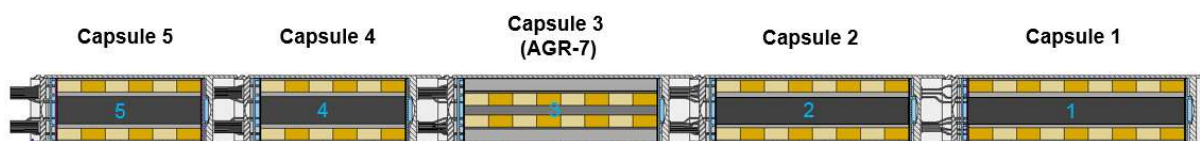


FIG. 63. Axial cross-sectional schematic of the AGR-5/6/7 test train (courtesy of INL).

TABLE 45. PROPERTIES FOR AGR-5/6/7 KERNELS

Property	Specified range for mean value	Actual mean value $\pm$ population standard deviation
Diameter ( $\mu\text{m}$ )	425 $\pm$ 10	425.78 $\pm$ 10.42
Density ( $\text{g}/\text{cm}^3$ )	Not specified	11.048 $\pm$ 0.044
U-235 enrichment (wt.%)	15.5 $\pm$ 0.1	15.477 $\pm$ 0.013
Carbon/uranium (atomic ratio)	0.40 $\pm$ 0.10	0.370 $\pm$ 0.000
Oxygen/uranium (atomic ratio)	1.50 $\pm$ 0.20	1.441 $\pm$ 0.004
(Carbon+oxygen)/uranium (atomic ratio)	Not specified	1.811 $\pm$ 0.004
Total uranium (wt.%)	Not specified	89.684 $\pm$ 0.040
Sulfur impurity (ppm-wt.)	Not specified	247 $\pm$ 14
Phosphorus impurity (ppm-wt.)	Not specified	25 $\pm$ 8

(a) Upper limit of the 95% confidence interval

TABLE 46. PROPERTIES FOR AGR-5/6/7 COATED PARTICLES

Property	Specified range for mean value	Actual mean value $\pm$ Population standard deviation
Buffer thickness ( $\mu\text{m}$ )	100 $\pm$ 15	100.37 $\pm$ 5.55
IPyC thickness ( $\mu\text{m}$ )	40 $\pm$ 4	39.24 $\pm$ 1.26
SiC thickness ( $\mu\text{m}$ )	35 $\pm$ 3	36.15 $\pm$ 0.65
OPyC thickness ( $\mu\text{m}$ )	40 $\pm$ 4	35.03 $\pm$ 1.99
Buffer density ( $\text{g}/\text{cm}^3$ )	1.05 $\pm$ 0.10	1.031 $\pm$ 0.022
IPyC density ( $\text{g}/\text{cm}^3$ )	1.90 $\pm$ 0.05	1.897 $\pm$ 0.010
SiC density ( $\text{g}/\text{cm}^3$ )	Not specified	3.195 $\pm$ 0.002
OPyC density [ $\text{g}/\text{cm}^3$ ]	1.90 $\pm$ 0.05	1.897 $\pm$ 0.004
IPyC optical anisotropy factor and diattenuation <sup>(a,b)</sup>	Not specified	1.031 $\pm$ 0.002 (0.0153 $\pm$ 0.0010)
OPyC optical anisotropy factor and diattenuation <sup>(a,b)</sup>	Not specified	1.021 $\pm$ 0.001 (0.0102 $\pm$ 0.0006)
IPyC optical anisotropy factor and diattenuation post compact anneal <sup>(a,b)</sup>	Not specified	1.0388 (0.0191 $\pm$ 0.0017)
OPyC optical anisotropy factor and diattenuation post compact anneal <sup>(a,b)</sup>	Not specified	1.0296 (0.0146 $\pm$ 0.0009)
SiC aspect ratio <sup>(c)</sup>	Not specified <sup>(d)</sup>	1.053 $\pm$ 0.009
Particle mass [mg]	Not specified	1.02

(a) The optical anisotropy factor (OAF) is defined as  $(1+N)/(1-N)$ .

(b) Values in parentheses are the diattenuation (N) that was measured with the Two-Modulator Generalized Ellipsometry Microscope (2-MGEM) developed at ORNL [112].

(c) Aspect ratio is defined as the ratio of maximum to minimum diameter of the coated particle and is measured on SiC-coated particles following burn back of the OPyC layer.

(d) Critical region is specified such that  $\leq 1\%$  of the particles must have an aspect ratio  $\geq 1.14$ .

TABLE 47. PROPERTIES FOR AGR-5/6/7 COMPACTS

Property	Specified range for mean value	Actual mean value $\pm$ Population standard deviation
Compact mass (g)		
Capsule 1	Not specified	6.676 $\pm$ 0.065
Capsule 2		6.182 $\pm$ 0.026
Capsule 3		6.187 $\pm$ 0.021
Capsule 4		6.100 $\pm$ 0.034
Capsule 5		6.603 $\pm$ 0.021
Mean uranium loading (g U/compact)		
Capsule 1	1.36 $\pm$ 0.10	1.362 $\pm$ 0.014
Capsule 2	0.90 $\pm$ 0.08	0.898 $\pm$ 0.004
Capsule 3	0.90 $\pm$ 0.08	0.898 $\pm$ 0.003
Capsule 4	0.90 $\pm$ 0.08	0.871 $\pm$ 0.005
Capsule 5	1.36 $\pm$ 0.10	1.346 $\pm$ 0.004
Diameter <sup>(a)</sup> (mm)		
Capsule 1	12.20 – 12.44	12.293 $\pm$ 0.007
Capsule 2		12.241 $\pm$ 0.007
Capsule 3		12.245 $\pm$ 0.006
Capsule 4		12.248 $\pm$ 0.006
Capsule 5		12.296 $\pm$ 0.006
Length <sup>(a)</sup> (mm)		
Capsule 1	24.40 – 25.30	24.947 $\pm$ 0.219
Capsule 2		24.991 $\pm$ 0.098
Capsule 3		25.000 $\pm$ 0.078
Capsule 4		24.770 $\pm$ 0.119

TABLE 47. PROPERTIES FOR AGR-5/6/7 COMPACTS

Property	Specified range for mean value	Actual mean value $\pm$ Population standard deviation
Capsule 5		24.675 $\pm$ 0.059
Estimated mean number of particles per compact <sup>(b)</sup>		
Capsule 1	Not specified	3434
Capsule 2		2265
Capsule 3		2265
Capsule 4		2197
Capsule 5		3392
Particle volume packing fraction (%)		
Capsule 1	40	38.4
Capsule 2	25	25.5
Capsule 3	25	25.5
Capsule 4	25	24.9
Capsule 5	40	38.4
Effective overall compact density <sup>(b)</sup> (g/cm <sup>3</sup> )		
Capsule 1	Not specified	2.26
Capsule 2		2.10
Capsule 3		2.10
Capsule 4		2.09
Capsule 5		2.25
Compact matrix density (g/cm <sup>3</sup> )		
Capsule 1	$\geq 1.65$	1.748 $\pm$ 0.007
Capsule 2		1.772 $\pm$ 0.005
Capsule 3		1.771 $\pm$ 0.005
Capsule 4		1.766 $\pm$ 0.006
Capsule 5		1.747 $\pm$ 0.007
Dispersed uranium fraction <sup>(c)</sup> (g leached U/g U in compact)		
Nominal 25% packing fraction	$\leq 1.0 \times 10^{-5}$	$\leq 2.95 \times 10^{-5}$ <sup>(d)</sup>
Nominal 40% packing fraction	$\leq 1.0 \times 10^{-5}$	$\leq 3.80 \times 10^{-5}$ <sup>(d)</sup>
Exposed kernel fraction <sup>(c)</sup> (kernel equivalent/particle count)		
Nominal 25% packing fraction	$\leq 5.0 \times 10^{-5}$	$\leq 1.48 \times 10^{-5}$
Nominal 40% packing fraction	$\leq 5.0 \times 10^{-5}$	$\leq 9.28 \times 10^{-5}$ <sup>(d)</sup>
Defective SiC coating fraction <sup>(c)</sup>		
Nominal 25% packing fraction	$\leq 1.0 \times 10^{-4}$	$\leq 1.22 \times 10^{-4}$ <sup>(d)</sup>
Nominal 40% packing fraction	$\leq 1.0 \times 10^{-4}$	$\leq 9.66 \times 10^{-5}$

- (a) Allowable range corresponding to upper and lower critical limits specified with no compacts exceeding the limits, which require 100% inspection of all compacts.
- (b) Calculated value derived from other characterized properties.
- (c) 95% confidence fraction.
- (d) The 95% confidence fraction exceeds the specification; despite the non-conformance, it was decided to accept the fuel as it is.

The irradiation period for the AGR-5/6/7 experiment spanned 361 EFPD, with time-average fuel temperatures calculated to range between 467 and 1231°C in the AGR-5/6 capsules and between 989 and 1432°C in the AGR-7 capsule. The AGR-5/6 irradiation temperatures aimed to cover the operational temperature range in a HTGR core, encompassing fuel temperatures substantially lower than those observed in previous AGR experiments. In contrast, the AGR-7 capsule experienced higher temperatures as part of the performance margin test, emphasizing the importance of time at temperature in TRISO fuel performance. The AGR-7 experiment was intentionally designed to induce some level of measurable fuel failure and/or fission product release, enabling the assessment of fuel performance beyond normal operating conditions and demonstrating the safety margin between typical operational conditions and temperatures where the fuel particle failure rate becomes unacceptable [146].

The burnup achieved in the experiment ranged from 5.7 to 15.3% FIMA on a compact-average basis. The range for fast neutron fluence was 1.62 to  $5.55 \times 10^{25}$  n/m<sup>2</sup> (E>0.18 MeV).

<sup>85m</sup>Kr R/B in the five AGR-5/6/7 capsules averaged  $3.5 \times 10^{-7}$  for the first five irradiation cycles (approximately half of the total experiment duration), with values slightly higher in Capsules 1 and 3 compared to the other capsules because of significantly higher fuel temperatures (Capsule 3) or relatively high fuel temperatures combined with a relatively high exposed kernel fraction in the 40% packing fraction fuel (Capsule 1) [148]. The R/B values were determined to be consistent with models based on the level of exposed kernel defects and dispersed uranium contamination in the fuel. The R/B values were similar to those of AGR-2 (which had similar exposed kernel defect and uranium contamination fractions) and appreciably higher than the values for AGR-1 (which had significantly lower exposed kernel defect and uranium contamination fractions).

After approximately 230 EFPD, there was a sharp increase in the fission gas release from Capsule 1, as well as smaller—but still quite significant—increases in fission gas release from the other capsules. The increase was apparently due to significant particle failure in Capsule 1, with the fission gas released in that capsule able to gradually diffuse into the other capsules because of the nature of the capsule and test train design. This effectively eliminated the ability to monitor fission gas release from Capsule 1 for the remainder of the experiment. In addition, the fission gas contamination that was able to diffuse from Capsule 1 severely complicated the measurement of fission gas release in the other capsules. As a result, the R/B data for capsules 2–5 was impacted and it was difficult to reliably estimate if particles failed in the other capsules during the remainder of the irradiation. It was determined that no particle failures occurred in capsules 4 and 5 (the furthest removed from Capsule 1 and therefore the least impacted by fission gas contamination), while the possibility of a small number of failures in capsules 2 and 3 could not be eliminated. The PIE of the capsules will help to clarify if any particle failures occurred.

The cause of particle failures in Capsule 1 remained unknown during the irradiation. Analysis of the internal components of this capsule during the initial stages of PIE indicated that the failures were caused by transition metal contamination (primarily Ni) from type N thermocouples embedded in the graphite holder adjacent to the fuel compacts [150]. The transport of Ni to the fuel compacts was caused by significant overheating of a region in the capsule, in which the fuel compacts and surrounding materials reached temperatures substantially above the intended range. This was determined to be due to a design flaw in the capsule not identified until after the irradiation was complete.

The PIE and annealing testing campaigns began in 2021 and 2022, respectively.

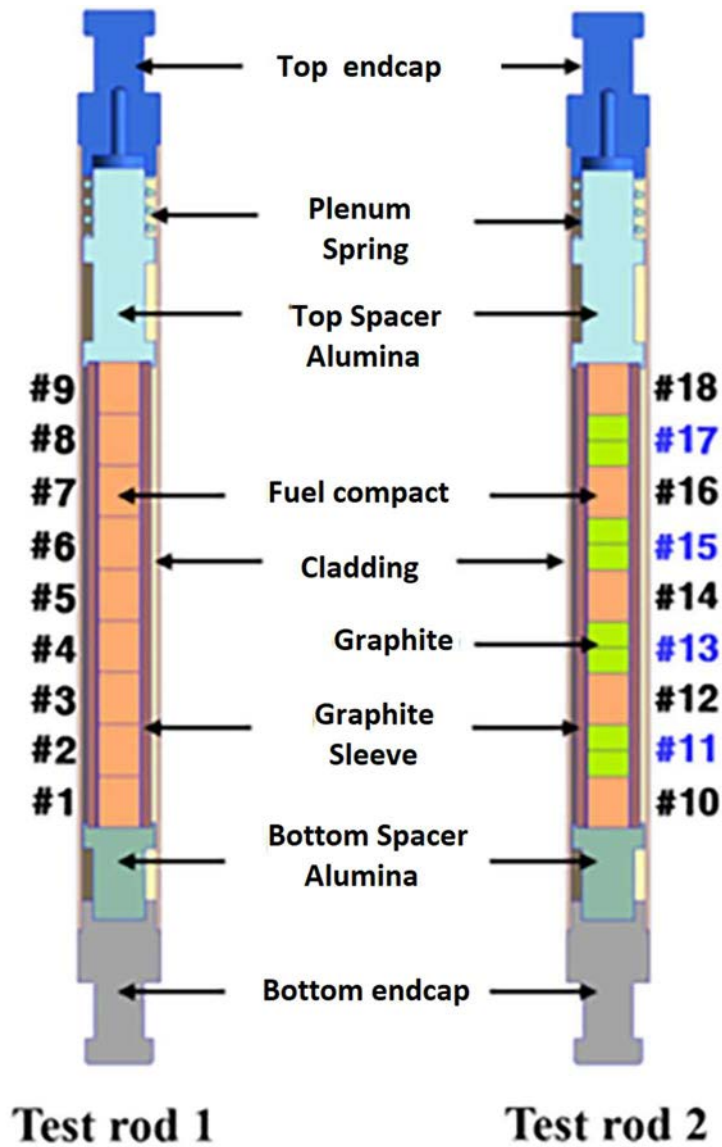
The primary objectives of the PIE and annealing testing for the AGR-5/6/7 experiment include:

- Evaluate and characterize the unexpected behaviour observed in Capsule 1;
- Determine the acceptability of fuel performance and behaviour under normal irradiation conditions, focusing on Capsules 2, 4, and 5, and integrate these findings with PIE results from earlier AGR irradiation;
- Assess the performance and characterize the behaviour of fuel under high irradiation temperatures in Capsule 3;
- Conduct post-irradiation high-temperature tests in helium to verify satisfactory fuel performance in accidents with conductive cooling;
- Conduct oxidation tests to characterize the behaviour of the fuel when exposed to air or moisture at normal and emergency temperatures [147].

#### *6.2.2.5. Korean irradiation programme*

The first irradiation test for TRISO-coated particle fuel to validate its application in a VHTR was conducted at the High-Flux Advanced Neutron Application Reactor (HANARO) of KAERI in 2014. Subsequently, a PIE of the irradiated TRISO-coated particle fuel was carried out. The irradiation apparatus comprised two test rods: one accommodating nine fuel compacts, and the other featuring five

compacts and eight graphite specimens positioned between the fuel compacts (Fig. 64 [151]). Table 48 presents the characteristics of kernels, particles, and compacts irradiated at HANARO, sourced from [151].



**Fuel compact: ## 1 - 9 (test rod 1)**  
**## 10, 12, 14, 16, 18 (test rod 2)**  
**Graphite: ## 11, 13, 15 17 (test rod 2)**

FIG. 64. Schematic layout of two kinds of test rods and position of compacts and graphite specimens in two test rods (courtesy of KAERI).

TABLE 48. CHARACTERISTICS OF TRISO-COATED PARTICLE FUEL AND GRAPHITE

Properties	Design value	Measured value	Remarks
<b>Kernel</b>			
Diameter ( $\mu\text{m}$ )	480 $\pm$ 30	483.50 $\pm$ 15	300-350 particles/batch (PSA*)
Density ( $\text{g}/\text{cm}^3$ )	10.65 $\pm$ 0.25	10.68 $\pm$ 0.023	6 g of sample weight (Pycnometer)
U-235 enrich. (wt.%)	4.5 $\pm$ 0.10	4.504 $\pm$ 0.004	Chemical analysis (TIMS)
O/U ratio	2.00 $\pm$ 0.01	2.003 $\pm$ 0.002	30 mg of sample weight (TG/DTA)
Total uranium (wt.%)	$\geq$ 87.0	88.13	calculated value
Sphericity (aspect ratio)	< 1.2	$\leq$ 1.04	Average
<b>Coated fuel particle</b>			
Buffer thickness ( $\mu\text{m}$ )	95 $\pm$ 45	102.91 $\pm$ 30	CG* (10 particles/batch)
Buffer density ( $\text{g}/\text{cm}^3$ )	1.00 $\pm$ 0.10	1.052 $\pm$ 0.002	X-ray (10 particles/batch)
IPyC thickness ( $\mu\text{m}$ )	40 $\pm$ 20	40.55 $\pm$ 0.53	CG* (10 particles/batch)
IPyC density ( $\text{g}/\text{cm}^3$ )	1.85 $\pm$ 0.20	1.91 $\pm$ 0.01	DC* (10 particles/batch)
Anisotropic index of IPyC	$\leq$ Ciso	1.0165 $\pm$ 0.003	OM* (10 particles/batch)
SiC thickness ( $\mu\text{m}$ )	35 $\pm$ 10	36.08 $\pm$ 0.15	CG* (10 particles/batch)
SiC density ( $\text{g}/\text{cm}^3$ )	$\geq$ iC d	3.182 $\pm$ 0.004	DC* (10 particles/batch)
OPyC thickness ( $\mu\text{m}$ )	40 $\pm$ 20	46.3 $\pm$ 3.05	CG* (10 particles/batch)
OPyC density ( $\text{g}/\text{cm}^3$ )	1.85 $\pm$ 0.20	1.88 $\pm$ 0.07	DC* (10 particles/batch)
Anisotropic index of OPyC	$\leq$ Ciso	1.019 $\pm$ 0.004	OM* (10 particles/batch)
Particle dia. (mm)	0.90 $\pm$ 0.10	0.95 $\pm$ 0.011	PSA* (10 particles/batch)
Average wt. (g)	0.001392	0.001392	
<b>Fuel compact</b>			
Compact mass (g)	1.050	1.028 $\pm$ 0.024	Average pf 14 compacts
Mean U loading (gU)	0.14	0.135	Average/compact
Diameter (mm)	8.0 $\pm$ 0.2	7.981 $\pm$ 0.006	Average of 14 compacts
Length (mm)	10.0 $\pm$ 0.5	9.995 $\pm$ 0.270	Average of 14 compacts
No. of compact	9(rod1)/5(rod2)	9(rod1)/5(rod2)	
Packing (volume) fraction (%)	20	19.703 $\pm$ 0.44	263 particles/compact
<b>Matrix graphite (M) &amp; structural graphite (G) specimen</b>			
Diameter (mm)	8.0 $\pm$ 0.2	7.976 $\pm$ 0.004	Average of 8 specimens
Length (mm)	5 $\pm$ 0.2	5.028 $\pm$ 0.008	Average of specimens
No. of specimens	8(rod2)	8(rod2)	
Density ( $\text{g}/\text{cm}^3$ )	1.7 $\pm$ 0.1	1.770 $\pm$ 0.004	Average of 8 specimens

\*CG; Ceramography, DC; Density column, PSA; Particle size analysis; OM; Optical microscopy.

The irradiation test was conducted under an inert gas atmosphere without sweep gas. Post-irradiation, the maximum power of the fuel compact was estimated to be approximately 56 W at 25 EFPD, and the maximum power of the particle reached 215.4 MW. The highest discharged burnup was evaluated to be around 37,344 MWd/tU (3.99% FIMA). The maximum fast fluence of the graphite specimen was estimated as  $2.99 \times 10^{20}$  n/cm<sup>2</sup> (E > 0.18 MeV).

Figure 65 shows dimensional changes of fuel compacts measured after the irradiation [151]. Figure 66 shows ceramographic, cross-sectional view of test compacts [151]. Figure 67 shows EPMS images of kernels [151].

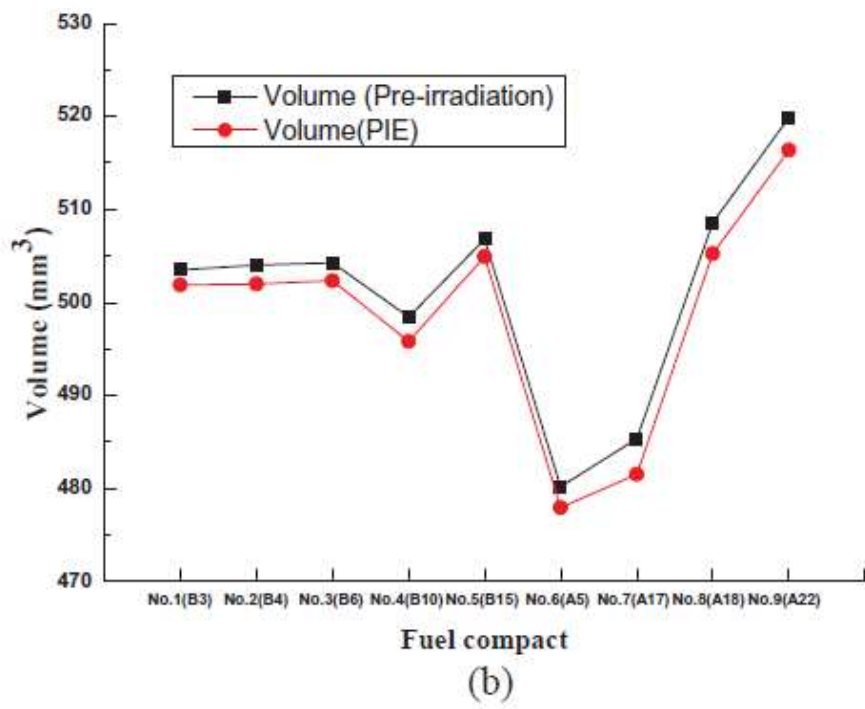
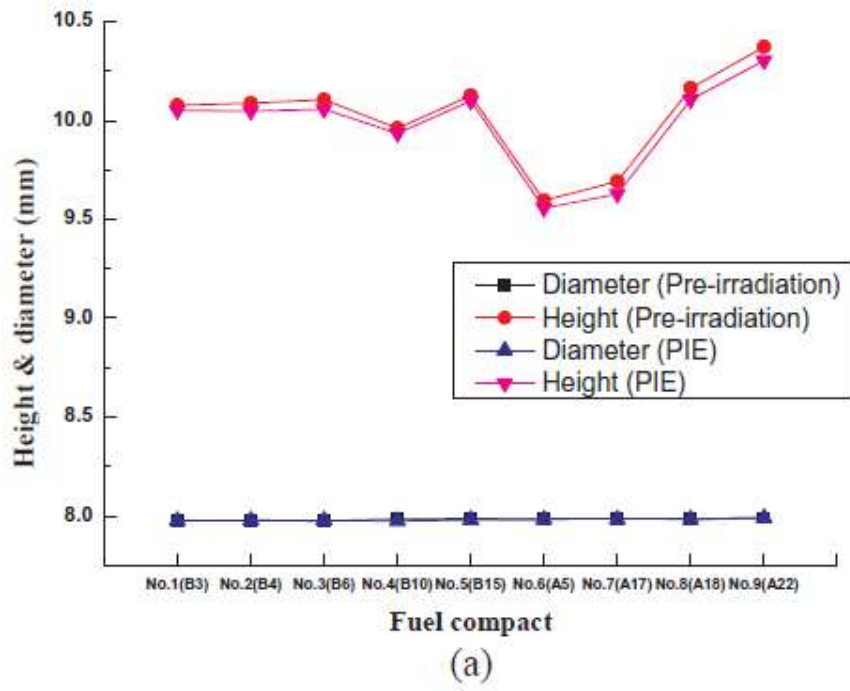
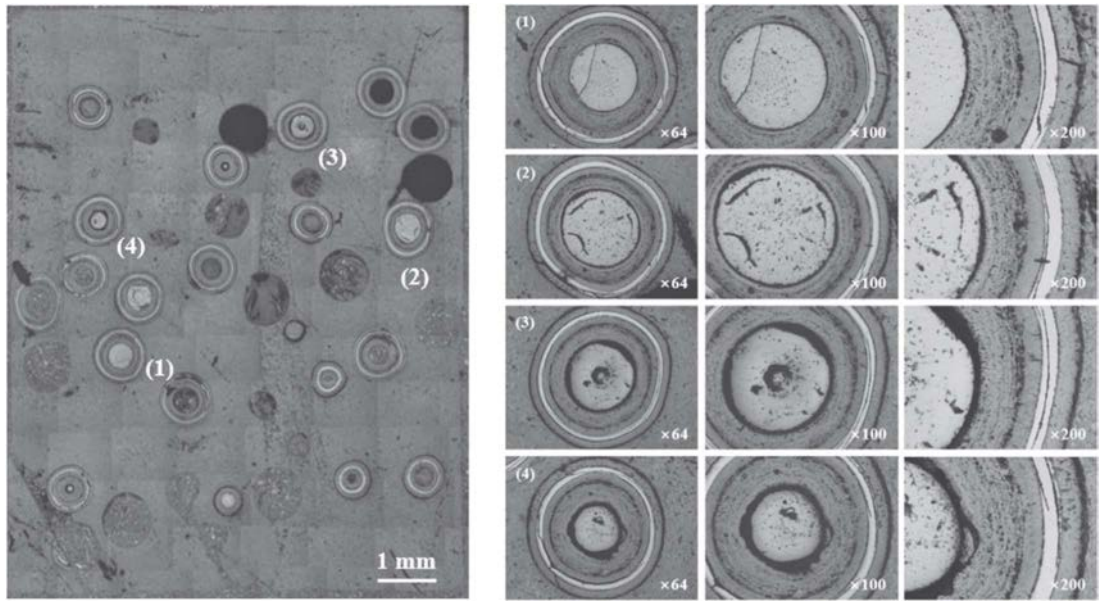


FIG. 65. Dimensional change of fuel compacts in test rod 1: (a) height and diameter and (b) volume (courtesy of KAERI).



(a)

(b)

FIG. 66. (a) Cross-section of one of fuel compacts in test rod 1, and (b) enlarged views of (1), (2), (3), and (4) in (a) (courtesy of KAERI).

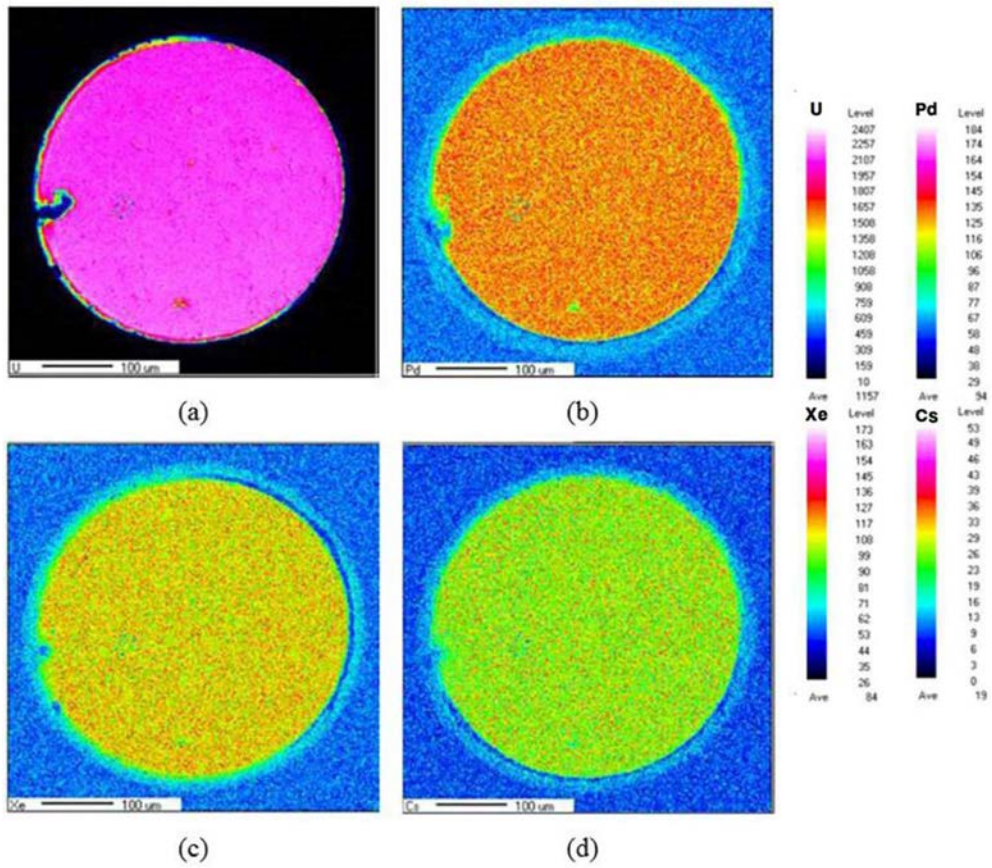


FIG.67. EPMA images from kernel: (a) U, (b) Pd, (c) Xe, and (d) Cs (courtesy of KAERI).

### 6.2.3. Loose TRISO particle fuels

Table 49 shows the status of irradiation test for loose TRISO fuel particles since 2000. There are three irradiation tests of loose coated particles; HTR-10 fuel particles in IVV-2M, PYCASSO-I and -II with  $ZrO_2$  and  $Al_2O_3$  surrogate kernel TRISO particles of CEA, JAEA, and KAERI in HFR.

### 6.2.4. Overall comparison of available irradiations in terms of fission gas release

Figure 69 [103] shows a comparison of the fractional release of  $^{85m}Kr$  between German spherical pebbles and US historic cylindrical compacts, where US cylindrical compacts show more release than German spherical pebbles. This difference was attributed in [103] mainly to as-manufactured fuel quality. The variation was attributed to differences in the microstructures of the PyC and SiC layers within the TRISO coating and the bonding of these layers. These distinctions were found to be associated with the utilization of different fabrication processes in Germany and the United States. The manufacturing process for coating layers in the US has been improved.

Figure 69 also shows additional mapping of measured fractional releases from AGR-1 and AGR-2 compacts to those from US historic compacts and German pebbles. Measurements from new US fuel compacts are comparable with those from German pebbles, which revealed the significance of improved coating quality.

In Fig. 69, the release from AGR-1 is quite low, indicating no particle failures during the irradiation. Taking into account high burnup operation of AGR-1 compacts, AGR-1 result of fractional release supported the good performance of UCO even at high burnup, with observations of no kernel migration, no evidence of CO attack of SiC, and no indication of severe SiC attack by noble metal or lanthanide fission products.

The measured releases from AGR-2 were higher than those from AGR-1, reflecting a higher number of defective particles and uranium contamination, and indicating the possibility of a particle failure.

Figure 69 [103] shows fractional releases per failed particle irradiated in AGR-3/4 and AGR-2 experiments and their best fit. The fractional releases per failed particle of both krypton and xenon isotopes were less than 1% and seemed not sensitive to fuel temperature below 1050°C. At fuel temperature greater than 1050°C, however, the fractional releases per failed particle increased exponentially with increasing fuel temperature. The clear downward trend of the fitted lines for AGR-2 and AGR-3/4 R/B data support the above observations.

## 6.3. REQUIREMENTS FOR FUTURE IRRADIATION TESTS

There exist a few datasets obtained from in-pile annealing tests with TRISO fuel. These tests include reactivity-initiated accident (RIA) tests at the Nuclear Safety Research Reactor (NSRR), Japan and control rod withdrawal tests at the operating HTGRs including HTR-10 [156]. Even though a small number of datasets are available as shown in Table 50 [3, 157, 158], these annealing tests may not be particularly relevant to the advanced TRISO fuel (e.g. FCM fuel) proposed for fluoride salt-cooled high-temperature reactors (FHRs) or LWRs, due to different fissile materials (e.g. UCO or UN kernels) contained in the FCM fuel and longer or shorter pulse widths in FHRs or LWRs. Combined irradiation using the HFIR MiniFuel and power pulse at the TREAT reactor could narrow these data gaps by clarifying the appropriate energy deposition limits and any concomitant energy deposition rate effects.

Irradiation tests with instrumentations are also recommended to reduce the time required for PIEs at hot cell facilities.

TABLE 49. IRRADIATIONS OF LOOSE COATED PARTICLE FUELS SINCE THE EARLY 2000s

Reactor	Experiment ID	Fuel type	Country	Irradiation time (FPDs)	Fast fluence ( $10^{21}$ n/cm <sup>2</sup> , E>0.18 MeV)	Burnup (%FIMA)	Irradiating temp. (°C)	Reference
IVV-2M (Russia)	(HTR-10 fuel particles)	Loose particle (capsule 1) (LEU UO <sub>2</sub> TRISO)	China	Jul. 2000 – Feb. 2003	-	-	1000±50	[70],[87],[89]
HFR (Petten, Netherlands)	PYCASSO-I	TRISO particles (surrogate kernel ZrO <sub>2</sub> , Al <sub>2</sub> O <sub>3</sub> )	France, Japan, Republic of Korea	18 Apr. 2008 – 26 Apr. 2009 (144)	1.93, 2.02, 1.87, 1.49	-	923 (ave. JAEA, KAERI) 988 (ave. CEA) 1058 (ave. JAEA, KAERI) 988 (ave. CEA)	[5],[152],[153]
HFR (Petten, Netherlands)	PYCASSO-II	TRISO particles (surrogate kernel ZrO <sub>2</sub> , Al <sub>2</sub> O <sub>3</sub> )	France, Japan, Republic of Korea	Jun. 2009 – Apr. 2010 (252)	3.66	-	855-1070 (ave.)	[5],[153–155]

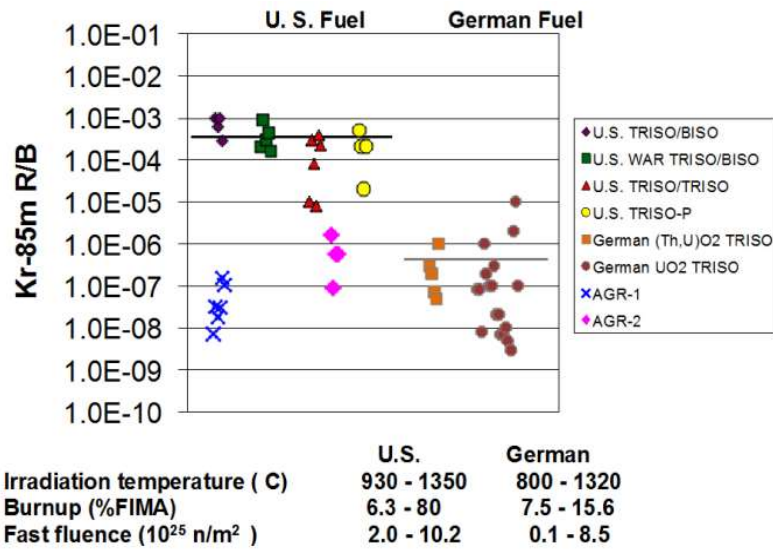


FIG. 68. End-of-life <sup>85m</sup>Kr fission gas release for AGR-1 and AGR-2 compared to historic performance in US and German TRISO fuel irradiations (courtesy of INL).

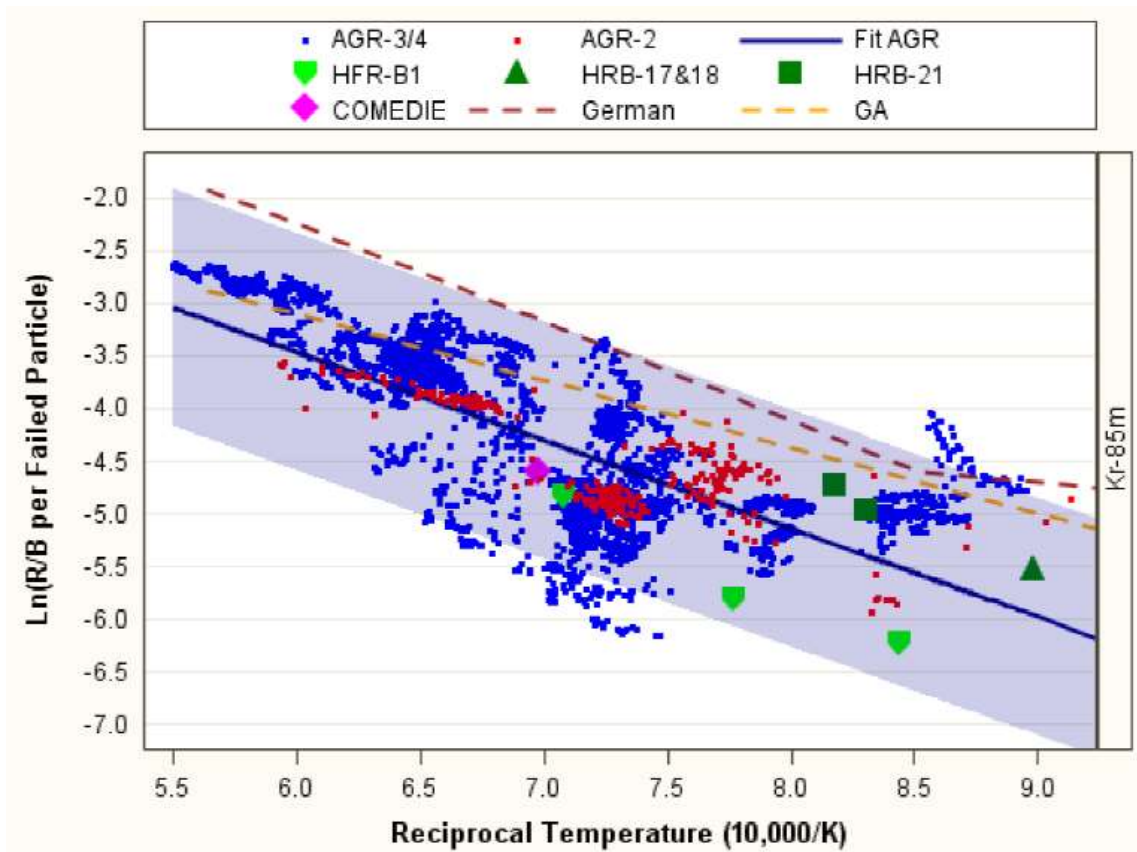


FIG. 69. Combined AGR fitted line and R/B per failed particle data for AGR irradiations, historical irradiations, and models (the blue shaded area is 95% bounds of the fitted line) (courtesy of INL).

TABLE 50. HISTORICAL TRANSIENT TESTS OF TRISO PARTICLE-BASED FUELS

Reference	Reactor	Kernel	Type of test	Energy deposition (J/g-fuel)	Pulse width (ms)	Failure
[157]	NSRR	UO <sub>2</sub>	Element and loose particle	500 – 2300	~5	> 1400 J/g-UO <sub>2</sub> (fuel) > 2300 J/g-UO <sub>2</sub> (matrix)
[158]	NSRR	UO <sub>2</sub>	Loose particle	500 – 1700	~5	> 1400 J/g-UO <sub>2</sub>
[3]	HYDRA	UO <sub>2</sub>	Element and loose particle	100 – 1700	1 – 2	> 1300 J/g-UO <sub>2</sub>
[3]	IGR	UO <sub>2</sub>	Element	> 10 000	7 – 30 000	Matrix

#### 6.4. SUMMARY AND DISCUSSION

A number of datasets that enable to support the good performance of TRISO particle fuel in either spherical pebbles or cylindrical compacts are available from the irradiation tests under normal operating conditions and from out-of-pile heating tests to simulate a LOCA.

The followings are expert observations for further study:

- Irradiation tests under normal operating conditions and post-irradiation annealing tests at elevated temperatures are needed for a better understanding of the fission product diffusion/transport in a UCO kernel, due to the presence of different phases (UO<sub>2</sub> and UC);
- Irradiation tests under normal operating conditions and post-irradiation annealing tests at elevated temperatures are necessary to understand the effect of SiC used for the matrix (replacing graphite) on the integrity of fuel elements and on the nuclear physics characteristics (e.g. neutron absorption/scattering effect);
- The effect of the use of uranium mononitride (UN) in the kernel on the fuel performance needs to be understood as the oxygen potential will change; in particular, an impact on the oxidation (and hence immobilization) of rare earth elements can be expected;
- Irradiation tests under normal operating conditions and accident conditions are necessary to support a licensing of advanced coated particle fuel for use in LWRs, MMRs, nuclear thermal propulsion, and molten salt-cooled reactors, since with the advanced coated particle fuel in non-HTGRs the temperature transients may occur much faster than in HTGR depressurized loss-of-forced cooling (DLOFC) accidents.

## 7. FUEL PERFORMANCE ASSESSMENTS

### 7.1. FISSION PRODUCTS

#### 7.1.1. Fission product yields and inventory

Figure 70 shows the inventory of some important elements contained in the TRISO particle fuel that achieved a burnup of 5.5% FIMA [4]. Zr and Mo constitute the larger inventory among metallic fission products, whereas Xe constitutes the larger inventory among gaseous fission products.

As burnup progresses, the concentration of Pu, in particular,  $^{239}\text{Pu}$ , and minor actinides increases. In nuclear data libraries, fission yields are given per nuclide (and per incident neutron energy). Therefore, the effective fission yield of a mixture of actinides (e.g. U, Pu, Am) depends on burnup.

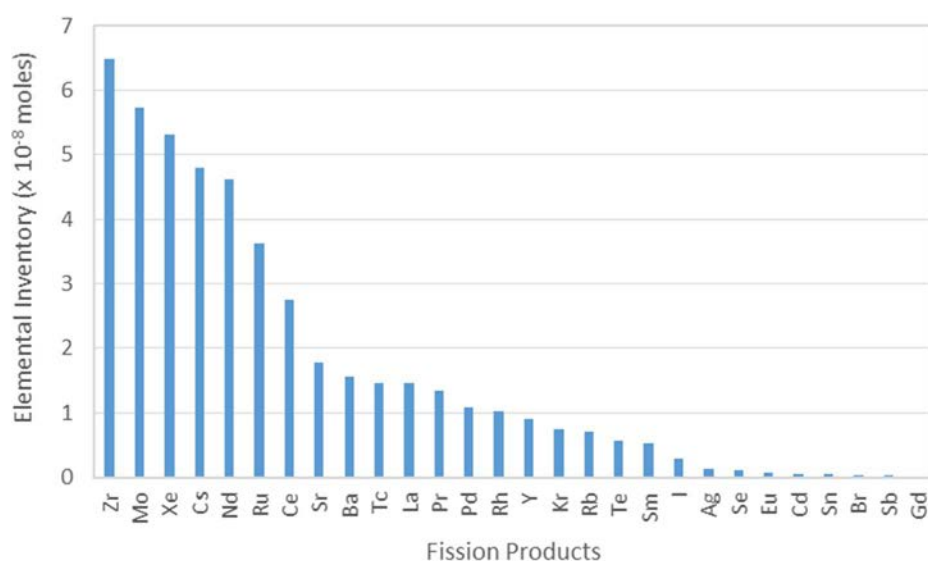


FIG.70. Elemental inventory in a TRISO particle fuel achieving a burnup of 5.5% FIMA (courtesy of IAEA).

#### 7.1.2. Fuel chemistry

The chemical state of fission product elements plays a crucial role in determining the physical properties of the fuel. This includes factors such as thermal conductivity, swelling, creep, and the onset of the melting point. Additionally, the chemical state influences the release behaviour of fission products from the fuel matrix. For instance, the relative volatility and mobility of these elements can be affected, leading to potential immobilization if rare earth elements oxidize and precipitate in the kernel as oxides. This influence is observed both under normal operating conditions and during transient events. Gaseous fission products (xenon and krypton) influence the thermal conductivity of a layer or the matrix (if it is released to the matrix in large amounts) and the gas pressure in the system.

Oxygen, liberated from uranium fissioning in  $\text{UO}_2$ , can combine with either the fission products or carbon from the PyC coatings to form CO and  $\text{CO}_2$  gases. It is important to identify the oxide compounds formed from the fission products in the fuel. The oxygen potential, which is dependent on the pressure of oxygen in the gas phase within the fuel, is the critical parameter determining which elements (i.e., fission products) form oxides.

The oxygen potential is determined by the amount of oxygen in the system and affected by the affinity of particular elements for it. In this closed system, fission products, carbon, and uranium engage in competition for oxygen. The oxygen potential of the system ultimately dictates which elements undergo oxidation and which remain unoxidized.

The oxygen potential,  $\mu_{O_2}$  is defined as:

$$\mu_{O_2} = RT \ln[P_{O_2}] \quad (10)$$

where

- $R$  is gas constant,
- $T$  is the absolute temperature,
- $P_{O_2}$  is oxygen partial pressure, atm.

In the reference case of pure  $UO_2$  fuel, the oxygen potential rises with increasing burnup, leading to the generation of carbon monoxide (CO). Unirradiated stoichiometric  $UO_2$  has an oxygen potential of roughly  $-400 \text{ kJ mol}^{-1}$  at nominal HTGR operating temperatures [4], see also Fig. 71 [159] for the oxygen potential of  $U^{4+}$  (i.e., stoichiometric fuel).

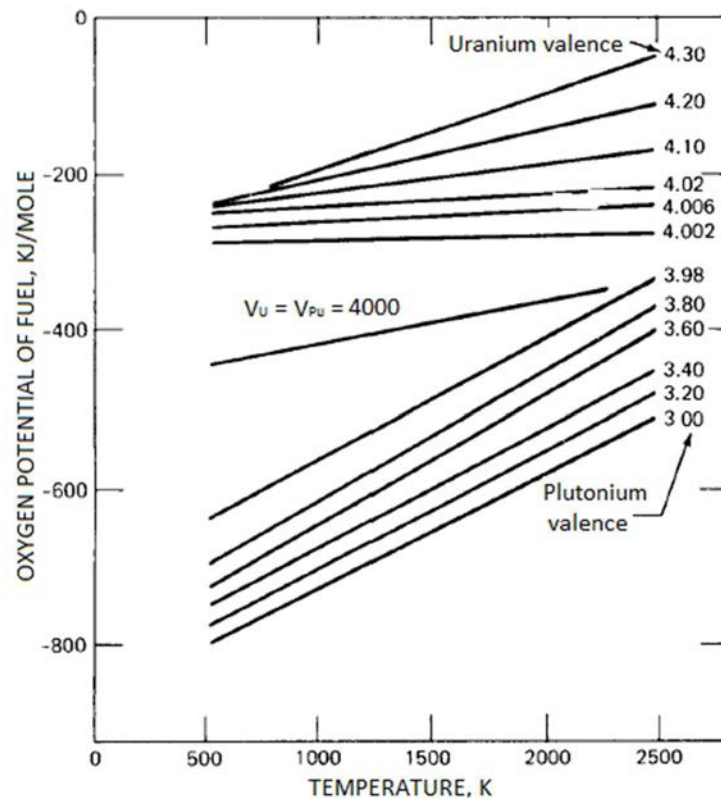


FIG. 71. Oxygen potentials of uranium and plutonium-based oxide fuels.

Depending on O/U ratio and the availability of excess C, two domains (see Fig. 72 [4]) were identified based on U-O-C phase diagram at 1573 K (1300°C):

- Triphasic domain with  $UC_2+UO_2+C$  when O/U ratio is  $< 2.0$ ;
- Diphasic domain with  $UO_{2+x}+C$  when O/U ratio is  $> 2.0$  [4].

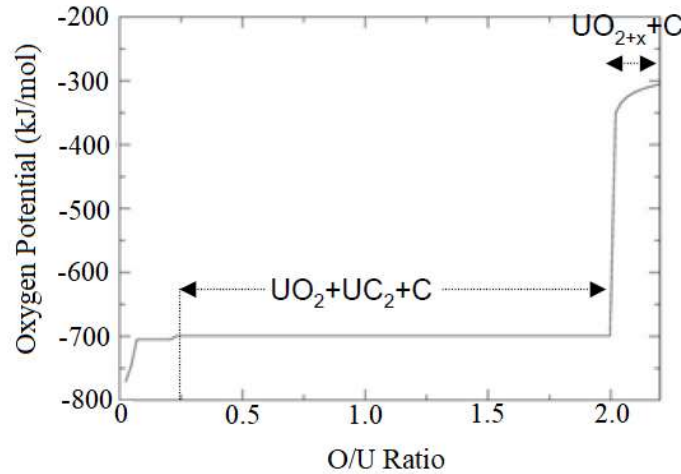


FIG. 72. Calculated oxygen potential as a function of O/U at 1300°C (courtesy of IAEA).

In an unirradiated fuel (or without taking into consideration of fission product affinity to oxygen), the oxygen potential,  $\mu_{O_2}$ , calculated at 1573 K (1300°C) is effectively reduced to  $-700$  kJ/mol in the triphasic domain  $UC_2+UO_2+C$  in comparison to the biphasic domain  $UO_{2+x}+C$  for which the calculated oxygen potential varied between  $-350$  and  $-300$  kJ/mol, as shown in Fig. 72. This shows that the oxygen affinity is increased in the UCO fuel in the triphasic domain (i.e., O/U ratio  $< 2$ ).

In general, the system is assumed to be in thermodynamic equilibrium. However, during and after irradiation, the chemistry of the fuel–fission product system changes due to:

- Fission product accumulation: The concentration of fission products progressively rises during irradiation.
- Chemical transformation: Post-irradiation, the chemical properties of fission products undergo modifications due to radioactive  $\beta$ -decay.
- Oxygen potential shift: The oxygen chemical potential of the fuel changes with burnup, influencing the production of fission products that, in turn, can alter the oxygen-to-metal ratio of the fuel.
- Temperature-induced element distribution: Axial and radial temperature gradients within the fuel impact the distribution of elements across phases, leading to compositional gradients through material transport facilitated by thermal diffusion processes.

Some elements, especially volatile fission products, may undergo significant migration, leading to a gradient in the oxygen chemical potential within the fuel. As a result, equilibrium calculations can only serve as a foundational reference for estimating the chemical state.

In an irradiated fuel, fission products start to accumulate and compete with U and C for oxygen. The free energy of formation of the fission product oxide per mole of oxygen,  $\Delta G_{FF}$ , is given by

$$\Delta G_{FF} [\text{kJ/mol of oxygen}] = RT \ln [P_{O_2} (\text{atm})] \quad (11)$$

Lewis illustrated the variation of  $\Delta G_{FF}$  graphically in Ref. [160].

At a temperature of 1500 K, PdO, with a standard Gibbs energy of formation of  $+50$  kJ/mol of  $O_2$ , results in a  $P_{O_2}$  (the partial pressure at which pure oxide and pure metal can coexist) of 50 atm. In contrast, for

La<sub>2</sub>O<sub>3</sub>, which has a standard Gibbs energy of formation of -960 kJ/mol of O<sub>2</sub>, the equilibrium  $P_{O_2}$  is approximately  $\sim 10^{-34}$  atm [159].

If the free energy of formation of the fission product oxide is smaller than the oxygen potential of the fuel, the element will be capable of removing oxygen from the fuel matrix and forming a stable oxide; otherwise, the fission product will exist as an element in the fuel under all reactor conditions. Accordingly, it is expected that palladium should always be found as a metal and lanthanum as an oxide, in a fuel with an oxygen potential of -400 kJ/mol. Based on the fuel oxygen potential and on the basis of numerous elemental analyses of irradiated LWR and fast breeder reactor fuels, the chemical state of the fission products in the LWR and fast breeder reactor fuel were identified [160] as:

- Fission gases and other volatile fission products: Kr, Xe, Br, and I;
- Fission products forming metallic precipitates: Mo, Tc, Ru, Rh, Pd, Ag, Cd, In, Sn, Sb, and Te;
- Fission products forming oxide precipitates: Rb, Cs, Ba, Zr, Nb, Mo, and Te;
- Fission products dissolved in the fuel matrix (i.e., solid solution): Sr, Zr, Nb, and the rare earths Y, La, Ce, Pr, Nd, Pm, and Sm.

The states of fission products are as follows [4]:

- Noble gases demonstrate almost insolubility in the fuel. Iodine, bromine (Br), and tellurium (Te) also exhibit high insolubility, while caesium (Cs) and barium (Ba) show only low solubility in hyper-stoichiometric fuel conditions. Solubility increases for zirconium (Zr), depending on temperature, and strontium (Sr). The rare earth (RE) elements, such as cerium (Ce), attain very high solubility.
- Fission-gases (Xe, Kr) have very low solubility in the fuel. The gases precipitate primarily as intragranular bubbles. These bubbles can grow by gas atom and vacancy absorption, and their mobility is limited.
- For the UO<sub>2</sub> kernel in TRISO fuel particles, both the fission rate and temperature play crucial roles in limiting bubble size and maintaining a substantial population of fission gas atoms in the fuel lattice through the resolution of gas from bubbles. Fission gases can migrate to grain boundaries through atomic or bubble diffusion, forming intergranular bubbles (porosities) where they can grow by the addition of gas and vacancies. Similar to intragranular bubbles, high levels of irradiation-induced resolution significantly restrict this growth (and the bubble-induced swelling of the kernel), while stresses in the particle may also limit the equilibrium bubble size. Once intergranular bubble growth becomes significant, causing interconnection of porosity, a path from within the kernel to the buffer is created, leading to fission gas release through a percolation mechanism.
- Regarding the behaviour of solid fission products, considerations include solubility, possible oxidation, and diffusion. In HTGR fuel particles with expected oxygen potentials, REs are highly soluble and are incorporated into the fuel lattice as stable oxides (REO<sub>2</sub> or RE<sub>2</sub>O<sub>3</sub>). In UCO fuel, as the UC<sub>2</sub>/UO<sub>2</sub> ratio increases, the mobility of the REs also increases since their trapping in the kernel in oxide form is reduced. Zirconium, Nb, and Sr exhibit significant solubility in UO<sub>2</sub>, with Zr showing more solubility at higher temperatures, and these elements are easily oxidized (ZrO<sub>2</sub>, Nb<sub>2</sub>O<sub>3</sub>, and SrO). Barium exists in the form of low-solubility BaO and can migrate to grain boundaries, forming separate complex ternary compounds with Sr, Zr, REs (and small amounts of Cs and Mo) of perovskite structure. Tellurium has low solubility and is challenging to oxidize; at grain boundaries, it forms intermetallic compounds (e.g. with Pd) and Cs<sub>2</sub>Te, and is significantly released from the kernel. Many other metallic elements also have relatively low solubility and are difficult to oxidize, except at high oxygen potentials. After segregation at grain boundaries, they form metallic inclusions, with noble metals (Mo, Ru, Rh, Tc, and Pd) constituting the main type of inclusion. Other inclusions like Te, Sn, or Ag, Cd are also observed. The size of inclusions is temperature-dependent. Pd and Ag, being highly volatile, are significantly released from the fuel kernel. Molybdenum exhibits complex behaviour due to its oxidation potential being close to the value corresponding to stoichiometric

fuel; a significant amount can be oxidized to  $\text{MoO}_2$  (limiting the increase of fuel stoichiometry), a low-solubility oxide. At high temperatures, Mo can form molybdate compounds with Cs or Ba. Caesium also has low solubility and might be oxidized to  $\text{Cs}_2\text{O}$  depending on the fuel temperature and oxygen potential, with this oxide having low solubility. Complex ternary phases can be formed at high temperatures and high burnups.

- In UCO-type fuel kernels, oxygen released during the fission process of  $\text{UO}_2$  initially oxidizes the carbide  $\text{UC}_2$  phase and then the RE fission products due to their high affinity for oxygen. When the  $\text{UC}_2$  phase is present in the kernel, the oxygen potential is maintained at a fixed value, approximately  $-700$  kJ/mol, at  $1573$  K ( $1300^\circ\text{C}$ ). Fission product elements with lower affinity for oxygen (Sr, Eu, Zr, Ba) exist as carbide compounds. As burnup increases, the  $\text{UC}_2$  phase in the kernel decreases, leading to an increase in the oxygen potential. This makes oxygen available to form.

The oxygen potential in a TRISO particle with  $\text{UO}_2$  kernel, calculated at  $1200$  K ( $927^\circ\text{C}$ ) and  $2000$  K ( $1727^\circ\text{C}$ ) for burnups up to  $8\%$  FIMA is shown in Ref. [161], and is illustrated in Fig. 73. The oxygen potential increases with burnup and temperature.

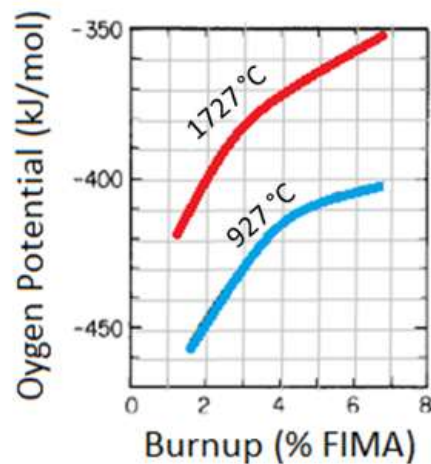


FIG. 73. Oxygen potential in the coated  $\text{UO}_2$  fuel particle calculated at  $1200$  K ( $927^\circ\text{C}$ ) and  $2000$  K ( $1727^\circ\text{C}$ ).

### 7.1.3. Chemical state and location of fission products in a TRISO particle fuel

#### 7.1.3.1. TRISO fuel with $\text{UO}_2$ kernel

Fission products in irradiated TRISO particle fuels with  $\text{UO}_2$  kernel were investigated using shielded EPMA, which is equipped with both wavelength dispersive X-ray spectrometer (WDX) and energy dispersive X-ray spectrometer (EDX), and by performing thermodynamic analysis [161]. The diameter of the fabricated kernels was  $\sim 600$   $\mu\text{m}$ ; the  $^{235}\text{U}$  enrichment was either  $4\%$  or  $8\%$ ; the thickness of buffer, IPyC, SiC and OPyC layers was on average  $60$   $\mu\text{m}$ ,  $30$   $\mu\text{m}$ ,  $26$   $\mu\text{m}$ ,  $45$   $\mu\text{m}$ , respectively; the density of the kernels, buffer, IPyC, SiC and OPyC layers was  $10.5$   $\text{g}/\text{cm}^3$ ,  $1.17$   $\text{g}/\text{cm}^3$ ,  $1.84$   $\text{g}/\text{cm}^3$ ,  $3.21$   $\text{g}/\text{cm}^3$ ,  $1.85$   $\text{g}/\text{cm}^3$ , respectively.

The particles were irradiated in the form of fuel compacts, achieving burnups up to  $5.16\%$  FIMA at time averaged irradiation temperatures of  $1613$  K ( $1340^\circ\text{C}$ ) –  $1783$  K ( $1510^\circ\text{C}$ ), though several samples achieved lower burnups or were exposed to lower time average irradiation temperatures [161]. The observations associated to the fission product composition, chemical state of the fission products and their locations in the fuel particle can be summarized as:

- In the UO<sub>2</sub> kernel: vastly, metallic precipitates consisting of molybdenum (Mo), technetium (Tc), ruthenium (Ru), rhodium (Rh) and palladium (Pd), were observed, though in some particles, the precipitates consisted of:
  - Mainly palladium and tellurium (Te);
  - Tin (Sn);
  - Predominantly molybdenum;
  - The Mo-Tc-Ru-Rh-Pd type reacting with silicon (Si).
- In the Pd-Te type precipitates, a minor presence of rhodium was noted. The Pd-Te precipitate exhibited a significantly higher concentration of palladium compared to the Mo-Tc-Ru-Rh-Pd precipitate, despite the Pd-Te precipitates being fewer in number than the Mo-Tc-Ru-Rh-Pd precipitates.
- The metallic precipitate containing Sn also included Mo, Pd and small amounts of Tc, Ru and Rh. (Mo, Tc, Ru, Rh, Pd) silicide precipitates were also observed when the precipitate predominantly consisted of Mo, though it was indicated [161] that the precipitates predominantly consisting of molybdenum were rarely observed in the experiment. The reason to observe (Mo, Tc, Ru, Rh, Pd) silicides was explained as the transfer of some silicon to the UO<sub>2</sub> kernel when the SiC layer of the particle is corroded by carbon monoxide due to the failure of the protective layer of the IPyC. It was also indicated [161] that oxide precipitates were not observed in the kernel.
- Within the coating layers, palladium tended to accumulate on the inner surface of the SiC layer, occasionally undergoing reactions with the SiC layer, particularly on the cold side of the particle. Unlike the fuel kernel, the other metal elements (i.e., Mo, Tc, Ru, Rh) accompanying Pd in the kernel were rarely observed in the coating, which is probably due to the high vapour pressure of Pd, compared to others.
- Tellurium was detected within the buffer PyC layer on the cold side of the particle, but unlike palladium, it did not permeate through the IPyC layer. Te did not form oxide but exists as elemental Te. Since the boiling point of Te is 1266 K (993°C), Te is present in the gas form at temperatures of interest to HTGR. Te was transferred into the buffer layer through the gas phase at irradiation temperatures (1340°C – 1510°C) and was condensed there during cooling. Although cerium and barium were often observed in the coating layers of the samples, they were detected more frequently in samples experienced higher irradiation temperatures (i.e., 1470–1510°C). Ce and Ba were observed in the buffer layer and at the interface of the IPyC-SiC layers in particles with both intact and breached IPyC layers. Ce and Ba were found in the coating layers in an oxide form.
- The coating layers did not show the presence of REs other than Ce, such as lanthanum and neodymium, as well as strontium, which belongs to the alkali earth metals along with barium. Based on the thermodynamic analysis, the vapour pressure of CeO<sub>2</sub> is the highest of the species containing the REs. Similarly, the vapour pressure of SrO is much lower than that of Ba-containing species, which may explain the absence of strontium.
- Caesium was observed in the buffer PyC and the IPyC layers, though the concentrations were low.
- Xenon was retained in the buffer PyC layer.

Another study was performed to investigate the TRISO particles for their potential for very high temperature performance and burnup. Five spherical pebbles of former German production with TRISO particles were irradiated, achieving a maximum burnup of 11% FIMA [93]. The central temperature of all pebbles was kept close to 1250°C and held constant during the entire irradiation. One of them was used for the analysis.

High porosity and a significant amount of metallic inclusions in the kernel were observed from particles at the centre of the fuel pebble (see Fig. 74 [93]), while particles at the periphery of the pebble fuel zone have porosities at the cold side of the kernel with hardly any visible grain boundaries and metallic islands, though a number of particles at the periphery of the pebble fuel zone have kernels with evenly distributed pores and metallic islands (see Fig. 74 [93]).

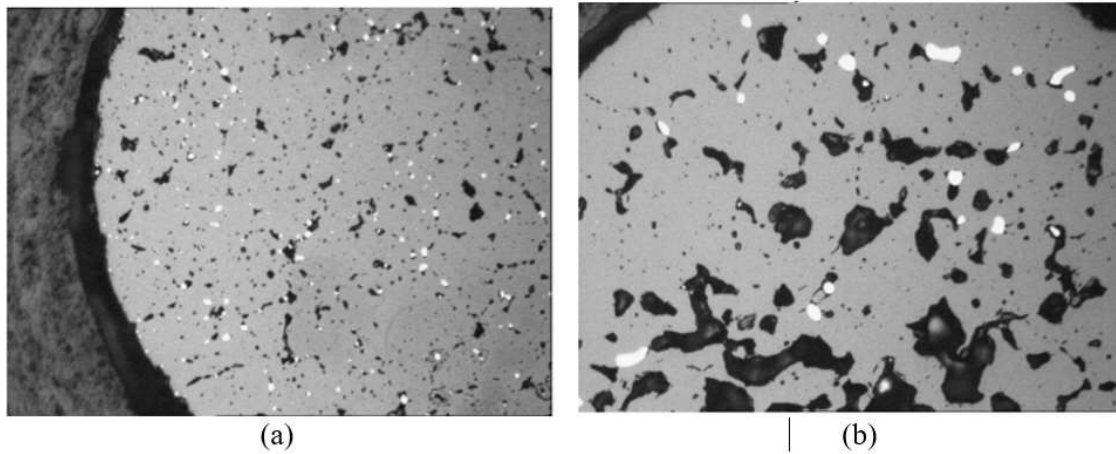


FIG. 74. Metallic islands and pores in the kernel in a particle at the: (a) periphery of the pebble, and (b) centre of the pebble (courtesy of INL).

Additionally, the followings were also reported in Ref. [93]:

- In the  $\text{UO}_2$  kernel:
  - Zirconium was retained in the kernel, which is expected, because Zr is a rather immobile fission product;
  - Ru and Mo are mainly contained in the metallic islands in the  $\text{UO}_2$  kernel;
  - Pd was observed both in the metallic islands in the kernel and as metallic element distributed in the kernel.
- In the coating layers:
  - Pd was observed at the interface of the IPyC-SiC layers and the inside of the SiC layer;
  - Cs and Xe were found accumulated in the buffer layer.

Table 51 shows the location of fission products of a TRISO particle with  $\text{UO}_2$  kernel that achieved burnups up to 11% FIMA.

TABLE 51. SUMMARY OF LOCATIONS OF FISSION PRODUCTS IN A TRISO PARTICLE WITH  $\text{UO}_2$  KERNEL

Location	Fission products and their chemical state
Kernel	<ul style="list-style-type: none"> <li>• Metallic precipitates consisting of Mo, Tc, Ru, Rh and Pd – Metallic</li> <li>• Pd-Te – Metallic</li> <li>• Metallic precipitate containing Sn, with Mo, Pd and small amounts of Tc, Ru and Rh – Metallic</li> <li>• (Mo, Tc, Ru, Rh, Pd) silicide precipitates, with high concentrations of Mo</li> </ul>
Coating Layers	<ul style="list-style-type: none"> <li>• Pd and Pd-Si at the inner surface of the SiC layer – Metallic and Silicide</li> <li>• Te in the buffer layer – Metallic</li> <li>• Ce and Ba in the buffer layer and at the interface of the IPyC-SiC layers (in particles with both intact and breached IPyC layers) – Oxide</li> <li>• Cs in the buffer and IPyC layers</li> <li>• Xe in the buffer layer</li> </ul>

### 7.1.3.2. TRISO fuel with UCO kernel

#### ***Fission product distribution in UCO kernel***

Fuel kernels from an unirradiated coated particle and irradiated AGR fuel compacts from the first and second irradiation test campaigns, achieving burnups of 17.4% FIMA (AGR-1; UCO kernel with an enrichment of 19.74%) and to 12.68% FIMA (AGR-2; UCO kernel with an enrichment of 14.03%), respectively, were examined (using scanning transmission electron microscopy (STEM), and energy dispersive spectroscopy (EDS) elemental mapping) to determine the microstructural and microchemical evolution of irradiated UCO fuel kernels, kernel-buffer interfaces, and recoil zones. In addition, the AGR-1 fuel was heated at 1600°C for 300 h, and a chemical analysis for fission products was performed to determine three-dimensional microstructure and chemical mapping (using atom probe tomography (APT) technique) at nanometric length scale [162]. The enrichment of the AGR-1 kernel (for the annealing test) was 19.74%, and the burnup achieved before the annealing test was 18.6% FIMA. Results can be summarized [162] as follows:

- The unirradiated fuel kernel exhibited a microstructure composed of several phases:  $\text{UO}_2$  and  $\text{UC}_2$  with UC platelets, as shown in Fig. 75 [162]. Higher-magnification transmission electron microscopy (TEM) images (see Fig. 76 [162]) of the structure of the fuel taken from the edge of the fuel kernel indicated some strain build-up, presumably due to a lattice mismatch between the  $\text{UC}_2$  and UC phases.
- The resultant microstructure after irradiation consisted of two primary phases, namely a ‘high-Z (atomic mass)’ UC(O) phase (rock salt;  $a=0.496$  nm) and a ‘low-Z’  $\text{UO}_2$  I phase (fluorite structure;  $a = 0.547$  nm).
- The  $\text{UO}_2$  phase contained multiple precipitates of the UC phase, whereas no precipitates of the  $\text{UO}_2$  phase were identified in the UC phase.
- The  $\text{UO}_2$  phase contained trace amounts of I, Nd, Pr, Cs, Ce, and Er, whereas the UC phase contained Zr, Mo, and/or Ru; the elements Zr, Mo, and Ru were often observed as segregated into separate UC grains. Figure 77 shows a higher-magnification STEM image and elemental spectral images from the fuel kernel centre, exhibiting the segregation of Mo and Zr (in the high-Z material) into distinct grains; arrows in the Xe spectral image in Fig. 77 indicates Xe bubbles.
- Xe bubbles were located exclusively in the Zr containing part of the UC phase (see also Fig. 77 [162]).
- APT analysis on a annealing tested AGR-1 particle also showed Xe preference for the UC phase, although Xe was also identified in the  $\text{UO}_2$  phase.
- Interaction between the fuel kernel and buffer layer was observed with sub-micron-sized carbon inclusions in the kernel side, and isolated UCO particles were located in the buffer layer.
- APT data revealed segregation of Te and Ag at the UO-UC interface.
- The APT results confirmed the selective association of specific elements for the two different U-phases. The UO phase showed presence of fission products such as Pd, Zr, Ce, Nd, Er, Dy, Gd, La, Y, Xe, and Sm, some of which are shown in Fig. 78, whereas the UC phase showed higher concentrations or segregation of Rh, Ru, Zr, Xe, Cd, In, Sn, Tc, and Nb, some of which are shown in Fig. 78 [162], Cs was not detected.
- The APT results confirmed the selective association of specific elements for the two different U-phases. The UO phase showed presence of fission products such as Pd, Zr, Ce, Nd, Er, Dy, Gd, La, Y, Xe, and Sm, some of which are shown in Fig. 78, whereas the UC phase showed higher concentrations or segregation of Rh, Ru, Zr, Xe, Cd, In, Sn, Tc, and Nb, some of which are shown in Fig. 78, Cs was not detected.

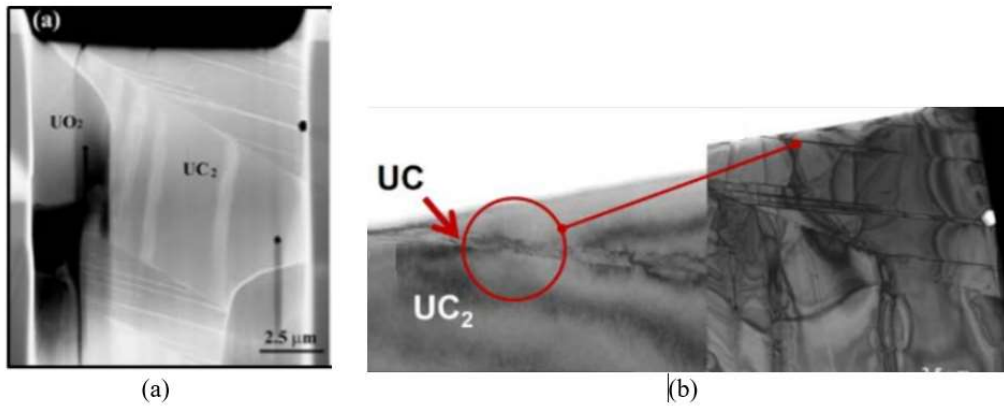


FIG. 75. Unirradiated UCO kernel: (a) STEM Z-contrast image, (b) TEM image for the identification of the UC phase (courtesy of INL).

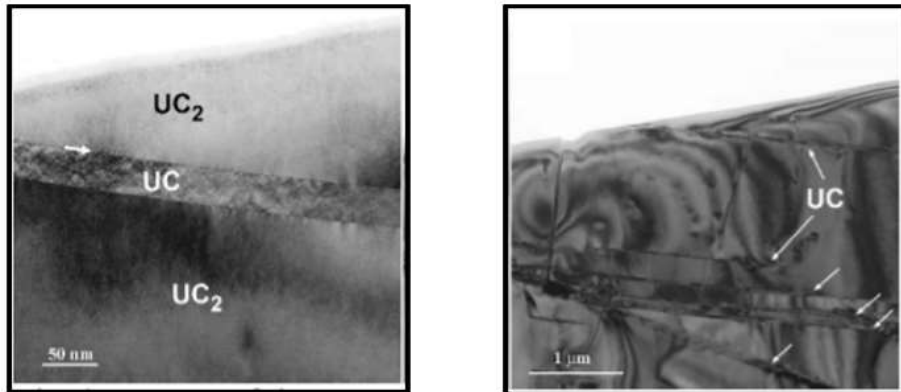


FIG. 76. Unirradiated UCO kernel TEM images of the structural arrangement of the UC platelets within the  $UC_2$  host phase (a) at a higher magnification, and (b) at a lower magnification (courtesy of INL).

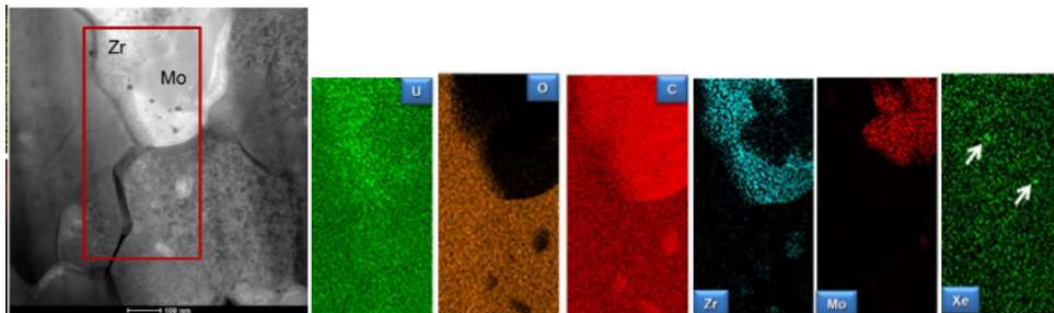


FIG. 77. Irradiated AGR-1 fuel: STEM Z-contrast image and corresponding spectral images for U, O, C, Zr, Mo and Xe from the indicated scan area of the fuel kernel (courtesy of INL).

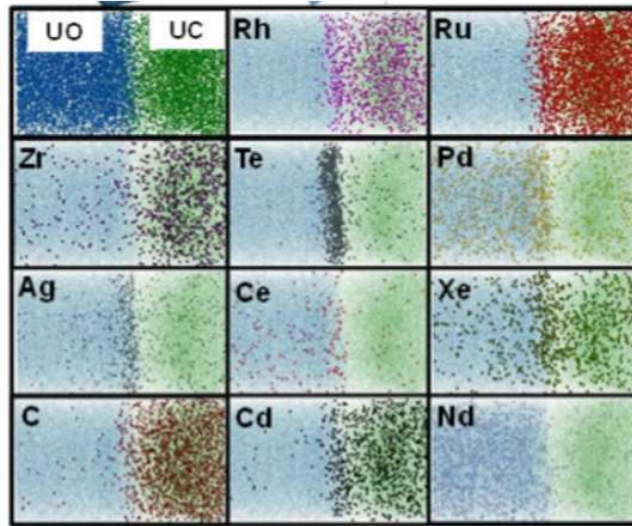


FIG. 78. 3-D APT data obtained at the centre of UCO Kernel; interfacial distribution of fission products Rh, Ru, Zr, Te, Pd, Ag, Ce, Xe, Cd, and Nd across the UO and UC phase (courtesy of INL).

Table 52 summarizes the location of the fission products in different phases of the UCO kernel.

TABLE 52. LOCATIONS OF FISSION PRODUCTS IN THE UCO KERNEL

Conditions	Fission products
Irradiated Fuel: AGR-1 and AGR-2	<ul style="list-style-type: none"> <li>• In UO<sub>2</sub> phase: trace amounts of I, Nd, Pr, Cs Ce, and Er</li> <li>• In UC phase: Zr, Mo, and/or Ru; Xe in the Zr-rich areas (in the UC phase)</li> </ul>
High temperature annealing tested (AGR- 1) fuel after irradiation	<ul style="list-style-type: none"> <li>• UO phase: Pd, Zr, Ce, Nd, Er, Dy, Gd, La, Y, Xe, and Sm</li> <li>• UC phase: Rh, Ru, Zr, Xe, Cd, In, Sn, Tc, and Nb</li> <li>• Te and Ag at the UO-UC interface</li> </ul>

Another study showed that I, Xe, and Cs mainly resided in the recoil zone (i.e., outer perimeter of the kernel, where the kernel interfaces with the buffer layer, and the thickness of the recoil zone is about 25  $\mu\text{m}$ ), buffer layer, and IPyC layer [163]. Elements of Zr, Ce, La, Sm, Pr, and Nd nearly all remained in the fuel kernel [163].

#### ***Fission product distribution in the coating layers***

Post-irradiation examination of fuel compacts irradiated under the AGR-1 test campaign focused on the fission product distribution in the coating layers, in particular in the SiC layer and at the IPyC-SiC interface, and revealed numerous clusters of fission product precipitates in the coating layers, as shown in Fig. 79 [107].

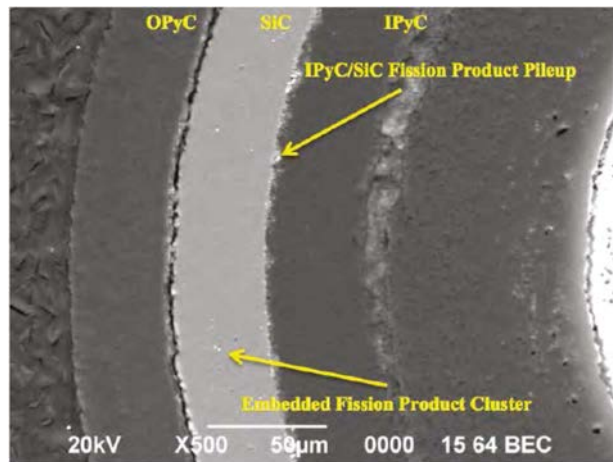


FIG. 79. Backscattered electron composition (BEC) micrograph of the TRISO layers (courtesy of INL).

Figure 80 shows the accumulation of fission products at the IPyC-SiC interface and fission product clusters embedded in the SiC layer [107]. The general observations can be summarized:

- Presence of Pd in SiC layer;
- Accumulation of Cs, Pd and U at the IPyC-SiC interface (see Fig. 80 [107]);
- Presence of Ba, Ce, Cs, Nd, O and Zr and also Ag, Cd, Pu, and Sr at the IPyC-SiC interface.

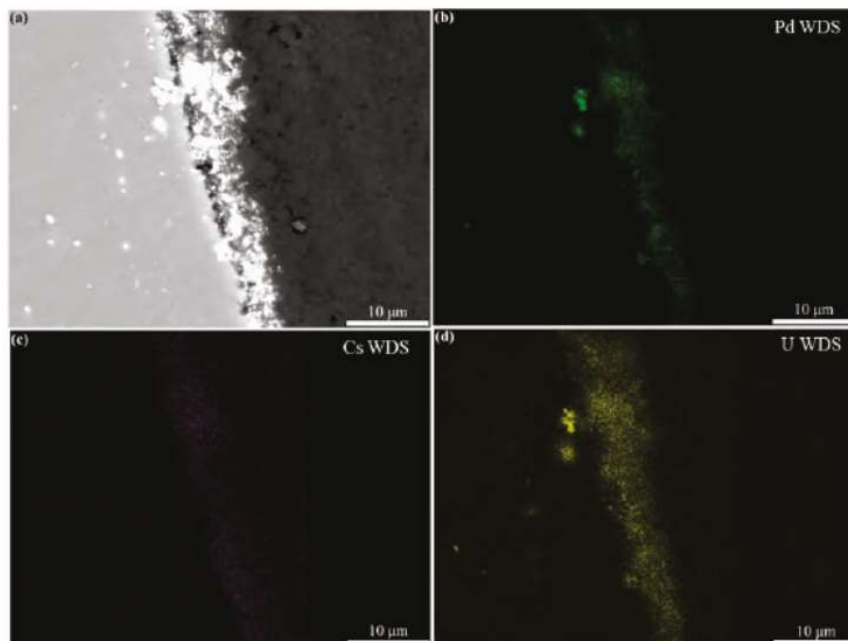


FIG. 80. Scanning electron microscopy (SEM) micrograph showing Pd/Cs/U rich fission product segment at the IPyC-SiC interface (courtesy of INL).

In the analysed particle, which represents the baseline fuel fabricated with coating conditions closely resembling the German reference fuel for the AGR-1 test campaign, U was consistently found in association with Pd in precipitates within the coating layers. Conversely, in another particle, fabricated under conditions similar to the baseline but with variations in the silicon carbide coating process (lower deposition temperature of 1425°C using argon and hydrogen gas for fluidization), uranium was identified separately in the SiC layer, and nearly all precipitates at the inner pyrolytic carbon-SiC interface contained uranium, as illustrated in Fig. 81 [107].

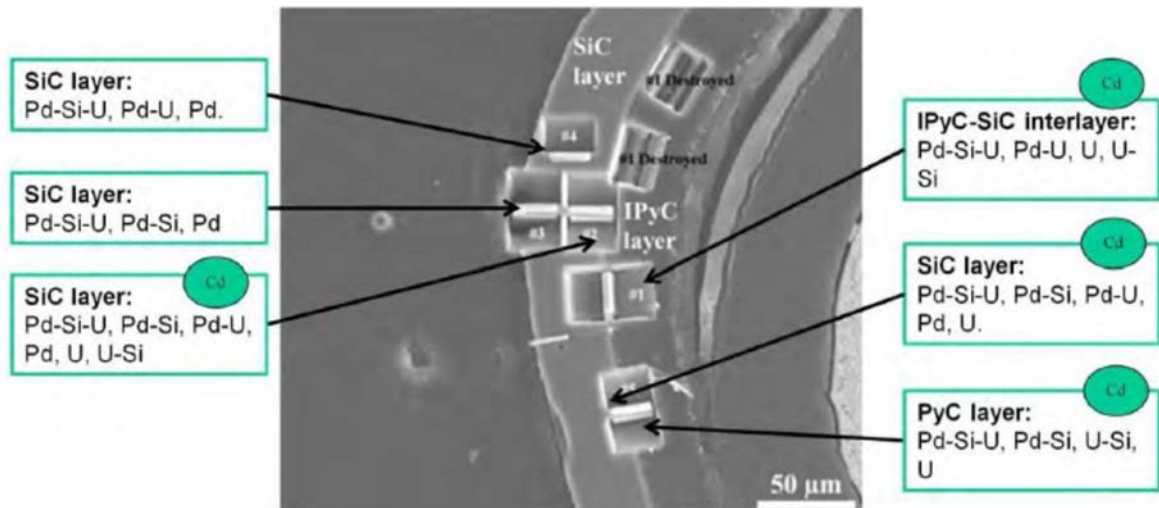


FIG.81. Fission product distribution in a particle with altered SiC coating conditions (courtesy of INL).

Ag was always found with Cd and Pd at grain boundaries and triple points (see Fig. 82 [164]).

Pd precipitates were found at stacking faults (see Fig. 83 [164]) in SiC layer; some black atoms (dark spots representing fission product atoms) are also observable in the SiC grain in Fig. 83 [164]. Phosphorus was also detected inside the SiC grain [165]; this may be due to Si (n, γ) reaction, which results in an unstable  $^{31}\text{Si}$  with a half-life time of 157 minutes, followed by stable phosphorus by β decay.

Figure 84 [107] shows the high-resolution STEM image of an area in the IPyC close to the IPyC-SiC interface. Single and multiphase precipitates can be identified. In addition, single phase precipitates in Fig. 85 [166] are indicated by red arrows. It looks like the selected area is carbon rich and Si is spotted at the low concentration of C. In the multiphase region, Si, Pd, U, Pu, Zr were identified [107]. Despite that the pattern for U and Zr in Fig. 84 looks like U and Zr formed a two-phase, it is indicated by arrows that those are single phases.

A TRISO particle from the compact irradiated in the ATR at INL to an average burnup of 17.42% FIMA, with a time-averaged, volume-averaged temperature of 1059°C and an average fast fluence of  $3.77 \times 10^{21}\text{n/cm}^2$  was used to investigate fission product behaviour in a TRISO particle [166]. X-ray tomography conducted on this particle revealed the presence of a crack extending through both the buffer layer and the IPyC layer. Additionally, localized degradation in the SiC layer was observed, specifically in a region connected to the tip of the IPyC crack. Notably, no crack was identified in the SiC layer. The initiation of the crack in the IPyC layer seems to be associated with the buffer layer pulling away from the IPyC layer as the buffer layer experienced shrinkage under irradiation. This crack is situated along a separation between the detached and attached portions of the buffer layer.

Close to the crack tip (see Fig. 85 for the SEM image), distribution and composition of fission products, and fission product transport mechanisms in the SiC layer of a TRISO particle exhibiting localized corrosion were investigated [166].

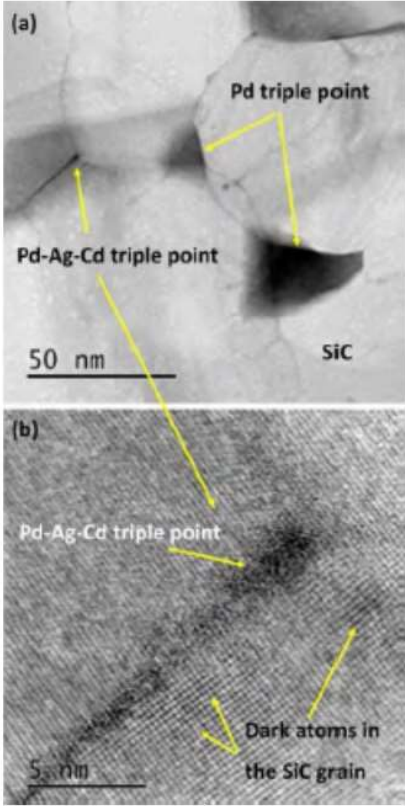


FIG. 82. Bright field STEM image (a) of a triple point containing Pd, Ag, and Cd, (b) high-Resolution bright field STEM image of the triple point containing Pd, Ag, and Cd with fission product atoms (dark spots) in the SiC grain (courtesy of INL).

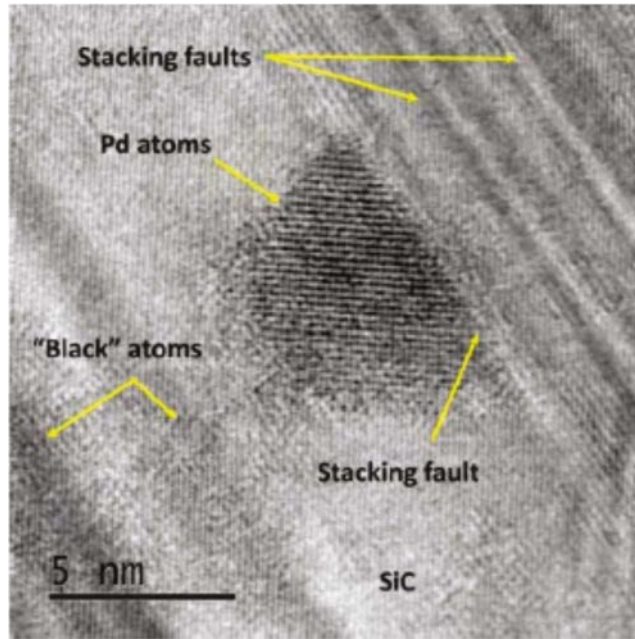


FIG. 83. High-resolution bright field STEM image of a Pd precipitate (courtesy of INL).

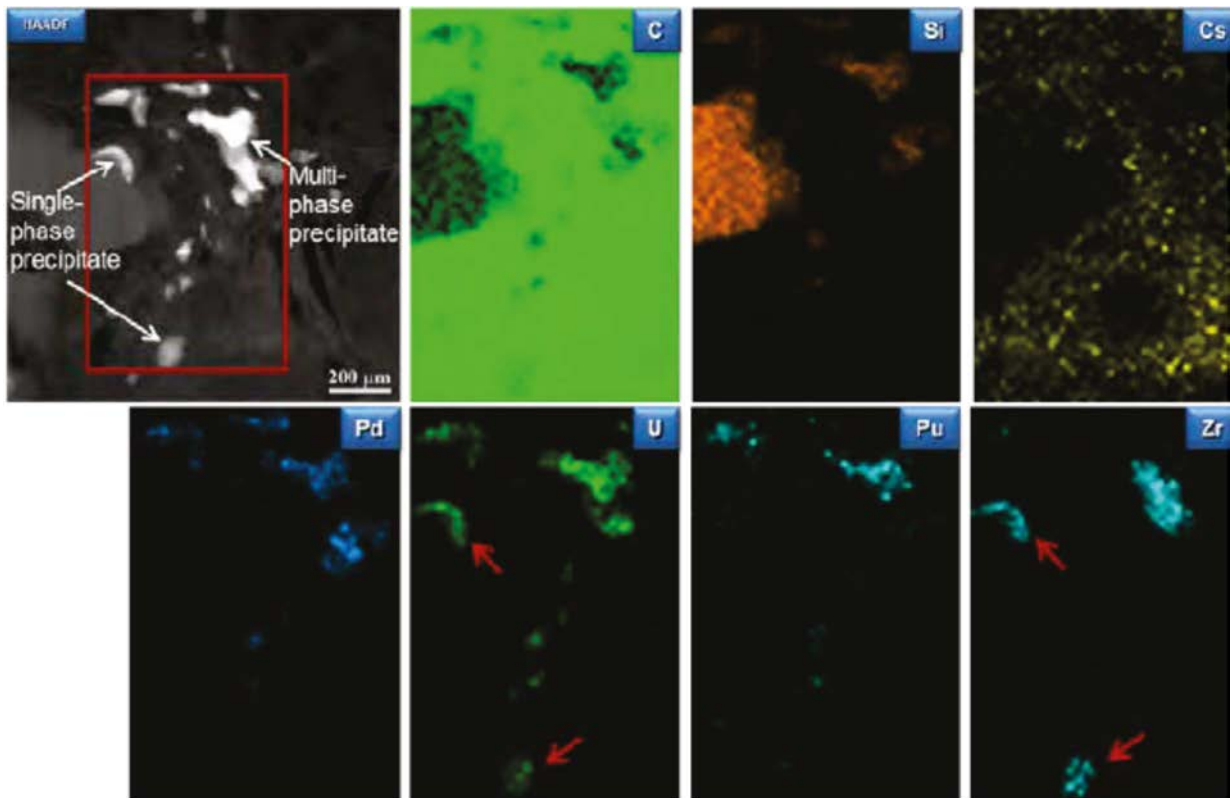


FIG. 84. High resolution STEM image and energy-dispersive X-ray spectroscopy (EDS) mapping in an area in the IPyC layer close to the IPyC-SiC interface (courtesy of INL).

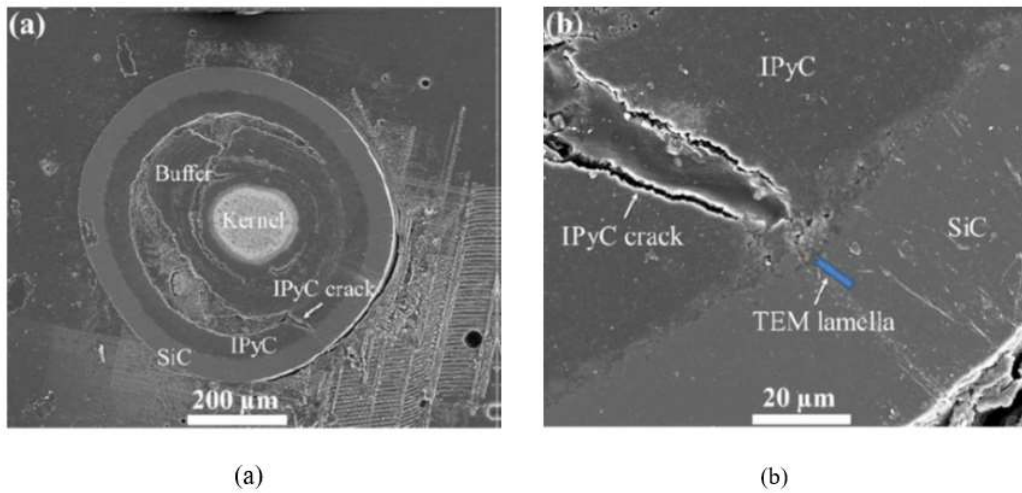


FIG. 85. SEM images showing the IPyC crack: (a) Lower magnification, (b) higher magnification (courtesy of INL).

SEM back-scattered electron and secondary electron images at the crack tip are represented in Fig. 86: locations 5 and 6 – no evident accumulation of fission products; location 7 – accumulated fission products in the IPyC layer right along an edge of the crack; location 8 – fission products accumulation at the IPyC-SiC interface right at the crack tip; location 9 – a slight accumulation of fission products in the region where delamination between IPyC and SiC occurred due to the IPyC crack; location 10 – locally corroded area within the SiC layer at the IPyC crack tip.

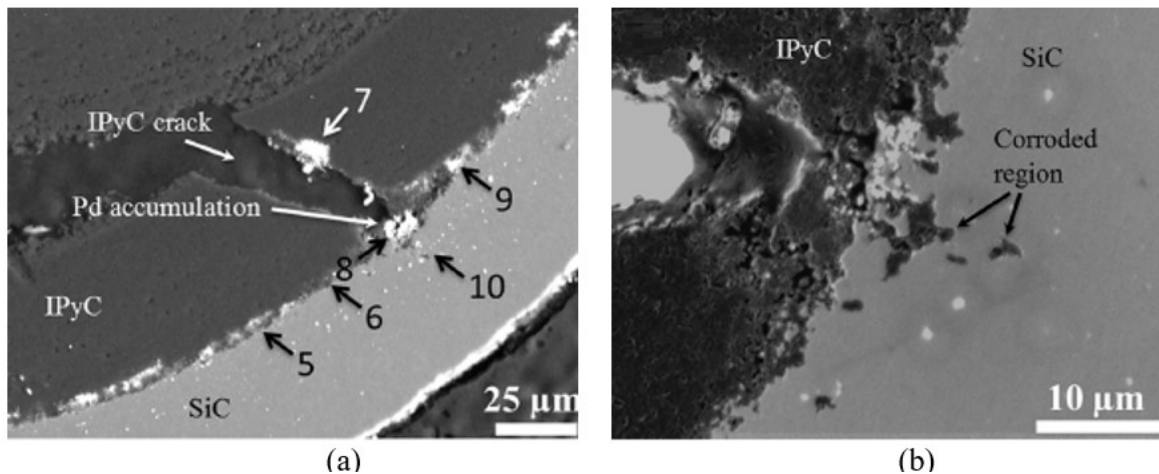


FIG. 86. SEM images of the crack tip: (a) Back scattered electron image, (b) secondary electron image (courtesy of INL).

### ***Fission products in the uncorroded areas***

Figure 87 [166] shows the precipitates at the SiC grain boundaries in the uncorroded SiC areas. Precipitates were mostly identified as Pd-Si-U, Pd-Si, Pd-U, and Pd. Ag and/or Cd were observed in some Pd and Pd-Si, though sometimes by themselves. Caesium (Cs) was not detected in any precipitates and no detectable amount of cerium (Ce) was observed. The analysis showed the following results [166]:

- Pd: Precipitates containing Pd-U, Pd-Si, and Pd-Si-U were all situated at the grain boundaries of SiC. Additionally, pure Pd precipitates were identified both at the grain boundaries and within the interiors of SiC grains. At ~1000°C, both lattice diffusion and grain boundary diffusion became significant for Pd transport in SiC. Neutron irradiation also significantly enhanced the diffusion due to high concentrations of defects generated in excess of thermal equilibrium values. Pd precipitates at SiC grain boundaries were larger than those inside SiC grains, possibly due to the faster grain boundary diffusion compared with lattice diffusion. At the IPyC-SiC interface, to some extent, Pd accumulated and reacted with SiC, creating Pd-Si. The Pd-Si created at the IPyC-SiC interface might have migrated into the SiC layer, explaining the presence of Pd-Si in the SiC layer. Otherwise, there were no notable chemical reactions observed between Pd and SiC in regions of the SiC layer that were distant from the crack in the IPyC layer of this specific TRISO particle. Additionally, no such reactions were noted in the SiC layers of TRISO particles originating from other compacts.
- Ag: The mechanisms for Ag migration were anticipated to be grain boundary diffusion, neutron enhanced diffusion, Pd-assisted transport, and vapour-phase migration. Cd was found with Ag. Since Cd is also a direct fission product, it can also be from Ag decay. Of the Ag/Cd containing precipitates, > 90% contained Pd, suggesting that Pd assisted Ag/Cd transport. Ag containing precipitates were predominantly observed at grain boundaries, indicating that grain boundary diffusion is one of the mechanisms for Ag transport. Another mechanism can be the intragranular transport of Ag enabled by Pd, based on the observation of an Ag-Pd-Cd precipitate at a stacking fault inside a SiC grain. The presence of intragranular Ag-Pd-Cd precipitate at a stacking fault indicates that the intragranular transport of Ag occurs via relatively high-energy pathways that have lower activation energy for diffusion because stacking faults have higher energies than lattice sites. With grain boundary diffusion being the predominant mechanism, the lattice diffusivity of Ag in SiC is expected to be low, though lattice diffusivity might be enhanced due to high concentrations of defects in the lattice created by neutron irradiations.
- U: U-containing precipitates, including Pd-Si-U and Pd-U, were identified in the uncorroded SiC areas. For the majority of Pd-Si-U and Pd-U precipitates (see Fig. 87), the U concentrations are much lower than the Pd concentrations. A significant density of uranium-rich precipitates was identified in the buffer layer, subsequently migrating deeper into the IPyC layer. Results from scanning transmission electron microscopy with energy-dispersive X-ray spectroscopy (STEM-EDS) on transmission electron microscope (TEM) lamellae extracted from the IPyC layer revealed that precipitates located several microns away from the IPyC-SiC interface were predominantly rich in uranium, while those in close proximity to the interface were mostly composed of Pd-Si or Pd-Si-U, with minor concentrations of uranium. At the IPyC-SiC interface, an increased concentration of U was observed due to the accumulation of U as its diffusion slows down while approaching to SiC layer, which is a much stronger barrier to U diffusion compared with carbon. At the IPyC-SiC interface, Pd and U react with SiC, creating Pd-Si-U precipitates that migrate toward the SiC layer or toward the IPyC layer, though some U is available to directly migrate into the SiC layer. Interestingly enough, Pd-U was not observed in the IPyC layer, possibly because U may not need assistance from Pd, if their diffusivities in carbon are at the same order.

Owing to constrained diffusivity, the count of Pd-Si-U or Pd-U precipitates diminishes as the distance from the IPyC-SiC interface increases. It was noted that all Pd-Si-U and Pd-U precipitates in the SiC layer were situated at grain boundaries, indicating that grain boundary diffusion serves as the primary mechanism. It is expected that the lattice diffusivity of U in SiC is significantly lower than the grain boundary diffusivity, and even with the assistance of Pd. Intermittently, Pd-U or even U in isolation was identified throughout the majority of the SiC layer, hinting at the possibility that the diffusivity of uranium in the SiC might be augmented by the particular irradiation conditions or certain microstructural features of the SiC.

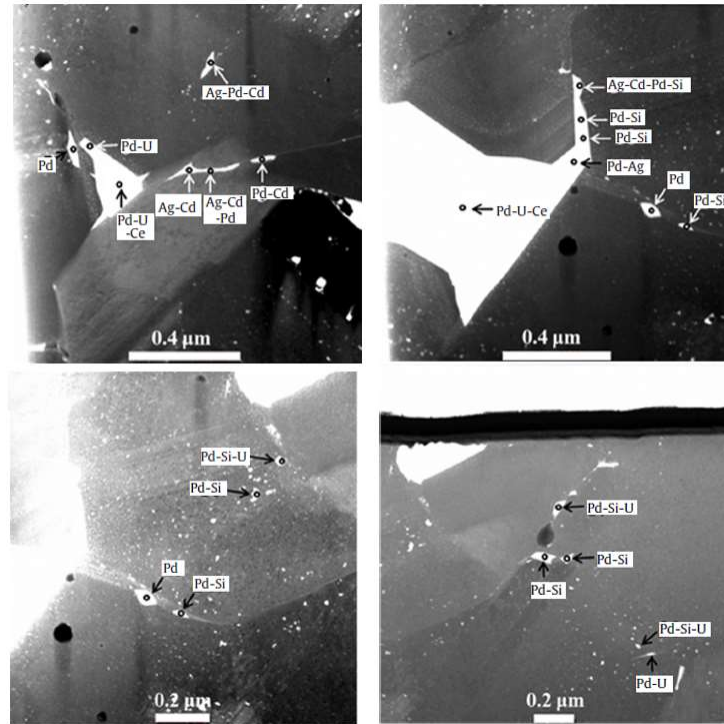


FIG. 87. Precipitates at SiC grain boundaries in unreacted SiC areas (courtesy of INL).

### ***Fission products in the corroded areas***

Apart from the primary crack in the IPyC layer and in the proximity of the IPyC-SiC interface, precipitates were typically small with a relatively sparse distribution, while a dense concentration of sizable precipitates was noted at or near the IPyC-SiC interface, particularly in the vicinity of the IPyC crack [167]. The crack across the buffer layer and the IPyC layer provided a pathway for fission products to migrate across the buffer and the IPyC layers and fission products distinctly accumulated at the IPyC-SiC interface where the crack terminated.

At the locations where fission products accumulated (locations 7 and 8 in Fig. 86), precipitates constituted of Pd-Si, Pd-Si-U, Pd-Si-Ce, Pd-Si-Ce-U. Only at one spot, the precipitate was composed of Pd-Ag. At the other locations, excluding corroded (location 10 in Fig. 86) and fission product accumulated locations (locations 7 and 8 in Fig. 86), precipitates constituted of Pd, Pd-Si, Pd-U, or Pd-Si-U at IPyC-SiC interface, whereas in the IPyC layer near the IPyC-SiC interface, precipitates comprised Pd-Si or Pd-Si-U, with no observations of Ag or Cd-containing precipitates.

In the corroded area (location 10 in Fig. 86) in the SiC layer close to the crack, C areas were detected with Pd silicides inside these areas (see Fig. 88(a)), indicating corrosion of SiC by Pd. For Pd chemical reaction with SiC, high Pd concentration is required. The elevated Pd concentrations in the SiC layer near the IPyC crack tip resulted from the localized accumulation of Pd, instigating the reaction with SiC. Silicides formed through this reaction migrated from the reaction site, leaving behind areas rich in carbon, and these silicides were observed in the IPyC layer. In C areas, the following precipitates were observed [167]:

- |               |             |             |                    |
|---------------|-------------|-------------|--------------------|
| — Pd          |             |             |                    |
| — Pd-Si;      | Pd-Ag;      | Pd-Cd       |                    |
| — Pd-Si-Ag;   | Pd-Si-U;    | Pd-Si-Cd;   | Pd-Si-Ce; Pd-Cd-Ag |
| — Pd-Si-Cd-U; | Pd-Si-U-Ce; | Pd-Si-Cd-Ag |                    |

— Pd-Si-Cd-U-Ce; Pd-Si-Ag-U-Ce; Pd-Si-Cd-Ag-U.

Xe was also observed (see Fig. 88(b)) in nano-cracks in the C areas in the SiC layer, indicating that nano-cracks provide short-range pathways for Xe transport. Cs was not detected in the corroded area, but it was hypothesized that the C areas in the SiC layer might have provided pathways for Cs transport, due to the nano-cracks, as indicated for Xe [167].

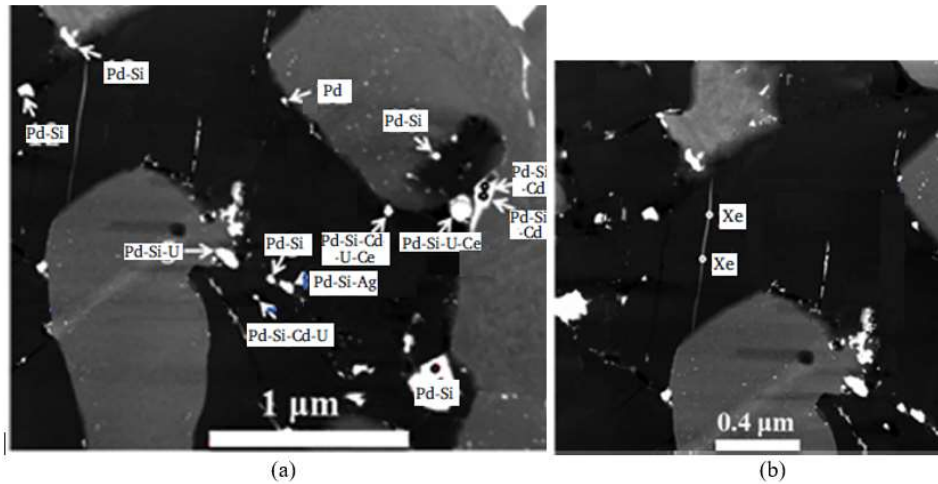


FIG. 88. Precipitates in the carbon areas in the SiC layer (a) Pd-Silicides, (b) Xe (courtesy of INL).

#### ***Fission product distribution in the coating layers after high temperature annealing tests***

High temperature annealing tests were performed at 1600°C, 1700°C and 1800°C on some of the compacts after having been irradiated in the ATR reactor (i.e., after the first irradiation campaign, AGR-1) [107].

Figure 89 [107] shows the backscattered electron composition (BEC) images of the TRISO layers in particles with low and high Ag retention after the annealing tests performed at 1600°C, 1700°C and 1800°C. The images clearly demonstrate the accumulation of fission products at the IPyC-SiC interface and fission product clusters distributed in the SiC layers. Low Ag retaining particles had a larger number density of fission product clusters distributed deeper into the SiC layer relative to high Ag retaining particles. It was noted that Pd-U based precipitates were predominant in the first 10 μm of the SiC layer and in the outer half of the SiC layer, Pd clusters with no detectable U were more frequently observed. In addition to Pd and U, other fission products, similar to those in the as-irradiated particles were observed. Unlike to ‘as-irradiated’ fuels (i.e., fuels that were irradiated but not exposed to high temperatures), fission products including Pd-U precipitates were U-rich following the annealing tests (i.e., irradiated fuels exposed to high temperatures). Particles exhibiting low Ag retention displayed an augmented presence of U in substantial clusters within the SiC layer, accompanied by a relative reduction in Pd at the IPyC-SiC interface.

Under the high temperature conditions corresponding to those at the high temperature annealing tests, U is liberated from the kernel, and migrates into the IPyC layer, and segregates at the IPyC-SiC interface. An increase in temperature results in higher number density of fission products in the SiC layer, as noted by large bright spots in the inner half of the SiC layer in Fig. 89 [107]. In the case of annealing test at 1800°C, a large number density of fission products in SiC layer (in the half of the layer close to the IPyC-SiC interface) was observed though this seemed not to lead to significant degradation of the SiC layer, as the IPyC-SiC interface remained intact [8]. The large U-rich fission product precipitates in the

half (close to the IPyC-SiC interface) of the SiC layer suggests that U transport in SiC is active at 1800°C. In addition, ‘dark’ spots in the half of the SiC layer close to the SiC-OPyC layer were detected. These areas were associated with ‘pits’ or possibly C-rich areas; similar observations, though with less number density of dark spots, were made for the particles tested at 1700°C [107]. It was argued [107] that voids or C-rich areas were left behind while Pd was leaving the SiC layer. In summary, U exhibits mobility within the graphite layers at temperatures of 1600°C and above, while both U and Pd demonstrate mobility within SiC at 1800°C and potentially at 1700°C [107].

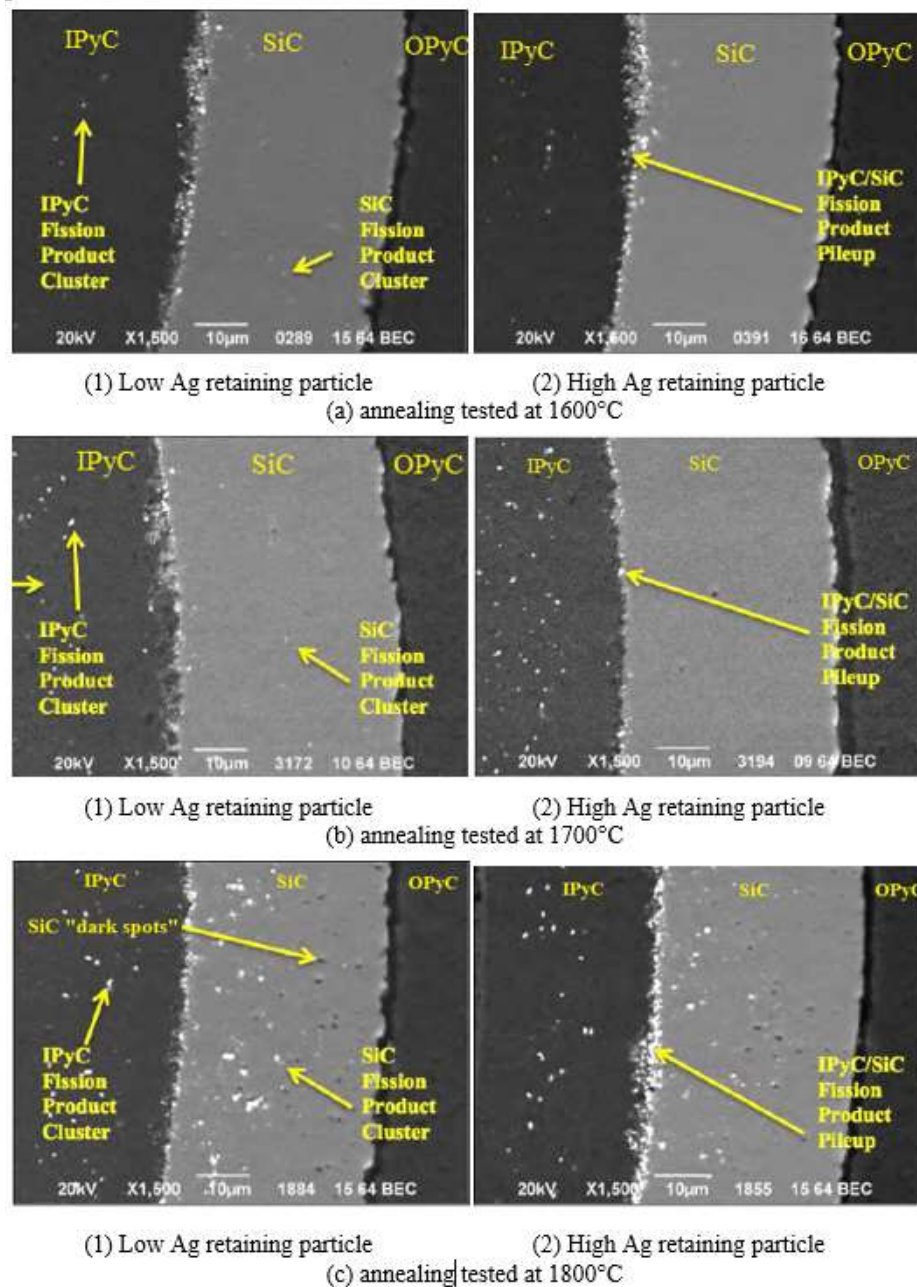


FIG. 89. BEC images of annealing tested low and high Ag retaining particles at (a) 1600°C, (b) 1700°C and (c) 1800°C (courtesy of INL).

#### 7.1.4. Fission product transport

Fission product transport is the main component of the source term calculation in the safety analysis. The source term is defined as the timing, fraction, and speciation of fission products released to the containment during an accident. Consequently, it is important to calculate the inventory of fission products and release during normal and abnormal operating conditions. During normal operating conditions, any defected elements (e.g. fabrication defects) can release small amounts of fission products into the coolant (i.e., helium gas). At very high temperatures and power surges, TRISO particles may start to fail, releasing fission products. Therefore, the release of fission product can be calculated with the knowledge of fission product transport in the coated particle. Calculations become complicated due to the chemical state of the fission products, the different mechanisms responsible for gaseous and metallic fission product transport in each layer, high burnups and fast neutron fluences.

Fission product transport includes:

- Release from failed or defective particles;
- Release from uranium contamination in the compact;
- Diffusive release through the intact coatings.

In the safety analysis, instead of evaluating all fission and activation products produced and transported in the fuel and released into the containment and environment, only the most significant radiological nuclides are analysed. The radiologically important fission products released from fuel elements are divided into two groups:

- Gaseous fission products;
- Metallic and activation products; activation products are formed when a fission product captures a neutron to form a new nuclide.

Key gaseous/volatile fission products that are selected based on the combination of their radiological hazard level, fission yield, and their transport and release properties, include  $^{131}\text{I}$ ,  $^{133}\text{I}$ ,  $^{88}\text{Kr}$ ,  $^{138}\text{Xe}$ ,  $^{133}\text{Xe}$ ,  $^{90}\text{Kr}$  and  $^{137}\text{Xe}$  and  $^{132}\text{Te}$  [4]. The long-lived metallic fission and activation products include  $^{137}\text{Cs}$ ,  $^{111}\text{Ag}$ ,  $^{134}\text{Cs}$ ,  $^{136}\text{Cs}$ ,  $^{110\text{m}}\text{Ag}$  (m indicates metastable) and  $^{90}\text{Sr}$ . For normal operating conditions, the inventories of the fourteen nuclides listed above are calculated, though for abnormal conditions,  $^{90}\text{Sr}$ ,  $^{131}\text{I}$ ,  $^{133}\text{I}$ ,  $^{137}\text{Cs}$  and  $^{111}\text{Ag}$  are of significance [4].

To model the release of long-lived fission gases from the kernel, the diffusion-controlled release from a sphere is employed. As for short-lived gaseous fission product species, where production and release from the kernel rapidly reach a steady state, the Booth model [168] is commonly utilized to determine the ratio of the release rate to the birth rate (R/B). This ratio, R/B, is influenced by the diffusion coefficient of the radionuclide, decay constants of the fission product isotopes, and the surface-to-volume ratio ( $S/V=3/a$ ) of a sphere equivalent to the representative grain of fuel with radius  $a$ . The Booth model is applicable only to the diffusive release of fission products from kernels and from matrix graphite grains (which contain the heavy metal contamination). In the most recent models, besides the Booth model, the effects of temperature, burnup, the mechanisms of athermal and vacancy migration diffusion, both irradiation-induced, intrinsic diffusion and a buffer-recoil contribution to release were incorporated [3].

Diffusion model can be applied to determine the transient release behaviour of metallic fission products. Excluding silver, under normal operation conditions, an intact TRISO particle coating prevents effectively metallic fission product release. Hence, estimating the release involves understanding the proportion of defective or failed particles and heavy metal contamination in the fuel element graphite, along with comprehending fission product transport in both the kernel material and the fuel element material. Beyond diffusion, other release mechanisms during normal operation include the recoil effect

and the knockout effect at low temperatures, with diffusion becoming dominant at elevated temperatures.

Fickian equation is applied to solve the diffusion of fission product species in different kinds of reactor materials using effective diffusion coefficients. Effective implies that all possible transport mechanisms are considered in a simplified single transport process. The diffusion coefficients are usually given as an Arrhenius type equation as a function of temperature. Separate effects, such as fast neutron fluence or fission product concentration or burnup, or by combining diffusion processes with different activation energies in different temperature ranges, are also considered.

Fission product transport mechanisms in the kernel and layers of a TRISO particle are described in Ref. [14] and summarized in Table 53.

TABLE 53. MECHANISMS FOR FISSION PRODUCT TRANSPORT IN TRISO PARTICLE FUELS

Layer	Mechanisms
Kernel	<ul style="list-style-type: none"> <li>• Recoil</li> <li>• Fuel restructuring due to kernel-buffer pyrocarbon chemical reaction</li> <li>• Diffusion of fission products to grain boundaries and to the surface of the kernel through the interconnected porosity of the kernel</li> <li>• Transport through vapour phases</li> </ul>
Buffer	<ul style="list-style-type: none"> <li>• Fission product transport in porous media: fission product transport in pores and through cracks created due to stresses in the buffer zone: binary diffusion (interdiffusion), pressure driven diffusion – Knudsen diffusion, the mass transport behaviour by: 1) free molecular flow, 2) viscous flow, and 3) diffusive flow</li> </ul>
IPyC and OPyC	<ul style="list-style-type: none"> <li>• Gas phase fission product transport: slow diffusion</li> <li>• Metallic fission product transport: diffusion and trapping</li> </ul>
SiC	<ul style="list-style-type: none"> <li>• Bulk diffusion – less likely</li> <li>• Grain boundary diffusion</li> <li>• Fission product transport along pre-existing nano-cracks</li> <li>• Pd assisted SiC corrosion</li> </ul>

Parameters that influence fission product transport in a coated particle fuel include [14]:

- Macroscopic parameters, such as particle burnup, fast fluence (linked to radiation damage), layer temperature, and gas or vapour partial pressure;
- Microscopic parameters related to material structure, such as porosity, tortuosity of the porous medium, and grain boundary microstructure;
- Parameters linked to the chemical speciation of fission products, encompassing fuel stoichiometry and its variations during normal and accident conditions, thermochemical data like free energies of formation, vapour pressures, adsorption isotherms, and transport properties like binary gas phase diffusivities and heat of transport;
- Physical parameters leading to multidimensional and multicomponent effects, including segregation and concentration of fission products due to cracking and azimuthal temperature gradients.

Fission product transport phenomena that are applicable to kernel and the layers are described in Ref. [16] and summarized in Table 54. Some of the factors may be unique to more than one layer.

TABLE 54. FISSION PRODUCT TRANSPORT PHENOMENA

Factor	Definition
Condensed phase diffusion	Transport of condensable fission products by intergranular diffusion and/or intragranular solid-state diffusion (grain boundary and/or bulk diffusion)
Gas phase diffusion	Diffusion of gaseous fission products through layer (Knudsen and bulk diffusion through pore structure, and pressure driven permeation with factors including cracking, adsorption, permeability, sintering and
Thermodynamics of fission product-SiC system	Chemical form of fission products including the effects of solubility, inter-metallics and chemical activity
Intercalation	Trapping of species between sheets of the graphite structure
Trapping	Adsorption of fission products on defects
Fission product release through failures, e.g. cracking	Fission product migration from the buffer layer through failed SiC

#### 7.1.4.1. Fuel kernel

Fission products can be transported in the kernel as a function of burnup (i.e., microstructure changes) and temperature (over the residing period in the reactor) due to:

- Recoil;
- Fuel restructuring due to UO<sub>2</sub> reaction with pyrocarbon buffer layer;
- Diffusion of fission products to grain boundaries and to the surface of the kernel through interconnected porosity of the kernel;
- Vaporization.

#### **Recoil**

Some of the fission products formed near the surface of a fuel kernel are released directly into the buffer region because of recoil, which is defined as the fission product movements in the surrounding material from their birth to their coming to a stop. The recoil range that a fission product travels in the material before coming to a stop is dependent on its mass, its kinetic energy and the material through which it penetrates.

The fractional release,  $F_{\text{recoil}}$ , of fission products from spherical kernel into the neighbouring buffer layer is independent from temperature and is calculated [14] as:

$$F_{\text{recoil}} = \frac{1}{4} \frac{r^3 - (r-a)^3}{r^3} \quad (12)$$

where  $r$  is the radius of the fuel kernel and  $a$  is the average fission fragment<sup>10</sup> range. Using fission energies of 107 MeV for krypton and 72 MeV for xenon, the average range is 5.8  $\mu\text{m}$  for krypton and 4.1  $\mu\text{m}$  for xenon in UO<sub>2</sub> with a density of 10.5 g/cm<sup>3</sup> [14]. For a 500  $\mu\text{m}$  kernel, the recoil release fraction is approximately 1.5%. For a 350  $\mu\text{m}$  kernel, the recoil release fraction is about 2%.

#### **Fuel restructuring**

Some fractions of the impurities including fission products can be expelled from the kernel, during restructuring of the fuel as a result of fuel kernel's chemical reaction with the surrounding pyrocarbon, producing surface layers of uranium carbide and oxy-carbide, and carbon monoxide (CO) [14]. These fission products are considered to be released from the kernel, as during the recrystallization process,

<sup>10</sup> Note that fission fragments are distinguished from fission products by their kinetic energy. Fission fragments possess all or part of the energy received from the fission event, whereas fission products are stationary.

they move to the exposed surfaces of the fuel kernel. Fission gas release based on kernel reaction with the surrounding carbon becomes important as the temperature increases due to the temperature dependence of the reaction of graphite with the kernel. It should also be noted that the irradiated carbon is more reactive toward the fuel kernel than the unirradiated carbon.

### ***Diffusion***

One of the most important fission product transport mechanisms is the conventional release process of diffusion through grains to the grain boundaries and subsequent transport through the interconnected porosity. The Booth diffusion model has been used to describe fission product release from the kernel [14]. The fractional release due to diffusion, originally developed for a grain [168] is given by:

$$F_{\text{diffusion}} = 1 - \frac{6}{\pi^2} \sum_{n=1}^{\infty} \frac{1}{n^2} \exp\left(\frac{-n^2 \pi^2 D t}{a^2}\right) \quad (13)$$

where  $D$  is the diffusion coefficient of fission products in the grain and  $a$  is the grain radius, and  $t$  is the irradiation time. For the fuel kernel, the reduced diffusion coefficient,  $D'$ , can be calculated by equating the kernel radius,  $r$ , to the equivalent grain radius [4] as

$$D' = \left(\frac{D}{a^2}\right)_{\text{grain}} = \frac{D_k}{r^2} \quad (14)$$

where  $D_k$  is the diffusion coefficient of the fission products in the fuel kernel.

When  $\pi^2 D' t \geq 1$  in Equation (13), the infinite series converges rapidly and the first term becomes dominant, resulting in Equation (15) [168]:

$$F_{\text{diffusion}} = 1 - \frac{6}{\pi^2} \exp(-\pi^2 D' t) \quad (15)$$

When  $\pi^2 D' t \leq 1$ , the fractional release can be estimated as [168]:

$$F_{\text{diffusion}} = 6 \sqrt{\frac{D' t}{\pi}} - 3 D' t \quad (16)$$

When  $\pi^2 D' t = 1$ , either of the equations can be used [168].

Further enhancements to the model to take into account effects, such as temperature were suggested and discussed in Refs. [3,10].

### ***Transport through vapour phases***

Gas phases of fission products need to be understood for the estimation of fission product transport through the layers of coated particle fuel. The chemical environment of the fuel particle is reducing and the fission products are sensitive to the reducing conditions. Fission products can also be affected by the existence of carbon monoxide produced by the reaction of pyrocarbon with oxygen liberated by the fission process. Elemental vapour species and oxide vapour species need to be determined. In addition, impurities left from the manufacturing process such as HCl can affect fission products by the formation of chlorides. Chlorides are typically volatile, in the form of monochloride and dichloride vapour or oxychloride vapour [14]. Vapour phases of BaC, SrC, ZrC and RuC were also identified to form [14].

Vapour phase metal carbonyls, in particular vapour, mono-carbonyls (MCO) and di-carbonyls (M(CO)<sub>2</sub>) may also be of interest for the analysis of fission product transport via vapour through the coated particle layers [14].

#### 7.1.4.2. Buffer layer

Since the buffer layer is porous (~50% theoretical density in the as-fabricated layer) and can crack due to tangential stresses developed under irradiation, it has the lowest thermal conductivity of any layer in the particle, and hence it has the largest temperature drop. Consequently, the temperature gradient in the buffer may cause thermal (Soret effect) fission product diffusion in the layer [14]. Depending on the specific irradiation conditions, the nature of the shrinkage and densification of the buffer establishes the initial condition for fission product transport.

Figure 90 [14] shows the temperature drop across the TRISO particle layers for an average particle that generates ~ 62 mW of power, which is about the average power per particle in a pebble bed reactor core, with the thermal conductivities of UO<sub>2</sub> kernel, and buffer, IPyC, SiC and OPyC layers being 2.5, 0.5, 4.0, 13.9, 4.0 W/m·K, respectively. The highest value of 10.88 K for the temperature drop was calculated for the buffer layer, while the lowest value of 0.07 was calculated for the SiC layer.

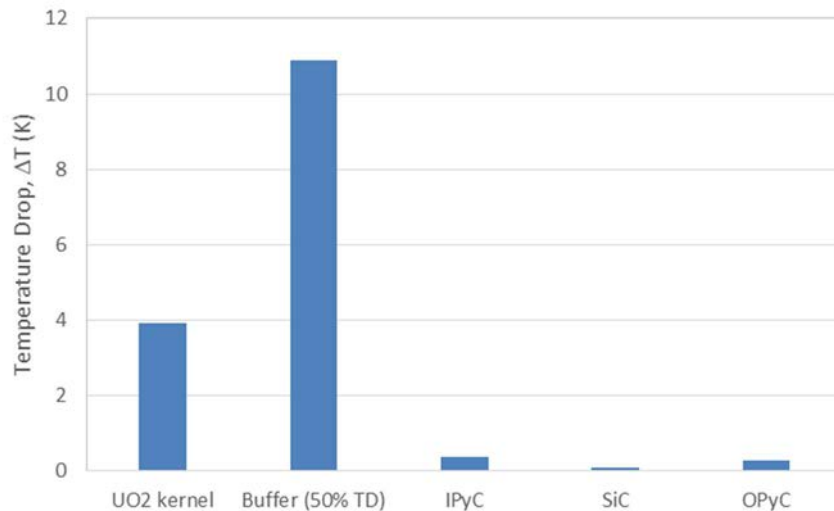


FIG. 90. Temperature drop across the TRISO particle layers for particle that generates a power of 62 mW (courtesy of US DOE).

As power levels increase, notable thermal gradients may arise, resulting in elevated thermal stresses within the layer. These stresses, particularly in the buffer, induced by thermal gradients and densification, have the potential to cause buffer cracking. Additionally, substantial thermal gradients exceeding approximately 1000 K/mm across the buffer can induce the thermal diffusion (Soret effect) of fission products within the layer [14]. Therefore, fission products can transport through cracks and by thermal diffusion. Table 55 shows the effects of particle power on the buffer layer. At relatively low powers, corresponding to the powers that a particle experiences in a pebble bed reactor, the buffer experiences uniform shrinkage. However, as the power increases and hence the thermal gradient, the particle experiences moderate to high tensile stresses and cracks, and at very high powers, excessive shrinkage of the buffer layer occurs, and the buffer is repositioned side-by-side with the kernel, as shown in Table 55 (from [14]).

TABLE 55. EFFECTS OF PARTICLE POWER ON THE BUFFER IN COATED PARTICLE FUEL

					
Description of location	PBMR low flux region; GT-MHR average	PBMR average	PBMR pebble and prismatic compact peak	Current prismatic irradiation limit	Very accelerated
Particle power	25 – 40 mW	60 mW	100 mW	400 mW	500–5000 mW
Thermal gradient across the buffer	< 50 K/mm	~ 100 K/mm	~ 250 K/mm	~ 750 K/mm	~ 9009000 K/mm
Condition of the buffer	Uniform shrinkage		Moderate tensile stress – some cracking	High tensile stress – many cracks	Excess shrinkage; buffer and fuel side by side

### *Fission product transport in a porous medium*

Multicomponent gas phase mass transport can be used to determine the behaviour of fission gases and vapour in porous media. On the contrary, the multicomponent diffusion equation, as formulated in the Chapman-Enskog approximation [16], postulates that mass transfer ensues due to:

- Temperature gradients (thermal diffusion or the Soret effect);
- Chemical composition gradients;
- Pressure gradients.

However, most investigators have used the Grad (the so-called '13-moment' method) version of mass transport through porous media because it allows the explicit consideration of the porous medium in the so-called 'dusty' gas' approximation [16].

In the model, the porosity of the material and tortuosity of the pore network were taken into account. In certain instances, a slip correction was incorporated for the pressure gradient term coefficient. This correction accommodates the relative velocity between the molecule and the surface, particularly when the characteristic size in the medium is comparable to the mean free path of the gas. In addition, for detailed analysis of fission product transport by gas phase mass transport, the vapour species transport properties such as binary diffusion coefficient, viscosity and thermal conductivity need to be known.

The molar flux of the substance through the porous medium is contingent on the pressure gradient across the material. Traditionally, three distinct regimes are recognized, contingent on the mean free path of the gas in relation to the characteristic size<sup>11</sup> of the medium, expressed as the Knudsen number ( $Kn = \lambda/d_{pore}$ , where  $\lambda$  denotes the mean free path and  $d_{pore}$  represents the average pore size in the medium) [20]:

- For  $Kn > 1$ , the mass transport behaviour can be described using the free molecular flow and the molar flux;
- In the transition region,  $0.01 < Kn < 1$ , both viscous flow and diffusive flow are considered;

<sup>11</sup> Characteristic sizes could range from nanopores, in a material like an as fabricated buffer, to microcracks as might be typical of a cracked buffer.

- In the continuum region, characterized by  $Kn < 0.01$ , the overall molar flux is determined by combining contributions from viscous flow and diffusive flow. It is important to note that molecular flow effects in this region are minimal.

When the pore diameter is smaller than the mean free path of diffusing gas molecules and the gas density is low, the molecules collide more frequently with the pore walls than with each other. A Knudsen number much greater than one indicates the Knudsen diffusion is important.

A sensitivity analysis was performed for pressure driven diffusion to determine effective diffusivities as a function of pore or crack size [167]. At conditions corresponding to normal operation and accidents, effective diffusivity of Kr gas at 1000° and 1600°C and pressures in the range of 0.5 MPa to 25 MPa, was analysed.

Figure 91 shows the calculated effective diffusivities at 1000°C and 1600°C, respectively [93]. Gas pressure becomes important for characteristic sizes greater than  $\sim 0.02$  mm. In addition, the effect of temperature on effective diffusivity is moderate, based on comparison of Fig. 92(a) with (b). For nanopores (where Knudsen diffusion becomes important), effective diffusivities are on the order of 3 to  $53 \times 10^{-7}$  m<sup>2</sup>/s. By contrast, transport through micropores or micron sized cracks (where viscous diffusion becomes important) is much faster, with effective diffusivities ranging between  $10^{-4}$  and  $10^{-2}$  m<sup>2</sup>/s depending on the pressure of the gas involved [93]. Note that the German scientists assumed the diffusivity of all species in the buffer to be  $10^{-8}$  m<sup>2</sup>/s and the US used a value of  $10^{-10}$  m<sup>2</sup>/s in their evaluations [14]. Depending on the pore or crack sizes, rapid transport of fission gases and fission product vapours could be expected through the buffer layer in a coated particle. From mass transport point of view, it is also important to identify connected porosities.

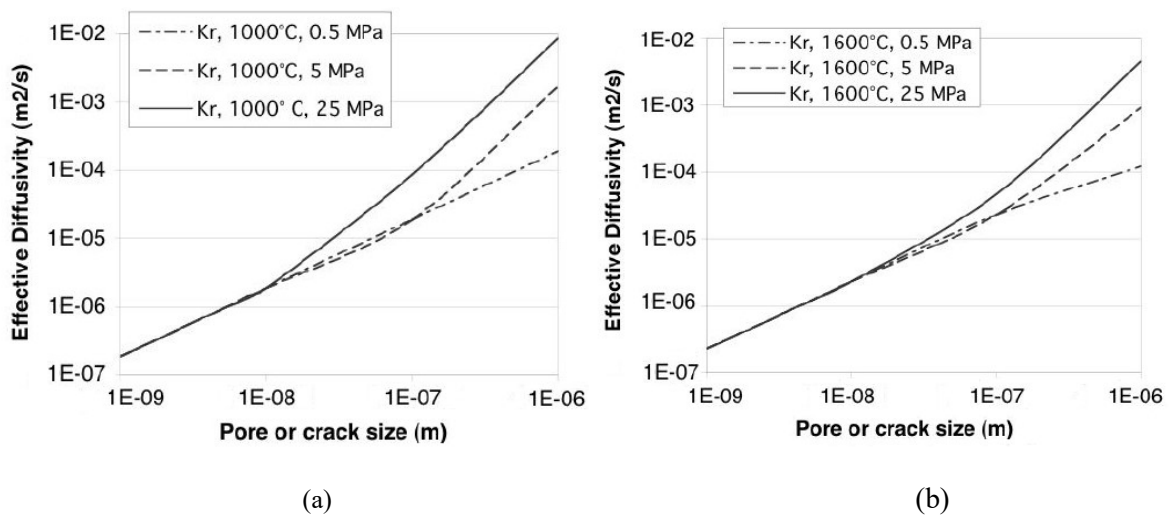


FIG. 91. Effective diffusivities for Knudsen and viscous diffusion at: a) 1000°C and b) 1600°C (courtesy of INL).

### Thermal diffusion

Besides the traditional concentration gradient driven Fickian diffusion across the layer, large thermal gradients in the buffer layer can lead to thermal diffusion (the Soret effect). Consequently, the combined diffusive flux for one species can be given by [14]:

$$J = -D \left( \underbrace{\nabla C}_{\text{Fickian diffusion}} + \underbrace{\frac{CQ}{RT^2} \nabla T}_{\text{Thermal diffusion (Soret effect)}} \right) \quad (17)$$

where  $D$  is the diffusion coefficient,  $Q$  is the heat of transport,  $T$  is the temperature,  $J$  diffusive flux,  $C$  is the concentration, and  $R$  is the ideal gas constant [14].

For low power/thermal gradients in pebbles in pebble bed reactors, thermal diffusion is expected to be much less important in fission product release, whereas at high powers, thermal diffusion becomes important.

#### 7.1.4.3. Inner pyrocarbon and outer pyrocarbon layers

For gas phase fission product transport, the measured diffusion coefficients suggest very slow transport through the PyC layer.

Beyond 1900°C, it is advisable to consider rapid diffusive transport (similar to the buffer layer) for metallic fission products within the IPyC. In the case of high-temperature isotropic PyC, this critical temperature has been presumed to be as low as 1200°C, with the exception of caesium, for which experimental evidence indicates much better retention than strontium or silver [3].

The proposed mechanism for the transport of Cs, Sr, and even iodine and CO in the PyC involves intercalation, which is the insertion of guest atoms into a host structure. A conventional diffusion and trapping model has been suggested for modelling the transport, with trapping taking place at the carbon crystallite edges and defects in the graphitic material [14].

#### 7.1.4.4. Silicon carbide layer

The mechanisms for fission product transport through SiC include [169]:

- Bulk diffusion through grains;
- Grain boundary diffusion;
- Diffusion along interconnected micro/nano cracks;
- Pd-assisted fission products transport.

#### **Bulk diffusion**

For the bulk diffusion, the first mechanism is fission product diffusion through the bulk of the SiC (single) crystal (i.e., grain).

While the SiC shell has the cubic (3C) crystal structure (with an ABC close-packed stacking of Si layers and C layers), SiC can form a wide variety of polymorphs, each characterized by a different stacking sequence of close packed planes, e.g. i) cubic SiC having zincblende structure, and ii) hexagonally packed (2H) SiC having a wurtzite structure [169]. Fission products can occupy two distinct types of interstitial sites (labelled as A and B) in both these crystal structures. In wurtzite, A is 6-fold coordinated by Si and by C, while the B site is 4-fold coordinated by Si and C. In cubic SiC, the A site is 6-fold coordinated by Si and 4-fold coordinated by C, while the B site is 4-fold coordinated by Si and 6-fold coordinated by C [169]. For example, for Ag, the site occupation energies were calculated using density functional theory, and then normalized to the cubic structure: for the interstitial site, the site occupation energy was the lowest, and hence Ag is expected to occupy an interstitial site in the cubic structure. Ag thermodynamically has a higher solubility in cubic SiC as compared to wurtzite.

The interstitial site energies of other fission products in cubic SiC, including I, Cs and Sr were calculated for two different interstitial sites: A and B [169]. Similar to Ag, I prefers A-site. Caesium prefers the B-site over the A-site, though the energy difference is small, in particular at high temperatures. Sr, while preferring the A site, only has a small energy penalty to overcome to occupy the B site. Consequently, I will have a similar interstitial diffusion coefficient as Ag, while Cs and Sr would have significantly higher interstitial diffusion coefficients.

Energies required to move fission product (atom) from their pure crystalline state into an isolated interstitial site of the SiC crystal were also calculated. The corresponding energies for Ag, I, Cs, Sr were 9.897, 21.654, 24.450 and 15.628 eV, respectively [169]. The required energies are quite high for I, Cs and Sr, indicating that these elements have low solubilities in SiC.

Since the interest is the calculation of the release rate of fission products through the SiC layer, the solubility of the fission products at the inner surface of the SiC layer when in contact with PyC and the diffusion coefficient for fission product transport through cubic SiC need to be taken into account. The integrated fission product flux,  $F$ , indicating fission products emerging at the outer surface of the SiC, can be calculated for a steady state concentration profile as [169]:

$$F = \frac{4\pi C_0}{\frac{1}{R_1} - \frac{1}{R_2}} \quad (18)$$

where  $D$  is the fission product diffusion coefficient,  $C_0$  is the fission product concentration on the inner surface of the SiC layer (number of atoms per unit volume of SiC),  $R_1$  and  $R_2$  are the inner and outer radii of the spherical SiC layer, respectively. The value of  $D$  is very sensitive to the diffusion mechanism, depending on whether fission product diffusion occurs through the bulk via an interstitial or a substitutional mechanism, or whether it occurs along grain boundaries or internal cracks.

Assuming interstitial solubility in the bulk and interstitial bulk diffusion, Ag release rate,  $F$ , was calculated using Equation (18), and plotted in Fig. 92. It is noted in Ref. [169] that bulk diffusion is highly unlikely as the transport mechanism for Ag passing through the SiC layer: the energy to take Ag from graphite to an interstitial SiC site is of the order of 6–7 eV, resulting in very low equilibrium Ag concentrations on the inner surface of the SiC layer, whereas the solubility of Ag along grain boundaries and internal surfaces was identified significantly high.

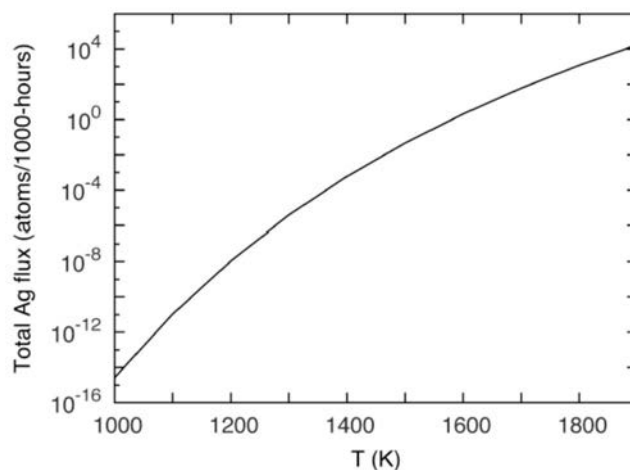


FIG. 92. Calculated Ag release rate from a TRISO particle.

### ***Grain boundary diffusion***

Despite that fission product escape through bulk diffusion is not likely, it may occur along short-circuit pathways such as grain boundaries. These boundaries, therefore, are expected to be a less constrained environment for diffusing fission products than the bulk, but more constrained than microcracks. More open structure of grain boundaries can raise the local thermodynamic solubility of fission products through segregation as well as their mobility [169].

Based on density functional theory (DFT) calculations, the formation energy for Ag in the grain boundaries was larger than for the C-rich surfaces, but much less than that for an interstitial in bulk SiC [169]. The energy required to move an Ag atom from pure Ag (precipitated metallic state) or from graphite to a site at the grain boundaries is still positive, indicating that there is no energetic driving force for Ag to segregate to SiC grain boundaries if it is already in the metallic state or inserted within graphite.

### ***Fission product transport along pre-existing nano-cracks***

In the presence of nano or micro cracks, very fast short-circuit diffusion pathways are provided to fission products. Transport along interconnected crack networks can occur either through surface diffusion or in gaseous form. SiC has both Si-rich and C-rich surfaces. Based on DFT calculations, adsorbed Ag has a formation energy near +2.0 eV for different sites on the carbon-rich surface, and at -1.246 eV for one site on the silicon-rich surface, which indicates that there is a thermodynamic driving force for Ag to segregate to Si-rich surfaces [169]. Based on first-principles calculations (i.e., DFT), when Ag is present in graphite (IPyC), it precipitates as metallic Ag particles in SiC or along grain boundaries in SiC. Only Si-rich surfaces exhibit an energetic attraction for Ag in the metallic state. Similarly, formation energies of other fission products (i.e., I, Cs, and Sr) were calculated to be lower at the Si-rich surface compared to C-rich, and even these formation energies are lower than the one for Ag, as shown in Table 56 (from [169]). The values for C were presented in a range, as calculations were performed for three sites for C. Caesium and strontium bind favourably to all of the surfaces and sites, while Ag binds favourably only to the Si-rich surface. Iodine is favourable in all locations except for one of the sites on the C-rich surface (with a positive value).

TABLE 56. FORMATION ENERGIES (IN EV) FOR AG, CS, I, AND SR ON SURFACES OF SiC-3C

Surface	Ag	Cs	I	Sr
C	1.974 – 2.050	(-1.436) – (-1.637)	(-0.242) – (+0.498)	(-1.868) – (-0.756)
Si	-1.246	-2.331	-2.280	-3.205

### ***Palladium assisted fission product transport***

There are two main factors that need to be understood under Pd assisted fission product transport: i) decohesion in SiC, and ii) the embrittlement effect of Pd.

Pd has a corrosive effect on SiC and it is believed to facilitate fission product transport in SiC. Pd makes SiC susceptible to crack opening in regions of high residual tensile stresses. The tensile stresses can emerge during growth or as a result of large temperature gradients [169]. An analysis was performed using the cohesive zone model<sup>12</sup> [168] to determine the response of the decohering<sup>13</sup> region to externally imposed loads or displacements: in the model, the energy of the decohering zone on a metric of

<sup>12</sup> The cohesive zone model in fracture mechanics treats fracture formation as a gradual process, where separation of the crack surfaces occurs along an extended crack tip, or cohesive zone, and is opposed by cohesive tractions.

<sup>13</sup> Decoherence is described as the separation of parallel crystallographic planes [169].

separation  $\delta$  was described; the derivative of this energy with respect to separation yielded a traction-separation curve.

SiC is brittle and has very little susceptibility to plastic deformation through dislocation glide [169], and in the presence of a crack, intergranular and transgranular crack propagation will occur. Although the atomic planes ahead of the crack tip share crystallographic identity with the atomic planes in the crystal adjacent to the crack path, they experience higher normal stress owing to the broken symmetry caused by the presence of the crack. There is little inclination between decohering atomic planes for the slow variation in the crack opening behind and ahead of the tip [169].

When subjected to a constant Pd chemical potential and stress, the equilibrium state of the cohesive zone in SiC was determined [169]. The maximum stress for decohesion of the Pd saturated cohesive zone is substantially lower than that of pure SiC: Pd acts as an embrittlement agent of SiC, dramatically lowering the maximum stress of decohesion. If the residual stresses at the crystallographic level are greater than the maximum stress of decohesion when Pd segregates to the cohesive zone, cracks will propagate. These cracks can serve as short-circuit diffusion paths for fission products escape. Pd segregation and precipitation along grain boundaries may also facilitate fission product diffusion along these grain boundaries, as the solubility of fission products such as Ag is higher in Pd than in SiC. Ag, for example, has an energetic driving force to adsorb to the Si-rich surfaces that form upon decohesion. Furthermore, Ag readily alloys with Pd, indicating an energetic attraction to Pd atoms [169].

#### **7.1.5. Fission product release**

Compacts containing TRISO particles were irradiated in the ATR under the AGR program; AGR-1 refers to the first irradiation test campaign and AGR-2 refers to the second irradiation test campaign. Radioactive fission products were measured in both compacts and capsules (see Fig. 93 [107]). The UCO fuel kernels fabricated for AGR-1 irradiation had a nominal enrichment of 19.7%  $^{235}\text{U}$  and a nominal diameter of 350  $\mu\text{m}$ . For the AGR-2 irradiation, the UCO kernels had a nominal enrichment of 14% and a nominal diameter of 425  $\mu\text{m}$ , whereas the  $\text{UO}_2$  kernels had a nominal enrichment of 9.6% and a nominal diameter of 500  $\mu\text{m}$  to be comparable with historic German fuel particles [108]. The coatings on both types of kernels featured a nominal thickness of 100  $\mu\text{m}$  (buffer), 40  $\mu\text{m}$  (inner and outer pyrolytic carbon), and 35  $\mu\text{m}$  (SiC). These TRISO particles were encased in graphitic matrix material and shaped into cylindrical compacts with a diameter of about 12.3 mm and a length of 25.1 mm. The packing fractions for the UCO and  $\text{UO}_2$  compacts were 37% and 23%, respectively [108]. The irradiated fuel compacts achieved burnups of 10% – 13%.

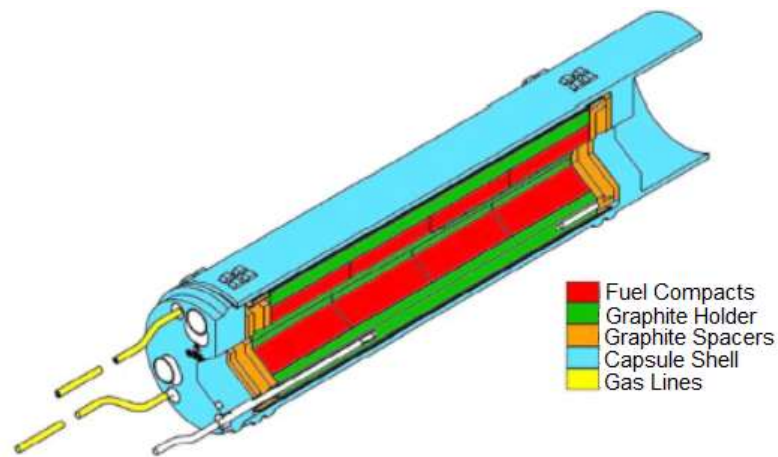


FIG. 93. Components of a Capsule used for AGR Irradiations (courtesy of INL).

Figure 94 [6] shows the fission product release pathway: 1) from kernel to coating layers, 2) from coating layers to compact matrix, 3) from compact matrix to structural graphite, 4) from structural graphite to capsule shell. Overall, the fission product release has been evaluated [6]:

- In fuel compacts;
- On capsule components;
- In compact matrix;
- In individual particles.

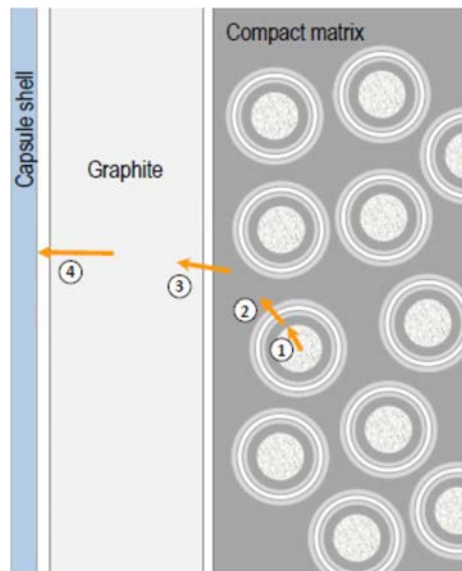


FIG. 94. In-pile fission product release evaluation (courtesy of INL).

Table 57 shows the fission product retained or released in the TRISO particles, taken from Ref. [6].

TABLE 57. FISSION PRODUCT RELEASE/RETENTION

Element	Retention/release in layers
Kr, Xe, I	<ul style="list-style-type: none"> <li>Retained by intact PyC or SiC layers</li> <li>Released from uranium contamination and exposed kernels</li> <li>Kr and Xe are key indicators of failed TRISO layers</li> </ul>
Cs	<ul style="list-style-type: none"> <li>Retained by SiC but released through intact PyC</li> <li>Key indicator of failed SiC layer</li> </ul>
Sr	<ul style="list-style-type: none"> <li>Moderate retention in the fuel kernel</li> <li>Modest release through intact coatings (<math>T &gt; 1100^{\circ}\text{C}</math>); significantly higher release for very high irradiation temperatures</li> <li>Some retention in the compact matrix</li> </ul>
Eu	<ul style="list-style-type: none"> <li>Similar to Sr, but slightly higher releases</li> </ul>
Ag	<ul style="list-style-type: none"> <li>Significant release through intact SiC (<math>T &gt; 1100^{\circ}\text{C}</math>)</li> <li>Relatively low retention in compact matrix</li> </ul>

Similarly, Fig. 95 [6] shows the release of fission products from fuel compacts irradiated in the ATR (corresponding to the first and second irradiation test campaigns, AGR-1 and AGR-2):

- Cs release is minimal when SiC remains intact; increased releases are linked to a restricted number of particles with compromised SiC;
- Sr and Eu may display moderate releases, with significantly higher release observed at elevated in-pile temperatures (AGR-2 Capsule 2 time-average peak temperatures of  $1360^{\circ}\text{C}$ );
- Ag release is notably high.

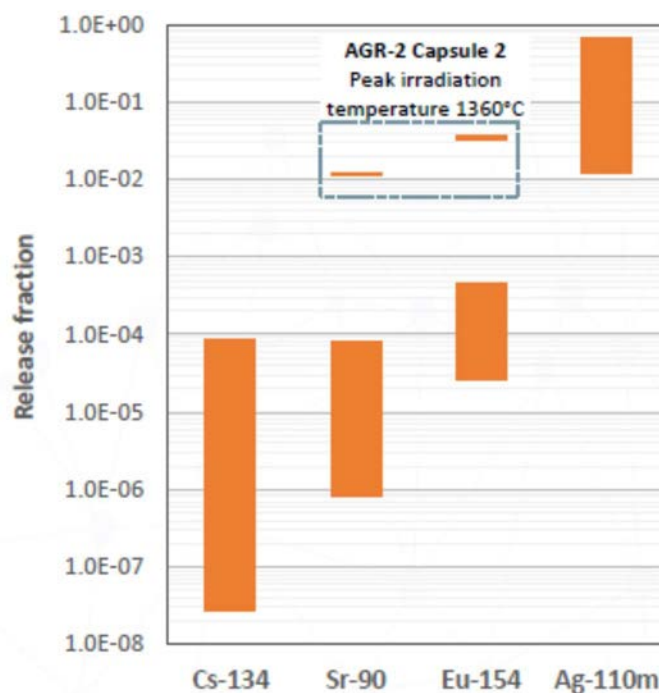


FIG. 95. Fission product release from AGR-1 and AGR-2 fuel compacts (courtesy of INL).

Figure 96 [108] shows the comparison of  $^{85\text{m}}\text{Kr}$  (m indicates metastable isotope) release from AGR-1 and AGR-2 fuel compacts with historic performance in US and German TRISO fuel irradiations. The observed values are elevated in AGR-2 irradiations compared to AGR-1, attributed partly to increased uranium contamination in AGR-2 compacts relative to AGR-1 (AGR-2 compacts exhibited uranium contamination around  $4 \times 10^{-6}$ , whereas the AGR-1 average was  $3 \times 10^{-7}$ ). It is worth noting that no particle failures were noted during the initial three cycles of the AGR-2 irradiation.

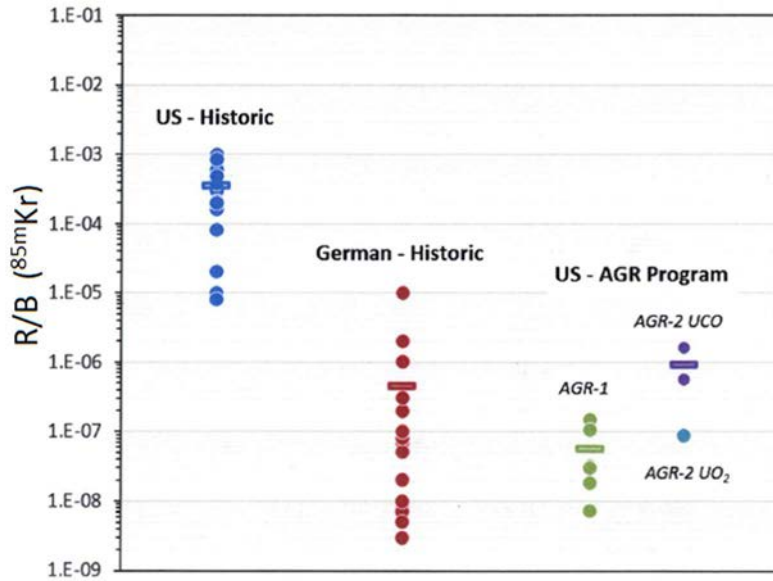


FIG. 96.  $^{85m}\text{Kr}$  fission gas release for AGR-1 (end of life) and AGR-2 (after the first three irradiation cycles) Compared to historic performance in US and German TRISO fuel irradiations (courtesy of EPRI).

It needs to be noted that  $\text{UO}_2$  kernels irradiated during the AGR-2 test campaign achieved relatively low burnups, as shown in Fig. 97 [108], and slightly lower irradiation temperatures, compared to UCO kernels.

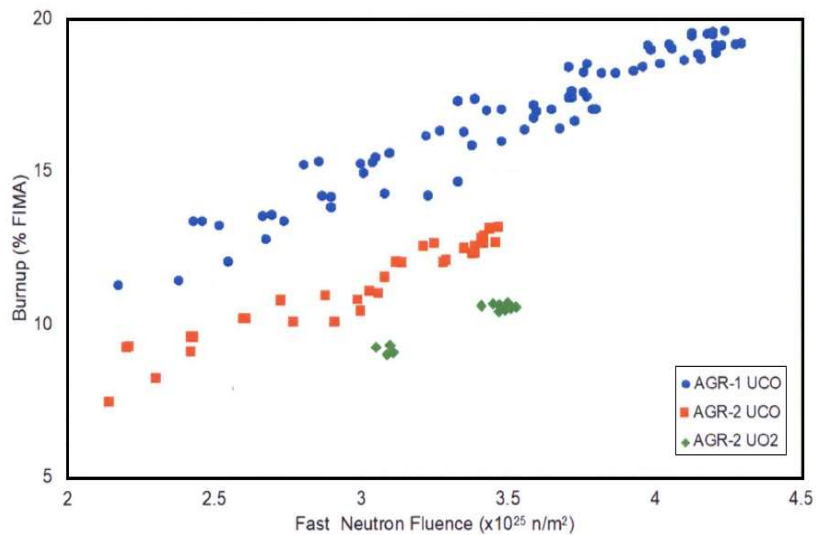


FIG. 97. Burnups achieved by AGR-1 and AGR-2 fuel compacts with UCO and  $\text{UO}_2$  fuel kernels (courtesy of EPRI).

In addition, annealing tests, isothermal tests at a temperature of 1600°C, 1700°C, or 1800°C for a nominal duration of 300 h, were performed on irradiated (i.e., AGR-1 and AGR-2) fuel compacts. As shown in Fig. 98 [108], 1600°C test results in an AGR-2 UCO compact exhibited very low fractional release of Cs isotopes for the duration of the test, modest release of Eu and Sr isotopes and fairly high release of  $^{110m}\text{Ag}$ .

$^{134}\text{Cs}$ ,  $^{110m}\text{Ag}$ ,  $^{154}\text{Eu}$  and  $^{90}\text{Sr}$  release were measured from heating of AGR-2 UCO and  $\text{UO}_2$  compacts (different symbols represent different compacts, stacks and compacts<sup>14</sup>) at temperatures of 1600°C, 1700°C and 1800°C. The releases for  $^{134}\text{Cs}$  and  $^{90}\text{Sr}$  are presented in Figs. 58 and 59 (in Section 6.2.2.2), respectively. Figures 99 and 100 [108] show releases of  $^{110m}\text{Ag}$  and  $^{154}\text{Eu}$ , respectively.  $^{134}\text{Cs}$  release was high for  $\text{UO}_2$  kernels, even at the temperature of 1600°C, compared to UCO kernels. Ag release was high for  $\text{UO}_2$  kernel at the temperature of 1700°C, though at the temperature of 1600°C, compacts with  $\text{UO}_2$  kernels exhibited similar releases to the UCO kernels.  $^{154}\text{Eu}$  and  $^{90}\text{Sr}$  releases from Capsule 2 with a UCO kernel that was exposed to high irradiation temperatures<sup>15</sup> were followed by the release from the compact with  $\text{UO}_2$  kernel exposed to a temperature of 1700°C during a post-irradiation annealing test.

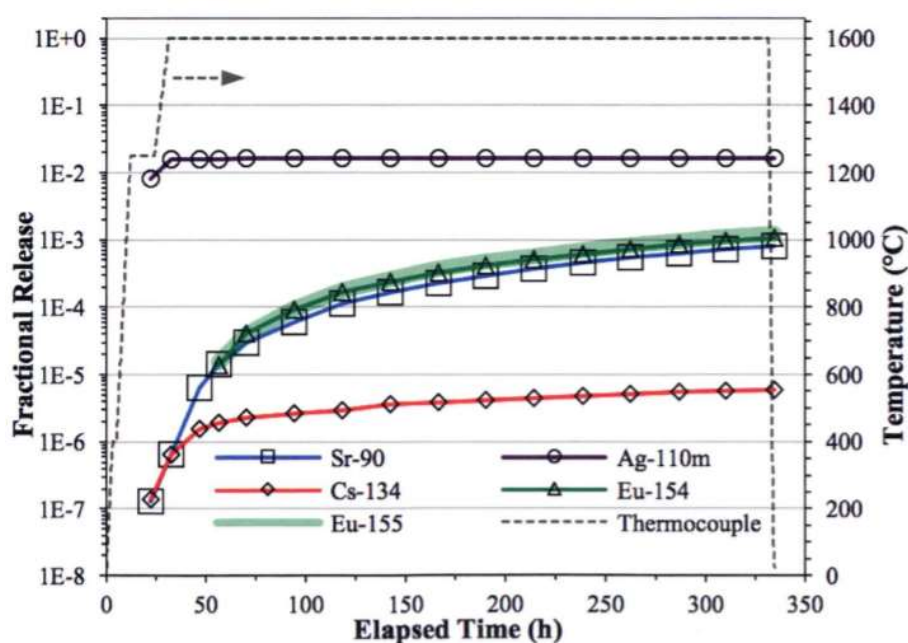


FIG. 98. Fission product release from heating of AGR-2 UCO compact at 1600°C (courtesy of EPRI).

<sup>14</sup> The AGR irradiation tests were multi-capsule, instrumented experiments. For each irradiation, six capsules, each independently controlled for temperature and independently monitored for fission product gas release, were used. Each capsule was 152.4 mm long and contained 12 fuel compacts arranged in three vertical stacks, with each stack containing four compacts.

<sup>15</sup> During irradiation in the reactor, while Capsule 2 was exposed to a time-averaged volume-averaged temperature of 1252°C, the other capsules including UCO kernels were exposed to 1101°C and 1074°C, and the capsule including  $\text{UO}_2$  kernels was exposed to 1032°C, due to the location of the capsules in the reactor, affecting the neutron fluxes.

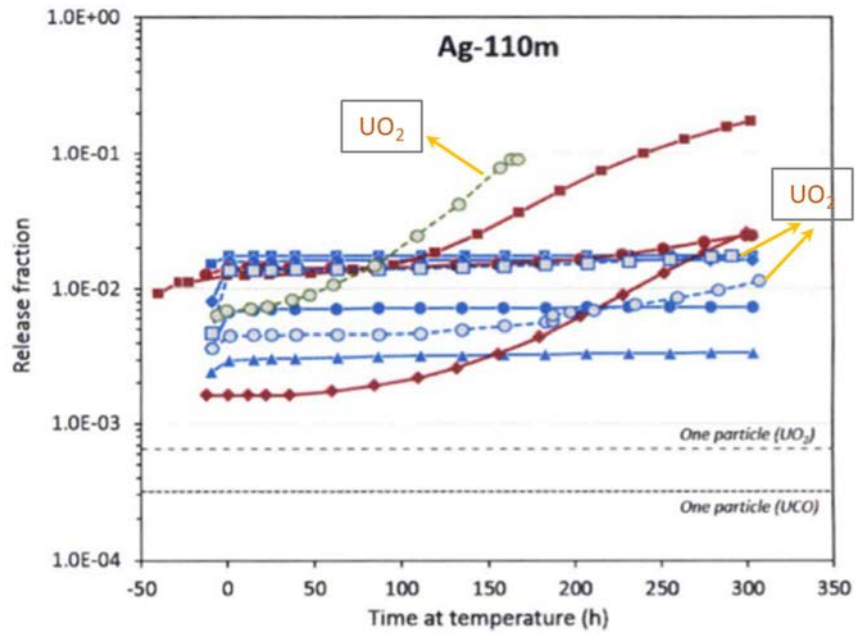


FIG. 99.  $^{110m}\text{Ag}$  release from heating of AGR-2 UCO and  $\text{UO}_2$  compacts at different temperatures. The plot colour indicates test temperature: 1600° (blue), 1700°C (green), or 1800°C (red) (courtesy of EPRI).

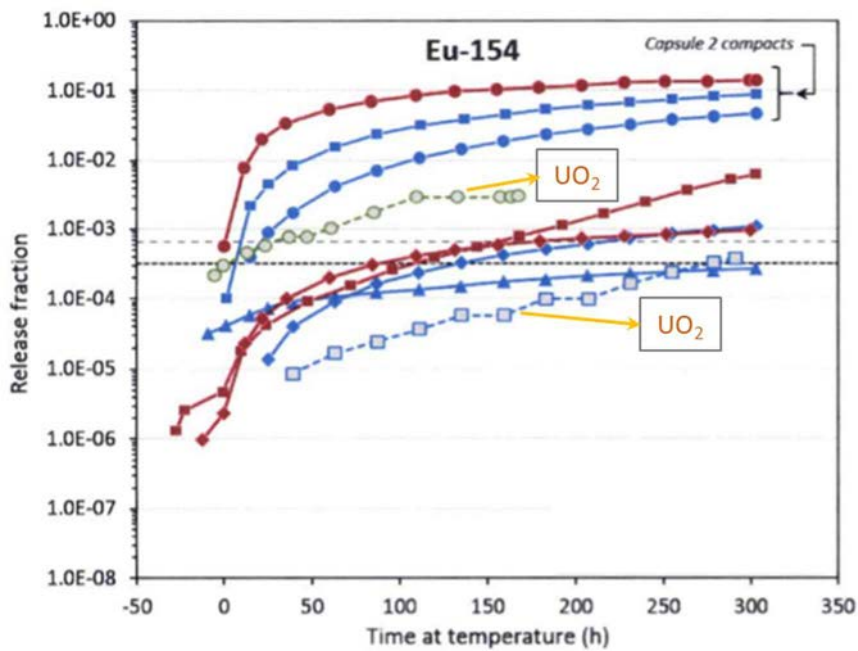


FIG. 100.  $^{154}\text{Eu}$  release from heating of AGR-2 UCO and  $\text{UO}_2$  compacts at different temperatures. The plot colour indicates test temperature: 1600° (blue), 1700°C (green), or 1800°C (red) (courtesy of EPRI).

## 7.2. EFFECT OF FABRICATION DIFFERENCES ON FUEL PERFORMANCE

Due to differences in the fabrication process, three specific differences in the coating layers, affecting the fuel performance, have been identified [10]:

- Pyrocarbon anisotropy and density;
- SiC microstructure;
- IPyC-SiC interface structure.

### 7.2.1. Pyrocarbon anisotropy and density

The density and anisotropy of PyC are dictated by the deposition conditions within the coater. Early US fuels produced under the New Production Reactor (NPR) program utilized low coating gas concentrations, leading to extremely low deposition rates for pyrocarbons, ranging from 1 to 4  $\mu\text{m}/\text{min}$ . These conditions resulted in obtaining high-density but anisotropic pyrocarbons with a laminar-like structure, as shown in Fig. 101(a) [10]. Note that high density IPyC is desirable to prevent chlorine attack of the kernel during deposition of the SiC layer. In contrast, the German fuels were manufactured using higher coating gas concentrations and correspondingly high coating rates resulting in more isotropic pyrocarbons, as shown in Fig. 101(b) [10]. Different irradiation behaviours were observed from these different microstructures: the highly dense, more anisotropic US PyC was more susceptible to cracking under irradiation.

Based on PIE of many of the NPR capsules, it was concluded that large shrinkage cracks in the inner pyrocarbon layer led to stress concentrations in the SiC layer and subsequent failure of the layer [10]. Such irradiation-induced shrinkage crack is shown in Fig. 102 [10].

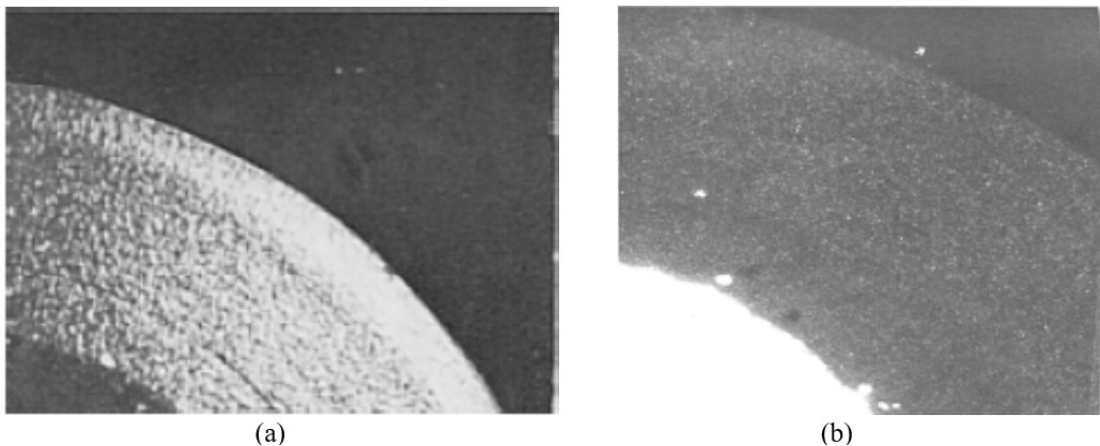


FIG. 101. Effect of the coating rate on the PyC microstructure: (a) US laminar – high density/more anisotropic PyC: low coating gas concentrations; (b) German isotropic PyC: higher coating gas concentrations (courtesy of INL).

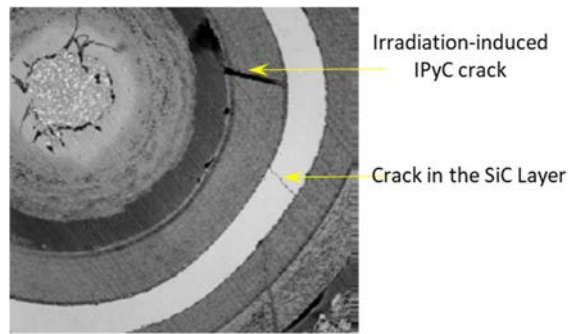


FIG. 102. Irradiation induced cracking of IPyC (courtesy of INL).

### 7.2.2. Nature of the IPyC-SiC interface

Due to differences in fabrication process (e.g. coating rates, temperatures) of the IPyC and SiC coating layers, differences in the surface porosity and microstructure between the German and US (NPR) IPyC were observed. The interface in German fuel was more tightly bonded because of the deposition of SiC into a PyC having more surface porosity (see Fig. 103(a) [10]). In the case of US NPR fuel for which SiC deposited on the reduced surface porosity in the IPyC layer, less strong bond between IPyC and SiC layer was observed (see Fig. 103(b) [10]). Under irradiation, debonding of the TRISO coating of German fuel was never observed but quite frequently observed for that of US NPR fuel [10]. The strength of the IPyC-SiC interface affects the debonding. Partial debonding can lead to stress intensification in the SiC layer that may cause failure.

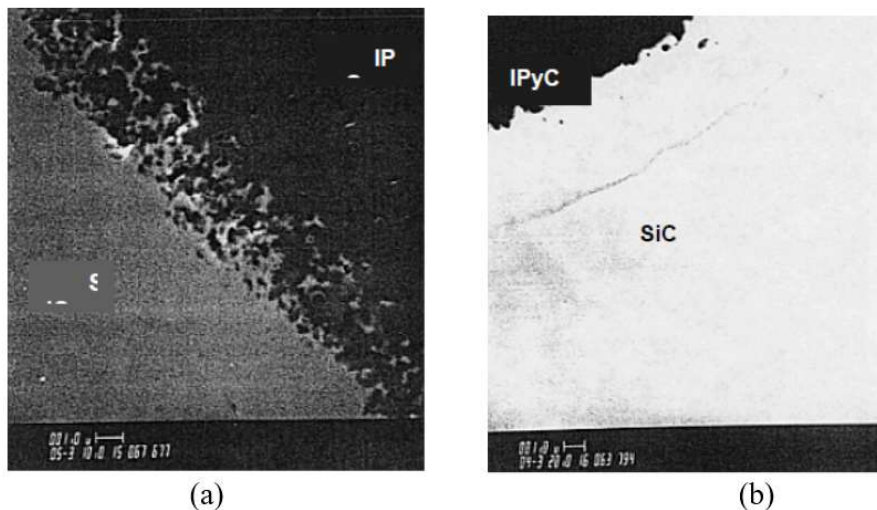


FIG. 103. SiC/IPyC Interface in (a) German and (b) US NPR Fuel (courtesy of INL).

### 7.2.3. SiC microstructure

Different temperatures used in the SiC coating process of US NPR and German TRISO fuels led to the different SiC microstructures: SiC layer was deposited at a temperature of 1500°C in the German process, whereas of 1650°C in the US NPR process. It was argued in Ref. [4]: “At higher temperatures

the grains can be as large as the SiC layer thickness<sup>16</sup>, which may result in poor retention of the fission products under high temperature conditions typical of accident situations. The smaller grained German SiC, with its longer grain pathway to the surface, should in principle retain metallic fission products better than the large columnar US SiC. Approximately 90% of the Ag was released from the large columnar grained SiC, whereas only ~ 30% was released in the smaller grained SiC microstructure". Figure 104 shows the different SiC microstructures of US coated particles with different kernels heated at 1500°C following irradiation [10]:

- The laminar SiC microstructures associated with UCO (see Fig. 104(a) [10]) showed very little release of Ag and none for Cs. The diffusivity of Cs through columnar SiC was given as an order of magnitude greater than through laminar SiC;
- Release of Ag was 100% from the UO<sub>2</sub> particles (see Fig. 104(b) [10]) with large columnar grained SiC, and 24% for Cs;
- The weaker laminar SiC structure observed for the UC<sub>2</sub> kernel (see Fig. 104(c) [10]) also showed very high Ag (82%) and Cs (12%) releases.

It is difficult to conclude the role of SiC microstructure in fission product release based on this US study using different kernels, because these data were obtained from different fuel kernel types whose ability to retain metallic fission products may be different.

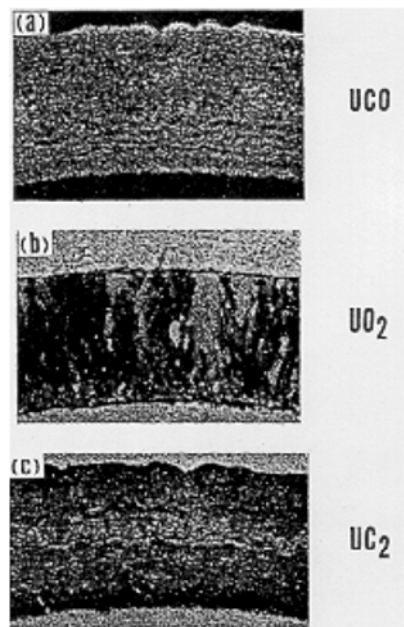


FIG. 104. Microstructures of different SiC layers on coated particles (courtesy of INL).

### 7.3. TENSILE STRESSES IN SiC LAYER AND FUEL FAILURES

During an irradiation, a coated particle fuel is subjected to several forces that put stress on the TRISO coatings. A particle failure is expected to take place, if the tangential stress reaches a tensile value that exceeds the strength of the SiC for that particle. Therefore, it is important to analyse the stresses in the SiC layer (see Fig. 105 [108]):

<sup>16</sup> Columnar SiC grains as long as 30 μm (comparable with the thickness of the SiC layer) in the US fuel, while only smaller grains (about 2 μm) in the German fuel [10].

- Fission gas pressure builds up in the kernel and buffer regions, while the IPyC, SiC, and OPyC act to retain this pressure. As irradiation progresses, a portion of the gas pressure is transferred through the IPyC layer to the SiC, leading to an increase in pressure and generating tensile hoop stress in the SiC layer.
- Early during irradiation, pyrolytic carbon layers shrink, inducing an increasing compressive stress in the SiC layer.
- As irradiation progresses, the creep of the pyrolytic carbon layers relieves some of the compressive stress, reducing the beneficial effect of pyrocarbon shrinkage, as compressive stress in SiC is desirable.
- During irradiation of the particle, the SiC exhibits only elastic response, while the IPyC and OPyC layers both shrink and creep.

In summary, the pressure load is pushing outward on the SiC while the shrinkage of the IPyC and OPyC causes them to push or pull inward on the SiC (see Fig. 105). Due to anisotropy, the PyC shrinkage behaviour differs in the radial and tangential directions (see Section 2.3.3 in general). The shrinkage in the radial direction reverses to swelling at moderate fluence levels, whereas shrinkage in the tangential direction continues to high fluence levels.

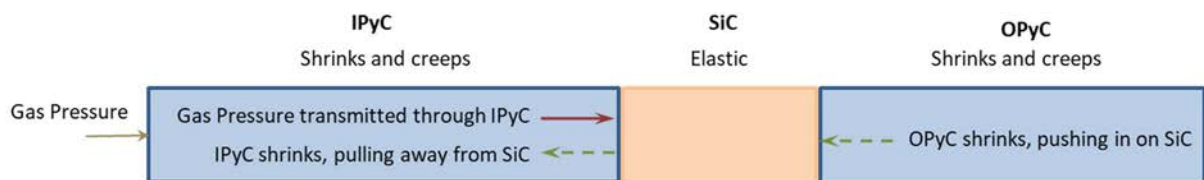


FIG. 105. Behaviour of coating layers in fuel particle (courtesy of EPRI).

Figure 106 shows tangential stress with burnup (fast fluence) at the inner surface of the SiC layer at three different temperatures (details can be found in Ref. [22]). The tangential stress in the SiC reaches a minimum value, and then steadily increases through the remainder of irradiation due to the PyC shrinkage and creep. In addition, the tangential stresses increase with increasing temperature.

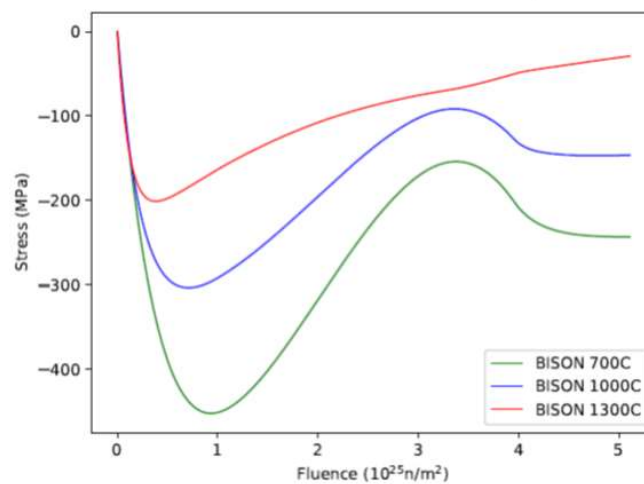


FIG. 106. Evolution of tangential stress with burnup (fast fluence) at the inner surface of the SiC layer (courtesy of INL).

The tensile stress in the SiC layer is contingent upon the pressure of fission gas in the buffer. Assuming complete fission gas release and maximum burnup, the stress in the SiC layer is directly proportional to the following parameters [170]:

$$\sigma \propto \frac{B \times V_k r_{SiC}}{V_b t_{SiC}} \quad (19)$$

where  $\sigma$  is the tensile stress,  $B$  is the maximum burnup,  $V_k$  is the kernel volume,  $V_b$  is the buffer volume,  $r_{SiC}$  is the radius of SiC layer, and  $t_{SiC}$  is the thickness of SiC layer.

Based on Equation (19), an analysis was performed to compare tensile stress metrics of the fuels fabricated using different specifications and in different countries [108]. The parameters that are used in the analysis and the results (calculated values) normalized to the German tensile stress metric are listed in Table 58. Tensile stress metrics normalized to the German values are within 20% of the German value indicating the tensile stress component should be similar in all these particle designs [108]. It was also indicated in the analysis that the irradiation-induced PyC shrinkage resulting in a strong compressive component to the stress in the SiC layer was not credited [108].

TABLE 58. PARAMETERS CONTRIBUTING TO TENSILE STRESSES IN THE SIC LAYER

Parameter	German	JAEA HTRR	JAERI Advanced	U.S. LEU	U.S. LEU Fertile	U.S. NPR	U.S. AGR
Particle design parameters							
Kernel composition	UO <sub>2</sub>	UO <sub>2</sub>	UO <sub>2</sub>	UCO	UCO	UCO	UCO
Kernel diameter (μm)	500	600	550	350	500	200	425
Buffer thickness (μm)	95	60	100	100	65	100	100
IPyC thickness (μm)	40	30	35	35	40	50	40
SiC thickness (μm)	35	30	35	35	35	35	35
OPyC thickness (μm)	40	45	40	40	40	40	40
Enrichment (%)	10.6	6	10	19.9	0.7	93	14.0
Burnup (% FIMA)	10	2.6	10	26	6	80	17
Calculated values							
Simple tensile stress metric	0.676	0.643	0.763	0.799	0.608	0.816	0.785
Normalized to German value	1.00	0.95	1.13	1.18	0.90	1.21	1.16

#### 7.4. PARAMETERS AFFECTING FUEL PERFORMANCE

A radar chart of the five most important parameters affecting fuel performance is shown in Fig. 107 [108]; NNGP project was established by US Department of Energy (DOE) in 2005:

- Fuel temperature is the key parameter for potential failure mechanisms and fission product transport mechanisms during normal operating conditions and under postulated accident condition;
- Fuel burnup is the parameter that determines the concentration of fission products in the kernel and thus the gas pressure and fission product concentration in the particles;
- Fuel fast fluence is the factor governing the extent of radiation damage in the particles and the potential alterations in properties and dimensions in the layers;
- Power density, along with thermal conductivity and the geometry of the fuel (such as compact or pebble), determines the temperature gradient across the fuel specimen, as some potential failure mechanisms are contingent on this temperature gradient;
- Particle packing fraction is the parameter employed with the global power density and it can be used to establish the power per particle, which establishes the temperature inside the particle.

Figure 107 shows the higher envelope for the five key parameters for the US program, NGNP: higher packing fraction (40% vs up to 30% for German and Japanese fuel), higher power density (10 W/cm<sup>3</sup> vs up to 4 W/cm<sup>3</sup> for German and Japanese fuel), higher burnups (20% FIMA vs up to 10% FIMA for German and Japanese fuel), higher fast fluence (5x10<sup>25</sup> n/m<sup>2</sup> vs 4x10<sup>25</sup> n/m<sup>2</sup> for German and Japanese fuel), and higher time-average fuel temperatures (1250°C vs up to 1200°C for German and Japanese fuel) based on information from Ref. [108].

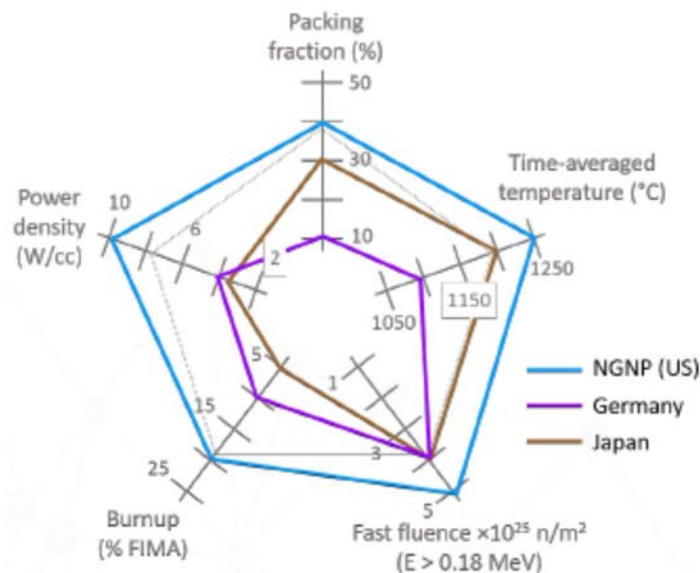


FIG. 107. Radar chart of key parameters for TRISO fuel performance (courtesy of EPRI).

## 7.5. FUEL FAILURE MECHANISMS

During normal and abnormal conditions, coating integrity is of paramount importance: coating layers should remain intact to retain fission products. Fission products can be retained in the kernel, in the intact layers (i.e., the coating integrity is maintained) and in the matrix. The main mechanism for the fission product transport is diffusion. In the case of SiC layer failure with at least one pyrocarbon layer intact, most condensable fission products will be released but fission gases will be retained. In the case of failure of all three dense coating layers of TRISO particle, both fission gas and condensable fission products will be released.

For the coating layers, a number of potential failure mechanisms have been identified [4,10,108], which are functions of temperature, burnup, fluence, and temperature gradient across the particle, as:

- Overpressure – SiC failure caused by internal gas pressure.
- IPyC related issues, leading to SiC failure:
  - Irradiation induced IPyC shrinkage and IPyC cracking;
  - Debonding between IPyC and SiC;
  - Thermal creep – thinning of IPyC;
  - Thermal shock – thermal stresses induced by the discontinuous fabrication process were well below the failure strength of IPyC.
- OPyC related issues, leading to SiC failure:

- Matrix-OPyC interaction – OPyC cracking;
  - Matrix-OPyC interaction – OPyC debonding from the SiC layer;
  - Thermal creep.
- Factors directly leading to SiC failures:
- Kernel migration (amoeba effect);
  - Fission product attack;
  - Non-retentive SiC: diffusive release through intact layers; SiC degradation resulting in permeability to fission products
  - 
  - SiC thermal decomposition.
- Kernel-coating mechanical interaction (KCMI).
- As-manufactured defects produced during fabrication of fuel particles or during pressing of fuel compacts/spheres.

Table 59 summarizes the fuel service conditions and the parameters that influence the fuel failure mechanisms.

TABLE 59. FUEL FAILURE MECHANISMS AND PARAMETERS INFLUENCING FAILURE MECHANISMS

<b>Failure mechanism</b>	<b>Service conditions</b>	<b>Parameters influencing failure mechanism</b>
Overpressure	Temperature Burnup Fast fluence	Strength of SiC Buffer density (void volume) Fission gas release Kernel type Layer thicknesses IPyC and OPyC performance
Irradiation induced PyC failure	Fast fluence Temperature	Dimensional change of PyC Irradiation induced creep of PyC Anisotropy of PyC Strength of PyC PyC thickness PyC density Tensile stress in SiC at IPyC crack tip SiC strength
PyC thermal creep	Time at temperature	Thickness of PyC Stress state of PyC <i>Only, at very high temperatures (&gt; 2000°C) and very long durations, where thermal creep can operate.</i>
Kernel migration	Temperature Burnup Temperature gradient	Kernel type (UO <sub>2</sub> , UCO, etc.) Buffer and IPyC thickness
Fission product attack	Temperature Burnup Temperature gradient Time at temperature	Chemical state/transport behaviour of fission products Kernel type (UO <sub>2</sub> , UCO, etc.) Microstructure of IPyC and SiC
Non-retentive SiC: Diffusive release through intact layers	Temperature Burnup Temperature gradient Time at temperature	Chemical state/transport behaviour of fission products Microstructure of SiC SiC thickness
Non-retentive SiC: corrosion of SiC by CO	Temperature Burnup Time at temperature	Kernel type (UO <sub>2</sub> , UCO, etc.) IPyC integrity

TABLE 59. FUEL FAILURE MECHANISMS AND PARAMETERS INFLUENCING FAILURE MECHANISMS

Failure mechanism	Service conditions	Parameters influencing failure mechanism
Non-retentive SiC: SiC degradation (by Cs) resulting in permeability to fission products	Burnup Temperature Fast fluence	Microstructure of SiC SiC thickness Permeability of SiC SiC impurities from fabrication process
SiC thermal decomposition	Temperature Time at temperature	Microstructure of SiC SiC thickness
Kernel coating mechanical interaction	Burnup Fast fluence Temperature	Initial kernel-coating gas gap Buffer properties IPyC properties Kernel swelling rate

### 7.5.1. Overpressure

Fission gases that are released from the kernel to the porous buffer layer and CO gas<sup>17</sup>, that is formed as a result of the reaction of the oxygen released during fission with the carbon buffer layer, exert tensile forces on the IPyC and SiC layer of the particle, as discussed in Section 7.2. The production of O, CO and fission gases depends primarily on burnup and temperature. To avoid the particle failure by overpressure, a large buffer layer is included. The particle failure is postulated to occur if particles are coated with an insufficient or missing buffer layer [4]. Fabrication specifications were imposed to limit the number of particles produced with thin or missing buffer layers and limits were imposed on the statistical variation in kernel diameter and buffer thickness. The pressure required to fail the SiC layer (or the particle) is given in Equation (1). Photomicrographs displaying overpressure failures for different fuel particles are presented in Fig. 108 [10].

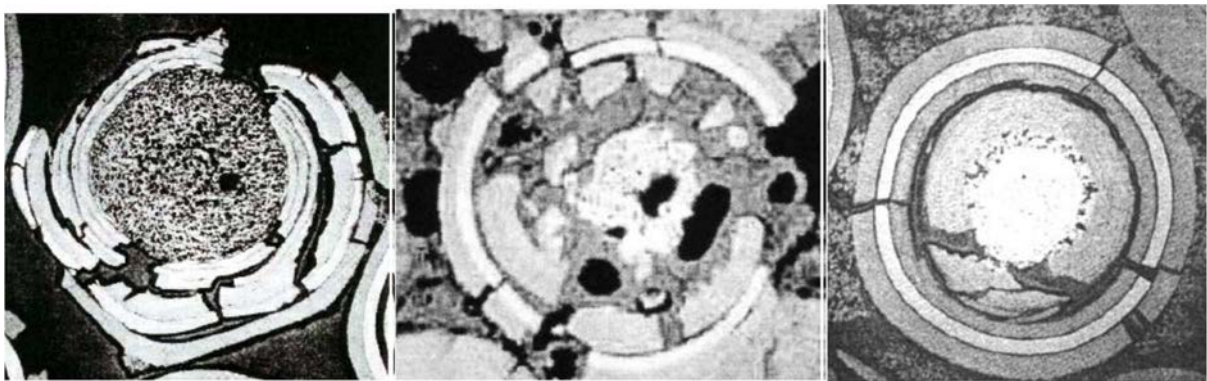


FIG. 108. Overpressure failures from different fuel particles (courtesy of INL).

### 7.5.2. Inner pyrocarbon layer related issues leading to SiC failure

IPyC related issues leading to SiC failure include:

- Irradiation induced IPyC shrinkage which ultimately leads to the failure of the SiC layer;
- Debonding between IPyC and SiC;

<sup>17</sup> “CO is not expected to be produced in a (UCO) kernel, provided enough uranium carbide is added to the kernel to ensure that there is no excess oxygen available from fission to react with the buffer layer over the burnup life of the fuel.” [4]

- Thermal creep – thinning of IPyC layer;
- Thermal shock.

#### 7.5.2.1. Irradiation-induced IPyC cracking

Early on the irradiation, PyC shrinks in both radial and tangential directions. At modest fluences ( $\sim 2 \times 10^{25}$  n/m<sup>2</sup>), it begins to swell in the radial direction and continues to shrink in the tangential direction, resulting in PyC layers to be in tension in the tangential direction. Later-on in the irradiation, irradiation induced creep works to relieve the tensile stress in the PyC layer. If there exists a robust bond between PyC and the SiC layer, the shrinkage of PyC imparts a robust compressive stress in the SiC layer, counteracting the tensile stresses induced by gas production. In essence, the particles are engineered so that in undamaged particles, the SiC layer sustains compressive stress throughout the irradiation [10].

Based on many US irradiation tests<sup>18</sup>, it was found that the shrinkage exceeded expectations, resulting in significant tangential stresses in the PyC layer, leading to its cracking. These cracks induced concentrated tensile stresses in the SiC layer, ultimately causing the failure of the SiC layer. The crack crosses the buffer layer and the IPyC layer and terminates at the IPyC-SiC interface.

High anisotropy in the PyC layer that was produced in the US fuels due to coating process with too low coating gas concentrations (corresponding to a very low coating rate) was found to be the reason for this failure mechanism, because this failure was not observed (i.e., excessive irradiation induced shrinkage was prevented) in the German fuels that achieved a better isotropy by coating at higher coating rates. In addition, the thicker the PyC layer, the larger are the stresses that may lead to failures [4].

Figure 109 shows the tangential stresses in the SiC layer of a TRISO particle with an initially cracked IPyC [22] (also see [171]). The stress in the SiC at the IPyC crack tip increases with irradiation time (fast fluence) as the IPyC shrinks, though it relaxes later due to irradiation-induced creep of the IPyC. When the IPyC is intact, SiC is under compression stresses. The higher the temperatures, the lower the compression stresses. Cracks in the IPyC causes the stresses in SiC layer changing from compression to tensile. The higher the temperatures, the lower the tensile stresses.

---

<sup>18</sup> “This is by far the most common fuel failure mechanism observed in the US GA NPR fuel...Thus, the experimental evidence to date suggests that this mechanism is most likely not important for very isotropic PyC – German fuel” [10].

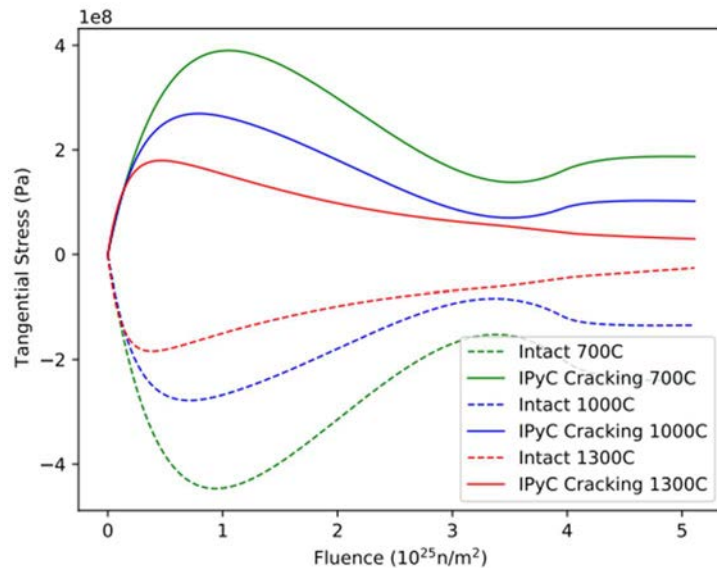


FIG. 109. Finite element model for TRISO-particle with cracked IPyC (courtesy of INL).

#### 7.5.2.2. Debonding between IPyC and SiC

In numerous US irradiations, separation at the IPyC-SiC interface has been noted, primarily ascribed to the characteristics of the IPyC-SiC interface. Coating layers with weak bonds, as seen in US fuel, may undergo partial detachment due to the radial tensile stresses induced by PyC shrinkage during irradiation. Large tensile stresses in the SiC layer can develop in a particle with partially debonded IPyC from the SiC.

Figure 110 shows the tangential stresses in the SiC layer of a TRISO particle with partially debonded IPyC from the SiC layer [10]. Tensile stresses occur at the point of IPyC-SiC contact as the IPyC shrinks under irradiation. Later, irradiation induced creep relieves the stress. With the Weibull statistics, these stresses were used to calculate the SiC failure probability, for which the analysis concluded that the SiC fails at a low rate.

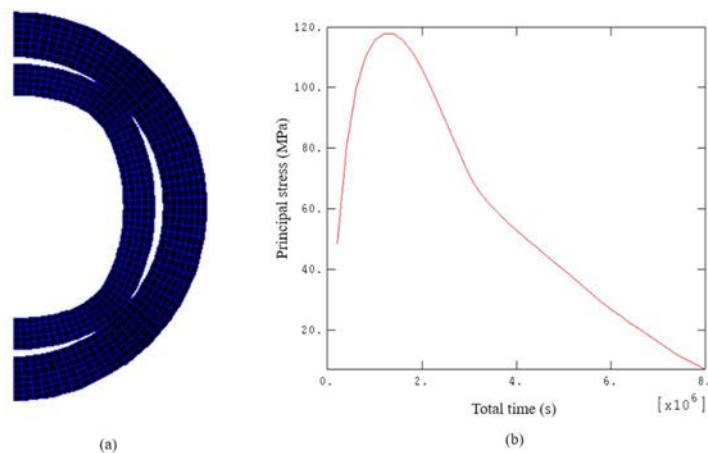


FIG. 110. (a) Finite element model for TRISO particle with partially debonded IPyC from SiC layer and (b) tangential stresses in the SiC layer (courtesy of INL).

### 7.5.2.3. Thermal creep

Some post-irradiation heating tests at very high temperatures ( $> 2000^{\circ}\text{C}$ ) and very long durations, where thermal creep can operate, revealed a thinning and failure of the IPyC, though such failures were not observed to lead to failure of the SiC layer [4].

### 7.5.2.4. Thermal shock

Unlike the German fuel, the US fabrication of TRISO particles includes a discontinuous coating process (i.e., after each coating layer, the process stops and is reinitiated for the other layer). Hence, the hypothesis posited that subjecting the particles to loading and unloading after depositing each layer in US fuel could induce thermal shock, potentially resulting in the formation of microcracks in the IPyC layer. Over time, these microcracks might propagate and contribute to fuel failure during irradiation [10]. An analysis was performed to quantify the effect of thermal stresses on the failure of IPyC with the conclusion that the thermal stresses induced by this discontinuous fabrication process were well below the failure strength of IPyC [10].

## 7.5.3. Outer pyrocarbon layer related issues leading to SiC failure

OPyC related issues leading to SiC failure include:

- Matrix-OPyC interaction – OPyC cracking;
- Matrix-OPyC interaction – OPyC debonding from the SiC layer;
- Thermal creep.

### 7.5.3.1. Matrix-OPyC interaction – OPyC cracking

Matrix-particle interaction involves in a strong bond between the outer coating and the matrix material. In the early US coated particle fuel development, OPyC layer failed by cracking (as shown in Fig. 111 [172]) because during the compact fabrication, the liquid carbonaceous matrix material intruded in the OPyC and both materials densified under irradiation, resulting in tensile forces that destroys coating integrity if their bond is not broken first. The German fuel did not exhibit such a behaviour because of the powdered matrix material, which was difficult to infiltrate into OPyC, and more isotropic OPyC [10].

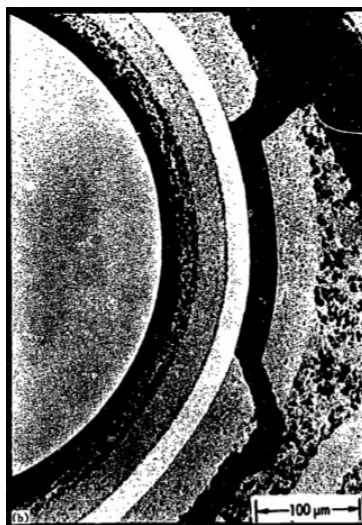


FIG. 111. Particles broken during irradiation due to matrix-particle interaction (courtesy of ORNL).

### 7.5.3.2. Matrix-OPyC interaction – OPyC debonding from SiC layer

In the early US coated particle fuel development, OPyC layer failed by debonding from SiC layer because during the compact fabrication, the liquid carbonaceous matrix material intruded in the OPyC and shrunk under irradiation. The German fuel did not exhibit such a behaviour because of the powdered matrix material, which was difficult to infiltrate into OPyC, and more isotropic OPyC [10].

### 7.5.3.3. Thermal creep

Some post-irradiation heating tests at very high temperatures ( $> 2000^{\circ}\text{C}$ ) and very long durations, where thermal creep can operate, revealed a thinning and failure of the OPyC, though such failures were not observed to lead to failure of the SiC layer [4].

## 7.5.4. Factors directly leading to SiC failures

The factors directly leading to SiC failures include:

- Kernel migration (amoeba effect);
- Fission product attack;
- Non-retentive SiC: diffusive release through intact layers; SiC degradation resulting in permeability to fission products;
- SiC thermal decomposition.

### 7.5.4.1. Kernel migration (Amoeba effect)

As discussed in section 2.3.1, kernel migration, also known as the amoeba effect, is associated with carbon transport in the particle when there is a temperature gradient. In the absence of temperature gradient, there is an equilibrium between C,  $\text{UO}_2$  and CO [10]. In the presence of a thermal gradient across the particle, different equilibrium conditions are reached on each side of the particle, resulting in the mass transport of carbon down the temperature gradient, which is visually evident in photomicrographs of the fuel as a displacement of the kernel up the temperature gradient. This phenomenon is referred to as "kernel migration," as illustrated in Fig. 112 [172], for  $\text{UO}_2$  that achieved 79.8% FIMA at a fast fluence of  $6 \times 10^{21}$  n/cm<sup>2</sup>, time-average temperature of  $1200\text{--}1220^{\circ}\text{C}$ , and a thermal gradient of  $1000\text{--}1030^{\circ}\text{C/cm}$  (based on fuel thermal conductivity).



FIG. 112.  $\text{UO}_2$  exhibiting the amoeba effect (courtesy of ORNL).

Figure 113 [172] shows the average kernel migration as a function of temperature, which can also be interpreted as the average thermal stability of kernels. The shaded area and the region above it indicate a performance deemed unacceptable. This determination involved calculating kernel migration coefficients associated with the movement of the kernel through the buffer layer during regular operation in various zones of a large HTGR core. Figure 113 illustrates that the  $\text{UO}_2$  curve intersects the shaded region within the temperature range crucial for the large HTGR. In contrast, the curves for  $\text{UC}_2$  and Th-based carbide and oxide consistently remain below the shaded area across all temperatures. Therefore, the favourable performance of  $\text{UC}_2$  and Th-based fuel relative to  $\text{UO}_2$  suggested dilution of  $\text{UO}_2$  either with enough  $\text{ThO}_2$  in Ref. [172] or with enough  $\text{UC}_2$  (as adapted in the UCO kernel) for stabilization.

The temperature and temperature gradient in the fuel are the main factors, followed by burnup, causing the kernel migration. In pebble bed cores, the occurrence of the phenomenon was not observed in German irradiation experiments or during AVR and THTR operation. This absence is attributed to the lower power densities and, consequently, smaller thermal gradients in pebble bed cores, preventing the manifestation of the phenomenon. However, in prismatic cores with  $\text{UO}_2$  fuel, where power densities in the particles are greater, kernel migration was observed in a number of US irradiations. Consequently, US decided to change the kernel design from  $\text{UO}_2$  to UCO with the anticipation of no CO production, and elimination of re-equilibration and carbon transport phenomena. With a proper C/O ratio, kernel migration in UCO fuel was not observed in US irradiation experiments [10].

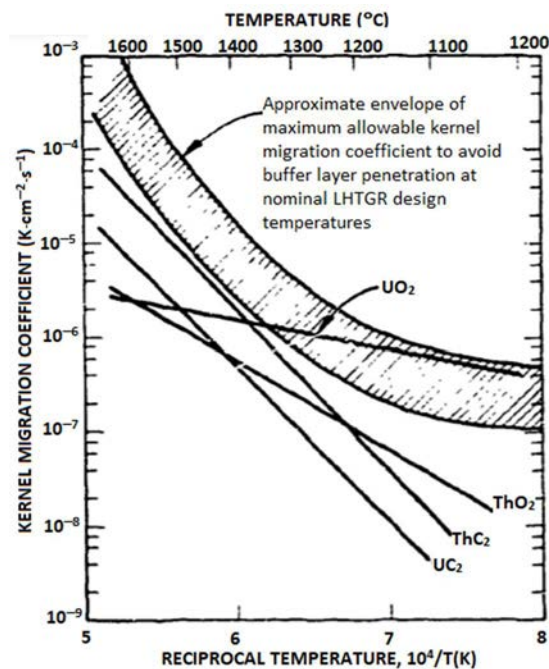


FIG. 113. Average fuel kernel migration coefficient with temperature (courtesy of ORNL).

#### 7.5.4.2. Kernel extrusion

HRB-14 experiments were performed in the HFIR at ORNL) using fertile and fissile TRISO particle fuels:  $\text{ThO}_2$ ,  $\text{UC}_x\text{O}_y$ ,  $(\text{Th,U})\text{O}_2$ ,  $\text{UO}_2$  [10]. Upon metallographic examination of fissile particles, findings revealed that 3% of the IPyC layers exhibited failure (cracking), and debonding from the SiC layer occurred in 7.7% of the particles. In  $\text{UO}_2$  or  $(\text{Th,U})\text{O}_2$  fuel, the buffer layers remained crack-free; however, in UCO fuel, 71% of the particles experienced cracking in the buffer layers. Notably, kernel extrusion, as depicted in Fig. 114 [10], was exclusively reported in UCO fuel.

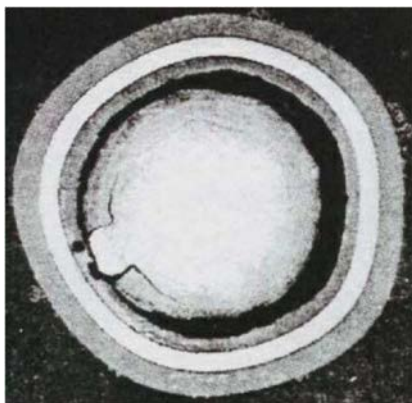


FIG. 114. Kernel extrusion (courtesy of INL).

#### 7.5.4.3. Fission product attack

Fission products, including the REs (cerium, neodymium, lanthanum, samarium, praseodymium, and europium), palladium, ruthenium, and rhodium of the platinum family, and strontium, were observed to be transported from the kernel to the inner surface of the SiC layer [173]. The concern is that fission products interact and can damage the SiC layer (see Fig. 115 [4]). SiC-fission product reactions occur in two modes:

- Based on temperature gradient; REs-SiC reactions on the inner surface of the cooler side of SiC coatings;
- Independent of temperature gradient at the localized reaction sites.

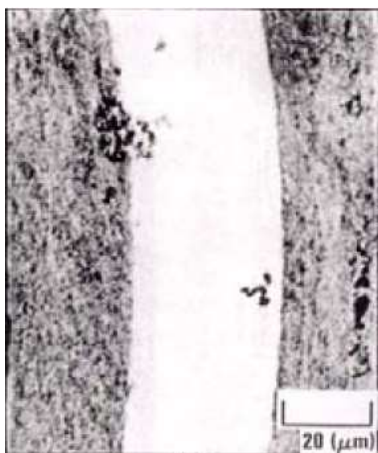


FIG. 115. Fission product attack of the SiC layer (courtesy of IAEA).

Although the second mode of attack is generally attributed to palladium, reactions of ruthenium, rhodium, strontium and silver with SiC reactions were also observed [173]. SiC corrosion by Pd was postulated to be a failure mechanism in TRISO fuels, however, the occurrence of a locally elevated Pd concentration, induced by a crack in the IPyC layer, is a crucial prerequisite for the chemical reaction between Pd and SiC. Without this condition, Pd undergoes migration in the SiC layer through diffusion without engaging in a chemical reaction with SiC [166]. Another noteworthy fission product is Cs, given its relatively high fission yield of radioactive isotopes  $^{134}\text{Cs}$  and  $^{137}\text{Cs}$ . Despite this, Cs is generally well retained in TRISO coated particles. Earlier studies indicated that even when half the SiC layer thickness

was corroded by Pd, the integrity of the layer and its ability to retain volatile fission products, such as Cs, remained uncompromised [167].

Drawing from HRB-14 experiments, significant concentrations of fission products were identified in small, localized regions at the interface between the SiC and IPyC layers. Alongside fission product accumulation, instances of localized chemical attack were observed in the SiC layers of various (Th,U)O<sub>2</sub> and UO<sub>2</sub> fuel particles [10]. This localized attack, penetrating approximately 2 μm into the SiC, was attributed to palladium and was present in 8% of the particles. In UCO fuel particles without localized chemical attack, uniform attack along the inner SiC layer was observed. This uniform attack was attributed to REs. With optimized UCO stoichiometry, the kernel retained RE fission products, preventing kernel migration observed in non-optimized UCO kernels containing excess UC<sub>2</sub>, leading to RE migration [10].

Palladium is not significantly retained in the kernel of any U-C-O composition. In irradiated kernels of dense LEU UO<sub>2</sub>, PuO<sub>2-x</sub>, ThO<sub>2</sub>PuO<sub>2-x</sub>, a portion of Pd was found to be incorporated into noble metal inclusions, while the majority of Pd had been released from the kernel and was located within the SiC coating. Therefore, Pd is of concern for both UO<sub>2</sub> and UCO kernels. In addition, some other noble fission products are of concern for the UO<sub>2</sub> kernels, whereas in the UCO kernel, metals (Ag, Cs) are of concern. Other fission products are tied up in the UCO kernel either in carbide or oxide form, and hence their mobility is limited in the particle. Though it is not a failure mechanism, in both UO<sub>2</sub> and UCO, the migration of silver was observed and there are concerns related to maintenance (worker dose) implications: Ag can migrate through intact particles and be released into the reactor coolant system and deposit on cold surfaces, which may happen to be in the turbine for direct cycle gas reactors [10].

### *Separate effects*

Enrichment, O/U ratio, density of the kernel and power density are some of the parameters affecting the concentration of the fission products or the permeability to fission product migration:

- Enrichment: The concentration of certain fission products that impact SiC integrity is influenced by the isotopic composition of HTGR fuel. This variation arises due to the differing ratios of fissioning isotopes (<sup>235</sup>U, <sup>239</sup>Pu, <sup>241</sup>Pu) with changes in uranium enrichment, and because the fission product yields from each isotope are not the same. Ag and Pd can be 25 to 50 times higher depending on the U or Pu concentrations in the fuel [173]. Therefore, the change in isotopic composition (and hence fission product concentrations) from HEU (93% enriched <sup>235</sup>U) to LEU (19.5% enriched <sup>235</sup>U) was investigated [173].
- In LEU fuels, where a substantial portion of fission arises from Pu at the end of life, the concentrations of Ag and Pd can be considerably higher than in HEU fuel with similar burnups [10]. At peak burnup (~25% FIMA), the fission products with great inventories in typical LEU fuel particles include Mo, Ru, Rh, Pd, Ag and Cd. Ag is 11 times, and Pd and Cd are 4.5 times higher in a 300 mm LEU kernel than in a 200 mm HEU kernel [173].
- O/U ratio: Based on the study performed at ORNL, RE fission products migrate down the temperature gradient to the cool side of the particle when O/U ≤ 1.1; however, at higher O/U ratios, the REs are retained in the kernel [173].
- Density: Kernels with lower densities do not retain any amount of Pd; palladium and strontium attack on SiC observed in LEU DRAGON TRISO UO<sub>2</sub> which had an 80% theoretical density;
- Power density (prismatic vs pebble bed): While temperature gradient is the most important parameter for the fission product migration, temperature and burnup also play a role in their migration. Fission product attack is expected to be more pronounced in particles in prismatic reactors due to larger power densities, compared to those in pebble bed reactors (see Section 7.4).

#### 7.5.4.1. Non-retentive SiC: diffusive release through intact layers

Based on the heating test data, some of the fission products (e.g. caesium) that are usually retained by the TRISO coating can diffuse out of the particle during normal operation, if the fuel temperatures during normal operation approach 1300°C [4].

#### 7.5.4.2. Non-retentive SiC: SiC degradation resulting in permeability to fission products

The permeability of the SiC layer to fission products can be compromised under irradiation and high temperatures. When the fuel was exposed to high fluences ( $4 \times 10^{25} - 6 \times 10^{25} \text{ n/m}^2$  vs.  $2-4 \times 10^{25} \text{ n/m}^2$ ) and high burnups (14% FIMA vs 8–9% FIMA), greater release of fission products (e.g. caesium) in heating tests was observed [2]. Two different mechanisms were suggested for the degradation of SiC layer: caesium attack of the SiC and/or CO corrosion of the SiC [4]:

- Caesium vapour can attack SiC at temperatures in excess of 1500°C. Pitting of the SiC layer was observed when SiC samples were exposed to caesium vapour.
- CO generated during irradiation of UO<sub>2</sub> kernels can attack the SiC layer (see Fig. 116 [108]) if the IPyC layer is either permeable or cracked.

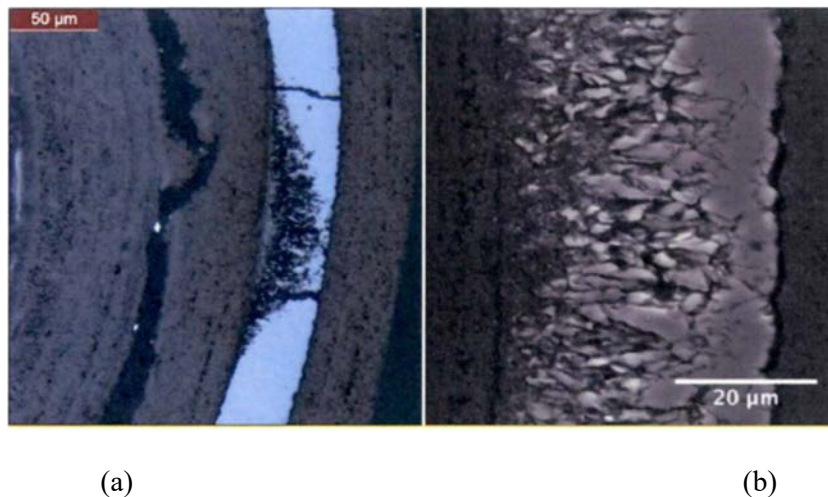


FIG. 116. A region of the SiC layer corroded by CO in an irradiated UO<sub>2</sub> particle heated to 1600°C: (a) optical image, (b) magnified electron image (courtesy of EPRI).

#### 7.5.4.3. SiC thermal decomposition

At temperatures above 2000°C, thermal decomposition of SiC occurs rapidly: SiC decomposes into its constituent elements, and silicon vaporizes, leaving a porous carbon structure. This failure mechanism is not expected to be an important contributor to fuel failure at normal operating or postulated accident conditions, based on calculations performed for previous core designs [108].

#### 7.5.5. Kernel-coating mechanical interaction

The KCMI is expected to occur at sufficiently high burnups when all gas gaps between the kernel and coatings close due to the swelling of kernel during the irradiation. Based on modelling, SiC layer was predicted to fail shortly after the onset of KCMI [4].

### 7.5.6. As-manufactured defects

Heavy metal contamination outside of the SiC layer and initially defective particles (i.e., as fabricated fuel defects) can contribute to the releases of fission products. Initially defective particles can be due to undetected as-fabricated defective particles, attack of the particles during fabrication or irradiation (experiments) by impurity metals (e.g. Fe), or particles that have failed during compacting the particles into a matrix (i.e., pebble or fuel compact). To minimize heavy metal contamination and as-fabricated defects, stringent control of key parameters during the fabrication was implemented in US during the NGR program.

### 7.5.7. Failure mechanisms during accidents

During accident conditions, when the TRISO particle is subjected to air and/or water exposure, carbon materials and fuel kernels undergo reactions with air and water [14]. Water ingress predominantly impacts exposed kernels, leading to the release of a significant portion of their stored inventory, while reactions with carbon materials are relatively moderate, resulting in less aggressive fuel damage. Air reacts not only with the exposed kernels, but also reacts with the carbon materials at a greater rate than water. In both cases, reactions with the carbon materials will release absorbed fission products.

In a reactivity insertion accident, the abrupt release of high energies within the coated particle fuel can induce overheating, overpressure, and ultimately rupture, leading to the release of fission products. Based on analysis, coated particle fuel is expected to fail with energy depositions in the range of 1000–2000 J/g [14]. The duration of the reactivity insertion accident was estimated to be a few seconds with energies much larger than that required to damage fuel particles.

## 7.6. PARAMETERS AFFECTING PARTICLE PERFORMANCE DURING NORMAL OPERATING CONDITIONS

During normal operation, it is expected that the fuel failure rate is very low. Fuel failures occur during operation due to design, manufacture and operating environment. The sources of fission product releases during normal operation include [14]:

- As –fabricated particle defects (e.g. flawed SiC particles, particles broken during fuel element fabrication) and the presence of uranium impurities in the fuel element fabrication will result in uranium outside of the SiC coating, the pyrocarbon, or both;
- Releases from particles experiencing failure (attributed to missing or thin buffer layers or poor-quality pyrocarbon prone to cracking) during routine operation will lead to elevated internal pressure, culminating in eventual rupture at some point during the core's operational life;
- Hot spots in the core increases the probability of failure from other sources such as amoeba (for UO<sub>2</sub> in particular) or fission product corrosion of the SiC layer;
- Silver (<sup>110m</sup>Ag) released from particles at temperatures above 1100°C (as SiC does not retain silver well above approximately 1100°C) is viewed as an occupational dose matter rather than a public health and safety issue in current designs.

Fission gases will transfer to the coolant and can be eliminated through the coolant gas clean up system, though metallic fission products will remain in the reactor internal components, because it appears to be no practical way to remove metallic releases from an operating reactor [14].

### 7.6.1. Kernel

Besides its functionality for power generation, the kernel is expected to control the oxygen potential to limit kernel migration and particle CO pressure, and to retain the REs [14]. The kernel contains gases to some extent, though at high burnups (and at high temperatures), the kernel may not be able to retain fission gases due to changes in the microstructure (i.e., void formation with burnup) and the change in lattice structure with burnup, increasing the diffusion of fission products.

Table 60 shows the operating parameters affecting the kernel performance and the performance of the particle via kernel during normal operating conditions.

TABLE 60. KERNEL OPERATING PARAMETERS

<b>Kernel operating parameter</b>	<b>Rationale</b>
CO production	CO production influences particle pressure and kernel migration.
Burnup	The level of burnup determines the chemical state in the kernel and its ability to retain fission products.
Swelling	The kernel swells because of fission products and the buffer layer is designed to accommodate the kernel distortion.
Microstructure changes	The crystal structure of the kernel can influence the retention of fission products.
Fission product chemical form	The chemical form of the fission products determines their mobility with the kernel and affects the CO pressure.
Buffer interaction	The periphery of the kernel may react with the buffer layer carbon.
Kernel migration ( <i>fuel dependent</i> )	Temperature gradients can drive carbon transfer and result in the movement of the kernel towards the coatings.
Fission product generation	Different fissile isotopes produce different mixes of fission products. Isotopes that generate more noble metals will cause degradation of performance due to the noble metal attacks to the SiC.
Temperature gradient	The temperature gradient across the kernel drives the amoeba effect and REs fission product migration.
Isotope half-life	Isotope half-life determines which fission products will survive the diffusion to and through the coatings.

### 7.6.2. Buffer layer

The buffer layer is to provide a free space for the released fission gases and any generated CO. The particle can fail by overpressure if sufficient volume to accommodate the volume of generated gas is not provided by the buffer layer. An excessively thick (out of specification) buffer could increase thermal impedance, though this extra impedance does not appear to adversely affect particle performance. Nevertheless, based on some calculations, thermal gradients can drive fission product diffusion [14].

Table 61 shows the operating parameters affecting the buffer performance and the performance of the particle via the buffer during normal operating conditions.

TABLE 61. BUFFER OPERATING PARAMETERS

<b>Buffer operating parameter</b>	<b>Rationale</b>
Pressure	The buffer function is to provide void volume to control particle pressure.
Shrinkage and cracking	It is desirable to control buffer shrinkage in order to control cracks and to minimize kernel extrusion. Cracking may also allow recoil path to IPyC.
Temperature gradient	An excessive gradient can lead to higher kernel temperatures.
Condensed/gas phase diffusion	Buffer is the first layer that encounters the fission product releases.
Recoil effects	The buffer layer protects the IPyC layer by attenuating the fission product recoils.

### 7.6.3. Inner pyrocarbon layer

The IPyC is engineered to maintain dimensional stability and integrity throughout the fuel's lifespan. The occurrence of cracks or debonding in the IPyC may generate localized tensile stresses in the SiC, leading to potential cracking if the bond between the two layers is robust. Cracks can expose the SiC to CO, causing corrosion at elevated temperatures. Additionally, the IPyC serves as a barrier to the transport of fission products to the SiC; it exhibits high permeability to fission gases while allowing the diffusion of metallic fission products.

Table 62 shows the operating parameters affecting the IPyC performance and the performance of the particle via IPyC during normal operating conditions.

TABLE 62. IPYC OPERATING PARAMETERS

IPyC operating parameter	Rationale
Irradiation-induced creep	Irradiation-induced IPyC creep relieves some of the stress in the IPyC caused by irradiation-induced shrinkage and pressure.
Fast fluence	The fluence dose has an impact on the shrinkage, creep and layer stresses.
Dimensional change	The stresses caused by irradiation can result distortion and debonding of the IPyC from the SiC.
Anisotropy	The anisotropy plays an important role for the IPyC dimensional stability.

### 7.6.4. Silicon carbide layer

With the SiC layer, being the main barrier to fission product release, releases to the coolant are expected to be dominated by the initial defective fuels and failures caused by other phenomena during normal operation. The exception is silver. Above 1100°C, silver will diffuse through the SiC into the coolant. Furthermore, prolonged operation of the fuel at elevated temperatures exceeding 1300°C may result in SiC corrosion by noble metals and CO, particularly in cases where the IPyC is cracked. Palladium is the primary noble metal of concern due to its facile diffusion into the SiC and its propensity to react with SiC, leading to the formation of silicide. The type of kernel is important for noble metal inventory: depending on the fissile material, the kernel may have higher or lower yields of noble metals. If the kernel does not retain the REs as oxides, they can attack the SiC. In the event of heavy metal contamination in the SiC layer during the fabrication process, the fissioning of this material can cause SiC damage, ultimately resulting in premature failure.

Table 63 shows the operating parameters affecting the SiC performance and the performance of the particle via SiC during normal operating conditions.

TABLE 63. SiC OPERATING PARAMETERS

SiC operating parameter	Rationale
Kernel interaction with SiC layer	Temperature gradients can drive carbon transfer and result in the movement of the kernel towards the coatings.
Fission product corrosion	Noble metals present a corrosion hazard at high temperatures.
CO attack	CO can attack SiC with a cracked IPyC at high temperatures
Heavy metal attack	If fissile material is present in the SiC layer from fabrication, fission in the SiC layer will damage it.

TABLE 63. SiC OPERATING PARAMETERS

SiC operating parameter	Rationale
Cracking	Cracking will cause the particle to release metallic fission products, but not gases, if one of the PyCs remain intact.
Condensed/gas phase diffusion	SiC is the primary diffusion barrier and it retains both metallic and gaseous fission products, with the exception of silver.

### 7.6.5. Outer pyrocarbon layer

The OPyC layer is designed to remain dimensionally stable and intact over the fuel lifetime. Failure of the OPyC could increase the failure probability of the SiC. The shrinkage of the OPyC is limited by OPyC creep, keeping the stresses in the layer within acceptable limits. The OPyC limits the transport of fission gases, but not the metallic fission products. The control of OPyC-matrix interactions is desirable so that the OPyC is not damaged by matrix shrinkage or micro cracks that occur in the matrix material.

Table 64 shows the operating parameters affecting the OPyC performance and the performance of the particle via OPyC during normal operating conditions.

TABLE 64. OPyC OPERATING PARAMETERS

OPyC operating parameter	Rationale
Irradiation-induced creep	Irradiation-induced creep relieves some of the stresses caused by shrinkage and pressure.
Dimensional change	The stresses caused by irradiation can result distortion and possible breakage of the OPyC layer.
Anisotropy	Anisotropy is the factor affecting the OPyC dimensional stability.
Condensed/gas phase diffusion	OPyC does not retain well metallic fission products, though serves as a barrier for fission gases in the case of SiC failure.
Cracking	Cracking causes easy transport of fission products, in the case of SiC failure to the fuel matrix.

### 7.6.6. Fuel element

The main functions of the fuel element include [14]:

- Maintain dimensional stability;
- Not transmit undue stresses to the fuel particles;
- Withstand external damage mechanisms, such as the fall of pebbles into the reactor core from the entrance;
- Maintain good thermal properties;
- Act as a sink for any released metallic fission products.

Elements made with a high filler concentration tend to be more stable than those with low filler concentration. Microcracks and voids may form in the fuel element due to shrinkage of the material, though minor cracking is tolerable for intact particles. Corrosion by coolant impurities can affect fuel elements and result in “peeling” or “spalling” of small regions (<200 mm deep) on the surface of pebbles [14].

Due to irradiation damage, matrix material's mechanical and thermophysical properties change. For the fuel pebbles, matrix irradiation performance was very good for the operating temperatures (<1400°C) and fast fluences of interest (<9×10<sup>25</sup> n/m<sup>2</sup>) [14]. Irradiation temperature and accumulated fast fluence strongly influence property changes, but the pebbles maintain integrity under the irradiation conditions of interest. Under irradiation [14]:

- Pebbles exhibited a diameter shrinkage of less than 2%, and this shrinkage was approximately equal in both radial and tangential directions up to a fast fluence of 5×10<sup>25</sup> n/m<sup>2</sup>. Beyond this value, it deviated by about 30%.
- Strength increased by about 10% at moderate fast fluences, and the elastic modulus showed an increase with irradiation, reaching up to 70% at 700°C. Subsequently, it only experienced a slight decrease at higher fast fluences. Crush strength almost doubled.
- Thermal conductivity decreased about 60% and the coefficient of thermal expansion increased by about 40% with irradiation.

Matrix material either sorbs metallic fission products or delays their migration into the coolant at normal operating temperatures, though gases readily migrate through the matrix material.

Table 65 shows the operating parameters affecting the fuel element performance and the performance of the particle via fuel element during normal operating conditions [93].

TABLE 65. FUEL ELEMENT OPERATING PARAMETERS

<b>Fuel element operating parameter</b>	<b>Rationale</b>
Temperature	Temperature and fast fluence affect the matrix behaviour (e.g. shrinkage, cracks) and stability.
Fast fluence	Fast fluence affects the matrix behaviour (e.g. shrinkage, cracks).
Power density	Power affects the operating temperature and gradients.
Temperature difference	The behaviour of fuel particles can be affected by micro temperature gradients in the fuel matrix.
Temperature histories	Time at temperature is a factor determining corrosion and diffusion.
Condensed phase diffusion	The matrix material can sorb/trap significant amounts of less volatile fission products.
Gas phase diffusion	The element does not retain gases significantly.
Corrosion by coolant impurities	Coolant impurities can corrode/damage the fuel element matrix.

### 7.6.7. Summary

A total of thirteen parameters, characteristics and phenomena were identified to be of high importance during normal operating conditions for kernel, coatings and the fuel element, as listed in Table 66.

TABLE 66. OPERATING PARAMETERS OF HIGH IMPORTANCE

Layer	Parameter
Kernel	Carbon monoxide production
Buffer	Pressure Cracking Temperature gradient
IPyC	Cracking Condensed phase diffusion Gas phase diffusion
SiC	Fission product corrosion Cracking Condensed phase diffusion Gas phase diffusion
OPyC	Gas phase diffusion
Fuel element	Condensed phase diffusion

## 7.7. FUEL FAILURES DURING NORMAL OPERATIONS

During normal operating conditions, it is expected that the integrity of the coating layers is maintained.

### 7.7.1. German fuel

For the German fuel, among approximately 380 000 UO<sub>2</sub> and 80 000 (Th,U)O<sub>2</sub> particles subjected to testing, there were no in-pile failures, and only a few particles were considered 'damaged' due to experimental anomalies [10]. Gas release was attributed solely to as-manufactured defects and heavy metal contamination.

Similarly, accelerated irradiation tests conducted for German LEU UO<sub>2</sub> TRISO particles showed no particle failures for 754 000 particles; however, at high burnups (14% FIMA) and temperatures (1700°C) some releases were observed [108].

Based on numerous studies, it has been concluded [108] that the German fuels had low as-manufactured particle defect fractions, low particle failure fractions during irradiation and during post-irradiation heating tests at postulated accident temperatures.

### 7.7.2. Chinese fuel

During irradiation tests in Russia, it was observed that two of the irradiated spheres had one or two exposed kernels from the initial stages of irradiation, aligning with the free-uranium measurements obtained during the manufacturing of early production batches. Similarly, performed on two Chinese pebbles irradiated in the HFR Petten reactor, the <sup>85m</sup>Kr R/B ratio for the capsule was approximately  $8 \times 10^{-8}$  [108]. The calculated release fraction of <sup>85m</sup>Kr from a single coated particle is  $3.26 \times 10^{-3}$ . In a capsule containing two pebbles (~16,600 particles), the release fraction from a single failed particle is  $1.96 \times 10^{-7}$  [108]. This suggests that there was no complete particle failure during the irradiation, and the observed fission gas release is attributed to uranium impurities in the carbonaceous matrix of the pebbles and the graphite cups used for pebble retention. The early batches had a free-uranium content (measured by the burn-leach procedure) of typically  $10^{-4}$ , whereas the last 15 batches were normally  $10^{-5}$  and lower [108].

For the development of HTR-PM (with a capacity of 210 MWe) in China, irradiation testing of five HTR-PM fuel spheres was performed in the Petten High Flux Reactor (HFR). The free uranium fraction in the pebbles decreased from  $5 \times 10^{-4}$  for the HTR-10 (existing prototype reactor) to  $6 \times 10^{-5}$  for the HTR-PM. According to neutronics calculations, the total fast fluence levels were estimated between

3.79 and  $4.95 \times 10^{25}$  n/m<sup>2</sup> (E >0.1 MeV), and burnup was between 11.1 % FIMA and 13.7% FIMA. Measured <sup>85m</sup>Kr R/B values during the last cycle were between  $2.4$  and  $3.3 \times 10^{-9}$ , indicating no particle failure [108]. Based on the preliminary post-irradiation experiments, the dimensional shrinkage in all five pebbles was between 0.88% and 1.25% [108].

### 7.7.3. US fuel

In most experiments of US fuel performed prior to the year 2000, a significant fraction of the TRISO-coated particles experienced failure of one or more layers. Failures of the coating layers were ascribed to various factors [10], including: (a) SiC failure, (b) kernel migration (amoeba effect), (c) fission product attack on the SiC layer, (d) irradiation-induced IPyC cracking and/or debonding leading to cracking in the SiC layer, and (e) carbon matrix-OPyC interaction and irradiation-induced OPyC failure. The PyC-related mechanisms are strongly influenced by the anisotropy and porosity in the coatings. Anisotropy has a significant impact on the shrinkage and swelling behaviour of the PyC layers under irradiation.

Figure 117 shows the frequency of layer failures observed during PIE of early US coated particle fuel from different irradiations [10].

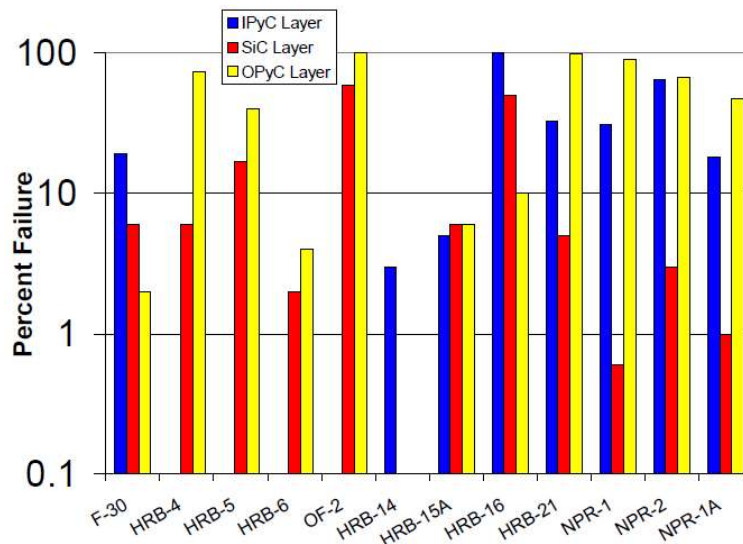


FIG. 117. Failures observed during PIE of US coated particle fuel from different irradiations (courtesy of INL).

Later under the AGR Program (with the objective to advance fabrication and characterization technologies and generate irradiation and annealing performance data necessary for licensing TRISO particle fuel for the NGNP and upcoming HTGRs) in the US, irradiation experiments were performed, and low-frequency SiC layer failure (i.e., failure of the SiC layer with at least one PyC layer remaining intact) was identified [108]. SiC failure was due to the buffer shrinkage contributed to IPyC fracture: IPyC fracture was due to the stress from the buffer pulling away from the IPyC and the IPyC fracture exposed the SiC layer to concentrated chemical attack of fission products (notably Pd), causing degradation through the entire layer. Very low fractions of TRISO failure (i.e., failure of all three dense coating layers such that fission gas is released) were observed [108].

Table 67 shows the specifications for particle defects and failure fractions for NGNP at the core outlet temperature of 750°C [6]. The design value of TRISO failure fraction during normal operating conditions at the core outlet temperature of 750°C is  $\leq 2.0 \times 10^{-4}$ .

TABLE 67. SPECIFICATIONS FOR PARTICLE DEFECTS AND FAILURE FRACTIONS FOR NGNP

Parameter	Maximum expected	Design
As manufactured fuel quality		
Heavy metal contamination	$\leq 1.0 \times 10^{-5}$	$\leq 2.0 \times 10^{-5}$
Defective SiC		
	$\leq 5.0 \times 10^{-5}$	$\leq 1.0 \times 10^{-4}$
In-service TRISO failure		
Normal operation	$\leq 5.0 \times 10^{-5}$	$\leq 2.0 \times 10^{-4}$
Accidents	$\leq 1.5 \times 10^{-4}$	$\leq 6.0 \times 10^{-4}$

The TRISO failure fraction in a fuel with UCO kernel after the AGR-1 and the AGR-2 capsule irradiation tests was  $\leq 2.3 \times 10^{-5}$  [108]. This represents an approximately nine-fold reduction compared to the standard reactor design specifications for acceptable in-service TRISO failures during normal operational conditions ( $2 \times 10^{-4}$ ).

Figure 118 [108] shows the SiC layer and TRISO particle failure fractions for combined AGR-1 and AGR-2 UCO results during irradiation and during annealing tests. The combined (AGR-1 + AGR-2) SiC failure fractions in a fuel with UCO kernel were  $\leq 3.6 \times 10^{-5}$  during irradiation [108]. Note that historic reactor performance requirements have not included specifications for SiC layer failure.

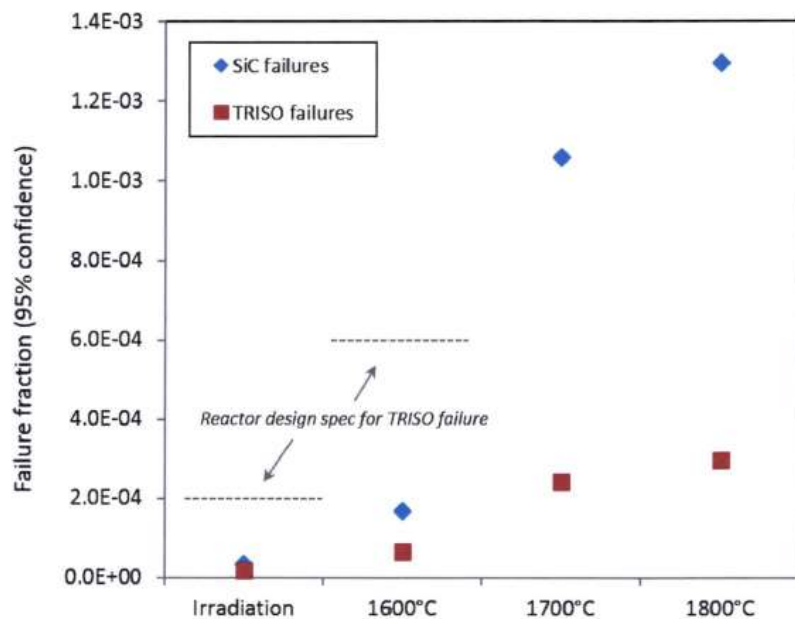


FIG. 118. SiC layer and TRISO particle failure fractions (upper limit at 95% confidence) for combined AGR-1 and AGR-2 UCO results during irradiation and during annealing tests (courtesy of EPRI).

There were no observed TRISO or SiC failures in the AGR-2  $UO_2$  fuel compacts following the irradiation. Despite a higher occurrence of SiC failures in annealing tests compared to UCO, there were no instances of TRISO failures in the three annealing tests conducted at 1600°C, 1700°C, and 1800°C [108].

Densification of the buffer layer and swelling of the kernel with related formation of gas filled bubbles were commonly observed [108]. The buffer layer experienced partial or complete debonding from the IPyC layer in most particles. This debonding was induced by buffer densification and volume shrinkage, resulting in the formation of a void between the buffer and IPyC layer. In the particles in which the buffer and IPyC layers remained completely bonded, the buffer densification resulted in the inner diameter increase while the kernel swelled to fill the increasing volume. Buffer fracture was common, and it was often accompanied by expansion of the kernel (i.e., kernel extrusion) into the gap formed at the point of fracture. Buffer failure fraction of 86% was observed for the compacts irradiated at a temperature of ~1100°C, whereas that of 1–2% was observed for those irradiated at a temperature above 1200°C, which is believed to be due to greater magnitude of thermal creep occurring at the higher temperatures, which relaxes stresses developed due to buffer densification and shrinkage [108]. However, buffer fracture seems not to pose a threat to the particle integrity, as there were very low SiC and TRISO coating failure fractions.

In the case where there was a buffer and IPyC layer separation and buffer fracture, no outer dense coating layer failure was observed, even in cases where the kernel was in direct contact with the IPyC layer [108]. When the buffer-IPyC interface remained intact, the fracture of the buffer layer coincided with the fracture of the IPyC layer. This often led to debonding of the IPyC layer from the SiC layer [108]. Without a buffer fracture, the partial debonding of the buffer-IPyC layer led to development of sufficient stress in the IPyC layer to cause fracture in some particles.

Caesium fractional release from compacts containing only particles with intact SiC was very low. The total Cs release from the fuel compacts will increase depending on the extent of SiC layer failure. The releases of Eu and Sr were modest through intact coatings, and they were significantly retained in the fuel matrix, though at higher irradiation temperatures (up to a time-average maximum of 1360°C), the releases of Eu and Sr became higher. Silver release was notably high, aligning with historical patterns. Interestingly, there was no widespread evidence of Pd attack or corrosion of SiC, even though measurable amounts of Pd were detected outside of the SiC layer [108].

#### 7.7.4. Japanese fuel

Based on the first core irradiation in the HTTR, the measured R/B ratio of <sup>88</sup>Kr at full power and at the coolant outlet temperature of 950°C was  $1.0 \times 10^{-8}$ , corresponding to gaseous diffusion from heavy metal contamination and no significant in-reactor fuel particle failures [108].

From the first batch core loading of HTTR, the TRISO particle design was slightly modified (i.e., larger buffer layer: 90 vs 60 μm in the original core loading, and slightly larger SiC layer: 35 vs. 25–30 μm) to operate at higher burnups (5–10% FIMA vs 2.4% FIMA which was the end-of-life core average burnup in the original core loading and 3.6% FIMA was the design limit peak burnup) [174]. The fuel compacts utilizing UO<sub>2</sub> fuel kernels, featuring a slightly modified particle design, underwent irradiation in the 91F-1A capsule at the Japan Materials Testing Reactor (JMTR) operated by JAERI and in the HRB-22 capsule at the HFIR operated by ORNL [175]. The maximum burnup and the fast neutron fluence were about 10% FIMA and  $3 \times 10^{25}$  n/m<sup>2</sup>, respectively [175]. Two through-coatings failed particles were detected at the beginning of irradiation for the HRB-22 capsules [175]. Post-irradiation examinations revealed the absence of kernel migration and SiC corrosion [174]. Within the deconsolidated coated fuel particles irradiated in the 91F 1A capsule, only one failed particle was identified, indicating that the OPyC layer experienced cracking due to tensile stress [174]. In addition, in the 91F-1A capsule irradiation test, it was estimated one fuel particle failure based on comparison of measured and calculated R/B ratios of <sup>88</sup>Kr. In the HRB-22 capsule irradiation test, four fuel particle failures were observed during irradiation. Calculation results showed [174] that no tensile stresses acted on the SiC layers even at the end of irradiation, and no SiC layer failure occurred in the intact particles even in a particle with thin buffer layer with failed OPyC layer. In conclusion, the presumed failure mechanisms were identified to be additional through-coatings failure of as-fabricated SiC failed particles, and an excessive increase of internal pressure by the accelerated irradiation [174].

The preliminary calculation findings indicate [175] that solely relying on mean fracture stress values for PyC and SiC does not allow for predicting particle failures, defined as the failure of all three load-bearing layers. In contrast, incorporating statistical variations in fracture stresses and particle specifications, as accomplished in the STAPLE code, enables the prediction of failures.

When high fracture stresses were employed for each of the three load bearing layers (IPyC, SiC and OPyC), namely 400 MPa, up to 8% FIMA, stresses in the SiC were always compressive, and neither of the PyC layers had failed [175]. However, experimentally, failures were observed. Therefore, for the failure of all three load bearing layers, one or both PyC layers must have fractured first. Setting the fracture stress of a PyC layer to 50 MPa resulted in early failure [175]. If the IPyC layer failed prematurely, the stress in the SiC layer at 8% FIMA became tensile, reaching 25 MPa. Premature OPyC layer failure increased the stress slightly to 36 MPa, while simultaneous IPyC and OPyC failure raised the tangential stress in the SiC layer at 8% FIMA to 125 MPa [175]. Clearly, failure of all three load-bearing layers is most likely if both the IPyC and OPyC layers fail first.

The compact contained 4400 particles, and in the calculation for better statistics, ten times that number of particles were used. Figure 119 [175] illustrates the number of calculated failed particles as a function of burnup, showing that 1 and 2 failures occurred at around 7.5 and 8% FIMA respectively, consistent with observations of 1–2 particle failures towards the end of irradiation.

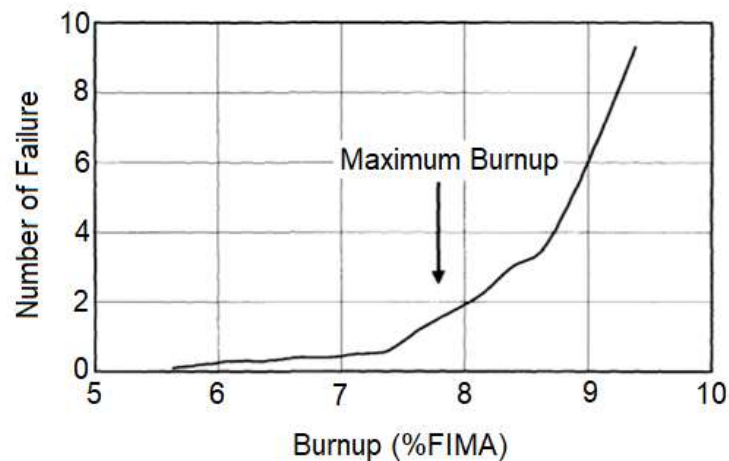


FIG. 119. Calculated number of fuel failures for the fuels irradiated in JMTR and HFIR (courtesy of JAEA).

Similarly, Fig. 120 shows the predicted failure fractions as a function of fuel burnup level for thorium and depleted uranium, based on Ref. [176]. Predicted fuel failure fraction exceeds the predefined safety limit of  $10^{-4}$  when the fuel achieves a burnup of 8% FIMA. In the analysis, the dominant failure mode for TRISO particles was expected to be failure of the SiC layer, and Weibull theory was used for predicting failure probabilities. Weibull statistical strength theory represents a distribution of SiC strengths within a population of TRISO particles and allows failure probability predictions for this population:

$$P_f = 1 - \exp \left[ - \ln 2 \left( \frac{\sigma_{t,SiC\_calc}}{\sigma_{t,SiC\_ms}} \right)^m \right] \quad (20)$$

where  $P_f$  is the failure probability of the SiC layer,  $\sigma_{t,SiC\_calc}$  is the maximum calculated tangential stress in SiC (MPa), which can be assumed to be equal to the tangential stress at the inner surface of the SiC,  $\sigma_{t,SiC\_ms}$  is the SiC Weibull mean strength (MPa), and  $m$  is the SiC Weibull modulus [176].

Assuming that the manufacturing results for each parameter conform to a truncated Gaussian distribution with user-specified values for the standard deviation and upper and lower truncation bounds, the TRIUNE code was utilized for calculating failure probabilities and simulating the lifetime history of each particle. At each time step, following the completion of stress-strain-displacement calculations, Weibull failure probabilities were computed for each particle. The effective predicted batch failure fraction (Batch FF) for the entire particle population is then determined as [176]:

$$\text{Batch FF} = \frac{\sum_{n=1}^N P_f^n}{N} \quad (21)$$

where Batch FF represents the overall predicted failure fraction for a batch comprising  $N$  particles (specified by the user),  $P_f^n$  stands for the Weibull failure probability of the particle with the number  $n$ .

A failure fraction limit of  $10^{-4}$  was adopted to ensure that radiation source terms, resulting from radiation escaping from the particles and passing through the pebbles into the coolant, do not surpass a predefined threshold [176].

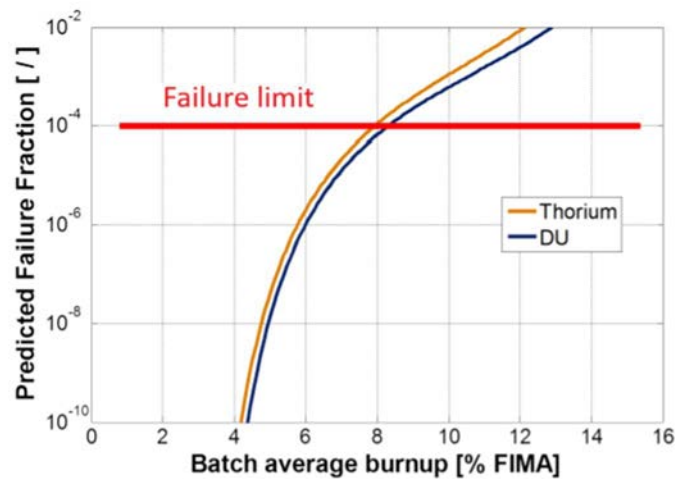


FIG. 120. Calculated failure fraction as a function of burnup for Th-based and depleted uranium fuels.

Furthermore, additional modifications in the HTTR particle design were made (e.g. increase in the buffer thickness: 95  $\mu\text{m}$ ), such that it closely resembled the standard TRISO particle design from the German programme [108]. Based on the irradiation tests of this fuel to a burnup of  $>9\%$  FIMA in the WWR-K reactor (Kazakhstan), no in-pile particle failures occurred, and R/B data indicated a few exposed kernels, which were postulated to be related to as-fabricated SiC defects [108].

#### 7.7.5. Summary

As discussed in Section 7.4, the operating parameters would affect the fuel performance: high temperature, large temperature gradient, high burnup, high power density and high particle packing fraction would adversely affect the fuel performance. Such differences have been identified for fuel compacts to be used in prismatic block HTGRs and spherical elements to be used in pebble bed HTGRs. Compared to the US fuel compacts, the German pebbles were being operated at lower burnups (10% FIMA for German pebbles vs 20% FIMA for US compacts), fast fluence ( $4 \text{ n/m}^2$  vs  $5 \times 10^{25} \text{ n/m}^2$ ), power density ( $4 \text{ W/cm}^3$  vs  $10 \text{ W/cm}^3$ ), packing fraction (10% vs 40%) and fuel time average temperatures ( $1100^\circ\text{C}$  vs  $1250^\circ\text{C}$ ). Therefore, the US fuel compacts have been exposed to harsher conditions.

The German pebbles exhibited minimal as-manufactured particle defects and low particle failure fractions both during irradiation and post-irradiation heating tests at anticipated accident temperatures. Conversely, in the case of Chinese pebbles, the releases were attributed to as-manufactured defects, specifically uranium impurities present in the carbonaceous matrix of the pebbles.

During the initial stages of US fuel compact development, a significant number of fuel failures occurred, attributed to various factors, including: (a) SiC failure, (b) kernel migration (amoeba effect), (c) fission product attack on the SiC layer, (d) irradiation-induced cracking and/or debonding of the IPyC layer resulting in SiC layer fractures, and (e) graphite matrix-OPyC interaction leading to irradiation-induced OPyC failure. Under the most recent AGR fuel development program, SiC failure was observed due to the buffer shrinkage contributed to IPyC fracture, and the fracture in the IPyC layer was ascribed to stress induced by the buffer pulling away from the IPyC due to buffer shrinkage. This IPyC fracture exposed the SiC layer to concentrated chemical attack from fission products, particularly Pd, resulting in degradation throughout the entire layer. Cs was significantly retained in the kernel and the release was low in a particle with intact SiC layer. The Eu and Sr releases through intact SiC layer were modest, though at higher irradiation temperatures (up to a time-average maximum of 1360°C), the release of Eu and Sr became higher. High silver release was consistent with historical patterns, yet there was no pervasive Pd attack or corrosion of SiC observed, despite the presence of substantial amounts of Pd outside the SiC layer.

Release from the early design of the Japanese fuel were attributed to the heavy metal contamination of the matrix and no significant in-reactor fuel particle failures were observed. Later, the design was slightly modified (e.g. thicker buffer layer) for fuels to operate at higher burnups. OPyC layer crack by tensile stress was observed for one particle. For the other fuel failures, based on calculations, it was concluded that additional through-coating failure of as-fabricated SiC failed particles, and an excessive increase of internal pressure by the accelerated irradiation were identified to be the failure mechanisms. The release fraction of fission gases increases with burnup due to the irradiation-enhanced diffusion.

Fuel failures may be expected to increase when the fuel reaches a burnup of 7–8% FIMA due to the internal pressure increase and the changes in the SiC layer tangential stresses from compression to tension, depending on particularly the layer thicknesses (i.e., buffer and SiC), and when the fuel is exposed to high temperatures exceeding 1600°C (which will be discussed in the next section) due to the degradation of the SiC layer by CO attack or increased fission product attack.

## 7.8. FUEL FAILURES UNDER ACCIDENT CONDITIONS

Four classes of accident conditions were considered in [14]:

- Core heat up due to the loss of helium pressure and flow, resulting in the fuel achieving a peak temperature of roughly 1600°C. Note that a temperature of 1800°C was considered to envelope phenomena of interest.
- Reactivity insertion due to rod ejection accident (that was considered to be the basis for the accident conditions). A sudden reactivity addition could result in locally high fuel temperatures and/or fuel damage.
- Air ingress, resulting from the complete severing of the horizontal vessel between the reactor vessel and the power conversion system vessel, is followed by depressurization and air diffusion into the core. To mitigate the depressurization accident with air ingress, it is crucial to control or limit the oxidation rate and exposure duration. This can be achieved by delaying the entry of air into the core until the core temperatures have sufficiently reduced and by restricting the air flow rate through the core. It is essential to keep fuel temperatures and reactant flow rates within limits to prevent fuel particle damage. Core matrix degradation occurs rapidly at temperatures exceeding 1600°C. The loss of protective matrix material may expose fuel particles, leading to chemical attack and the release of retained fission products into the coolant. Sustained air ingress with high carbon reaction rates is only possible if a self-sustaining flow of air is established while the fuel is still at a relatively high temperature. Once the OPyC is breached, SiO<sub>2</sub> is

produced as SiC oxidizes, forming a layer on the particle that impedes further reaction. However, in an oxygen-limited atmosphere above 1300°C, SiO<sub>2</sub> may convert to volatile SiO, allowing the SiC to SiO reaction to continue unabated.

- Water ingress due to failure of a heat exchanger tube with reactor depressurization: the failure of the pressure boundary and depressurizing the core with a heat exchanger failure would allow water entry under low driving pressure.

Table 68 lists the behaviour of kernel and coating layers during the four postulated accidents: depressurization – core heat up, reactivity insertion, air and water ingress accidents. Table 69 through Table 74 list the parameters of interest identified for the kernel and the coating layers under the four postulated accidents. The parameters with high importance were marked with ‘X’ in the tables.

TABLE 68. BEHAVIOUR OF KERNEL AND COATING LAYERS DURING ACCIDENTS

Layer	Depressurization (core heat-up)	Reactivity insertion	Air ingress	Water ingress
Kernel	The temperatures in the fuel are expected to be below the melting point of the kernel material. The diffusion of fission products from the kernel will be increased at high temperatures during a heat up accident, having an impact on the integrity of the SiC, which is the primary barrier to the release of fission products. In particular, noble metals are of interest as they are known to attack the SiC layer. If the time at temperature is long enough and if SiC is corroded during normal operation, the SiC layer may fail by the additional diffusion of the fission products at higher temperatures. In addition, CO that migrates through cracks in IPyC can attack SiC and increase the stresses in the layers. As the temperature increases, the oxygen potential of the kernel may change, shifting the equilibrium. The vapour pressure of the volatile species is expected to increase.	In a reactivity insertion accident, the abrupt deposition of energy leads to a rapid increase in the kernel temperature, causing the sudden release of fission products that were trapped within the grains and crystal structure. Additionally, there is a possibility of kernel melting during this event. Sudden release of fission products will result in a sudden pressure increase or pressure pulse, over-pressurizing and breaking the coating layers, and further increasing the temperature of the coatings. Based on experiments, the energy deposition rate for fuel damage is in the range of 1000–2000 J/g.	It is expected that the kernel will behave similarly as in the case of a core heat up accident, if the fuel particle is intact; however, it can be oxidized by oxygen or CO (the oxygen is converted to CO by the large amount of carbon in the reactor system) if the kernel is exposed. In the course of oxidation, the structure of the kernel changes and it releases much of its stored fission product inventory relatively quickly. It is possible that a catalyst can increase reaction rates under certain conditions.	If the fuel particle remains intact during a water ingress accident, the behaviour of the kernel is similar to that during a core heat up event. However, when the kernel is exposed, it can undergo oxidation by water. This oxidation process alters the structure of the kernel, leading to a rapid release of a significant portion of its stored fission product inventory. The extent of this effect seems to be influenced by the burnup level. Exposed kernels are particularly vulnerable to water vapour, reacting swiftly and releasing fission products at a faster rate, while intact particles experience minimal impact. Therefore, under water ingress conditions, the predominant fuel releases are governed by the releases from exposed kernels,

TABLE 68. BEHAVIOUR OF KERNEL AND COATING LAYERS DURING ACCIDENTS

Layer	Depressurization (core heat-up)	Reactivity insertion	Air ingress	Water ingress
				especially at moderate temperatures. The behaviour is contingent on the partial pressure of water, and the potential influence of catalysts on reaction rates under specific conditions remains uncertain.
Buffer	Similar to the normal operating conditions, during a core heat up accident, the buffer layer is to provide void volume for gases in order to control the gas pressure in the fuel particle. It also provides little retention of fission products.	Since the buffer layer provides the expansion space for any gases suddenly released from the kernel during the accident, it affects the response of the coated fuel particle to a reactivity event, which could result in a short pressure pulse that could damage the coating.	For an intact particle, the buffer will behave similarly as in the case of a core heat up accident; however, once exposed, it will be oxidized, and the oxidizer will be quickly transported to the kernel. The buffer in an exposed particle provides little resistance to fission product transport. A catalyst can increase reaction rates under certain conditions.	The buffer layer functions similarly to its role in a core heat up accident for an intact particle. However, when exposed, it provides minimal resistance to the transport of fission products and may undergo slow oxidation upon exposure to water. Additionally, the buffer layer facilitates the rapid transport of water vapour to the kernel.
IPyC	Generally, the IPyC layer maintains the SiC layer in compression. Nevertheless, if the IPyC layer breaks or cracks, it can lead to elevated localized stresses in the SiC layer. Moreover, a crack in the IPyC layer can expose the SiC layer to CO, potentially causing corrosion at elevated temperatures during accidents. Full debonding of the IPyC may result in a change in the pressure loading. Decomposition or chemical reactions of the IPyC layer are not of importance for a core heat up accident. Similar to the normal operating conditions, dimensional	During the pulse, the particle pressure may increase the stresses in the IPyC layer. The particle integrity can be maintained by accommodating the particle pressure.	For an intact particle, the IPyC will behave similarly as in the case of a core heat up accident; however, once exposed (i.e., the OPyC and SiC layers are damaged), the IPyC undergoes a chemical reaction. This layer serves as the final barrier for gases (metals would have initiated diffusion through the layer), and thus, the failure of this layer results in the release of any contained	During water ingress, the considerations for the IPyC are akin to those during a core heat up event, with the additional factor of chemical attack. If the OPyC and SiC layers remain intact, the IPyC will not be exposed to a new environment. However, if the other layers become damaged or cracked, the IPyC would be exposed to water and susceptible to a chemical reaction. Given that this

TABLE 68. BEHAVIOUR OF KERNEL AND COATING LAYERS DURING ACCIDENTS

Layer	Depressurization (core heat-up)	Reactivity insertion	Air ingress	Water ingress
	<p>stability is important for a core heat up accident. Metallic fission products will diffuse through the layer at a greater rate, but the gaseous diffusion should still be small for an intact layer.</p>		<p>gases and exposes the kernel to the oxidizing environment, triggering subsequent reactions within the kernel.</p>	<p>layer serves as the final barrier for gases (metals will have started diffusing through the layer), its failure would result in the release of any stored gases and expose the kernel to the oxidizing environment, initiating subsequent reactions within the kernel.</p>
SiC	<p>The integrity of the layer can be compromised by pressure, corrosion, and decomposition. Pressure can be managed through particle design, corrosion by sequestering most fission products, and controlling operating temperature to mitigate Pd attack (and CO attack in case of IPyC cracking). Decomposition can be addressed by restricting the maximum accident temperature. Above 1600°C, porosities start developing in SiC, indicating that thermal decomposition mechanisms are active, and above 2000°C, thermal decomposition of SiC is a dominant failure mechanism. Corrosion of SiC layer during normal operation can weaken the SiC layer and can cause the failure under the greater pressure at accident temperatures. Silver and radiological important fission products diffuse through the SiC, as the temperatures increase and the time at temperature becomes significant. Accident releases tend to increase with peak accident</p>	<p>The SiC layer has to remain undamaged despite the induced stresses. In the event of a substantial internal pressure pulse, the fracture toughness of SiC becomes crucial. The temperature of the layer during and after the incident is a significant factor, as elevated pressures and layer temperatures around or above 1600°C could lead to failure.</p>	<p>Under air ingress conditions, the SiC layer behaves similarly to a core heat up accident until the OPyC is subjected to chemical attack. If the OPyC weakens and fails, the stress state of the SiC may change, potentially leading to failure if the SiC has been weakened by other factors. Following OPyC loss, the SiC is exposed to air and CO. Depending on the conditions, either SiO<sub>2</sub> or SiO (lower oxygen content) can form. SiO<sub>2</sub> is non-volatile and impedes the reaction rate, as the reactant has to diffuse through it. On the other hand, SiO is gaseous and does not provide this protection. The specific details of the reacting environment determine the damage and rate of damage to the SiC layer. Thinning of</p>	<p>Under water ingress conditions, the SiC layer behaves similarly to a core heat up accident until the OPyC is subjected to chemical attack. As the OPyC weakens and fails, the stress state of the SiC may change, potentially leading to failure if the SiC has been weakened by other factors. The SiC would then be exposed to water and possibly some generated CO. Thinning of this layer can result in particle failure due to SiC failure as pressure vessel, and penetration of the layer will lead to the release of metallic fission products and expose the IPyC to oxidation.</p>

TABLE 68. BEHAVIOUR OF KERNEL AND COATING LAYERS DURING ACCIDENTS

Layer	Depressurization (core heat-up)	Reactivity insertion	Air ingress	Water ingress
	temperature, and larger releases occur above 1600°C. SiC can be attacked by both fission products and fabrication impurities.		this layer can result in particle failure due to SiC failure as the pressure vessel, and penetration of the layer will lead to the release of metallic fission products and expose the IPyC to oxidation.	
OPyC	The OPyC maintains the SiC layer in compression, and the rupture or cracking of the OPyC can result in heightened local stresses in the SiC, increasing the risk of its failure. For a core heat up accident, the decomposition or chemical reactions of the OPyC layer are not critical, though dimensional stability remains important. During a core heat up accident, metallic fission products may diffuse through the layer at an accelerated rate, but the gaseous diffusion is anticipated to be minimal for an intact layer. There is a possibility that fission products trapped within the layer (intercalation) could be released at higher temperatures. Additional interaction between the OPyC and the matrix is not expected.	The OPyC layer is to support the SiC during a power pulse to keep it from exceeding its ultimate stress	In the presence of air ingress, the OPyC initially behaves similarly to its role in a core heat up scenario. However, over time, it experiences erosion. The loss of OPyC due to chemical attack has a comparable impact, with the added consequence that the SiC layer is now vulnerable to attack.	In the presence of water ingress, the OPyC initially functions similarly to its role in a core heat up scenario, followed by erosion. The loss of OPyC due to chemical attack has a comparable effect, with the additional consequence that the SiC layer is now exposed to attack.

TABLE 69. PARAMETERS, CHARACTERISTICS AND PHENOMENA OF HIGH IMPORTANCE TO ACCIDENT CONDITIONS FOR KERNEL

	Depressurization (core heat-up)	Reactivity insertion	Air ingress	Water ingress
<b>ALL ACCIDENTS</b>				
Maximum fuel temperature: Temperature affects chemical reactions and fission product diffusion.	X	X	X	X
Time at temperature:	X	X	X	X

TABLE 69. PARAMETERS, CHARACTERISTICS AND PHENOMENA OF HIGH IMPORTANCE TO ACCIDENT CONDITIONS FOR KERNEL

	Depressurization (core heat-up)	Reactivity insertion	Air ingress	Water ingress
Diffusive releases are determined based on time at temperature. Time at temperature has an impact on the amount of material reacted and fission product release.				
Thermodynamic state of fission products: Chemical form of fission products affects their diffusion/mobility. The chemical state of fission products, which is a function of temperature for oxidizing elements, determines the vapour pressure and how they migrate. The goal is to tie rare earth elements and limit CO production.	X	X	X	X
Energy transport: Determines kernel temperature and fission product diffusion from the kernel.				
Oxygen flux: Oxygen diffusion can increase at high temperatures. A substantial repositioning of oxygen has the potential to alter the oxygen potential and, consequently, the chemical species of fission products within the kernel.				
Grain growth: Grain growth is expected to occur <sup>19</sup> at high temperatures, affecting the fission product diffusion from kernel to the kernel-buffer interface: “Grain growth could release fission products from the grain to the grain boundary region, thus enhancing transport.”				
Buffer carbon-kernel interaction: Some interaction between the kernel and the buffer carbon is possible at high temperatures: the kernel periphery may react with the buffer carbon.				
<b>DEPRESSURIZATION AND REACTIVITY ACCIDENTS</b>				
Condensed phase diffusion: Higher temperatures increase the diffusion rate. Diffusion of fission products is affected by how the accident phenomena progress (e.g. grain growth, occurrence of kernel melting).	X	X		
Gas phase diffusion Higher temperatures increase the diffusion rate.	X			
<b>REACTIVITY ACCIDENTS</b>				
Energy deposition (total):		X		

<sup>19</sup> In Ref. [14], it was indicated “grain growth may increase fission product transport”, though the reason was not explained. In the conventional UO<sub>2</sub> pellets, larger grains would provide longer mean free path to fission product diffusion to the grain boundaries and hence delays the fission product release, as grain boundaries provides an easy path for fission product/gas release. However, in TRISO, if the grain size becomes as large as the kernel size, the diffusion of fission products to the kernel-buffer interface will be facilitated, and hence fission product transport is increased.

TABLE 69. PARAMETERS, CHARACTERISTICS AND PHENOMENA OF HIGH IMPORTANCE TO ACCIDENT CONDITIONS FOR KERNEL

	<b>Depressurization (core heat-up)</b>	<b>Reactivity insertion</b>	<b>Air ingress</b>	<b>Water ingress</b>
Energy deposition determines the fuel and core temperature.				
Energy deposition rate: Energy deposition rate determines the likelihood of impulsive fuel damage and system response time.				
<b>AIR/WATER INGRESS ACCIDENTS</b>				
The kinetics of chemical attack by air or water will govern the rates at which fission products are released.				
Chemical attack by air / water – catalysis: Some fission products or impurities can increase the reaction rate.				
Chemical attack by air / water – changes in chemical form of fission products: The availability of oxygen may elevate the oxygen potential of the kernel, leading to alterations in the chemical form of fission products, thereby influencing transport properties.				
<b>AIR INGRESS ACCIDENTS</b>				
Chemical attack by air – changes in graphite properties: Modifications in the characteristics of graphite (or PyC) have the potential to impact the transport of fission products or the liberation of entrapped fission products.				
Chemical attack by air – holdup reversal: Structural and chemical changes to the kernel may release stored fission products.				
Chemical attack by air – temperature distribution: The temperature of the kernel and surrounding material will affect reaction rates and the transport of fission products.				
<b>WATER INGRESS ACCIDENTS</b>				
Chemical attack by water – changes in kernel properties: Structural and chemical changes to the kernel may release stored fission products.				

TABLE 70. PARAMETERS, CHARACTERISTICS AND PHENOMENA OF HIGH IMPORTANCE TO ACCIDENT CONDITIONS FOR THE BUFFER LAYER

<b>Parameters, characteristics and phenomena</b>	<b>Depressurization (core heat-up)</b>	<b>Reactivity</b>	<b>Air ingress</b>	<b>Water ingress</b>
<b>ALL ACCIDENTS</b>				

TABLE 70. PARAMETERS, CHARACTERISTICS AND PHENOMENA OF HIGH IMPORTANCE TO ACCIDENT CONDITIONS FOR THE BUFFER LAYER

Parameters, characteristics and phenomena	Depressurization (core heat-up)	Reactivity	Air ingress	Water ingress
Gas phase diffusion The fission product transport through the buffer layer is expected to be high at accident temperatures. This layer offers little impedance to the transport of fission products.	X	X		
Response to kernel swelling: The buffer layer must be weak enough that it will deform to accommodate the kernel.		X		
Condensed phase diffusion The fission product transport through the buffer layer is expected to be high at accident temperatures. This layer offers little impedance to the transport of fission products.				
Maximum fuel gaseous fission product uptake: The buffer layer is designed to have sufficient free volume to accommodate the fission products, and to withstand the pressure.				
Layer oxidation: Any oxygen released from the kernel will oxidize a small portion of the buffer. In addition, in the case of water ingress, the buffer will be oxidized from the outside if the particle is cracked or broken.				
Thermal gradient: The gradient may influence the transport of fission products to the other layers. 1) During core heat up conditions, the gradient across the buffer is much less than normal operation. Thermal gradient can cause carbon transfer from side to other side of the kernel. 2) During reactivity insertion accident, gradients can be high for a high energy pulse.				
Irradiation and thermal shrinkage: Irradiation and thermal shrinkage can cause cracks in the buffer layer. Due to these cracks, fission products can locally accumulate (at higher temperatures) on the IPyC.				
<b>AIR/WATER INGRESS ACCIDENTS</b>				
Chemical attack by air/water- kinetics: The reaction rates will control the fission product release rate.				

TABLE 70. PARAMETERS, CHARACTERISTICS AND PHENOMENA OF HIGH IMPORTANCE TO ACCIDENT CONDITIONS FOR THE BUFFER LAYER

Parameters, characteristics and phenomena	Depressurization (core heat-up)	Reactivity	Air ingress	Water ingress
Chemical attack by air/water – changes in chemical form of fission products: The variation in chemical form of the fission products may change their transport.				
Chemical attack by air/water – changes in graphite properties: Changes in the graphite (or PyC) properties may influence the fission product transport and release.				
Chemical attack by air/water – holdup reversal: Fission products stored in the buffer may be released quickly if the buffer structure is attacked.				
Chemical attack by air/water – temperature distribution: The temperature determines reaction rates and transport.				
<b>AIR INGRESS ACCIDENTS</b>				
Chemical attack by air- catalysis: Some impurities or fission products may increase the reaction rate.				

TABLE 71. PARAMETERS, CHARACTERISTICS AND PHENOMENA OF HIGH IMPORTANCE TO ACCIDENT CONDITIONS FOR THE IPYC LAYER

Parameters, characteristics and phenomena	Depressurization (core heat-up)	Reactivity	Air ingress	Water ingress
<b>ALL ACCIDENTS</b>				
Gas phase diffusion Gaseous fission products are generally maintained by IPyC. High local accident temperatures and chemical attack can increase the diffusion rate.	X	X	X	
Cracking: Cracks can change the stress distribution. In the case of air/water ingress, if other layers are broken, cracking will allow the oxidizer to the kernel.	X		X	X
Pressure loading (CO): High CO production will result in high pressures. High pressures can challenge IPyC layer. The IPyC can help keep the SiC in compression if the bonding between layers is strong.	X	X		X

TABLE 71. PARAMETERS, CHARACTERISTICS AND PHENOMENA OF HIGH IMPORTANCE TO ACCIDENT CONDITIONS FOR THE IPYC LAYER

Parameters, characteristics and phenomena	Depressurization (core heat-up)	Reactivity	Air ingress	Water ingress
Pressure loading (fission products): High pressure could challenge this layer. The IPyC products can help keep the SiC in tension if the bonding between layers is strong.		X		
Layer oxidation: In some cases, internal oxidation of the layer can be significant. IPyC cracks can allow CO to the SiC, resulting in corrosion of SiC (inside out). In the case of air/water ingress accident, cracks in the OPyC and SiC will allow oxidation of the IPyC (outside in).			X	X
Condensed phase diffusion Metallic fission products are not well retained. In addition, high local accident temperatures and chemical attack can increase the diffusion rate.				
Stress state (compression/tension): Breaking or debonding of IPyC results in changes in stress distribution of the particle, and hence failures.				
Intercalation/trapping: The IPyC can accumulate fission products during normal operation that can be released during an accident. Chemical attack of the IPyC may allow release of trapped fission products.				
<b>AIR/WATER INGRESS ACCIDENTS</b>				
Chemical attack by air/water- kinetics: The reaction rates will control the fission product release rate.			X	X
Chemical attack by air/water – changes in chemical form of fission products: The changes in chemical form of the fission products may change transport properties.			X	X
Chemical attack by air/water – temperature distribution: The temperature of the IPyC and surrounding materials determines reaction rates and transport.			X	X
Chemical attack by air/water - catalysis: Some impurities or fission products may increase the reaction rate.				

TABLE 71. PARAMETERS, CHARACTERISTICS AND PHENOMENA OF HIGH IMPORTANCE TO ACCIDENT CONDITIONS FOR THE IPyC LAYER

Parameters, characteristics and phenomena	Depressurization (core heat-up)	Reactivity	Air ingress	Water ingress
Chemical attack by air/water – changes in graphite properties: Changes in the graphite (or PyC) properties may influence the transport or release of fission products.				
Chemical attack by air/water – holdup reversal: Serious damage to the IPyC will allow access to the buffer and its relatively large inventory of fission products.				

TABLE 72. PARAMETERS, CHARACTERISTICS AND PHENOMENA OF HIGH IMPORTANCE TO ACCIDENT CONDITIONS FOR THE SiC LAYER

Parameters, characteristics and phenomena	Depressurization (core heat-up)	Reactivity insertion	Air ingress	Water ingress
<b>ALL ACCIDENTS</b>				
Gas phase diffusion Fission product diffusion is low through the SiC even at accident temperatures.	X		X	X
Condensed phase diffusion: Silver can diffuse through SiC at temperatures above 1100°C.				
Thermal deterioration or decomposition: Above 1600-1800°C, SiC begins to decompose and its ability to retain fission products is greatly reduced.				
Fission product corrosion: Some fission products may migrate into the SiC and corrode it. This corrosion process is a function of temperature and can begin during normal operation. Pd is of main concern, though other fission products can also cause corrosion of SiC layer.				
Heavy metal diffusion: The diffusion of fissile material can change the core configuration. A concern is major particle cracking and the expulsion of the kernel material during the pulse.				
Layer Oxidation: Attack of the SiC layer by CO can be due to a failed OPyC at high temperatures or due to IPyC failure (e.g. cracks at high temperatures) (inside out). The formation of either SiO or SiO <sub>2</sub> can determine the rate at which the SiC is eroded.				

TABLE 72. PARAMETERS, CHARACTERISTICS AND PHENOMENA OF HIGH IMPORTANCE TO ACCIDENT CONDITIONS FOR THE SiC LAYER

Parameters, characteristics and phenomena	Depressurization (core heat-up)	Reactivity insertion	Air ingress	Water ingress
Fission gas release through undetected defects: In order to release gases, both PyCs have to be cracked in addition to a failed SiC. The SiC can be attacked by fission products and fabrication impurities. Undetected defective SiC could have poor accident behaviour not apparent during normal operations.	X			
Fission gas release through failures (e.g. cracking): Failure of the SiC will allow the release of metallic fission products even with intact PyCs.	X	X	X	X
Thermodynamics of the SiC fission product system: At the higher temperatures of interest, SiC is just stable to oxidation in its intact particle environment, though SiC is known to be attacked by some noble metals. At higher burnups and temperatures, other chemical concerns may arise.	X			
Sintering: Accident temperatures can result in microstructural changes: change the crystal or grain structure of the SiC layer.				
<b>AIR/WATER INGRESS ACCIDENTS</b>				
Chemical attack by air/water- kinetics: The reaction rates will determine the rate of fission product release.			X	
Chemical attack by air/water – changes in chemical form of fission products: The variation in chemical form of the fission products may change their transport.			X	X
Chemical attack by air/water – temperature distribution: The temperature of the SiC and surrounding materials determines reaction rates and transport.			X	X
Chemical attack by air/water - catalysis: Some impurities or fission products may increase the reaction rate.				
Chemical attack by air/water – changes in SiC properties: Changes in the SiC properties may influence the transport or release of fission products.				

TABLE 72. PARAMETERS, CHARACTERISTICS AND PHENOMENA OF HIGH IMPORTANCE TO ACCIDENT CONDITIONS FOR THE SiC LAYER

Parameters, characteristics and phenomena	Depressurization (core heat-up)	Reactivity insertion	Air ingress	Water ingress
Chemical attack by air/water – holdup reversal: Significant harm to the SiC layer will permit entry to the IPyC layer, which exhibits relatively poor retention of metallic fission products.				

TABLE 73. PARAMETERS, CHARACTERISTICS AND PHENOMENA OF HIGH IMPORTANCE TO ACCIDENT CONDITIONS FOR THE OPyC LAYER

Parameters, characteristics and phenomena	Depressurization (core heat-up)	Reactivity insertion	Air ingress	Water ingress
<b>ALL ACCIDENTS</b>				
Gas phase diffusion: Gaseous fission product diffusion is low.	X		X	
Condensed phase diffusion: Metallic fission product diffusion is high.				
Layer Oxidation: The OPyC is the most exposed layer. It would be the first layer subjected to oxidation (sound particle). Cracked layers may allow CO to the OPyC or coolant impurities may attack it.			X	X
Stress state (compression/tension): Debonding of OPyC from SiC results in changes in stress distribution but the effect is not as significant as that of IPyC debonding from SiC, though failure will increase the likelihood of SiC failure.				
Cracking: Cracks can lead to higher probability of SiC failure. Gaseous will be released if the other layers fail.	X			
Trapping: Chemical attack of the OPyC may allow release of trapped fission products.				
Intercalation: Chemical attack of the OPyC may allow release of trapped fission products.				
Fission gas release through failures (e.g. cracking): Failure of the SiC will allow the release of metallic fission products even with intact PyCs.	X		X	

TABLE 73. PARAMETERS, CHARACTERISTICS AND PHENOMENA OF HIGH IMPORTANCE TO ACCIDENT CONDITIONS FOR THE OPYC LAYER

Parameters, characteristics and phenomena	Depressurization (core heat-up)	Reactivity insertion	Air ingress	Water ingress
Thermodynamics of the SiC fission product system: At the higher temperatures of interest, SiC is just stable to oxidation in its intact particle environment, though SiC can be attacked by some noble metals.	X			
Sintering: Accident temperatures can result in changes of the crystal or grain structure of the SiC layer.				
<b>AIR/WATER INGRESS ACCIDENTS</b>				
Chemical attack by air/water- kinetics: The reaction rates will control the fission product release rate.			X	X
Chemical attack by air/water – changes in chemical form of fission products: Changes in chemical form of the fission products can change transport properties.			X	X
Chemical attack by air/water – temperature distribution: The temperature of the SiC and surrounding materials determines reaction rates and transport.			X	X
Chemical attack by air/water - catalysis: Some impurities or fission products may increase the reaction rate.				
Chemical attack by air/water – changes in graphite properties: Changes in the graphite properties may influence the transport or release of fission products.				
Chemical attack by air/water – holdup reversal: Attack of the OPyC may result in the release of any stored fission products.				

TABLE 74. PARAMETERS, CHARACTERISTICS AND PHENOMENA OF HIGH IMPORTANCE TO ACCIDENT CONDITIONS FOR THE FUEL ELEMENT

Parameters, characteristics and phenomena	Depressurization (core heat-up)	Reactivity	Air ingress	Water ingress
<b>ALL ACCIDENTS</b>				
Irradiation history: Matrix behaviour (shrinkage) is related to time temperature history, and particularly temperatures and fast fluence, changing its chemical reactivity.	X			

TABLE 74. PARAMETERS, CHARACTERISTICS AND PHENOMENA OF HIGH IMPORTANCE TO ACCIDENT CONDITIONS FOR THE FUEL ELEMENT

Parameters, characteristics and phenomena	Depressurization (core heat-up)	Reactivity	Air ingress	Water ingress
Gas phase diffusion: In the matrix, gas diffusion is high. Chemical attack can increase the transport of gases outside the fuel element.		X	X	X
Condensed phase diffusion: Metallic diffusion varies, with less volatile metals exhibiting a high degree of retention in the matrix material.				
Transport of metallic fission products through fuel element-chemical form: The chemical form of fission product controls its transport behaviour. Significant retention of metallic fission products has been observed.	X		X	X
<b>AIR/WATER INGRESS ACCIDENTS</b>				
Chemical attack by air/water- kinetics: The reaction rates will determine the rate of fission product release.			X	X
Chemical attack by air/water – changes in chemical form of fission products: Changes in chemical form of the fission products can change transport properties.			X	X
Chemical attack by air/water – temperature distribution: The temperature of the SiC and surrounding materials determines reaction rates and transport.			X	X
Chemical attack by air/water - catalysis: Some impurities or fission products may increase the reaction rate.				
Chemical attack by air/water – changes in graphite properties: Changes in the graphite properties can affect the transport and release of fission products.			X	
Chemical attack by air/water – holdup reversal: Damage of the matrix material can enhance the release of fission products.				

### 7.8.1. Summary of parameters of high importance identified for accident conditions

Parameters, characteristics and phenomena were identified to be of high importance during depressurization/ core heat up accident for kernel, coatings and the fuel element, as listed in Table 75. In addition, several parameters were identified by the majority (but not by all the experts) as of high importance, including [14]:

- For the kernel, buffer carbon-kernel interaction below and above 1600°C;
- For the buffer layer, layer oxidation below and above 1600°C;

- For the SiC layer, thermal deterioration or decomposition of SiC layer and fission product corrosion of the SiC layer above 1600°C.

A consensus on their importance of several other parameters for the depressurization/ core heat up accident was not reached; these parameters include [14]:

- For the kernel, oxygen flux;
- For the buffer layer, condensed phase diffusion and thermal gradient.

A total of 12 parameters, characteristics and phenomena were identified to be of high importance during reactivity initiated accident for kernel, coatings and the fuel element, as listed in Table 76. Several parameters were identified by the majority (but not by all the experts) as of high importance, including [14]:

- For the kernel, gas phase diffusion, energy transport – conduction within the kernel;
- For the buffer layer, maximum fuel gaseous fission product uptake;
- For the fuel element, condensed phase diffusion.

A consensus on the importance of several other parameters for the reactivity initiated accident was not reached; these parameters include [14]:

- For the kernel, buffer carbon-kernel interaction;
- For the buffer layer, condensed phase diffusion and thermal gradient;
- For the IPyC layer, stress state (compression/tension);
- For the OPyC layer, gas phase diffusion.

TABLE 75. DEPRESSURIZATION/HEATUP ACCIDENT PARAMETERS OF HIGH IMPORTANCE

Layer	Parameter
Kernel	Condensed phase diffusion
	Gas phase diffusion
	Maximum fuel temperature
	Time at temperature
	Energy transport
	<del>Thermodynamic state of fission products</del>
Buffer	Gas phase diffusion
IPyC	Cracking
	Gas phase diffusion
	Pressure loading
SiC	Fission product release through failures (e.g. cracking)
	Fission product release through undetected failures
	Gas phase diffusion
	Thermodynamics of the SiC fission product system
OPyC	Cracking
	Gas phase diffusion
Fuel element	Irradiation history
	Transport of metallic fission products – chemical form

TABLE 76. REACTIVITY INSERTION ACCIDENT PARAMETERS OF HIGH IMPORTANCE

Layer	Parameter
Kernel	Condensed phase diffusion Maximum fuel temperature Time at temperature Energy deposition (total) Thermodynamic state of fission products
Buffer	Gas phase diffusion Response to kernel swelling
IPyC	Gas phase diffusion Pressure loading (fission products) Pressure loading (CO)
SiC	Fission product release through failures (e.g. cracking)
OPyC	None
Fuel element	Gas phase diffusion

Parameters, characteristics and phenomena were identified to be of high importance during air ingress accident for kernel, coatings and the fuel element, as listed in Table 77. Several parameters were identified by the majority (but not by all the experts) as of high importance, including [14]:

- For the kernel, buffer carbon-kernel interaction;
- For the buffer layer, layer oxidation;
- For the SiC layer, layer oxidation;
- For the OPyC layer, cracking;
- For the fuel element, condensed phase diffusion, chemical attack by air – catalysis.

A consensus on their importance of several other parameters for the air ingress accident was not reached; these parameters include [14]:

- For the kernel, chemical attack by air – kinetics, chemical attack by air – change in chemical form of fission products;
- For the buffer layer, gap phase diffusion, condensed phase diffusion, maximum fuel gaseous fission product uptake, thermal gradient, chemical attack by air – change in chemical form of fission products;
- For the IPyC layer, pressure loading (fission products), pressure loading (CO), stress state (compression/tension);
- For the SiC layer, fission product corrosion;
- For the fuel element, chemical attack by air – holdup reversals.

TABLE 77. AIR INGRESS ACCIDENT PARAMETERS OF HIGH IMPORTANCE

Layer	Parameter
Kernel	Maximum fuel temperature Time at temperature Thermodynamic state of fission products
Buffer	None
IPyC	Gas phase diffusion Layer oxidation Cracking Chemical attack by air: kinetics Chemical attack by air: changes in chemical form of fission products Chemical attack by air: temperature distribution
SiC	Gas phase diffusion Fission product release through failures (e.g. cracking) Chemical attack by air: temperature distribution Chemical attack by air: kinetics
OPyC	Gas phase diffusion Layer oxidation Chemical attack by air: kinetics Chemical attack by air: temperature distribution Chemical attack by air: changes in chemical form of fission products
Fuel element	Gas phase diffusion Transport of metallic fission products through fuel element – chemical form Chemical attack by air: kinetics Chemical attack by air: temperature distribution Chemical attack by air: changes in chemical form of fission products Chemical attack by air: changes in graphite properties

A total of twenty-two parameters, characteristics and phenomena were identified to be of high importance during water ingress accident for kernel, coatings and the fuel element, as listed in Table 78. Several parameters were identified by the majority (but not by all the experts) as of high importance, including [14]:

- For the kernel, buffer carbon-kernel interaction;
- For the buffer layer, layer oxidation;
- For the IPyC layer, gas phase diffusion;
- For the SiC layer, chemical attack by water – kinetics;
- For the OPyC layer, cracking;
- For the fuel element, condensed phase diffusion, chemical attack by water – changes in graphite properties.

A consensus on their importance of several other parameters for the water ingress accident was not reached; these parameters include [14]:

- For the kernel, chemical attack by water – kinetics, chemical attack by water – change in chemical form of fission products;
- For the buffer layer, gas phase diffusion, condensed phase diffusion, maximum fuel gaseous fission product uptake, thermal gradient;
- For the IPyC layer, pressure loading (fission products), stress state (compression/tension), chemical attack by water – changes in graphite properties;
- For the SiC layer, layer oxidation;
- For the OPyC layer, chemical attack by water – changes in graphite properties;
- For the fuel element, chemical attack by air – holdup reversals.

TABLE 78. WATER INGRESS ACCIDENT PARAMETERS OF HIGH IMPORTANCE

Layer	Parameter
Kernel	Maximum fuel temperature Time at temperature Thermodynamic state of fission products
Buffer	None
IPyC	Pressure loading (CO) Layer oxidation Cracking Chemical attack by water: kinetics Chemical attack by water: changes in chemical form of fission products Chemical attack by water: temperature distribution
SiC	Gas phase diffusion Fission product release through failures (e.g. cracking) Chemical attack by water: temperature distribution Chemical attack by air: changes in chemical form of fission products
OPyC	Layer oxidation Chemical attack by water: kinetics Chemical attack by water: temperature distribution Chemical attack by water: changes in chemical form of fission products
Fuel element	Gas phase diffusion Transport of metallic fission products through fuel element – chemical form Chemical attack by water: kinetics Chemical attack by water: temperature distribution Chemical attack by water: changes in chemical form of fission products

### 7.8.2. Fuel failures under accident conditions (corresponding to core heat up)

Figure 121 [6] shows the fractional release of  $^{85}\text{Kr}$  of German  $\text{UO}_2$  fuel at temperatures up to  $2100^\circ\text{C}$  [6]. No TRISO failures were observed at the temperature of  $1600^\circ\text{C}$ , however, TRISO failures occurred after short periods at  $1800^\circ\text{C}$ . At the test temperature of  $1600^\circ\text{C}$  (see Fig. 122 [6]), no TRISO failures were observed at burnups lower than 10% FIMA, but failures were observed at burnups at  $\sim 14\%$  FIMA. Cs release as a function of burnup and temperature is shown in Fig. 123: at  $1600^\circ\text{C}$  and burnup  $< 10\%$  FIMA, Cs release remained relatively low, however, increasing burnup and temperature increases SiC layer degradation and Cs release.

Prior to 2000 in US, selected TRISO fuels irradiated in the HFIR at ORNL were subjected to heating tests. HRB-15B capsule included various fuel types of  $\text{UO}_2$ ,  $\text{UC}_2$ ,  $\text{UCO}$ ,  $\text{UO}_2^*(1)$ , and  $\text{UO}_2^*(2)$  fuel particles. The irradiation was performed for 169 EFPDs at an accelerated condition up to fuel burnup of 21–25 % FIMA. The PIE of irradiated fuel particles revealed some SiC layer was cracked in each TRISO coated fuel type but mostly in the  $\text{UCO}$  particles [3,4,10]. Subsequent heating tests were conducted at temperatures up to  $1500^\circ\text{C}$ . Ten particles of each fuel type were annealed for 11,866 h at  $1500^\circ\text{C}$  [10]. Caesium and silver were released from the  $\text{UO}_2$  and  $\text{UC}_2$  fuel particles as shown in Figure 124 (a) and (b). These releases exhibited a maximum for the particles with SiC of a columnar grain structure as shown in Fig. 104. The fashion of releasing caesium and silver from the  $\text{UO}_2$  fuel particles supported a diffusional release mechanism through the SiC layer.

Individual  $\text{UO}_2$  TRISO fuel particles deconsolidated from a compact of Japanese manufacture were heated at  $1700^\circ\text{C}$  for 270 h and at  $1800^\circ\text{C}$  for 222 h at ORNL [31]. The fuel underwent irradiation at HFIR in the HRB-22 capsule, reaching a burnup of 4.8% FIMA and a fast neutron fluence of  $2.1 \times 10^{25}$  n/m<sup>2</sup> over 89 EFPDs, with a time-averaged maximum temperature of  $1100^\circ\text{C}$ . Releases of silver, caesium, europium, and krypton were monitored over time, as illustrated in Figures 125 and 126 for batches of 25 particles at each temperature [10] The krypton release in Fig. 126 showed that one particle failed early in the heating with a release of antimony.

As shown in Table 67, the design value of TRISO failure fraction for fuels developed for NGNP during accidents is  $\leq 6.0 \times 10^{-4}$  [6]. Based on annealing testing of US AGR-1 and AGR-2 fuels in the 1600–1800°C range, no TRISO failures in a fuel with UCO kernel were observed in any of the 1600°C annealing tests. Combining the results gives a total TRISO failure fraction in a fuel with UCO kernel of  $\leq 6.6 \times 10^{-5}$  [108]. This is a factor of 9 lower than typical reactor design specifications for allowable failures during 1600°C accidents ( $6 \times 10^{-4}$ ). Fractional release of  $^{134}\text{Cs}$  from compacts containing only intact particles at 1600°C was  $< 6 \times 10^{-5}$ . When a SiC layer in a particle failed, some of the Cs from that particle was released. TRISO failure fraction in a fuel with UCO kernel for the tests at 1800°C after the AGR-1 and AGR-2 irradiations was  $\leq 3.0 \times 10^{-4}$ . Conversely, the combined (AGR-1 + AGR-2) SiC failure fractions in a fuel with UCO kernel were  $\leq 1.7 \times 10^{-4}$  and  $\leq 1.3 \times 10^{-3}$  during annealing testing at 1600°C and 1800°C, respectively [108]. In spite of the much higher frequency of SiC failure observed for the irradiated AGR-2  $\text{UO}_2$  fuel compacts during annealing tests relative to UCO, no TRISO failures were observed in the three annealing tests (i.e., tests at 1600, 1700 and 1800°C) [108]. Releases of Ag, Sr, and Eu observed at 1600 and 1700°C is ascribed to the diffusion of these fission products in the fuel matrix during irradiation. Subsequently, these elements are released from the matrix upon exposure to high-temperature heating [108]. In summary, the findings suggest a minimal incremental release of annealing-critical fission products under accident conditions.

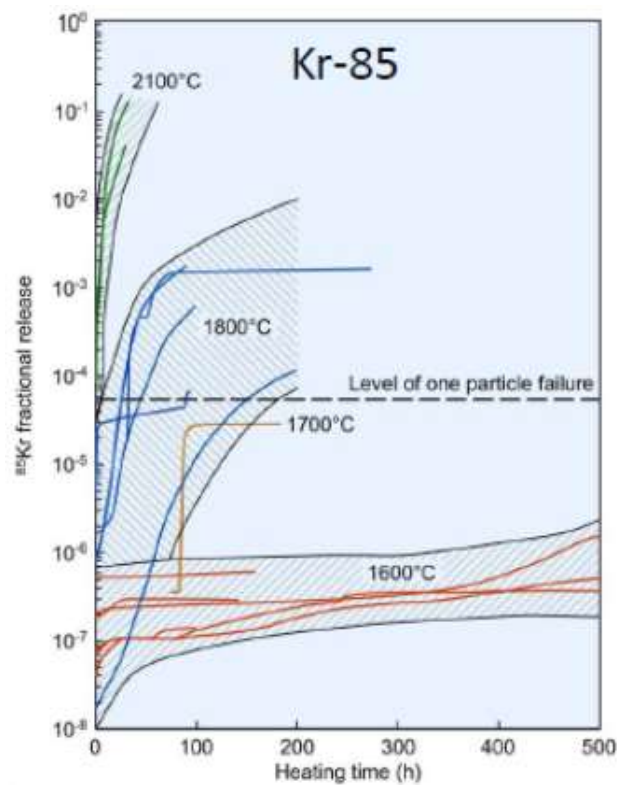


FIG. 121. Temperature effect on  $^{85}\text{Kr}$  fractional release of German  $\text{UO}_2$  fuel (courtesy of INL).

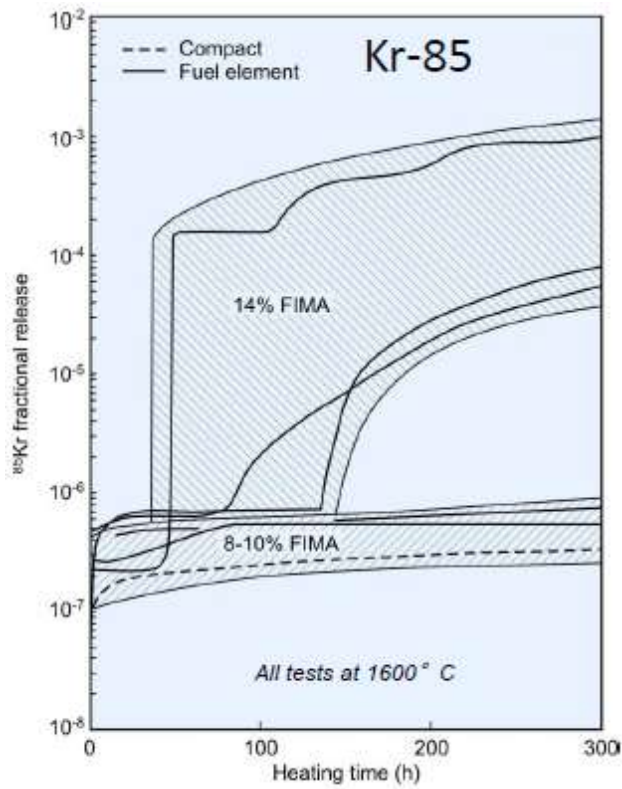


FIG. 122. Burnup effect on  $^{85}\text{Kr}$  fractional release of the German  $\text{UO}_2$  fuel at the temperature of 1600°C (courtesy of INL).

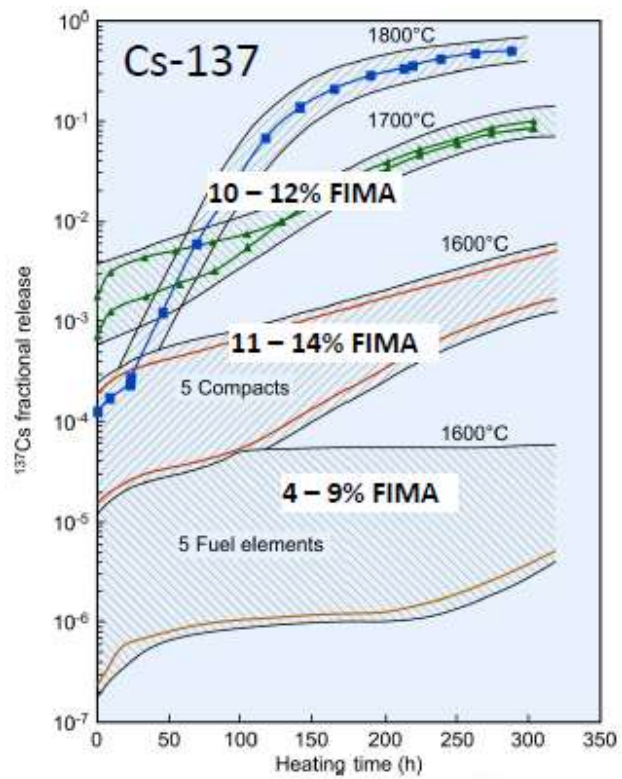
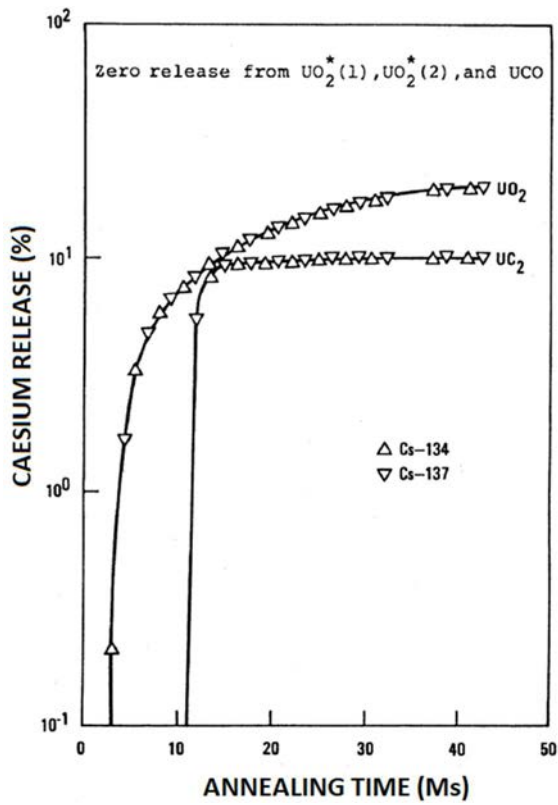
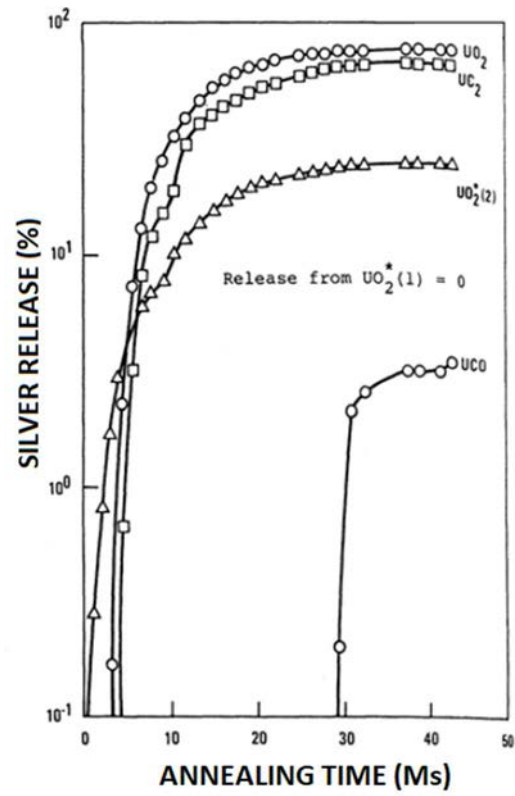


FIG. 123. Burnup and temperature effects on  $^{137}\text{Cs}$  fractional release of German  $\text{UO}_2$  fuel (courtesy of INL).



(a)



(b)

FIG. 124. Release of Cs (a) and Ag (b) from various types of TRISO-coated fuel particles at 1500 °C (courtesy of INL).

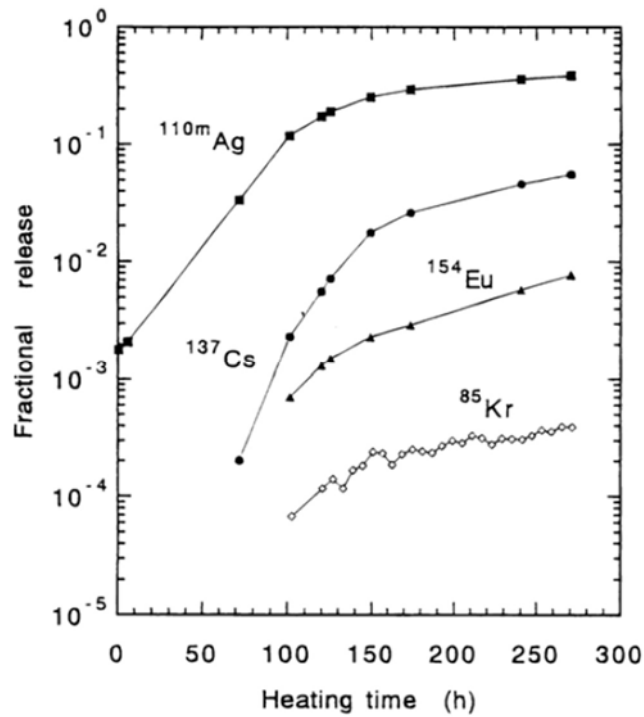


FIG.125. Time-dependent fractional releases of fission products during the ACT3 annealing test at 1700 °C for 270 h, obtained by the online measurements of fission gas release and intermittent measurements of metallic fission product release (courtesy of INL).

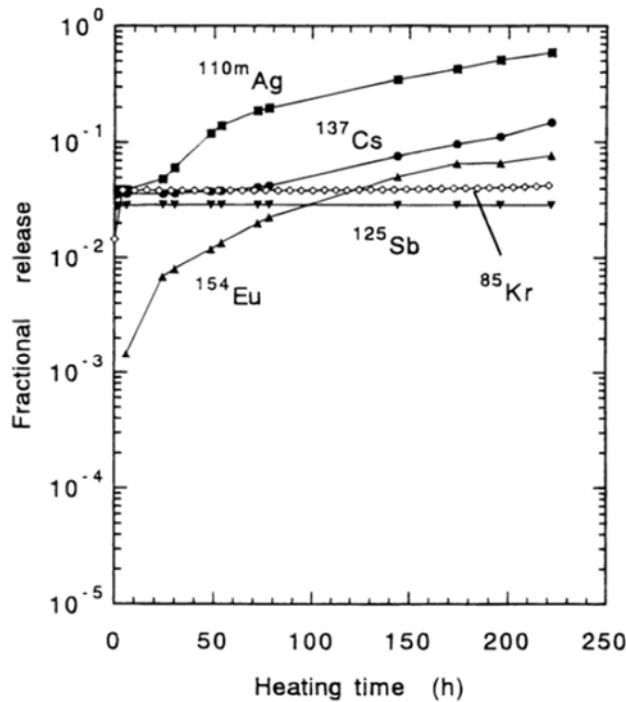


FIG. 126. Time-dependent fractional releases of fission products during the ACT4 heating test at 1800 °C for 222 h, obtained by the online measurements of fission gas release and intermittent measurements of metallic fission product release (courtesy of INL).

### 7.8.3. Fuel failures under accident conditions (corresponding to reactivity insertion accident)

A rapid escalation in reactor local or core-wide power resulting from a surge in reactivity can stem from malfunctions in the control system, inadvertent control rod ejection, or sudden alterations in the core's internal configuration, such as pebble compaction in a pebble bed reactor [20]. Notably, a pebble bed reactor exhibits low excess reactivity due to continual fuel cycling, while the prismatic core design initially features excess reactivity and burnable poisons that diminish as the core approaches the end of its operational life. In the event of a sudden power pulse, there is a risk of damaging the fuel element and fuel particles, potentially leading to a substantial release of fission products from the fuel. For pulse durations on the order of seconds, it is assumed that a portion of the fuel may fail through the cracking of PyC and SiC layers, while the kernel and buffer layers remain intact [20].

The UO<sub>2</sub> kernel melting and central vaporization for coated particles with an energy deposition of 2300 J/g UO<sub>2</sub> were observed for the Japanese fuel compacts after pulse testing (10–30 ms): uranium vapour penetrated the cracks in the coating layers, though at lower energies, the particle remained almost unchanged, but layer cracking was observed [20].

- Two sets of pulse tests (i.e., short pulses and long pulses) were performed by in a Russian research reactor [20]: a pulse of duration (half width peak) of 0.7 seconds with an energy deposition of 26,000 J/g UO<sub>2</sub> into spherical fuel elements resulted in no failure (i.e., intact) of fuel elements.
- A pulse lasting 30 s, with an energy deposition of 90,000 J/g UO<sub>2</sub>, led to the failure of the coated particles and the fragmentation of the fuel element spheres. In addition, Russian scientists performed a set of short pulse (1–2 ms) tests with energy deposition of 100 to 1700 J/g UO<sub>2</sub>: they observed coating cracking at < 1050 J/g UO<sub>2</sub> and kernel restructuring at > 1300 J/g UO<sub>2</sub>.

A distinct investigation aimed at identifying the necessity for in-pile testing data to support the licensing of TRISO fuel in non-HTGR applications (e.g. LWRs, microreactors, nuclear thermal propulsion, and salt-cooled reactors) revealed that temperature transients might occur much faster than in HTGR DLOFC accidents (e.g.  $0.05^{\circ}\text{C/s}$  in a HTGR DLOFC versus up to  $1000^{\circ}\text{C/s}$  in a non-high temperature reactor using TRISO fuel) [156]. Notably, significant fuel particle failures were observed at energy depositions exceeding  $1400\text{ J/g}$  fuel due to kernel melting, while fuel compact graphite matrix failures were observed above  $2300\text{ J/g}$  fuel [156]. It is essential to recognize that failure thresholds and mechanisms may differ for particles with fuel materials distinct from  $\text{UO}_2$  (e.g. UCO and UN), particles with different irradiation histories, and particles with different structural configurations (layers and relative thickness). Although historical tests have predominantly identified kernel melting as the primary failure mechanism, it is acknowledged that other mechanisms, such as thermal stresses between coating layers during rapid temperature increases, leading to crack propagation and delamination of coating layers, may also be possible.

The failure fraction of particles was generally observed to be  $\sim 0.01$  at an energy deposition of  $1000\text{ J/g}$   $\text{UO}_2$  and  $1.0$  at  $1700\text{ J/g}$   $\text{UO}_2$  (the trend of failure fraction as a function of energy deposition is shown in Fig. 127) (refer to Ref. [156] for details). At the highest energy deposition,  $\sim 2300\text{ J/g}$   $\text{UO}_2$ , the fuel compact graphite matrix exhibited cracking on the surface and failed due to stresses within the compact. Recent in-pile tests using fresh  $\text{UO}_2$  kernels ( $7.26\%$   $^{235}\text{U}$  enrichment) demonstrated consistent failure of coated fuel particles above  $1400\text{ J/g}$   $\text{UO}_2$ , coinciding with the point at which the kernels melted.

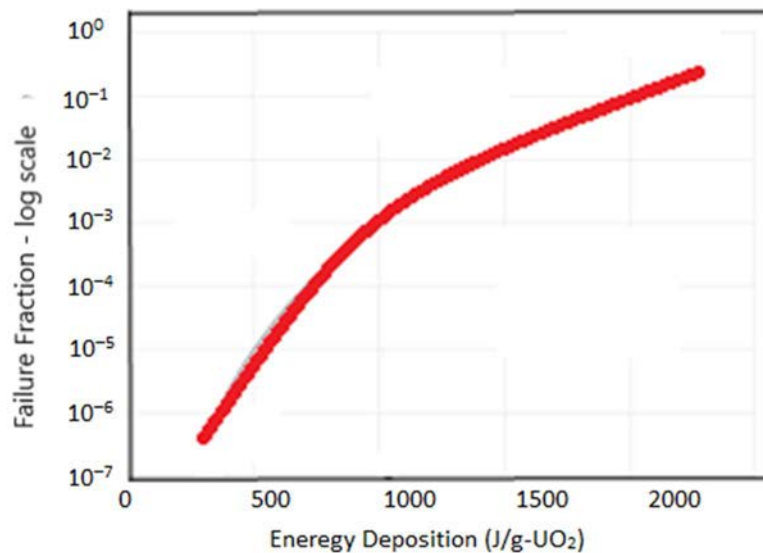


FIG. 127. Failure fraction of fuel particles as a function of energy deposition.

## 8. FUEL MODELLING AND CODE DEVELOPMENTS

### 8.1. MODELLING OF COATED PARTICLE FUEL PERFORMANCE

This section describes important fuel models that are necessary in evaluating the integrity and performance of coated particle fuel for use in high-temperature gas cooled SMRs.

#### 8.1.1. Fuel burnup and depletion

Fuel burnup and depletion analysis for a reactor core provides information on the time-dependent variation of fuel burnup, flux and fluence, and the production and depletion of fission product nuclei. The fuel burnup and depletion can be evaluated using various reactor core analysis computer codes such as MCNP-MOCUP-ORIGEN2 [177–179] and MCCARD [180]. The calculated fuel burnup and fast fluence are used as input to material property correlations of a fuel material in order to determine the specific values of the material properties during the operation of the reactor. The nuclide inventory is used as a fission product source term for design and annealing analyses. A chemical equilibrium calculation using the nuclide inventory gives the fission yields of gas species over time that are used in the evaluation of gas pressure build-up in a coated particle.

#### 8.1.2. Pressure build-up in a coated particle

Excess oxygen generated in a kernel is a major contributor to the build-up of the internal gas pressure of a particle. There exist some models which predicts the free oxygen release from an oxide kernel [181–188].

A thermochemical equilibrium calculation using the nuclide inventory generated in the kernel and buffer can produce the yields of gas species in a particle. This method is applicable to any type of kernel i.e., nitride, oxy-carbide, and even oxide kernel. The Booth model is capable of estimating the release quantity of gas atoms from the kernel into the void volume within the kernel and the buffer [189]. The void volume, constituting the open-pore space in the kernel and the buffer, undergoes changes with burnup due to solid and gaseous swelling of the kernel. This swelling leads to densification of the buffer, resulting in a reduction of the void volume. The gas pressure within the void volume can be approximated using the ideal gas law or other relevant equations of state (e.g. [190]). Figure 128 shows an example of the calculation process of the internal gas pressure (that employs the HSC Chemistry™ Software [191] and the Microsoft Excel).

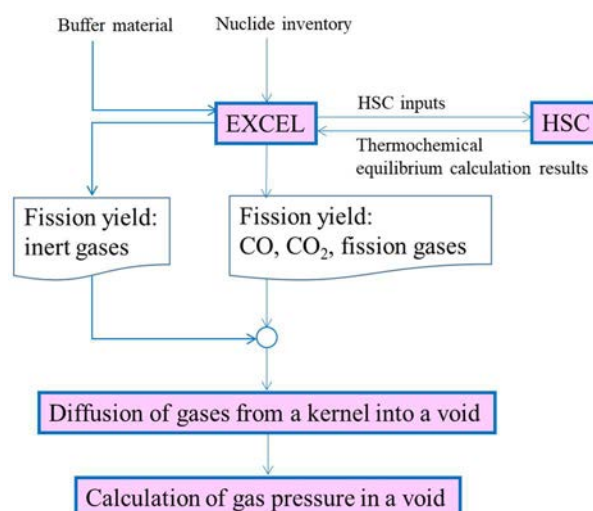


FIG. 128. Calculation process of gas pressure in a particle.

### 8.1.3. Failure of pressure-bearing layers

Gas pressure built up in a buffer of a particle develops tangential stresses on the coating layers of the particle. The calculated stresses are used to determine the integrity of pressure-bearing layers of the particle. A coating layer is considered failed if the tangential stress acting on the layer exceeds the ultimate tensile strength (UTS) of the material. During irradiation, a coating layer experiences elastic, plastic, thermal, creep deformation together with irradiation-induced dimensional change [192,193]. Gas pressure due to fission gases, CO, and CO<sub>2</sub> applies to the inner surface of the innermost layer, whilst an ambient pressure acts on the outer surface of the outermost layer by a matrix material surrounding the particle.

Three mathematical formulas are used in expressing the mechanical state of coating layers: a stress-strain relation, a strain-displacement relationship, and an equilibrium equation.

The stress-strain relation for a shell-like coating layer at fluence  $f$  can be represented in the following matrix equation:

$$[C]\{\sigma\} = \{\varepsilon\} - \{\varepsilon^{pl}\} - \{\varepsilon^{th}\} - \{\varepsilon^{sw}\} - \{\varepsilon^{cr}\} \quad (22)$$

where

$$\begin{aligned} \{\sigma\}^T &= \{\sigma_r \quad \sigma_\theta\} \\ \{\varepsilon\}^T &= \{\varepsilon_r \quad \varepsilon_\theta\} \\ \{\varepsilon^{pl}\}^T &= \{\varepsilon_r^{pl} \quad \varepsilon_\theta^{pl}\} \\ \{\varepsilon^{th}\}^T &= \{\varepsilon_r^{th} \quad \varepsilon_\theta^{th}\} \\ \{\varepsilon^{sw}\}^T &= \{\varepsilon_r^{sw} \quad \varepsilon_\theta^{sw}\} \\ \{\varepsilon^{cr}\}^T &= \{\varepsilon_r^{cr} \quad \varepsilon_\theta^{cr}\} \\ [C] &= \frac{1}{E} \begin{bmatrix} 1 & -2\nu \\ -\nu & 1 - \nu \end{bmatrix} \end{aligned} \quad (23)$$

$\sigma$  is the stress (MPa),

$\varepsilon$  is the total strain (dimensionless),

$\varepsilon^{pl}$  is the plastic strain (dimensionless),

$\varepsilon^{th}$  is the thermal strain (dimensionless),

$\varepsilon^{sw}$  is the irradiation-induced dimensional change (dimensionless),

$\varepsilon^{cr}$  is the irradiation creep strain (dimensionless),

$E$  is the modulus of elasticity (MPa),

$\nu$  is the Poisson's ratio (dimensionless),

the subscripts  $r$  and  $\theta$  indicate the radial and circumferential directions, respectively.

The irradiation creep strain vector is given as follows [194]:

$$\{\varepsilon^{cr}\} = \int_0^\phi [A]\{\sigma\} d\tau \quad (24)$$

where

$$[A] = K \begin{bmatrix} 1 & -2\mu \\ -\mu & 1 - \mu \end{bmatrix} \quad (25)$$

$K$  is the irradiation creep coefficient [MPa ( $10^{25}$  n/m<sup>2</sup>;  $E_n > 0.18$  MeV)]<sup>-1</sup>,

$\mu$  is the Poisson's ratio in irradiation creep,

$\phi$  is the neutron flux.

The PyC layer experiences elastic deformation, thermal expansion, irradiation-induced creep and irradiation-induced dimensional change under fast neutron irradiation, however, does not experience plastic deformation [192]. At fluence up to  $5 \times 10^{26}$  n/m<sup>2</sup>,  $\beta$ -SiC swells in small amount which is insignificant compared with PyC dimensional change [195]. The SiC layer has been assumed to experience only elastic deformation and thermal expansion under the fast neutron irradiation condition of a conventional HTGR. The new coating layer candidate material, ZrC, has an additional plastic deformation property unlike PyC and SiC [193].

For a spherical shell layer, the strain-displacement relationship and the equilibrium equation are expressed by the following two equations [196]:

$$\begin{Bmatrix} \varepsilon_r \\ \varepsilon_\theta \end{Bmatrix} = \begin{Bmatrix} \frac{\partial u}{\partial r} \\ \frac{u}{r} \end{Bmatrix} \quad (26)$$

$$\frac{\partial \sigma_r}{\partial r} + \frac{2}{r}(\sigma_r - \sigma_\theta) = 0 \quad (27)$$

where  $u$  is the radial displacement ( $\mu\text{m}$ ) and  $r$  is the radial coordinate ( $\mu\text{m}$ ).

In an HTGR compact whose matrix material is graphite, a very small amount of ambient pressure, for example 0.1 MPa, is applied to the outer surface of the outermost layer of a particle. A stiffer compact matrix material like dense SiC put more ambient pressure on the outer surface of the outermost layer of the particle. The existing models for predicting stresses in coated particles were extended in [197] to treat stresses induced by the matrix graphite and neighbouring particles in a pebble.

#### 8.1.4. Kernel migration

In oxide, carbide or oxy-carbide fuel, the kernel of a particle can move in the direction of increasing temperature. This phenomenon, known as the amoeba effect, results from the transport of carbon from the hot side of the kernel to the cool side in the presence of a temperature gradient. The failure of the coating layers of a coated fuel particle is assumed to occur when the kernel touches the coating layers. The following equation expresses the kernel migration within a particle [198]:

$$x_{KM}(t) = \int_0^t KMC(t) \frac{1}{[T(\tau)]^2} \frac{dT(\tau)}{dx} d\tau \quad (28)$$

where

$x_{KM}$  is the kernel migration distance (m),

$KMC(T)$  is the kernel migration coefficient (m<sup>2</sup> K/s),

$dT/dx$  is the temperature gradient across the particle (K/m),

$T$  is the average particle temperature at time  $t$  (K), and

$t$  is the total time (s).

Table 79 shows Arrhenius-type kernel migration coefficients, taken from Ref. [198].

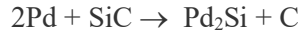
TABLE 79. KERNEL MIGRATION COEFFICIENTS

$KMC = KMC_0 e^{-\frac{Q}{RT}}, \quad R = 8.3145 \text{ J/(mol K)}, \quad T = \text{temperature (K)}$		
	$KMC_0 \text{ (m}^2 \text{ K/s)}$	$Q \text{ (J/mol)}$
UO <sub>2</sub> (Dragon)	$8.106 \times 10^{-7}$	24 737
UO <sub>2</sub> (FZJ)	$1.053 \times 10^{-6}$	34 742
UC <sub>2</sub> and UCO	$4.811 \times 10^{-1}$	299 217

### 8.1.5. Fission product attack

High concentrations of silver will attack SiC, however, at the low concentrations typical of operating fuel particles, silver can escape from a particle by diffusing through an intact SiC [199,200]. It has been known that, in all fuel kernel types, palladium is released from the kernel and moves to the inner surface of the SiC layer [201,202]. Rare earths such as lanthanum, cerium, praseodymium, and neodymium mostly form immobile, refractory oxide compounds in oxide-based kernels, such as ThO<sub>2</sub>, UCO, and UO<sub>2</sub>, whose O/U ratios are 1.1 or more [201,202]. They are released and migrate down the thermal gradient in UC<sub>2</sub> kernel or kernels whose O/U ratios are less than 1.1. In UC<sub>2</sub> kernel or kernels whose O/U ratios are less than 1.1, palladium corrodes the SiC layer at rates faster than the REs at temperatures below 1400°C. But the reverse is true at temperatures above 1400°C [201]. The normal operation temperature of an HTGR is much less than 1400°C. Therefore, palladium is the main corroder of the SiC layer.

The fission product palladium is generated in a kernel during irradiation. Palladium isotopes are produced more in low-enriched uranium kernels than in high-enriched uranium kernels because the fission yield of palladium from plutonium is much larger than that from uranium. The palladium atoms in a kernel diffuse out of the kernel, and then, they transport to the SiC layer through the buffer and IPyC layers. The Pd-SiC interaction starts to occur at the inner surface of the SiC layer. Very small precipitates or nodules of a noble metal compound occur along SiC grain boundaries and inside the SiC grains [200,203]. The nodules move SiC by dissociating SiC at the leading edge of a nodule through the following possible chemical interaction [204]:



and by re-forming SiC at the trailing edge. The presence of other fission product elements in an operating particle could inhibit the repair process. This leads to local corrosion and thinning of the SiC layer [26].

The rate of SiC corrosion by palladium typically depends on irradiation temperature, kernel composition, palladium concentration, other fission product compositions, and SiC properties. A correlation describing the Pd-SiC reaction has to include the effects of the above factors. The threshold amount of palladium for the Pd-SiC reaction has not been clearly observed [201,204]. It can be assumed that the SiC begins to corrode once a small amount of palladium reaches the inner surface of the SiC layer. It was suggested in [204] that, in a UO<sub>2</sub> kernel, the release from a kernel limits the Pd-SiC interaction rate. They concluded qualitatively that the SiC corroded even in the small number of palladium atoms, and the corrosion depth of SiC is proportional to the one third power of the number of palladium atoms.

The following corrosion rate of SiC through a data base of SiC attack by fission products compiled from irradiation and out-of-pile heating tests was introduced in [205]:

$$\dot{v} = 5.872 \times 10^{-7} e^{-\frac{179500}{RT}} \quad (29)$$

where  $\dot{v}$  is the corrosion rate (m/s),  $T$  is the temperature (K),  $R$  is the gas constant (8.3145 J/mol·K).

Equation (29) was made by using SiC attack data which had been obtained by covering in-pile and out-of-pile tests, REs and Pd attack, accelerated and real time irradiations, HEU and LEU fuel [205].

Equation (29) describes only the temperature dependence of the corrosion rate, but not the enrichment or heavy metal burnup dependence of the reaction rate.

No reaction was found on the ZrC TRISO particles heated in the palladium vapour as a result of out-of-pile heating tests of 1830–2150 K [206]. No fission product attack was found [206] in (1) the ZrC TRISO UC<sub>4.6</sub>O<sub>1.1</sub> particles irradiated at 1523K to 86%, (2) the ZrC-TRISO UO<sub>2</sub> and UC<sub>2</sub> particles irradiated at 1328–1403 K to 24.9–28.8% FIMA, (3) the ZrC-TRISO UO<sub>2</sub> particles irradiated at 1673–1923 K to 4.5% FIMA.

### 8.1.6. Thermal decomposition

At very high temperatures above 2000°C, the SiC layer decomposes into its constituent elements: the silicon vaporizes, leaving a porous carbon structure [207]. The SiC thinning rate due to the thermal decomposition is given as follows [198]:

$$k(T) = \frac{375}{d_0} e^{-\frac{556000}{RT}} \quad (30)$$

where  $k$  is the SiC thinning rate (s<sup>-1</sup>),  $T$  is the temperature (K),  $R$  is the gas constant (8.3145 J/mol-K).

Equation (30) is useful to evaluate how much the SiC layer of individual particles is thermally decomposed.

Out-of-pile high-temperature heating experiments conducted on unirradiated ZrC-TRISO particles demonstrated the stability of ZrC itself up to the eutectic point of ZrC-C at approximately 3123 K. However, the ZrC-TRISO particles could not endure heating above 2773 K, leading to failure induced by substantial internal pressures [206]. In the post-irradiation heating test involving 101 ZrC-TRISO UO<sub>2</sub> particles sampled from an irradiated fuel compact at 1373 K to 4% FIMA, no failure was detected during the initial heat-up stage, with one particle failure occurring after maintaining the particles at 2673 K for 100 minutes [206]. No ZrC failure was observed in isothermal post-irradiation heating tests on ZrC-TRISO UO<sub>2</sub> particles carried out at 1873 K for 4500 h and at 2073 K for 3000 h. The IPyC and ZrC coating layers were damaged in isothermal post-irradiation heating tests carried out at 2273 K for 100 h. The ZrC damage was attributed to the reaction of ZrC with CO gas caused by the failure of the IPyC layers [206].

### 8.1.7. Failure analysis for a batch of particles

The current particle manufacturing methods such as gelation of kernel and chemical vapour deposition of coating layers do not produce uniform particles. The sizes and material properties of the prepared particle are statistically indicated. The particle quantities with Gaussian statistical distribution are the diameter of the kernel, the thickness and density of the buffer, and the thicknesses, densities, and BAFs of coating layers. The particle quantities with Weibull statistical distribution are the coating layer strengths. They are stochastically independent of each other.

Failure analysis is applied statistically to each individual particle. The failure of a particle occurs due to mechanical failure, fission product attack, and thermal decomposition during a reactor operation. Many models for mechanical failure mechanisms have been developed [70]: SiC failure, kernel migration, pyrocarbon crack, layer debonding, matrix-OPyC interaction. Some researchers [185,208] used the Monte Carlo method to analyse the SiC failure of TRISOs. The Monte Carlo failure analysis consists of random particle generation and failure judgement using criteria for various failure mechanisms.

The particle quantities can be generated using uniform deviates whose range is from 0 to 1, where the uniform deviate is just a random number that comes from a uniform distribution. Two independent standard normal distribution deviates are produced from two independent uniform distribution deviates using the Box-Muller method [209]:

$$y_1 = \sqrt{-2 \ln R^2/R^2} (2x_1 - 1) \quad (31)$$

$$y_2 = \sqrt{-2 \ln R^2/R^2} (2x_2 - 1) \quad (32)$$

$$R^2 = (2x_1 - 1)^2 + (2x_2 - 1)^2 \quad (33)$$

where

$y$  is the standard normal distribution deviate  $\hat{I}(-\infty, \infty)$ ,

$x$  is the uniform distribution deviate  $\hat{I}(0, 1)$ .

A usual random number generator produces  $x_1$  and  $x_2$ . Then, the particle quantities with normal distribution can be calculated using a standard normal distribution deviate  $y$ :

$$t = \bar{t} + y \cdot STD_t \quad (34)$$

where  $\bar{t}$  and  $STD_t$  is the mean value and standard deviation of  $t$ , respectively, that are experimentally given.

The probability distribution for the strength of a particle coating layer is defined by a Weibull distribution [210]:

$$F(s) = 1 - e^{-\ln 2 \cdot (s/s_{med})^m} \quad (35)$$

where

$F(s)$  is the Weibull cumulative distribution function of  $s$ ,

$s$  is the strength of a coating layer (MPa),

$s_{med}$  is the median strength of a coating layer (MPa), and

$m$  is the Weibull modulus.

Equation (35) gives the following strength of a coating layer:

$$s = s_{med} \left[ -\frac{\ln(1-F(s))}{\ln 2} \right]^{1/m} \quad (36)$$

A usual random number generator produces  $F$  in  $(0, 1)$ .

It is judged that the coating layer is broken if the tangential stress calculated using the particle quantities with normal distribution is greater than the strength calculated using Eq. (36).

### 8.1.8. Fission product releases from a coated particle

Within a particle embedded in a matrix material, fission products are generated through nuclear fission in the kernel material and heavy metal contamination in the coating layers, with some being transferred to adjacent layers through recoil. In the kernel, fission products diffuse through grains to the grain boundaries and then move through interconnected open pores to reach the kernel surface. Released fission products from the kernel swiftly migrate to the IPyC layer through the buffer's pores and subsequently diffuse through the various coating layers. The fission product transport within each layer of a particle is influenced by various complex mechanisms. While the actual transport behaviour is not fully understood, a simplified approach using classic Fickian diffusion has been employed due to incomplete knowledge. The Fickian diffusivity can be correlated to temperature, burnup, or fluence, as well as the material microstructure.

The fission product transport within a coated fuel particle can be described by the following Fickian diffusion equation:

$$\frac{\partial C_{i,j}(r,t)}{\partial t} = \dot{B}_{i,j}(r,t) + \lambda_{j-1}C_{i,j-1}(r,t) - \lambda_j C_{i,j}(r,t) + \frac{1}{r^2} \frac{\partial}{\partial r} \left[ r^2 D_{i,j} \frac{\partial C_{i,j}(r,t)}{\partial r} \right] \quad (37)$$

where

$C$  is the concentration (mol/m<sup>3</sup>),

$\dot{B}$  is the volumetric birth rate (mol/m<sup>3</sup>s),

$\lambda$  is the decay constant (s<sup>-1</sup>),

$D$  is the diffusion coefficient (m<sup>2</sup>/s),

$r$  is the radial coordinate (m) – see Fig. 129,

$t$  is the time (s),

the subscript  $i$  is the layer of a particle (K for kernel, B for buffer, I for IPyC, S for SiC, O for OPyC),

the subscript  $j$  is the  $j$ -th nuclide.

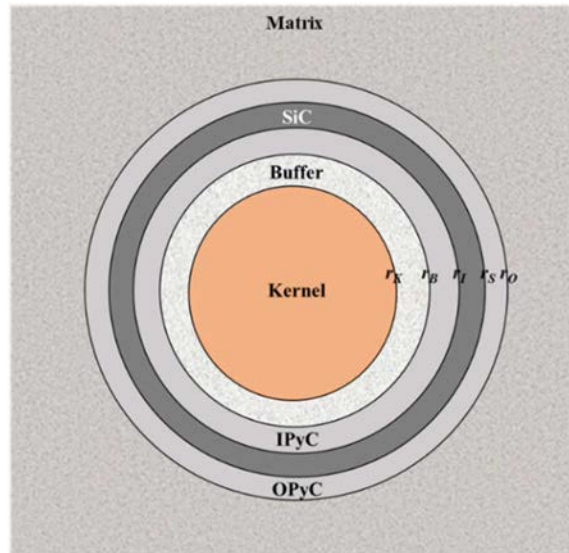


FIG. 129. A TRISO particle in a matrix material.

The initial concentration distribution within a particle is described as a function of the radial coordinate, assuming radial symmetry with a zero diffusion current at the kernel centre. At the particle surface, the concentration is assumed to be zero. Additionally, at the interfaces between two adjacent layers, it is assumed that the mass current flowing out from the left layer surface is equal to that entering the right layer surface. The volumetric birth rate of the fission product in a layer  $i$  can be expressed by equation:

$$\dot{B}_i = b_i \dot{B}_{\text{fission},i} + \Delta \dot{B}_{\text{recoil},i} \quad (38)$$

where

$b$  is the heavy metal contamination fraction,

$\dot{B}_{\text{fission}} = \xi \dot{F} / 6.023 \times 10^{23}$  is the volumetric birth rate due to nuclear fission (mol/m<sup>3</sup>·s),  
 $\xi$  is the fission yield (atom/fission),  
 $\dot{F}$  is the volumetric fission rate (fissions/m<sup>3</sup>·s),  
 $\dot{B}_{\text{recoil}} = \pi(hr^2 - h^3/12)\dot{B}_{\text{fission}}$  is the volumetric birth rate due to recoil (mol/m<sup>3</sup>·s) [211],  
 $h$  is the recoil length (m) and  $r$  is the radial position of the outer surface of a layer (m).

The heat within a particle originates from the nuclear fission of fissile materials and gamma heating of the particle materials. This heat is conducted through the particle materials into a fuel element. For a conservative calculation, it can be assumed that the temperature distribution within a particle reaches an equilibrium state instantly. The temperature distribution is then described by the following steady-state heat transfer equation:

$$\dot{q}_i(r, t) + \frac{1}{r^2} \frac{\partial}{\partial r} \left( k_i r^2 \frac{\partial T_i}{\partial r} \right) = 0 \quad (39)$$

where  $T$  is the temperature (K),  $\dot{q}$  is the volumetric heat generation rate (W/m<sup>3</sup>),  $k$  is the thermal conductivity (W/m·K).

The thermal current at the centre of the kernel is assumed to be zero due to radial symmetry. The temperature at the surface of the particle is considered equal to the temperature of the corresponding part of the fuel element in which the particle is located.

#### 8.1.9. Fission product releases into the coolant

In a fuel region, the fission products are released from the particles and generated from nuclear fissions in heavy metal contamination in the fuel matrix. Metallic fission products migrate through the fuel region, traverse the gap in the case of a fuel block, and pass through the graphite region before ultimately being released into the helium coolant. Gaseous fission products are released from the fuel region into a gap, flowing through the gap into the mainstream of the coolant. Alternatively, they may enter the graphite and diffuse into a coolant hole. This migration is primarily governed by the concentration and temperature within the fuel matrix and structural graphite. Figure 130 represents fission product concentration within a fuel compact.

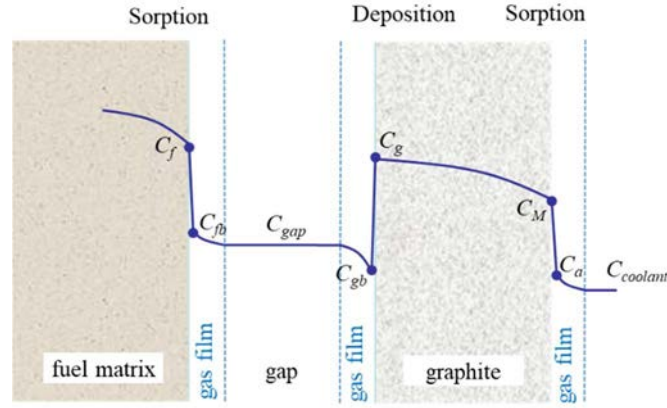


FIG. 130. Concentration profile inside and between a fuel compact and a structural graphite.

The fission product transport within a fuel element can be described by the following Fickian diffusion equation:

$$\frac{\partial C_{i,j}(r,t)}{\partial t} = \dot{S}_{i,j}(r,t) + \lambda_{j-1}C_{i,j-1}(r,t) - \lambda_j C_{i,j}(r,t) + \frac{1}{r^z} \frac{\partial}{\partial r} \left[ r^z D_{i,j} \frac{\partial C_{i,j}(r,t)}{\partial r} \right] \quad (40)$$

where

$C$  is the concentration (mol/m<sup>3</sup>),

$\dot{S}$  is the volumetric generation rate (mol/m<sup>3</sup>·s),

$\lambda$  is the decay constant (s<sup>-1</sup>),

$D$  is the diffusion coefficient (m<sup>2</sup>/s),

$r$  is the radial coordinate (m),

$t$  is the time (s),

the subscript  $i$  means the layer of a fuel element,

the subscript  $j$  means the  $j$ -th nuclide,

the superscript  $z$  is 0 for a slab, 1 for a cylinder, 2 for a sphere.

The initial concentration distribution is expressed by a function of  $r$  coordinate. The generation term is the fission product release rates from the intact, defective and broken particles and the volumetric birth rate due to nuclear fissions in heavy metal contamination:

$$\dot{S}(r,t) = n \sum_{i=0}^M f_i \dot{R}_{CFP,i} + f_{HM} \dot{B}_{fission} \quad (41)$$

where

$n$  is the particle density (particles/m<sup>3</sup>),

$i$  is the failure mode of a particle,

$M$  is the total number of failure modes of a particle,

$f$  is the failure fraction,

$\dot{R}_{\text{CFP}}$  is the release rate from a particle (mol/s),

$f_{\text{HM}}$  is the heavy metal contamination fraction,

$\dot{B}_{\text{fission}} = \xi \dot{F} / 6.023 \times 10^{23}$  is the volumetric birth rate due to nuclear fission (mol/(m<sup>3</sup>·s)),

$\xi$  is the fission yield (atom/fission) and  $\dot{F}$  is the volumetric fission rate (fissions/m<sup>3</sup>·s).

At the centre of a fuel region, the current is assumed to be zero due to radial coordinate symmetry. Concerning metallic fission products, two boundary layers emerge on both surfaces of a fuel region and within the graphite gap separating them. A sorption isotherm is established between the vapour phases [212], facilitating mass transfers across these two boundary layers. If the mass transfers are rapid, the gas pressures on both sides of a gap equalize. Subsequently, the gas pressures can be described by the sorption isotherms in the following manner:

$$e^{x_f} \left( C_{m,f}^{y_f} + C_{m,t,f}^{y_f-1} C_{m,f} \right) = e^{x_g} \left( C_{m,g}^{y_g} + C_{m,t,g}^{y_g-1} C_{m,g} \right) \quad (42)$$

where

$C_m$  is the mass concentration on the graphite surface (mmol/g),

$C_{m,t}$  is the transition mass concentration (mmol/g) =  $\exp(d_1 - d_2 T)$ ,

$X = A + B/T$ ,  $y = G + E/T$ ,  $T$  is the temperature (K),

$A$ ,  $G$ ,  $d_1$  are the sorption isotherm parameters (dimensionless),

$B$ ,  $E$ ,  $d_2$  are the sorption isotherm parameters (K),

the subscripts  $f$  and  $g$  indicate the fuel and graphite, respectively.

For gaseous fission products in the gap, it can be assumed that the rate of flowing out from the fuel is equal to the rate of entering into the graphite, and the concentrations at the fuel surface and the inner surface of the graphite are the same.

The concentration of a gaseous fission product is zero at the graphite surface facing the coolant. Metallic fission products undergo evaporation on the graphite surface adjacent to the coolant. The concentration on the graphite surface facing the coolant is assumed to achieve sorption isotherm equilibrium with the vapour pressure on the graphite side of the boundary layer, formed between the graphite surface and the bulk coolant. The equilibrium relationships can be expressed using a sorption isotherm [213]:

$$P = e^{x_g} \left( C_{m,g}^{y_g} + C_{m,t,g}^{y_g-1} C_{m,g} \right) \quad (43)$$

where  $P$  is the vapour pressure in the graphite side of the boundary layer (Pa).

For metallic fission products, a mass transfer occurs through the boundary layer into the bulk coolant:

$$J(r_c, t) = h(C_a - C_\infty) \quad (44)$$

where

$J$  is the current (mol/m<sup>2</sup>·s),

$C_\infty$  is the mixed mean concentration of a fission product in the coolant and is usually assumed to be zero (mol/m<sup>3</sup>),

$C_a$  is the concentration of a fission product in the graphite side of the boundary layer and is calculated by an ideal gas law and the corresponding vapour pressure (mol/m<sup>3</sup>) =  $P/(RT)$ ,

$R$  is the gas constant (8.3145 J/mol·K),

$T$  is the temperature (K),  $h$  is the mass transfer coefficient of a fission product in helium coolant

(m/s),

$r_c$  is the  $r$  coordinate of graphite surface facing a coolant (m).

It is known that the fission product sorptivity of the graphite increases with exposure to fast neutron fluence, while for the compact matrix material, the sorptivity does not change [213]. For an irradiated graphite, the right-hand side in Equations (42) and (43) is replaced with a modified expression [213]:

$$e^{x_g} \left[ \left( \frac{C_{m,g,irr}}{1+g_F C_{m,g,irr}^{\beta_F}} \right)^{y_g} + C_{m,t,g}^{y_g-1} \frac{C_{m,g,irr}}{1+g_H} \right] \quad (45)$$

where

$C_{m,g,irr}$  is the mass concentration on the irradiated graphite surface (mmol/g),

$$g_F = \gamma_F \varphi e^{\alpha_F},$$

$$g_H = \gamma_H \varphi (10^4/T)^{\alpha_H} e^{-\beta_H(10^4/T)},$$

$$\gamma_i = \text{the annealing factor (dimensionless)} = \frac{\delta_i}{1+e^{\varepsilon(T-1423)}},$$

$i = H, F$  denote the Henrian and Freundlich isotherm regions, respectively,

$$\alpha_F = \frac{\xi}{T} - \frac{\theta}{T^2},$$

$$\beta_H = \kappa - \frac{\lambda}{T} + \frac{\mu}{T^2},$$

$\varphi$  is the fast neutron fluence ( $\text{n/m}^2$ ;  $E_n > 0.18 \text{ MeV}$ ),

$\alpha_H, \delta_H, \delta_F, \kappa$  are constants (dimensionless),

$\varepsilon$  is constant ( $\text{K}^{-1}$ ),

$\xi, \lambda$  are constants (K),

$\theta, \mu$  are constants ( $\text{K}^2$ ).

In a fuel element, the heat is generated from nuclear fissions in nuclear materials and heavy metal contamination, and from gamma heating. It is conducted through the fuel region and the structural graphite and removed by the coolant. The temperature distribution in a fuel element is described by the following steady state heat transfer equation:

$$\dot{q}_i(r, t) + \frac{1}{r^z} \frac{\partial}{\partial r} \left( k_i r^z \frac{\partial T_i}{\partial r} \right) = 0 \quad (46)$$

where

$T$  is the temperature (K),

$\dot{q}$  is the volumetric heat generation rate ( $\text{W/m}^3$ ),

$k$  is the thermal conductivity ( $\text{W/(m K)}$ ),

$r$  is the  $r$ -coordinate (m),

$z$  is 0 for a slab, 1 for a cylinder, 2 for a sphere.

The thermal current at the centre of the fuel region is assumed to be zero due to radial symmetry. The thermal current at the fuel surface is calculated as the product of the heat transfer coefficient of the gap and the temperature difference between the fuel surface and the gap. Similarly, the thermal current at the graphite surface facing a gap is determined as the product of the heat transfer coefficient of the gap and the temperature difference between the graphite surface and the gap. Heat at the graphite surface facing the coolant is transferred to the helium coolant through convection.

## 8.2. DEVELOPMENT OF COATED PARTICLE FUEL PERFORMANCE ANALYSIS CODES

Computer codes for predicting the performance of coated particle fuels are described in various references, such as [3,207,212,214]. Table 80 shows some examples of these computer codes.

TABLE 80. AN INTEGRATED SUITE OF COMPUTER CODES FOR PREDICTING THE AMOUNT AND DISTRIBUTION OF RADIONUCLIDES IN A HTGR

<b>Code</b>	<b>Developer</b>	<b>Function</b>	<b>Reference</b>
GARGOYLE	GA, USA	- Radionuclide inventories	[215]
ORIGEN-2	ORNL, USA		[179]
RADC	GA, USA	- Overall radionuclide mass balance for a plant	[216]
RANDI		- Advanced plant mass balance	[217]
TRITGO		- Overall mass balance for tritium	[218]
PISA	GA, USA	- Mechanical analysis for a coated particle fuel	[219]
SOLGASMIX-PV		- Thermochemical equilibrium calculation	[220]
SURVEY	GA, USA	- Full-core coated particle fuel failure and fission gas release rate	[221]
		- Corrosion of fuel element graphite and hydrolysis of failed fuel particles by coolant impurities	
COPAR-FD	GA, USA	- Transient fission product release from coated particle fuels	[222]
TRAFIC-FD		- Full-core release of metallic fission products and actinides	[223]
SORS/NP1	GA, USA	- Transient releases of gaseous and metallic fission products	[224]
OXIDE-4	GA, USA	- Transient response following in leakage of steam and/or air into the primary system	[225]
PADLOC	GA, USA	- Plate out activity distributions of condensable fission products	[226,227]
POLO	GA, USA	- Fractional re-entrainment of plate out activity in the primary coolant circuit during depressurization accidents	[228]
MACCS	SNL, USA	- Radionuclide transport from the primary coolant circuit to the site boundary and the attendant site-boundary doses during postulated accidents	[229]

IAEA's Coordinated Research Project (CRP), CRP-6 [5] was conducted to assess some codes for predicting the performance of coated particle fuels in HTGR through benchmark exercises. Participating codes are listed in Table 81.

TABLE 81. COATED PARTICLE FUEL PERFORMANCE ANALYSIS CODES PARTICIPATED IN THE IAEA CRP-6 BENCHMARK EXERCISES

Code	Institution	Function	Reference
PANAMA	FZJ, Germany	- Mechanical and failure analysis for TRISOs	[230]
FRESCO II		- Fission product release analysis	[211]
GETTER <sup>a</sup>	PBMR, South Africa	- Fission product inventory and release	-
STRESS3	D.G. Martin, UK	- Mechanical analysis for failure analysis of a batch of TRISOs	-
STAPLE			
TRFUEL	Turkey	- Mechanical and failure analysis for TRISO	-
B-2 <sup>b</sup>	JAEA, Japan	- Stress calculation for a SiC TRISO	-
FORNAX-A <sup>b</sup>		- Fission product release analysis	-
GOLT	VNIINM, Russia	- Mechanical and failure analysis for TRISO	-
PISA	GA, USA	- Mechanical analysis for a TRISO	[219]
CAPPER		- Analysis of failure and fission gas release	[231]
SORS		- Analysis of release of fission products, transuranics, and other radionuclides	[232]
NRCDFI	NRC, USA	- Fission product release analysis	
MELDIF	SNL, USA	- Fission product release analysis	[233]
PARFUME	INL, USA	- Integrated code	[234]
ATLAS	CEA Cadarache, France	- Integrated code	[235]
COPA	KAERI, Republic of Korea	- Integrated code	[236]

<sup>a</sup> GETTER was developed by the German utility consortium HRB (Hochtemperatur Reaktorbau).

<sup>b</sup> There were no code names at the time of participation.

The normal operation benchmark problems of the IAEA CRP-6 [5] consisted of five parts:

- The first part deals with simple analytical cases to test simple thermo-mechanical behaviours (cases 1 to 3);
- The second part tests a pyrocarbon layer behaviour (cases 4a to 4d);
- The third part treats a single particle with more complexity added with each subsequent case (cases 5 to 8);
- The fourth part treats more complicated benchmarks of actual experiments that have been completed (cases 9 to 12);
- The fifth part encompasses planned experiments (case 13).

Table 82 shows fuel characteristics [5] for the normal operation benchmark, case 8. Table 83 shows the material properties for case 8 [5]. Table 84 shows the internal gas pressure for case 8 [5]. It was assumed that both burnup and fast fluence accumulated linearly with time. The assumed scenario involved subjecting the particle to ten temperature cycles, with the temperature initially held at 873 K, then linearly increasing to 1273 K, followed by an immediate decrease back to 873 K. Each cycle had a period equal to one-tenth of the total irradiation time, corresponding to 100 days.

TABLE 82. FUEL CHARACTERISTICS FOR THE NORMAL OPERATION BENCHMARK, CASE 8

Parameter	Units	Case 8: TRISO cyclic temp.
Oxygen to uranium ratio	Atom ratio	2
Carbon to uranium ratio	Atom ratio	0
U-235 enrichment	Weight %	10
Kernel diameter	mm	500
Buffer thickness	mm	100
IPyC thickness	mm	40
SiC thickness	mm	35
OPyC thickness	mm	40
Kernel density	Mg/m <sup>3</sup>	10.8
Buffer density	Mg/m <sup>3</sup>	0.95
IPyC density	Mg/m <sup>3</sup>	1.9
SiC density	Mg/m <sup>3</sup>	3.20
OPyC density	Mg/m <sup>3</sup>	1.9
IPyC BAF		1.03
OPyC BAF		1.03
Irradiation conditions		
Irradiation duration	EFPD	1000
End of life burnup	% FIMA	10
End of life fluence	10 <sup>25</sup> n/m <sup>2</sup> ; $E_n > 0.18$ MeV	3
Constant irradiation temperature <sup>a</sup>	K	873 to 1273 (10 cycles)
End of life internal pressure	MPa	see Table 83
Ambient pressure	MPa	0.1

<sup>a</sup> Temperature increases linearly from 873 to 1273 K for each 100-day cycle and is constant throughout the particle.

TABLE 83. MATERIAL PROPERTIES FOR THE NORMAL OPERATION BENCHMARK CASE 8

Parameter	Units	Case 8: TRISO cyclic temp.
PyC modulus of elasticity	MPa	$3.96 \times 10^4$
PyC Poisson's ratio		0.33
PyC Poisson's ratio in creep		0.50
PyC coefficient of thermal expansion	K <sup>-1</sup>	$5.35 \times 10^{-6}$
PyC creep coefficient	(MPa × 10 <sup>25</sup> n/m <sup>2</sup> ; $E_n > 0.18$ MeV) <sup>-1</sup>	Creep coefficient [(MPa × 10 <sup>25</sup> n/m <sup>2</sup> ) <sup>-1</sup> , $E_n > 0.18$ MeV] = $4.386 \times 10^{-4} - 9.70 \times 10^{-7} T + 8.0294 \times 10^{-10} T^2$ , $T$ in °C.
PyC swelling strain rate	(DL/L)/(10 <sup>25</sup> n/m <sup>2</sup> ; $E_n > 0.18$ MeV)	Radial swelling/shrinkage rate [(DL/L)/10 <sup>25</sup> n/m <sup>2</sup> ] = $4.03266 \times 10^{-4} j^3 - 2.25937 \times 10^{-3} j^2 + 9.82884 \times 10^{-3} j - 1.80613 \times 10^{-2}$ Tangential swelling/shrinkage rate [(DL/L)/10 <sup>25</sup> n/m <sup>2</sup> ] = $-4.91648 \times 10^{-4} j^3 + 2.32979 \times 10^{-3} j^2 + 1.71315 \times 10^{-3} j - 1.78392 \times 10^{-2}$ where $j = (\text{fast neutron fluence})/10^{25}$ n/m <sup>2</sup> for $E_n > 0.18$ MeV. Note: divide fast neutron fluences for $E_n > 0.10$ MeV by a factor of 1.10 to obtain fast neutron fluences for $E_n > 0.18$ MeV.
SiC modulus of elasticity	MPa	$3.70 \times 10^5$
SiC Poisson's ratio		0.13
SiC coefficient of thermal expansion	K <sup>-1</sup>	$4.90 \times 10^{-6}$

TABLE 84. INTERNAL PRESSURE FOR THE NORMAL OPERATION BENCHMARK CASE 8

Fast fluence ( $10^{25}$ n/m <sup>2</sup> ; $E_n > 0.18$ MeV)	Irradiation duration (EFPD)	Internal pressure (MPa)
0.00	0.00	0.00
0.29	96.67	0.14
0.30	100.00	0.02
0.59	196.67	0.94
0.60	200.00	0.04
0.89	296.67	2.59
0.90	300.00	0.07
1.19	396.67	4.87
1.20	400.00	0.10
1.49	496.67	7.64
1.50	500.00	0.14
1.79	596.67	10.79
1.80	600.00	0.20
2.09	696.67	14.26
2.10	700.00	0.26
2.39	796.67	17.99
2.40	800.00	0.33
2.69	896.67	21.96
2.70	900.00	0.41
2.99	996.67	26.13
3.00	1000.00	0.50

The following observations were made from the normal operation benchmark exercises under the IAEA CRP-6 [5]:

- As for cases 1 to 7, codes' predictions were reasonably in agreement with the analytical solutions, and between codes;
- As for case 8 with cyclic temperature history in a pebble bed fuel, the predicted stresses were in good agreement between codes;
- As for cases 9 to 13 with a real irradiation history, codes' predictions showed discrepancies owing to the uncertainties that could largely be attributed to the physical-chemical models employed. In the case of German-type particles with low gas pressures, the stress in the SiC layer was primarily influenced by the shrinkage of the PyC layer rather than the internal gas pressure within the particle.

The accident condition benchmark conducted in the IAEA CRP-6 [5] consisted of three parts:

- A sensitivity study was conducted to investigate the release of fission products from a fuel particle, commencing with a bare kernel and concluding with an irradiated TRISO particle (cases 1a, 1b, 2a, 2b, 3a, 3b, 3c, 3d, 3e, 4a, 4b, 4c, 4d, 5a, 5b);
- The post-calculation of some well documented irradiation and heating experiments (cases 6a, 6b, 7a, 7b, 8a, 8b, 9);
- The prediction of heating tests which are planned in future (cases 10, 11).

A total of 24 cases have been suggested.

Tables 85 and 86 show the characteristics of the fuel element and the particles in an accident benchmark, case 8b [5], which is the heating test HFR-K3/3. Table 87 describes the irradiation time, temperature, burnup, fast fluence, heating time and temperature information on the irradiation and heating phases of HFR-K3/3 [5]. Diffusion coefficients used for accident analysis are provided in Table 88. Uranium inventory fractions ( $U/U_{\text{total}}$ ) outside the fuel kernel are  $1.0 \times 10^{-3}$  in the buffer,  $1.0 \times 10^{-4}$  in the IPyC layer,  $1.0 \times 10^{-6}$  in the SiC layer,  $1.0 \times 10^{-6}$  in the OPyC layer, and  $1.0 \times 10^{-7}$  in the matrix graphite, respectively.

TABLE 85. CHARACTERISTICS OF THE FUEL ELEMENT FOR THE ACCIDENT BENCHMARK CASE 8b

Parameters	HFR-K3
Fuel	Sphere
Fuel element type	GLE-3 LEU phase 1
Matrix graphite grade	A3-27
Matrix density (kg/m <sup>3</sup> )	1750
Total fuel element diameter (mm)	59.98
Fuel zone diameter (mm)	47
No of coated particle fuels per sphere/compact	16,350
Packing fraction (%)	-
Heavy metal loading (g/fuel element)	10.22
U-235 content (g/fuel element)	1.004
Fraction of free uranium	3.5×10 <sup>-5</sup>

TABLE 86. CHARACTERISTICS OF THE COATED FUEL PARTICLES FOR THE ACCIDENT BENCHMARK CASE 8b

Parameters	HFR-K3
Coated particle batch	EUO 2308
Kernel composition	LEU UO <sub>2</sub>
Enrichment (U-235 wt.%)	9.82
Kernel diameter (μm)	497 ± 14.1
Buffer layer thickness (μm)	94 ± 10.3
IPyC layer thickness (μm)	41 ± 4.0
SiC layer thickness (μm)	36 ± 1.7
OPyC layer thickness (μm)	40 ± 2.2
Kernel density (g/cm <sup>3</sup> )	10.81
Buffer density (g/cm <sup>3</sup> )	1.00
IPyC density (g/cm <sup>3</sup> )	~ 1.9
SiC density (g/cm <sup>3</sup> )	3.20
OPyC density (g/cm <sup>3</sup> )	1.88
IPyC Anisotropy BAF	
OPyC Anisotropy BAF	
Fraction of defective SiC	4×10 <sup>-5</sup>

TABLE 87. POST-CALCULATION OF A HEATING TEST HFR-K3/3

Case	Irradiation phase				Heating phase		
	Time (EFPD)	Temperature	Burnup (% FIMA)	Fast neutron fluence (10 <sup>25</sup> n/m <sup>2</sup> , E <sub>n</sub> > 0.1 MeV)	Temperature T (°C)	Time to reach T (h)	Time at T (h)
8b HFR- K3/3	359 (8616 h)	700(surface)- 983(centre)	10.6	5.9	300	-	0.5
					1050	1.5	5.5
					1250	0.5	13.5
					1800	12	25.5
					300	1	-
					1050	1.5	19.5
					1250	0.5	19
					1800	12	74.5
							Total: 187

TABLE 88. DIFFUSION COEFFICIENTS FOR ACCIDENT CONDITIONS

	<sup>a</sup> $D = \sum_i D_{0,i} Q_i / (RT)$			
	$D_{0,1}$ (m <sup>2</sup> /s)	$Q_1$ (kJ/mol)	$D_{0,2}$ (m <sup>2</sup> /s)	$Q_2$ (kJ/mol)
<b>Caesium</b>				
in UO <sub>2</sub>	5.6×10 <sup>-8</sup>	209	5.2×10 <sup>-4</sup>	362
in buffer	1×10 <sup>-8</sup>	0		
in PyC	6.3×10 <sup>-8</sup>	222		
in SiC	<sup>b</sup> 5.5×10 <sup>-14</sup> e <sup>φ/5</sup>	125	1.6×10 <sup>-2</sup>	514
in matrix A3-3	3.6×10 <sup>-4</sup>			
in matrix A3-27	3.6×10 <sup>-3</sup>			
<b>Strontium</b>				
in UO <sub>2</sub>	2.2×10 <sup>-3</sup>	488		
in buffer	1×10 <sup>-8</sup>	0		
in PyC	2.3×10 <sup>-6</sup>	197		
in SiC	1.2×10 <sup>-9</sup>	205	1.8×10 <sup>6</sup>	791
in matrix	1.0×10 <sup>-2</sup>			
<b>Silver</b>				
in UO <sub>2</sub>	6.7×10 <sup>-9</sup>	165		
in buffer	1×10 <sup>-8</sup>	0		
in PyC	5.3×10 <sup>-9</sup>	154		
in SiC	3.6×10 <sup>-9</sup>	215		
in irradiated matrix A3-3	1.6			
<b>Krypton (Iodine)</b>				
in UO <sub>2</sub>	8.8×10 <sup>-15</sup>	54	6.0×10 <sup>-1</sup>	480
in buffer	1×10 <sup>-8</sup>	0		
in PyC	1×10 <sup>-30</sup>	0		
in SiC	1×10 <sup>-30</sup>	0		
in matrix	6.0×10 <sup>-6</sup>			

<sup>a</sup>  $D_0$  = the pre-exponent factor (m<sup>2</sup>/s),  $Q$  = the activation energy (J/mol),

$R$  = the gas constant = 8.3145 (J K<sup>-1</sup> mol<sup>-1</sup>),  $T$  = the temperature (K).

<sup>b</sup>  $\phi$  = the fast neutron fluence (10<sup>25</sup> n/m<sup>2</sup>;  $E_n > 0.1$  MeV), which is reactor-specific.

Figures 131 and 132 shows the fractional releases of <sup>110m</sup>Ag and <sup>137</sup>Cs from HFR-K3/3 [5], respectively. Detailed discussion on measured and predicted releases are referred in Ref. [5].

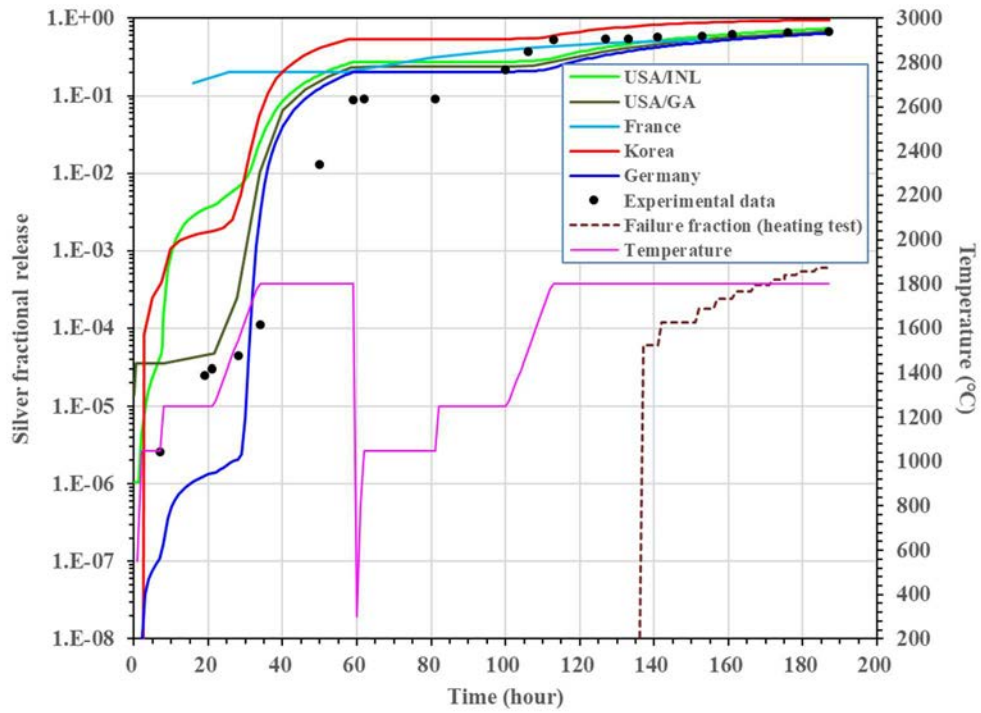


Fig. 131. Fractional release of  $^{110m}\text{Ag}$  from HFR-K3/3 (courtesy of IAEA).

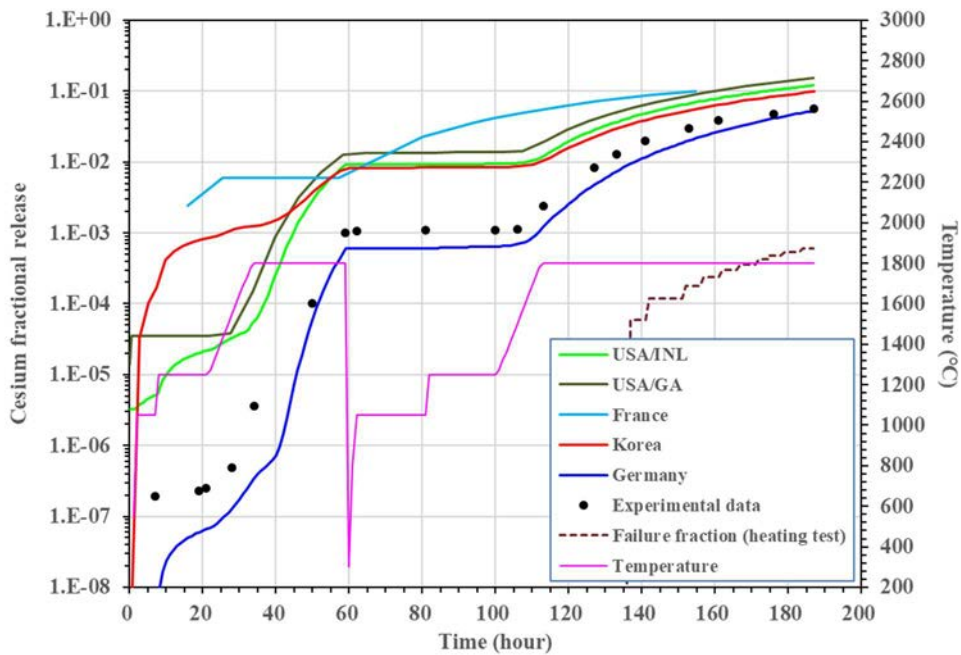


Fig. 132. Fractional release of  $^{137}\text{Cs}$  from HFR-K3/3 (courtesy of IAEA).

The Generation IV International Forum (GIF) is a collaborative international initiative involving fourteen members, aimed at conducting research and development to assess the feasibility and performance capabilities of the next generation of nuclear energy systems. In late 2015, GIF initiated a three-year program for benchmarking TRISO fuel performance models under accident conditions, with INL, USA steering the effort. Other participating institutions included the Japan Atomic Energy Agency

(JAEA, Japan) and the Korea Atomic Energy Research Institute (KAERI, Republic of Korea), utilizing the PARFUME code (INL), B-2 and FORNAX-A codes (JAEA), and COPA code (KAERI). The benchmark focused on three main components:

- Modelling a simplified benchmark problem to assess potential numerical calculation issues at low levels of fission product release;
- Modelling fission product release during annealing testing experiments for AGR 1 [237], AGR-2 [118], and HFR EU1bis [69];
- Comparing all modelling results of AGR 1, AGR-2, and HFR EU1bis with corresponding experimental data.

The simplified benchmark case, referred to as NCC (numerical calculation case), aligned with case 5 of the IAEA CRP-6 benchmark on fission product release behaviour models under accident conditions. This case was intended to evaluate the low levels of fission product release. Case 5 of the IAEA CRP-6 showed large discrepancy between the codes' predictions of fission products release, mainly owing to the "effects of the numerical calculation method rather than the physical model" [5]. The NCC was therefore intended to examine if these numerical effects subsisted.

Tables 89–92 list the modelling parameters, irradiation characteristics and temperatures, and annealing test heating plan for the NCC. Selected annealing tests for modelling encompass the initial and subsequent experiments from the AGR program (AGR-1 and AGR-2) and the HFR EU1bis experiment. The radionuclides chosen for the benchmark calculations are a long-lived activation product ( $^{110m}\text{Ag}$ ) and three fission products ( $^{90}\text{Sr}$ ,  $^{137}\text{Cs}$ , and  $^{85}\text{Kr}$ ). The AGR-1 fuel, particle, and compact properties are referred to Section 6.2.2.1.

TABLE 89. NUMERICAL CALCULATION CASE FUEL MODELLING PARAMETERS

Category	Parameter	Mean value
Fuel properties	U-235 enrichment (wt.%)	10
	Oxygen/uranium (atomic ratio)	2
	Carbon/uranium (atomic ratio)	0
	Uranium contamination fraction	0
Particle properties	Kernel diameter ( $\mu\text{m}$ )	350
	Buffer thickness ( $\mu\text{m}$ )	100
	IPyC thickness ( $\mu\text{m}$ )	40
	SiC thickness ( $\mu\text{m}$ )	35
	OPyC thickness ( $\mu\text{m}$ )	40
	Kernel density ( $\text{g}/\text{cm}^3$ )	10.8
	Kernel theoretical density ( $\text{g}/\text{cm}^3$ )	10.96
	Buffer density ( $\text{g}/\text{cm}^3$ )	0.95
	Buffer theoretical density ( $\text{g}/\text{cm}^3$ )	2.25
	IPyC density ( $\text{g}/\text{cm}^3$ )	1.9
	SiC density ( $\text{g}/\text{cm}^3$ )	3.20
	OPyC density ( $\text{g}/\text{cm}^3$ )	1.9
	IPyC anisotropy (BAF)	1.03
OPyC anisotropy (BAF)	1.03	
Particle asphericity (SiC level)	1.0	
Boundary conditions	Ambient pressure (MPa)	0.1

TABLE 90. NUMERICAL CALCULATION CASE IRRADIATION CHARACTERISTICS

Case	Burnup (%FIMA)	Fast fluence ( $10^{25}$ n/m <sup>2</sup> $E > 0.18$ MeV)	Irradiation length (EFPD)
NCC	10 <sup>(a)</sup>	2 <sup>(a,b)</sup>	1000

- a. Burnup and fast fluence assumed to follow linear evolution throughout irradiation.  
b. Fast fluence ( $E > 0.18$  MeV) = 0.91 × Fast fluence ( $E > 0.1$  MeV)

TABLE 91. NUMERICAL CALCULATION CASE IRRADIATION CHARACTERISTICS

Cycle number	Cycle EFPD	Surface temperature (°C)
1	100	Ramp 600 → 1000
2	100	Ramp 600 → 1000
3	100	Ramp 600 → 1000
4	100	Ramp 600 → 1000
5	100	Ramp 600 → 1000
6	100	Ramp 600 → 1000
7	100	Ramp 600 → 1000
8	100	Ramp 600 → 1000
9	100	Ramp 600 → 1000
10	100	Ramp 600 → 1000

TABLE 92. NUMERICAL CALCULATION CASE ANNEALING TEST HEATING PLAN

Time, (h:min)	Temperature, °C
00:00	1000
00:01	1600
200:01	1600

Table 93 lists the irradiation characteristics and annealing test temperatures of the AGR-1 compacts [118]. Table 94 details the timeline of the AGR-1 annealing test heating plans [118].

TABLE 93. AGR-1 COMPACT SELECTION AND IRRADIATION CHARACTERISTICS

Annealing test temperature (°C)	Compact	Number of particles with failed SiC during annealing test	Burnup <sup>(a)</sup> (%FIMA)	Fast fluence <sup>(a,b)</sup> ( $10^{25}$ n/m <sup>2</sup> $E > 0.18$ MeV)	Average temperature (°C)	Irradiation length (EFPD)	Variant
1600	6-4-1	1	13.22	2.43	1041	620.2	Baseline
	4-3-3	0	18.52	4.16	1094	620.2	3
1700	4-4-3	0	18.83	4.06	1059	620.2	3
	3-3-1	4	19.00	4.23	1051	620.2	Baseline
1800	5-1-3	7	18.17	3.82	1042	620.2	1
	4-4-1	2	18.84	3.99	1057	620.2	3
	4-3-2	3 <sup>c</sup>	16.24	3.68	1057	620.2	3
	3-2-3	11	19.03	4.28	1053	620.2	Baseline
Transient	1-4-2	0	14.83	3.01	1045	620.2	3
	1-1-3	0	15.21	2.86	1018	620.2	3
	1-1-1	0	15.05	2.81	1017	620.2	3

a. Burnup and fast fluence are assumed to follow linear evolution throughout irradiation.

b. Fast fluence ( $E > 0.18$  MeV) =  $0.91 \times$  Fast fluence ( $E > 0.1$  MeV)

c. Compact 4-3-2 modelled with 2 particles with exposed kernel and 1 particle with failed IPyC and SiC.

TABLE 94. AGR-1 ANNEALING TEST HEATING PLANS

Transient		1600°C		1700°C		1800°C	
Time (h:min)	Temperature (°C)	Time (h:min)	Temperature (°C)	Time (h:min)	Temperature (°C)	Time (h:min)	Temperature (°C)
00:00	30	00:00	30	0:00	30	0:00	30
00:30	300	03:05	400	3:05	400	3:05	400
22:30	300	05:05	400	5:05	400	5:05	400
24:00	857	12:10	1250	12:10	1250	12:10	1250
94:00	857	24:10	1250	24:10	1250	24:10	1250
97:48	1300	31:10	1600	33:10	1700	35:10	1800
104:30	1585	331:10	1600	333:10	1700	335:10	1800
112:00	1670	333:47	30	335:57	30	338:07	30
124:00	1695						
136:00	1680						
164:00	1620						
214:00	1508						
294:00	1342						
394:00	1200						
396:00	20						

The AGR-2 fuel, particle, and compact properties are described in Section 6.2.2.2. Table 95 lists the AGR-2 irradiation characteristics and annealing test temperatures. Table 96 details the timeline of the AGR-2 annealing test heating plans.

TABLE 95. AGR-2 COMPACT SELECTION AND IRRADIATION CHARACTERISTICS

Annealing test temperature (°C)	Compact	Number of particles with failed SiC during annealing test	Burnup <sup>(a)</sup> (%FIMA)	Fast fluence <sup>(a,b)</sup> ( $10^{25}$ n/m <sup>2</sup> $E > 0.18$ MeV)	Average temperature (°C)	Irradiation length (EFPD)	Fuel type
1600	5-2-2	0	12.34	3.39	1141	559.2	UCO
	3-3-2	0 <sup>l</sup>	10.54	3.53	1062	559.2	UO <sub>2</sub>
1700	3-4-1	0 <sup>l</sup>	10.62	3.47	1013	559.2	UO <sub>2</sub>
1800	5-4-1	1	12.05	3.12	1071	559.2	UCO

a. Burnup and fast fluence are assumed to follow linear evolution throughout irradiation.

b. Fast fluence ( $E > 0.18$  MeV) =  $0.91 \times$  Fast fluence ( $E > 0.1$  MeV)

c. UO<sub>2</sub> compacts were modelled with zero SiC failures because their exact number could not be determined by post-heating examination.

TABLE 96. AGR-2 ANNEALING TEST HEATING PLANS

1600 °C		1700 °C		1800 °C	
Time (h:min)	Temperature	Time (h:min)	Temperature (em)	Time (h:min)	Temperature (em)
00:00	30	0:00	30	0:00	30
03:05	400	3:05	400	3:05	400
05:05	400	5:05	400	5:05	400
12:10	1250	12:10	1250	12:10	1250
24:10	1250	24:10	1250	24:10	1250
31:10	1600	33:10	1700	35:10	1800
331:10	1600	196:10	1700 <sup>(a)</sup>	37:00	1800
333:47	30	201:50	30	41:00	30 <sup>(b)</sup>
				51:00	1200
				63:00	1800
				363:00	1800
				366:00	30

a. The test was terminated after ~163 h at 1700 °C.

b. The furnace shut down after ~37 h.

The HFR-EU1bis fuel, particle, and pebble properties are detailed in Table 97 [68,238]. Tables 98 and 99 list the HFR-EU1bis irradiation characteristics and irradiation temperatures, respectively. Table 100 details the timeline of the HFR-EU1bis annealing test heating plans.

TABLE 97. HFR-EU1BIS FUEL, PARTICLE, AND PEBBLE PROPERTIES

Category	Parameter	Mean value ± standard deviation
Fuel properties	U-235 enrichment (wt%)	16.76
	Oxygen/uranium (atomic ratio) <sup>(a)</sup>	2
	Carbon/uranium (atomic ratio) <sup>(a)</sup>	0
	Uranium contamination fraction	7.8×10 <sup>-6</sup>
Particle properties	Kernel diameter (mm)	502.2 ± 10.6
	Buffer thickness (mm)	94.3 ± 13.0
	IPyC thickness (mm)	40.6 ± 3.7
	SiC thickness (mm)	35.9 ± 2.2
	OPyC thickness (mm)	39.8 ± 3.3
	Kernel density (g/cm <sup>3</sup> )	10.86
	Kernel theoretical density (g/cm <sup>3</sup> )	10.96
	Buffer density (g/cm <sup>3</sup> )	1.012
	Buffer theoretical density (g/cm <sup>3</sup> )	2.25
	IPyC density (g/cm <sup>3</sup> )	1.87
	SiC density (g/cm <sup>3</sup> )	3.20
	OPyC density (g/cm <sup>3</sup> )	1.87
	IPyC anisotropy (BAF)	1.02
	OPyC anisotropy (BAF)	1.02
	Particle asphericity (SiC level)	1.04
Pebble properties	Sphere diameter (mm) <sup>(a)</sup>	60
	Fuel zone diameter (mm)	50
	U-235 content (g/pebble)	1.00 ± 0.01
	Heavy metal loading (g/pebble)	6.0
	Number of particles per sphere	9560
	Volume packing fraction (%)	6.2
	A3-3 matrix density (g/cm <sup>3</sup> )	1.75
Boundary conditions	Ambient pressure (MPa)	0.1

TABLE 98. HFR-EU1BIS IRRADIATION CHARACTERISTICS

Sphere	Burnup <sup>(a)</sup> (%FIMA)	Fast fluence <sup>(a,b)</sup> (10 <sup>25</sup> n/m <sup>2</sup> $E > 0.1$ MeV)	Irradiation length (EFPD)
1	9.34	2.41	249.55
3	11.07	2.86	249.55
4	11.07	2.86	249.55
5	9.70	2.51	249.55

a. Burnup and fast fluence are assumed to follow linear evolution throughout irradiation.

b. Fast fluence ( $E > 0.18$  MeV) = 0.91 × Fast fluence ( $E > 0.1$  MeV)

TABLE 99. HFR-EU1BIS IRRADIATION TEMPERATURES

Cycle number	Cycle name	Cycle EFPD	Time (EFPD)	Surface Temperature (°C)				Central temperature (°C)			
				\1	\3	\4	\5	\1	\3	\4	\5
1	04-08	24.97	24.97	1014	1009	1015	1006	1216	1250	1247	1227
2	04-09	24.72	49.69	1026	1024	1030	1020	1215	1251	1248	1227
3	05-01	25.99	75.68	1036	1038	1043	1032	1215	1252	1249	1228
4	05-02	25.67	101.35	1042	1047	1052	1040	1211	1249	1246	1224
5	05-03	25.29	126.64	1053	1062	1066	1052	1211	1252	1249	1226
6	05-04	25.67	152.31	1058	1072	1075	1060	1208	1251	1248	1224
7	05-06	24.26	176.57	1065	1082	1086	1069	1207	1252	1249	1224
8	05-07	25.19	201.76	1067	1088	1091	1073	1202	1248	1245	1220
9	05-08	22.19	223.95	1076	1101	1103	1083	1203	1253	1250	1223
10	05-09	25.60	249.55	1079	1108	1109	1088	1199	1252	1248	1220

TABLE 100. HFR-EU1BIS ANNEALING TEST HEATING PLANS

HFR-EU1bis/1		HFR-EU1bis/3		HFR-EU1bis/4		HFR-EU1bis/5			
Time (h:min)	Temp.	Time (h:min)	Temp. (em)						
00:00	20	00:00	20	00:00	20	00:00	300	848:00	300
00:30	300	01:00	20	00:30	300	16:00	300	850:00	1800
06:30	300	01:30	300	03:30	300	23:00	950	852:00	300
09:30	1250	04:30	300	05:30	800	126:00	950	854:00	1800
209:30	1250	06:30	1250	53:30	800	136:00	300	856:00	300
215:30	20	96:00	1250	56:30	1250	157:00	300	858:00	1800
216:30	20	98:00	20	66:30	1250	161:00	950	860:00	300
217:00	300	99:00	20	71:30	1320	185:00	950	862:00	1800
220:00	300	99:30	300	76:30	1390	186:00	1050	864:00	300
222:00	1250	102:30	300	86:30	1500	207:00	1050	866:00	1800
232:00	1250	104:30	1250	91:30	1535	210:00	1250	868:00	300
233:30	1320	114:30	1250	96:30	1570	280:00	1250	870:00	1800
239:30	1600	118:00	1412	106:30	1630	284:00	1500	872:00	300
439:30	1600	122:00	1600	115:30	1666	374:00	1500	874:00	1800
455:00	20	322:00	1600	116:30	1670	378:00	1250	876:00	300
456:00	20	324:00	20	126:30	1695	455:00	1250	878:00	1800
456:30	300			136:30	1710	457:00	300	880:00	300
459:30	300			140:00	1711.5	461:00	300	900:00	300
461:30	1250			160:30	1720	481:00	1250	906:00	1800
471:30	1250			280:30	1720	505:00	1250	980:00	1800
473:00	1321			282:00	20	511:00	1600		
479:00	1605					624:00	1600		
481:00	1700					631:00	1800		
631:00	1700					821:00	1800		
646:00	20					844:00	300		

The NCC consists of a 200-h heating phase at 1600°C following a 1000-day irradiation phase of 10 temperature cycles in the range 600–1000 °C. Calculated fractional release data for Ag, Cs, Sr, and Kr after irradiation and the subsequent heating phase are presented in Table 101.

TABLE 101. CALCULATED AG, CS, SR, AND KR RELEASE FRACTIONS FOR THE NCC

	After irradiation				After 200 h heating			
	Ag	Cs	Sr	Kr	Ag	Cs	Sr	Kr
INL	$6.7 \times 10^{-5}$	$1.8 \times 10^{-12}$	$4.3 \times 10^{-11}$	$2.1 \times 10^{-89}$	$5.0 \times 10^{-1}$	$6.7 \times 10^{-4}$	$3.1 \times 10^{-2}$	$4.0 \times 10^{-14}$
JAEA	$2.8 \times 10^{-5}$	$1.2 \times 10^{-14}$	$4.2 \times 10^{-6}$	$7 \times 10^{-122}$	$4.6 \times 10^{-1}$	$2.9 \times 10^{-4}$	$5.5 \times 10^{-2}$	$1.2 \times 10^{-17}$
KAERI	$1.6 \times 10^{-5}$	$9.8 \times 10^{-14}$	$2.2 \times 10^{-6}$	$2.6 \times 10^{-90}$	$4.6 \times 10^{-1}$	$4.2 \times 10^{-4}$	$3.3 \times 10^{-2}$	$1.3 \times 10^{-16}$

### 8.3. SUMMARY AND DISCUSSION

Many countries are developing their own HTGR fuel performance analysis codes. Two benchmarking exercises were conducted with observations:

- The IAEA CRP-6 provided a platform to exchange information on the verification and validation of the codes under normal operating and accident conditions. For the benchmark cases on simple problems most codes provided good agreement with each other, whilst for the benchmark cases on simulating real irradiation or heating experiments, a large discrepancy in predictions among codes were recognized;
- Under Generation IV programme, “Benchmarking of TRISO Fuel Performance Models under Accident Conditions” was carried out after the IAEA CRP-6. The code-to-code comparison showed reasonable agreement for the release of Ag, Cs and Sr; however, it also showed a large discrepancy for Kr. In comparison with measurements, overall codes overpredicted the fission gas releases.

As next steps, the following are considered:

- Fuel codes need to be extended to model UCO;
- Simplified, fast running codes are used for quick design and safety evaluations. On the other hand, multiscale fuel performance analysis codes are also necessary for better understanding of changes in the microstructures and material properties of nuclear fuels. Separate effects tests are necessary to support modelling parameters taken account of the multiscale codes.

## REFERENCES

- [1] BREY, H.L., “The evolution and future development of the high temperature gas cooled reactor”, Presented at GENES4/ANP2003, Paper 1194, Kyoto, Japan, 15-19 September 2003.
- [2] INTERNATIONAL ATOMIC ENERGY AGENCY, Fuel Performance and Fission product Behaviour in Gas Cooled Reactors, IAEA-TECDOC-978, IAEA, Vienna (1997).
- [3] INTERNATIONAL ATOMIC ENERGY AGENCY, High Temperature Gas Cooled Reactor Fuels and Materials, IAEA-TECDOC-CD-1645, IAEA, Vienna (2010).
- [4] INTERNATIONAL ATOMIC ENERGY AGENCY, Advances in High Temperature Gas Cooled Reactor Fuel Technology, IAEA-TECDOC-CD-1674, IAEA, Vienna (2012).
- [5] INTERNATIONAL ATOMIC ENERGY AGENCY, Performance Analysis Review of Thorium TRISO Coated Particles during Manufacture, Irradiation and Accident Condition Heating Tests, IAEA-TECDOC -1761, IAEA, Vienna (2015).
- [6] DEMKOWICZ, P.A., TRISO Fuel: Design, Manufacturing, and Performance, INL/MIS-19-52869, INL, Idaho Falls (2019).
- [7] INTERNATIONAL ATOMIC ENERGY AGENCY, Safety of Nuclear Power Plants: Design, Specific Safety Requirements No. SSR-2/1 (Rev 1), IAEA, Vienna (2016).
- [8] INTERNATIONAL ATOMIC ENERGY AGENCY, IAEA Safety Glossary – Terminology Used in Nuclear Safety and Radiation Protection, 2018 Edition, IAEA, Vienna (2019).
- [9] BELLES, R., POORE, W., BROWN, N., FLANAGAN, G., HOLBROOK, M., MOE, W., SOFU, T., Proposed Adaptation of the Standard Review Plan NUREG-0800, Chapter 4 (Reactor) for Sodium-Cooled Fast Reactors and Modular High-Temperature Gas-Cooled Reactors, ORNL/TM-2017/151, Oak Ridge National Laboratory (2017).
- [10] PETTI, D.A., MAKI, J.T., BUONGIORNO, J., HOBBS, R.R., MILLER, G.K., Key Differences in the Fabrication, Irradiation and Safety Testing of US and German TRISO-coated Particle Fuel and Their Implications on Fuel Performance, INEEL/EXT-02-00300, INL, Idaho Falls (2002).
- [11] POWERS, J., WORRALL, A., TERRANI, K.A., GEHIN, J.C., SNEAD, L.L., “Fully ceramic microencapsulated fuels: characteristics and potential LWR applications”, Presented to PHYSOR 2014, Kyoto, Japan, September 28 – October 3, 2014.
- [12] DEMKOWICZ, P.A., LIU, B., HUNN, J.D., Coated particle fuel: historical perspectives and current progress, *J. Nucl. Mater.* **515** (2019) 434-450.
- [13] DEMKOWICZ, P.A., HUNN, J.D., Two decades of DOE investment lays foundation for TRISO-fuelled reactors in the US, *Nuclear News* **63**, August 2020.
- [14] MORRIS, R.N., PETTI, D.A., POWERS, D.A., BOYACK, B.E., RUBIN, M.B., TRISO-Coated Particle Fuel Phenomenon Identification and Ranking Tables (PIRTs) for Fission Product Transport Due to Manufacturing, Operations, and Accidents, NUREG/CR-6844, Vol. 1 (2004).
- [15] MAKI, J.T., PETTI, D.A., KNUDSON, D.L., MILLER, G.K., The challenges associated with high burnup, high temperature and accelerated irradiation for TRISO-coated particle fuel, *J. Nucl. Mater.* **371** (2007) 270-280.
- [16] SKERJANC, W.F., MAKI, J. T., COLLIN, B. P., PETTI, D. A., Evaluation of Design Parameters for TRISO-coated Fuel Particles to Establish Manufacturing Critical Limits Using PARFUME, INL/JOU-15-34392, INL, Idaho Falls (2016); also see *J. Nucl. Mater.* **469** (2016) 99-105.
- [17] MARSDEN, B.J., HAVERTY, M., BODEL, W., HALL, G.N., JONES, A.N., MUMMERY, P.M., TREIFI, M., Dimensional change, irradiation creep and thermal/mechanical property changes in nuclear graphite, *International Materials Reviews* **61** (2016) 155-182.
- [18] HAVERTY, M., The Microstructure, Texture and Thermal Expansion of Nuclear Graphite, PhD Thesis, Faculty of Engineering and Physical Sciences, University of Manchester (2015).

- [19] BOER, B., OUGOUAG, A.M., Final Report on Utilization of TRU TRISO Fuel as Applied to HTR Systems Part I: Pebble Bed Reactors, INL/EXT-11-21436, INL, Idaho Falls (2011).
- [20] LOWE, T., BRADLEY, R.S., YUE, S., BARI, K., GELB, J., ROHBECK, N., TURNER, J., WITHERS, P.J., Microstructural analysis of TRISO particles using multi-scale X-ray computed tomography, *J. Nucl. Mater.* **461** (2015) pp. 29-36.
- [21] KOVACS, W.J., YOUNG, C.A., HARMON, D.P., Pre-Irradiation Report of TRISO and BISO Coated ThO<sub>2</sub> Particles for Irradiation in Capsules HT-31 and HT-33, GA-A13923 / UC-77 (1976).
- [22] HALES, J.D., JIANG, W., TOPTAN, A., GAMBLE, K., BISON TRISO Modelling Advancements and Validation to AGR-1 Data, INL/EXT-20-59368, INL, Idaho Falls (2020).
- [23] SCHAPPEL, D.P., Improvements to the Predictive Capability of FCM Fuel Performance Modelling, PhD thesis, University of Tennessee (2017).
- [24] MARTIN, D.G., Considerations pertaining to the achievement of high burn-ups in HTR fuel *Nucl. Eng. Des.* **213** (2002) 241–258.
- [25] INTERNATIONAL ATOMIC ENERGY AGENCY, Irradiation Damage in Graphite Due to Fast Neutrons in Fission and Fusion Systems, IAEA-TECDOC-1154, IAEA, Vienna (2000).
- [26] TERRANI, K.A., KIGGANS, J.O., KATOH, Y., SHIMODA, K., MONTGOMERY, F.C., ARMSTRONG, B.L., PARISH, C.M., HINOKI, T., HUNN, J.D., SNEAD, L.L., Fabrication and characterization of fully ceramic microencapsulated fuels, *J. Nucl. Mater.* **426** (2012) 268–276.
- [27] HUSCHKA, H., VENET, P., Préparation et propriétés des particules de combustible nucléaire pour réacteurs à gaz à haute température, *Bulletin de la Société Française Céramique* **73** (1966) 51–63 (in French).
- [28] HUSCHKA, H., VYGEN, P., Coated fuel particles: requirements and status of fabrication technology, *Nucl. Techn.* **35** (1977) 238–245.
- [29] PODO, L.A., HORSLEY, G. W., Studies on the Preparation of Th/U Dicarbide and Thoria/Urania Fuel Kernels by the Sol-Gel Technique in the Dragon Fuel Element Development Laboratory, Dragon Project Report DP-431, Winfrith (1966).
- [30] COGLIATI, G., et al., Proc. Symposium on Sol-Gel-Processes for the Production of Ceramic Nuclear Fuels, Turin/Italy (1968).
- [31] FERGUSON, D.E., DEAN, O.C., HASS, P.A., ORNL Report 542, Oak Ridge (1968).
- [32] WYMER, R.G., Laboratory and Engineering Studies of Sol-Gel Processes at Oak Ridge National Laboratory, ORNL-TM-2205, Oak Ridge (1968).
- [33] FOERTHMANN, R., NAOUMIDIS, A., NICKEL, H., Untersuchungen zur Herstellung Kugelförmiger Kernbrennstoffteilchen Nach Einem Sol-Gel-Verfahren, KFA Report, Jül 583 RW (1969) (in German).
- [34] BOND, W.D., FINNEY, B.C., HAAS, P.A., HAWS, C.C., PARROTT, J.R., Proc. Symposium on Sol-Gel-Processes and Reactor Fuel Cycles, CONF 700502 Gatlinburg/USA, (1970) 123.
- [35] COGLIATI, G., FACCHINI, A., Proc. Symposium on Sol-Gel Processes and Reactor Fuel Cycles, CONF 700502, Gatlinburg/USA, May (1970) 210.
- [36] KADNER, M., BAIER J., Production of Fuel Kernels for High Temperature Reactor Fuel Elements, *Kerntechnik* **18** (1977) 413–420.
- [37] NAEFE, P., ZIMMER, E. Preparation of uranium kernels by an external gelation process, *Nucl. Techn.* **42** (1979) 163–171.
- [38] KADNER, M., BAIER J., Production of fuel kernels for high temperature reactor fuel elements, *Kerntechnik* **18** (1977) 413–420.
- [39] MINATO, K., FUKUDA, K., Structure of chemically vapour deposited silicon carbide for coated fuel particles, *J. Mater. Sci.* **23** (1988) 699.
- [40] CHAROLLAIS F., et al., CEA and AREVA R&D on HTR fuel fabrication and presentation of the CAPRI experimental manufacturing line, *Nucl. Eng. Des.* **236** (2006) 534–542.

- [41] HAASE, V., et al., Handbook of Inorganic Chemistry, Silicon, 8th Ed., vol. B3, Springer-Verlag, New York (1986) pp.31.
- [42] KRAUTWASSER, P., et al., Raman spectral characterization of silicon carbide nuclear fuel coatings, Journal of American Ceramic Society **66** (1983) 424–434.
- [43] LÓPEZ-HONORATO, E., MEADOWS, P.J., TAN, J., XIAO, P., Control of stoichiometry, microstructure, and mechanical properties in SiC coatings produced by fluidized bed chemical vapour deposition, Journal of Material Research **23** (2008) 1785.
- [44] CHIN, J., et al., The structure of chemical vapour deposited silicon carbide, Thin Solid Films **40** (1977) 57–72.
- [45] XU, S.J., ZHOU, J.G., YANG, B., ZHANG, B.Z., Effect of deposition temperature on the properties of pyrolytic SiC, Journal of Nuclear Materials **224** (1995) 12–16.
- [46] VOICE, E.H., Silicon Carbide as a Fission Product Barrier in Nuclear Fuels, in Silicon Carbide (Eds. HENISCH, H & ROY, R.), Pergamon Press, New York (1969).
- [47] VOICE, E.H., LAMB, D.N., The Deposition and Structure of Pyrolytic Silicon Carbide, DRAGON Project Report DP-677, Winfrith (1969).
- [48] ABLITZER, C., CHAROLLAIS, F., DUGNE, O., MENDES, A., MOULINIER, D., PEREZ, M., in Euro Course on Coated Particle Fuel, IAEA-EU-RAPHAEL-PUMA, held in NRG, Petten, The Netherlands (2007).
- [49] OXLEY, J.H., BROWNING, M.F., VEIGEL, N.D., J.M. BLOCHER, J.M., Microminiaturized Fuel elements by vapour-deposition techniques, Industrial and Engineering Chemistry **1** (1962) 102–107.
- [50] OXLEY, J.H., in Vapour Deposition, (Edited by. POWELL, C.F., OXLEY, J.H., BLOCHER, J.M.), Wiley, New York (1966).
- [51] HROVAT, M., NICKEL, H., KOIZLIK, K., Über die Entwicklung eines Matrixmaterials zu Herstellung gepresster Brennelemente für Hochtemperatur Reaktoren, Forschungszentrum Jülich Report Jül-969 (1973) (in German).
- [52] SCHULZE, R.E., SCHULZE, H.A., RIND, W., Graphite Matrix Materials for Spherical HTR Fuel Elements, Forschungsanlage Jülich report Jül-Spec-167 (1982).
- [53] LIANG, T.X., “Recent R&D of HTR fuel in INET”, Presented at the IAEA Technical Meeting on HTR Fuel and Fuel Cycle, Vienna, 6–9 September 2010.
- [54] DELLE, W.W., et al., Quality Control Procedures for HTR Fuel Element Components. Report Jül-1333, Forschungszentrum Jülich, Germany (1976).
- [55] NELSON, A.T., HUNN, J.D., KARNOWSKI, T.P., Current Development Status of a Particle Size Analyzer for Coated Particle Fuel, Oak Ridge National Laboratory, <<http://info.ornl.gov/sites/publications/files/Pub6657.pdf>>, (2004).
- [56] HUNN, J.D., JELLISON, G.E., LOWDEN, R.A., Increase in pyrolytic carbon optical Anisotropy and density during processing of coated particle fuel due to heat treatment, J. Nucl. Mat. **374** (2008) 445–452.
- [57] LIU, B., Fabricating Process and Quality Control Diagram of the Fuel Element, Institute of Nuclear and New Energy Technologies, Tsinghua University, Beijing, China (2011).
- [58] KIM, K.W., LEE, Y.W., CHO, M.S., PARK, J.Y., RA, S.W and PARK, J.B., Non-destructive measurement of the coating thickness for simulated TRISO coated fuel particles using phase contrast X ray radiography, Nuclear Eng. And Des. **238** (2008) 3285–3291.
- [59] HITTNER, D., LOMMERS, L., SHAHROKHI, F., “R&D needs for near-term HTRs”, Proc. of HTR-2010, Prague (2010).
- [60] BANCHET, J., TISSEUR, D., GUILLERMIER, P., “X-ray radiography: A alternative method for determining HTR fuel particle coating layer thickness and density”, Proc. HTR-2008, Washington D.C., U.S.A. (2008).
- [61] KASHYAP, Y.S., YADAV, P.S., SARKAR, P.S., AGGARWAL, A., ROY, T., SINHA, A., DASGUPTA, K., SATHIYAMOORTHY, D., Application of X ray phase contrast imaging

- technique in the study of pyrocarbon-coated zirconia kernels, *Nondestructive Testing and Evaluation International* **42** (2009) 388–388.
- [62] RAGOSS, H., Experimentelle Absicherung des Brennelementverhaltens für Normalbetriebs- und Störfallbedingungen des HTR-Moduls, Siemens Report No. 76.00526.9, Bensberg (1987) (in German).
- [63] RAGOSS, H., NABLIEK, H., Fuel Specifications for the Siemens MODUL, Interatom-Forschungszentrum Jülich Joint Technical Note, Bensberg (1989).
- [64] VENTER, J.H., and NABIELEK, H., “Performance Envelope of Modern HTR TRISO Fuel”, Proc. HTR2006, Johannesburg (2006).
- [65] HACKSTEIN, K.G., et al., Stand der brennelementtechnologie für hochtemperaturreaktor-kugelhaufenreaktoren. *Atomkernenergie/Atomtechnik* **47** (1985)163–169 ) (in German).
- [66] MEHNER, A. W., HEIT, W., RÖLLIG, K., RAGOSS, H., MÜLLER, H., Spherical fuel Elements for HTR manufacture and qualification by irradiation testing, *J. Nucl. Mat.* **171** (1990) 9–18.
- [67] INTERNATIONAL ATOMIC ENERGY AGENCY, Safety Related Design and Economic Aspects for HTGRs, IAEA-TECDOC-1210, IAEA, Vienna (1999).
- [68] NABIELEK, H., et al., Selection of Benchmark Cases for Mechanical Failure Prediction, Technical Note in EU HTR-F Project No. HTR-F1-04/08-D-3.1.1, Forschungszentrum, Jülich, Germany (2005).
- [69] FÜTTERER, M., BERG, G., MARMIE, A., TOSCANO, E.H., FRIES, D., BAKKER, K., De GROOT, S., Results of AVR fuel pebble irradiation at increased temperature and burnup in the HFR Petten, *Nucl. Eng. Des.* **238** (2008) 2877–2885.
- [70] PETTI, D.A., DEMKOWICZ, P.A., MAKI, J.T., HOBBS, R.R., “TRISO-coated particle fuel performance”, Section 3.07, *Comprehensive Nuclear materials*, ed. by Rudy M. KONINGS and Roger E. STOLLER, Elsevier Inc. (2012).
- [71] AHLF, J., CONRAD, R., CUNDY, M., SCHEURER, H., Irradiation experiments on high temperature gas-cooled reactor fuels and graphite at the High Flux Reactor Petten, *J. Nucl. Mater.* **171** (1990) 31-36.
- [72] MAKI, J.T., et al., NP-MHTGR Fuel Development Program Results, INEEL-EXT-02-01268, INL, Idaho Falls (2002).
- [73] HAYASHI, K., et al., Irradiation Experiments of the 13<sup>th</sup> – 15<sup>th</sup> OGL-1 Fuel Assemblies, JAERI-Research 2000-001, JAERI (2000).
- [74] MONTGOMERY, F.C., et al., HRB-22 Irradiation Test Data Report, ORNL/M-4080, Rev. 0, ORNL, Oak Ridge (1995).
- [75] HAYASHI, K., et al., Distribution of fission and activation products in the graphite sleeves of HTGR fuel rods: First and second OGL-1 fuels, *J. Nucl. Mater.* **116** (1983) 233-243.
- [76] FUKUDA, K., et al., Irradiation experiments of VHTR reference fuels by in-pile gas loop (OGL-1), *J. Atomic Energy Society of Japan*, **26 [1]** (1984) 57-74. (1984).
- [77] HAYASHI, K., et al., Distribution of fission products in irradiated graphite materials of HTGR fuel assemblies: Third and fourth OGL-1 fuels, *J. Nucl. Mater.* **136** (1985) 207-217.
- [78] HAYASHI, K., et al., Irradiation Experiments of the 6<sup>th</sup> – 12<sup>th</sup> OGL-1 Fuel Assemblies, JAERI-Research 94-017, JAERI (1994).
- [79] INTERNATIONAL ATOMIC ENERGY AGENCY, Fuel Technology and Performance of Non-Water Cooled Reactors, IAEA-TECDOC-850 (1995).
- [80] MINATO, K., et al., HRB-22 Capsule Irradiation Test for HTGR Fuel (JAERI/US DOE Collaborative Irradiation Test), JAERI-Research 98-021, JAERI (1998).
- [81] ACHARYA, R., SAWA, K., HRB-22 Pre-irradiation Thermal Analysis, ORNL/M-3563, ORNL, Oak Ridge (1995).
- [82] TOBITA, T., et al., Metallic Fission Product Release from Failed Coated Fuel Particles (ICF-51H Capsule Irradiation Test), JAERI-Research 96-014, JAERI (1996).

- [83] MORRIS, R.N., et al., The Core Conduction Cooldown Test Facility: Current Status and Issues, ORNL/NPR-91/7, ORNL, Oak Ridge (1992).
- [84] BULLOCK, R.E., Fission product release during post-irradiation annealing of several types of coated fuel particles, *J. Nucl. Mater.* **125** (1984) 304-319.
- [85] SAWA, K., et al., Development of ceramics-coated particle fuel for very high-temperature gas-cooled reactors, *J. Atomic Energy Society of Japan* **6** [2] (2007) 113-125.
- [86] DE GROOT, S., et al., Modelling of the HFR-EU1bis experiment and thermos-mechanical evaluation, *Nucl. Eng. Des.* **238** (2008) 3114-3120.
- [87] TANG, C., et al., Fuel irradiation of the first batches produced for the Chinese HTR-10, *Nucl. Eng. Des.* **236** (2006) 107-113.
- [88] LAURIE, M., et al., Results of the HTR-EU1 fuel irradiation of INET and AVR pebbles in the HFR Petten, *Nucl. Eng. Des.* **251** (2012) 117-123.
- [89] TANG, C., et al., Irradiation testing of matrix material for spherical HTR-10 fuel elements, *Nucl. Eng. Des.* **238** (2008) 2886-2892.
- [90] DONG, Y., Design, safety features & progress of HTR-PM, 24 January 24 2018, gif\_webinar\_htr-pm\_dong\_201801v2\_final.
- [91] KNOL, S., et al., HTR-PM Fuel pebble irradiation qualification in the high flux reactor in Petten, *Nucl. Eng. Des.* **329** (2018) 82-88.
- [92] FREIS, D., et al., Burn-up determination and accident testing of HTR-PM fuel elements irradiated in the HFR Petten, *Nucl. Eng. Des.* **357** (2020) 110414.
- [93] DE GROOT, S., et al., Fission-Product Behaviour during Irradiation of TRISO-Coated Particles in the HFREU1bis Experiment, HTR2008-58125 (2008).
- [94] BARRACHIN, M., et al., Fission-product behaviour in irradiated TRISO-coated particles: Results of the HFR-EU1bis experiment and their interpretation, *J. Nucl. Mater.* **415** (2011) 104-116.
- [95] RAY, I.L.E., THIELE, H., MATZKE, H.J., Transmission electron microscopy study of fission product behaviour in high burnup  $UO_2$ , *J. Nucl. Mater.* **188** (1992) 90-95.
- [96] MINATO, K., et al., Fission Product behaviour in TRISO-coated  $UO_2$  fuel particles, *J. Nucl. Mater.* **208** (1994) 266-281.
- [97] KLEYKAMP, H., The chemical state of the fission product in oxide fuels, *J. Nucl. Mater.* **131** (1985) 221-246.
- [98] FREIS, D., Störfallsimulationen und Nachbestrahlungsuntersuchungen an kugelförmigen Brennelementen für Hochtemperaturreaktoren, Ph.D. Thesis (2010) (in German)
- [99] FREIS, D., et al., Accident testing of high-temperature reactor fuel elements from the HFR-EU1bis irradiation, *Nucl. Eng. Des.* **241** (2011) 2813-2821.
- [100] LAURIE, M., et al., JRC's on-line fission gas release monitoring system in the high flux reactor Petten, *Nucl. Eng. Des.* **251** (2012) 325-329.
- [101] DE GROOT, S., et al., "RAPHAEL-FT & generation IV PYCASSO-I irradiation", Proc. 4th Int. Top. Meeting on High Temperature Reactor Technology HTR2008, Washington, DC (2008).
- [102] DEMKOWICZ, P.A., TRISO Fuel Part II: Accident Performance and NRC Engagement, INL/MIS-21-62430, INL, Idaho Falls (2021).
- [103] PETTI, D., COLLIN, B., MARSHALL, D., A Summary of the Results from the DOE AGR Fuel Development and Qualification Program, INL-EXT-16-40784 Rev 0, INL (2017).
- [104] DEMKOWICZ, P.A., AGR Program Highlights – 2020 ART-GCR Status Meeting, INL/MIS-20-60355 Rev. 0, INL (2020).
- [105] MITCHELL, T.R., Technical Program Plan for the Next Generation Nuclear Plant Advanced Gas Reactor Fuel Development and Qualification Program, PLN-3636 Rev. 9, INL/MIS-10-20662, INL (2020).

- [106] DEMKOWICZ, P., et al., “TRISO fuel experience and capabilities in the DOE advanced gas, reactor program”, GAIN-EPRI-NEI Advanced Fuels Workshop, March 5-6, 2019, Boise State University, USA.
- [107] DEMKOWICZ, P.A., et al., AGR-1 Post Irradiation Examination Final Report, INL/EXT-15-36407 Rev.0, INL (2015).
- [108] SCHILTHELM, S., MCINTYRE, B., SLOAN, S., Uranium Oxycarbide (UCO) Tristructural Isotropic (TRISO) Coated Particle Fuel Performance, EPRI-AR-1 (NP), 3002015750, Electric Power Research Institute (EPRI) (2019).
- [109] KIM, B.G., et al., The first irradiation testing and PIE of TRISO-coated particle fuel in Korea, Nucl. Eng. Des. **329** (2018) 34-45.
- [110] MAKI, J.T., AGR-1 Irradiation Experiment Test Plan, INL/EXT-05-00593 Rev. 3, INL (2009).
- [111] HUNN, J.D., LOWDEN, R.A., Data Compilation for AGR-1 Baseline Coated Particle Composite LEU01-46T, Rev. 1, ORNL/TM-2006/019, ORNL (2006).
- [112] JELLISON, G.E. JR. and HUNN, J.D., Optical anisotropy measurements of TRISO nuclear fuel particle cross sections: the method. J. Nucl. Mater. **372** (2008) 36–44.
- [113] HUNN, J.D., SAVAGE, T.W., KEHN, J.S., AGR-1 Fuel Compact Pre-Irradiation Characterization Summary Report, ORNL/TM-2012/295, ORNL (2012).
- [114] MAKI, J.T., PARFUME User’s Guide, INL/EXT-10-18317, INL (2010).
- [115] PLOGER, S.A., et al., Microscopic analysis of irradiated AGR-1 coated particle fuel compacts, Nucl. Eng. Des. **271** (2014) 221-230.
- [116] DEMKOWICZ, P.A., et al., Key results from irradiation and post-irradiation examination of AGR-1 UCO TRISO fuel, Nucl. Eng. Des. **329** (2018) 102-109.
- [117] COLLIN, B.P., AGR-2 Irradiation Experiment Test Plan, PLN-3798 Rev. 2 (2018).
- [118] COLLIN, B.P., AGR-2 Irradiation Test Final As-Run Report. INL/EXT-14-32277, Rev. 4 (2018).
- [119] DEMKOWICZ, P.A., AGR-2 Post-Irradiation Examination Plan, PLN-4616 Rev. 0, INL/MIS-13-30534, INL (2013).
- [120] DEMKOWICZ, P.A., et al., Results of the AGR-2 TRISO fuel performance demonstration irradiation experiment in the advanced test reactor, Annals of Nuclear Energy **150** (2021) 107833.
- [121] STEMPIEN, J.D., et al., AGR-2 TRISO Fuel Post-Irradiation Examination Final Report, INL/EXT-21-64279, INL (2021).
- [122] GROVER, S.B., et al., Completion of the First NGNP Advanced Gas Reactor Fuel Irradiation Experiment, AGR-1, in the Advanced Test Reactor, INL/CON-10-18032, INL (2010); also Proceedings of HTR 2010 Prague, Czech Republic, October 18-20, 2010, Paper 104.
- [123] HUNN, J.D., et al., Safety Testing and Destructive Examination of AGR-2 UCO Compacts 2-3-2 and AGR-2 UO<sub>2</sub> Compact 3-4-1, ORNL/TM-2018/956, ORNL (2018).
- [124] HUNN, J.D., et al., Safety Testing and Destructive Examination of AGR-2 UCO Compacts 2-1-2, ORNL/TM-2019/1201, ORNL (2019).
- [125] HUNN, J.D., et al., Safety Testing and Destructive Examination of AGR-2 UO<sub>2</sub> Compacts 3-1-1, ORNL/TM-2020/1451, ORNL (2020).
- [126] GERCZAK, T.J., et al., AGR-2 Loose Particle Heating Tests in the Furnace for Irradiated TRISO Testing, ORNL/TM-2020/1715, ORNL (2020).
- [127] HUNN, J.D., et al., Safety Testing and Destructive Examination of AGR-2 UCO Compacts 6-4-3, ORNL/TM-2019/1200, ORNL (2019).
- [128] Advanced Reactor Technologies: Gas-Cooled Reactor Research and Development Quarterly Report, July, August, and September 2020, INL/EXT-21-61295, INL (2021).
- [129] Final Safety Evaluation; Uranium Oxycarbide (UCO) Tristructural Isotropic (TRISO) Coated

Particle Fuel Performance: EPRI-AR-1(NP), EPRI; ML20216A453, (visited [www.nrc.gov](http://www.nrc.gov) on Aug. 10, 2021).

- [130] Advanced Reactor Technologies: Very High Temperature Reactor Research and Development Quarterly Report (Jan., Feb., Mar. 2020), INL/EXT-20-59634, Rev. 0, INL (2020).
- [131] GERCZAK, T.J., HUNN, J.D., MORRIS, R.N., MONTGOMERY, F.C., SKITT, D.J., BALDWIN, C.A., DYER, J.A., ECKHART, B.D., analysis of fission product distribution and composition in the TRISO layers of AGR-2 fuel, Nucl. Eng. Des. **364** (2020) 110656.
- [132] HUNN, J.D., BALDWIN, C.A., MONTGOMERY, F.C., GERCZAK, T.J., MORRIS, R.N., HELMREICH, G.W., DEMKOWICZ, P.A., HARP, J.M., STEMPIEN, J.D., Initial examination of fuel compacts and TRISO particles from the US AGR-2 irradiation test, Nuclear Engineering and Design **329** (2018) 89-101.
- [133] RICE, F.J., STEMPIEN, J.D., DEMKOWICZ, P.A., Ceramography of irradiated TRISO fuel from the AGR-2 experiment, Nuclear Engineering and Design **329** (2018) 73-81.
- [134] MORRIS, R.N., HUNN, J.D., BALDWIN, C.A., MONTGOMERY, F.C., GERCZAK, T., DEMKOWICZ, P.A., Initial results from safety testing of US AGR-2 irradiation test fuel, Nuclear Engineering and Design **329** (2018) 124-133.
- [135] RICE, F.J., STEMPIEN, J.D., DEMKOWICZ, P.A., Ceramography of Irradiated TRISO Fuel from the AGR-2 Experiment, INL/EXT-16-39462, INL (2016).
- [136] HUNN, J.D., et al., Destructive PIE and Safety Testing of Six AGR-2 UO<sub>2</sub> Capsule 3 Compacts. ORNL/TM-2020/1612, ORNL (2020).
- [137] COLLIN, B.P., AGR-3/4 Irradiation Experiment Test Plan, PLN-3867 Rev. 1, INL/MIS-11-22351, INL (2015).
- [138] COLLIN, B.P., AGR-3/4 Irradiation Test Final As-Run Report, INL/EXT-15-35550, Rev. 1, INL (2016).
- [139] HARP, J.M., et al., Initial Gamma Spectrometry Examination of the AGR-3/4 Irradiation, INL/CON-16-39738, INL (2016); also International Topical Meeting on High Temperature Reactor Technology (HTR 2016).
- [140] DEMKOWICZ, P.A., AGR-3/4 Phase 2 Post-Irradiation Examination Plan, PLN-5382 Rev. 0, INL/MIS-17-41954, May 2017.
- [141] STEMPIEN, J. et al., AGR-3/4 TRISO Fuel Compact Ceramography, INL/EXT-20-57610, INL (2020).
- [142] EINERSON, J.J., et al., Analysis of fission gas release-to-birth ratio data from the AGR irradiations, Nucl. Eng. Des. **306** (2016) 14-23.
- [143] PHAM, B.T., SCATES, D.M., AGR-1, AGR-2 and AGR-3/4 Release-to-Birth Ratio Data Analysis, INL/EXT-14-32970-Rev002, INL (2019).
- [144] STEMPIEN, J.D., et al., Measurement of Fission product Concentration Profiles in AGR-3/4 TRISO Fuel Graphite Matrix and Nuclear Graphites, INL/EXT-21-62863, INL (2021).
- [145] STEMPIEN, J.D., et al., AGR-3/4 Irradiation Test Train Disassembly and Component Metrology First Look Report, INL/EXT-16-38005, INL (2016).
- [146] COLLIN, B.P., AGR-5/6/7 Irradiation Experiment Test Plan, PLN-5245, Rev. 1, INL (2018).
- [147] STEMPIEN, J.D., AGR-5/6/7 Post-Irradiation Examination Plan, PLN-6110 Rev. 0, INL/EXT-20-59111, INL (2020).
- [148] PHAM, B.T. et al., AGR-5/6/7 Irradiation Test Final As-Run Report, INL/EXT-21-64221, INL (2021).
- [149] HELMREICH, G.W., HUNN, J.D., SKITT, D.J., DYER, J.A., SCHUMACHER, A.T. Acceptance Test Data for the AGR-5/6/7 Irradiation Test Fuel TRISO Composite. ORNL/TM-2017/037, ORNL (2017).
- [150] STEMPIEN, J.D. et al., Initial Observations from Advanced Gas Reactor (AGR)-5/6/7 Capsule 1, INL/RPT-22-66720, Idaho National Laboratory (2022).

- [151] KIM, B.G., et al., Irradiation Test Plan of Coated Particle Fuel at HANARO, KAERI/TR-4875/2013. KAERI (2013).
- [152] DE GROOT, S., et al., HTR fuel coating separate effect test PYCASSO, Nucl. Eng. Des. **240** (2010) 2392-2400.
- [153] KNOL, S., et al., PYCASSO: irradiation of HTR coated particles at high temperatures, Nucl. Eng. Des. **251** (2012) 150-156.
- [154] KNOL, S., et al., PYCASSO: X-ray tomography on HTR coated particles, Nucl. Eng. Des. **271** (2014) 206-208.
- [155] LIU, D., et al., X-ray tomography study on the crushing strength and irradiation behaviour of dedicated tristructural isotropic nuclear fuel particles at 1000°C, Mater. Des. **187** (2020) 108382.
- [156] BROWN, N.R., A review of in-pile fuel safety tests of TRISO fuel forms and future testing opportunities in non-HTGR applications, J. Nucl. Mater. **534** (2020) 152139.
- [157] FUKUDA, K., HAYASHI, K., SHIBA, K., “Fuel Behaviour and Fission Product Release under HTGR Accident Conditions-Fission Product Transport Processes in Reactor Accidents”, Fission Product Transport Processes in Reactor Accidents ed. by J.T. Rogers, Hemisphere Publishing, New York, NY (USA), 1990, ISBN 0-89116-876-1, pp. 197-204. Hemisphere Publishing, 79 Madison Avenue, New York, NY 10016 (USA).
- [158] UMEDA, M., SUGIYAMA, T., NAGASE, F., FUKETA, T., UETA, S., SAWA, K., Behaviour of coated fuel particle of high-temperature gas-cooled reactor under reactivity initiated accident conditions, J. Nucl. Sci. Technol. **47**[11] (2010) 991-997.
- [159] OLANDER, D.R., Fundamental Aspects of Nuclear Reactor Fuel Elements, TID-26711-P1, Technical Information Centre, US Department of Energy (1976).
- [160] LEWIS, B.J., THOMPSON, W.T., IGLESIAS, F.C., “Fission Product Chemistry in Oxide Fuels”, Comprehensive Nuclear Materials, ed. by R.J.M. Konings, Volume 2, pp. 515-546, Elsevier.
- [161] MINATO, K., OGAWA, T., FUKUDA, K., SHIMIZU, M., TAYAMA, Y., TAKAHASHI, I., Fission product behaviour in TRISO-coated UO<sub>2</sub> fuel particles, Journal of Nuclear Materials **208** (1994) 266-281.
- [162] VAN ROOYEN, I.J., YANG, Y., HOLESINGER, T., BACHHAV, M., FU, Z., Microstructure and Fission Product Distribution Examination in the UCO kernel of TRISO Fuel Particles, INL/CON-18-44479-Revision-0, INL (2018); Also in the Proceedings of High Temperature Reactor Technology (HTR) 2018, Paper HTR 2018-3012, Warsaw, Poland, October 8-10, 2018.
- [163] WRIGHT, K.E., VAN ROOYEN, I.J., “EPMA of irradiated AGR-1 TRISO fuel particles”, Proceedings of 8th International Topical Meeting on High Temperature Reactor Technology, HTR2016, Las Vegas, 2016.
- [164] VAN ROOYEN I.J., OLIVIER, E. J., NEETHLING, J.H., “Fission products silver, palladium and cadmium identification in neutron irradiated SiC using a Cs-corrected HRTEM”, Proceedings of the 7<sup>th</sup> International Topical Meeting on High Temperature Reactor Technology, Weihai, China, October 27-31, 2014, (HTR2014), Paper HTR2014-31255.
- [165] VAN ROOYEN, I.J., OLIVIER, E. J., NEETHLING, J.H., Fission products silver, palladium and cadmium identification in neutron irradiated SiC using a Cs-corrected HRTEM, Journal of Nuclear Materials **476** (2016) pp. 93-101.
- [166] WEN, H., VAN ROOYEN, I.J., Distribution of fission products palladium, silver, cerium and caesium in the uncorroded areas of the locally corroded SiC layer of a neutron irradiated TRISO fuel particle, Journal of the European Ceramic Society **37** (2017) pp. 380051-3284.
- [167] WEN, H., VAN ROOYEN, I.J., HUNN, J.D., GERCZAK, T.J., Electron microscopy study of Pd, Ag, and Cs in carbon areas in the locally corroded SiC layer in a neutron-irradiated TRISO fuel particle, Journal of the European Ceramic Society **38** (2018) pp. 978-4188.
- [168] BOOTH, A.H., A Method of Calculating Fission Gas Release from UO<sub>2</sub> Fuel and its Application to the X-2-f Loop Test, AECL- 496 (1957).

- [169] VAN DER VEN, A., Fission Product Transport in TRISO Particle Layers under Operating and Off-Normal Conditions, Nuclear Energy University Program, Project No. 10-924 (2014).
- [170] JIANG, W., HALES, J.D., SPENCER, B.W., COLLIN, B.P., SLAUGHTER, A.E., NOVASCONE, S.R., TOPTAN, A., GAMBLE, K.A., GARDNER, R., TRISO particle fuel performance and failure analysis with BISON, *Journal of Nuclear Materials* **548** (2021) 152795.
- [171] MILLER, G.K., PETTI, D.A., VARACALLE, D.J., MAKI, J.T., Consideration of the effects on fuel particle behaviour from shrinkage cracks in the inner pyrocarbon layer, *Journal of Nuclear Materials* **295** (2001) pp. 205-212.
- [172] HOMAN, F.J., LONG, E.L., Jr., "Irradiation Performance of HTGR Recycle Fissile Fuel", ORNL/TM-5502 (1976).
- [173] MONTGOMERY, F., "Fission-Product SiC Reaction in HTGR Fuel", GA 1485(Rev. 11/80), PED-81-2200 (Rev/1), DOE/ET/35300—T3, 1981.
- [174] SAWA, K., TOBITA, T., Investigation of irradiation behaviour of sic-coated fuel particle at extended burnup, *Nuclear Technology* **142** (2003) pp. 250-259.
- [175] MARTIN, D.G., SAWA, K., UETA, S., SUMITA, J., "A Study of Fuel Failure Behaviour in High Burnup HTGR Fuel – Analysis by STRESS3 and STAPLE Codes", JAERI-Research 2001-033 (2001).
- [176] KOVACS, W.J., BONGARTZ, K., GOODIN, D., TRISO-Coated HTGR Fuel Pressure-Vessel Performance Models, GA-A16807 UC-77 (1983).
- [177] WERNER, C.J., MCNP<sup>®</sup> User's Manual Code Version 6.2. LA-UR-17-29981 (2017).
- [178] MOORE, R.L., SCHNITZLER, B.G., WEMPLE, C.A., BABCOCK, R.S., WESSOL, D.E., MOCUP: MCNP-ORIGEN2 Coupled Utility Program. INEL-95/0523 (1995).
- [179] CROFF, G., A User's Manual for the ORIGEN2 Computer Code. ORNL/TM-7175 (1980).
- [180] SHIM, H.J., HAN B.S., JUNG J.S., PARK, H.J., KIM, C.H., MCCARD: Monte Carlo Code for Advanced Reactor Design and Analysis. *Nuclear Engineering and Technology* **44** (2012) pp. 161-176.
- [181] PROKSCH, E., STRIGL, A., NABIELEK, H., Production of Carbon Monoxide during Burn-up of UO<sub>2</sub> Kerneled HTR Fuel Particles, *J. Nucl. Mater.* **107** (1982) 280-285.
- [182] HORSLEY, G.W. et al., Influence of irradiation temperature, burnup, and fuel composition on gas pressure (Xe, Kr, CO, CO<sub>2</sub>) in coated particle fuels, *J. Am. Ceram. Soc.* **59** [1-2] (1976) 1-4.
- [183] LINDEMER, T.B., Measurement and interpretation of CO and Kr + Xe in irradiated ThO<sub>2</sub>-Containing HTGR fuel particles, *Journal of American Ceramic Society* **60** (1977) pp.409-416.
- [184] HOMAN, F., NABIELEK, H., YANG, L., Low Enriched Fuel Particle Performance Review. GA-A14759 (1978).
- [185] KOVACS, W.J., BONGARTZ, K., GOODIN, D.T., High-temperature gas-cooled reactor fuel pressure vessel performance models, *Nuclear Technology* **68** (1985) pp. 344-354.
- [186] Deep-Burn Modular Helium Reactor Fuel Development Plan, ORNL/TM-2002/135, GA-224-0-TRT-000167. P. 3-17 (2002).
- [187] RICHARDS, M.B., SHENOY, A.S., BROWN, L.C., BUCKINGHAM, R.T., HARVEGO, E.A., PEDDICORD, K.L., REZA, S.M.M., COUPEY, J.P., "H2-MHR pre-conceptual design report: SI-based plant", GA-A25401, P. 3-40 (2002).
- [188] Development of Improved Models and Designs For Coated-Particle Gas Reactor Fuels, INEEL/EXT-05-02615 (2004).
- [189] BECK, S.D., The Diffusion of Radioactive Fission Products from Porous Fuel Elements, BMI-1433 (1960).
- [190] REDLICH, O., KWONG, J.N.S., On the thermodynamics of solutions; an equation of state; fugacity of gaseous solutions, *Chemical Reviews* **44** [1] (1949) pp. 233-244.
- [191] Outotec Oy, Outotec HSC Chemistry<sup>®</sup> 7.1. Outotec Oy, Finland, 2009.

- [192] NP-MHTGR Material Models of Pyrocarbon and Pyrolytic Silicon Carbide. CEQA-002820, Rev. 1 (1993).
- [193] JACKSON, H.F., LEE, W.E., “2.13 properties and characteristics of ZrC”, *Comprehensive Nuclear Materials*, ed. by J.M. Konings, Elsevier Ltd. (2012).
- [194] KAAE, J.L., On Irradiation-induced creep of pyrolytic carbon in a general state of stress, *Journal of Nuclear Materials* **34** (1970) pp. 206-208.
- [195] PRICE, R.J., Properties of silicon carbide for nuclear fuel particle coatings, *Nuclear Technology* **35** (1977) pp. 320-336.
- [196] TIMOSHENKO, S.P., GOODIER, J.N., *Theory of Elasticity*, 3rd ed. McGraw-Hill, Inc. (1970).
- [197] BOER, B., OUGOUAG, A.M., KLOOSTERMAN, J.L., MILLER, G.K., Stress analysis of coated particle fuel in graphite of high-temperature reactors, *Nuclear Technology* **162** (2008) pp. 276-292.
- [198] VERFONDERN, K., “3.24 TRISO fuel performance modelling and simulation”, *Comprehensive Nuclear Materials*, Ed. by J.M. Konings, Elsevier Ltd. (2012).
- [199] PEARSON, R.L., LINDEMER, T.B., BEAHM, E.C., Simulated Fission Product-SiC Interaction in TRISO-Coated LEU or MEU HTGR Fuel Particles. ORNL/TM-6991 (1980).
- [200] PEARSON, R.L., LAUF, R.J., LINDEMER, T.B., The Interaction of Palladium, the Rare Earths, and Silver with Silicon Carbide in HTGR Fuel Particles, ORNL/TM-8059 (1982).
- [201] TIEGS, T.N., Fission product Pd-SiC interaction in irradiated coated-particle fuels, *Nuclear Technology* **57** (1981) pp. 389-398.
- [202] STANSFIELD, O.M., HOMAN, F.J., SIMON, W.A., TURNER, R.F., Interaction of Fission Products and SiC in TRISO Fuel Particles: A Limiting Design Parameter, GA-A17183 (1983).
- [203] VAN ROOYEN, I.J., LILLO, T.M., WU, Y.Q., 2014. Identification of silver and palladium in irradiated TRISO coated particles of the AGR-1 experiment. *Journal of Nuclear Materials* **446** (2014) pp. 178-186.
- [204] MINATO, K., et al., Fission product palladium-silicon carbide interaction in HTGR fuel particles, *J. Nucl. Mater.* **172** (1990) 184-196.
- [205] MONTGOMERY, F., Fission product SiC Reaction in HTGR Fuel. GA-905837 (1981).
- [206] MINATO, K., OGAWA, T., “3.08. Advanced concepts in TRISO fuel”, *Comprehensive Nuclear materials*, 1st Ed., Editors-in-Chief; Rudy M. Konings and Roger E. Stoller, Vol. 3; *Advanced Fuels/Fuel Cladding/Nuclear Fuel Performance Modelling and Simulation*, Elsevier Inc. (2012).
- [207] HANSON, D.L., A Review of Radionuclide Release from HTGR Cores during Normal Operation. EPRI Report 1009382 (2004).
- [208] MILLER, G.K., MAKI, J.T., KNUDSON, D.L., PETTI, D.A., Calculating failure probabilities for TRISO-coated fuel particles using an integral formulation, *Journal of Nuclear Materials* **399** (2010) pp. 154-161.
- [209] BOX, G.E.P., MULLER, M.E., A note on the generation of random normal deviates, *The Annals of Mathematical Statistics* **29** (1958) 610-611.
- [210] GREEN, A.E., BOURNE, A.J., *Reliability Technology*, John Wiley & Sons Ltd. (1958).
- [211] KROHN, H., FINKEN, R., FRESCO-II: Ein Rechenprogramm zur Berechnung der Spaltproduktfreisetzung aus kugelförmigen HTR-Brennelementen in Bestrahlungs- und Ausheizexperimenten, Rep. Jül-Spez-212. Research Centre Jülich (1983) (in German).
- [212] MARTIN, R.C., *Compilation of Fuel Performance and Fission Product Transport Models and Database for MHTGR Design* (1993).
- [213] MYERS, B.F., BELL, W.E., Caesium Transport Data for HTGR Systems, GA-A13990 (1979).
- [214] HANSON, D.L., *Software Requirement for Predicting Radionuclide Transport*, PC-000537, Rev. 0. General Atomics (2007).
- [215] SHIRLEY, G., *User’s Manual and Description for GARGOYLE: A Fuel Cycle Analysis Code with a Decay Heat Calculation Capability*. CEQA-002922, Rev. 0. CEQA Corporation (1993).

- [216] EICHENBERG, T.W., RADC Users Manual, CEGA-002814 (1993).
- [217] HUDRITSCH, W.W., RANDI, A Zero Dimensional Computer Program for Calculating HTGR Activities, GA-A14091 (1977).
- [218] HANSON, D.L., Review of Tritium Behaviour in High Temperature Gas-Cooled Reactors, PC-000535, Rev. 0. General Atomics (2006).
- [219] PELESSONE, D., PISA: A One-Dimensional Spherically Symmetric Computer Program to Perform Thermal and Stress Analysis of Irradiated Fuel Particles, General Atomics Unpublished report CEGA-M-92-2052 (1992).
- [220] BESMANN, T.M., SOLGASMIX-PV, a Computer Program to Calculate Equilibrium Relationships in Complex Chemical Systems, ORNL/TM-5775 (1977).
- [221] PFREMMER, R.D., Software Description and User's Manual for GT MHR Fuel Performance Code, SURVEY. GA Document 911009/0 (2002).
- [222] TZUNG, F., COPAR-FD, A Finite Difference Program to Compute Release of Metallic Fission Products from Coated Fuel Particles: Code Theory and Users Manual, CEGA-002098 (1992).
- [223] TZUNG, F., TRAFIC-FD, A Finite Difference Program to Compute Release of Metallic Fission Products from an HTGR Core: Code Theory and Users Manual, CEGA-001904 (1992).
- [224] CADWALLADER, G.J., SORS/NP1 Code Description and User's Manual, CEGA-002092 (1993).
- [225] TANGIRALA, V., BETTS. W., OXIDE-4 Software Design Description and User's Manual, CEGA-001871, Rev. 0 (1993).
- [226] HUDRITSCH, W.W., SMITH, P.D., PADLOC, A One Dimensional Computer Program for Calculating Coolant and Plateout Fission Product Concentrations, USDOE Report GA-A14401 (1977).
- [227] HUDRITSCH, W.W., PADLOC, A One Dimensional Computer Program for Calculating Coolant and Plateout Fission Product Concentrations, Part II. GA-A14401 (1981).
- [228] BOLIN, J.M., POLO Users Manual, DOE-HTGR-88332, Rev. 0 (1989).
- [229] CHANIN, D., YOUNG, M.L., Code manual for MACCS2: Volume 1, User's Guide, NUREG/CR-6613 SAND97-0594 Vol. 1 (1998).
- [230] PELLETIER, M., NABIELEK, H., ABRAM, T., MARTIN, D., HTR-F Project: Selection of properties and models for the coated particle – Fuel kernel. Commissariat a l'Energie Atomique et aux Energies Alternatives, Technical Note SESC/LSC 03-028, August 2003.
- [231] BRADLEY, J.S., RICHARDS, M.B., Software Design Description and User's Manual for CAPPER Irradiation Capsule Performance Computer Code, CEGA-002309. General Atomics, San Diego, CA (1992).
- [232] SCHWARTZ, M.H., SEDGELEY, D.B., MENDONCA, M.M., SORS: Computer Programs for Analyzing Fission Product Release from HTGR Cores During Transient Temperature Excursions, GA-A12462 (1974).
- [233] HUMPHRIES, L.L., BEENY, B.A., GELBARD, F., LOUIE, D.L., PHILLIPS, J., Computer Code Manuals, Vol. 1: Primer and Users' Guide, Version 2.2.9541 2017. SAND2017-0455 O (2017)
- [234] MILLER, G.K., PETTI, D.A., MAKI, J.T., KNUDSON, D.L., PARFUME Theory and Model Basis Report, INL/EXT-08-14497 (2009).
- [235] PHÉLIP, M., MICHEL, F., PELLETIER, M., DEGENEVE, G., GUILLERMIER, P., "The ATLAS HTR fuel simulation code objectives, description and first results", #Paper B03. In: 2nd International Topical Meeting on High Temperature Reactor Technology, Beijing, China, September 22-24, 2004.
- [236] KIM, Y.M., JO, C.K., COPA Ver. 1.0: Theory Report. KAERI/TR-7945/2019 (2019).
- [237] COLLIN, B.P., AGR-1 Irradiation Test Final As-Run Report, INL/EXT-10-18097 Rev. 3 (2015).

- [238] VERFONDERN, K., NABIELEK, H., PANAMA Ein Rechenprogramm zur Vorhersage des Partikelbruchanteils von TRISO-Partikeln unter Störfallbedingungen. Report Jül-Spez-298. Research Centre Jülich, Germany (1985) (in German).

## **ANNEX I.**

### **LIST OF MODULAR HTGRS AND ADVANCED HTGR-TYPE REACTORS**

Table I-1 provides a list of modular HTGRs and advanced HTGR-type reactors, taken from Ref. [I-1].

### **REFERENCES**

[I-1] INTERNATIONAL ATOMIC ENERGY AGENCY, Advances in Small Modular Reactor Technology Developments, A Supplement to: IAEA Advanced Reactors Information System (ARIS), 2022 Edition, IAEA, Vienna (2022).

Table I-1 LIST OF MODULAR HTGRS AND ADVANCED HTGR-TYPE REACTORS

Reactor	Type	Output MW(th)/MW(e)	Fuel type	Enrichment (%)	Core discharge burnup (GWd/t)	Temp. (°C) (Inlet/outlet)	Designers	Country	Status
<b>HIGH TEMPERATURE GAS COOLED SMALL MODULAR REACTORS</b>									
HTR-PM	HTGR	2×250/210	Sphere (TRISO coated particle fuel)	8.5	90	250/750	INET, Tsinghua University	China	In operation
StarCore	HTGR	Block One: 35/14 Block Two: 50/20 Block Three: 150/60 One to six modules /plant	TRISO prismatic	15	60	280/750	StarCore Nuclear	Canada/UK/USA	Pre-conceptual design
GTHT300	HTGR	<600/100–300	UO <sub>2</sub> TRISO ceramic coated particle	14	120	587–633/ 850–950	JAEA	Japan	Basic Design
GT-MHR	HTGR	600/288	Coated particle fuel in compacts, hexagonal prism graphite blocks of 0.36 m	14–18 LEU or wt.Pu	100–720 (depends on fuel type)	490/850	JSC Afrikantov OKBM	Russian Federation	Preliminary design completed
MHR-T	HTGR	4×600/4×205.5	Coated particle fuel in compacts, hexagonal prism graphite block of 0.36 m	< 20 LEU	125	578/950	JSC Afrikantov OKBM	Russian Federation	Conceptual design
MHR-100	HTGR	215/25–87 (depends on configuration)	Hexagonal prism graphite blocks with coated particle fuel	LEU < 20	-	490–553/795–950 (depends on configuration)	JSC Afrikantov OKBM	Russian Federation	Conceptual design
PBMR-400	HTGR	400/165	Pebble bed with coated particle fuel	9.6 LEU or wt.Pu	-	500/900	PBMR SOC Ltd	South Africa	Preliminary design
A-HTR-100	HTGR	100/50	Pebble bed with coated particle fuel	LEU or WPU	86	406/1200	Eskom Holdings SOC Ltd	South Africa	Conceptual design completed
HTMR-100	HTGR	100/35 single module plant	TRISO particles in pebbles: LEU, Th/LEU, Th/HEU or Th/Pu	Various*	80–90	250/750	Steenkampskraal Thorium Limited	South Africa	Basic design
Xe-100	HTGR	200/82.5	UCO TRISO/pebbles	15.5	165	260/750	X-Energy LLC	USA	Basic design
SC-HTGR	HTGR	625/272	UCO TRISO particle fuel in hexagonal graphite blocks	14.5 ave. / 18.5 max.	165	325/750	Framatome, Inc.	USA	Preliminary design

Table I-1 LIST OF MODULAR HTGRS AND ADVANCED HTGR-TYPE REACTORS

Reactor	Type	Output MW(th)/MW(e)	Fuel type	Enrichment (%)	Core discharge burnup (GWd/t)	Temp. (°C) (Inlet/outlet)	Designers	Country	Status
HTR-10	HTGR	10/2.5	Spherical elements with TRISO particles fuel (UO <sub>2</sub> kernel)	17	80	250/700	INET, Tsinghua University	China	Operable
HTTR-30	HTGR	30/	UO <sub>2</sub> TRISO ceramic coated particle	3 – 10 (6 avg.)	22 (33 max.) Ave. fuel discharged burnup, GWd/tHM	395/850 (950 max.)	JAEA	Japan	In operation
RDE/Micro-PeLUIt	HTGR	10/3	Spherical elements with coated particle fuel	17	80	250/750	BATAN	Indonesia	Conceptual design
<b>MOLTEN SALT SMALL MODULAR REACTORS</b>									
KP-FHR	Pebble-bed salt cooled Reactor	320/140	TRISO particles in graphite pebble matrix / pebble bed	19.75	-	550/650	KAIROS Power, LLC.	USA	Conceptual design
Mk1 PB-FHR	FHR	236/100	TRISO particles in graphite pebble matrix / pebble bed	19.9	180 (Fuel burnup)	600/700	University of California Berkeley	USA	Pre-conceptual design
<b>MICRO-SIZED SMALL MODULAR REACTORS</b>									
Energy Well	FHTR	20/8	TRISO	15	70	650/700	Centrum výzkumu Řež	Czech Republic	Pre-conceptual design
U-Battery	HTGR	10/4	TRISO / Hexagonal	< 20	~80 (ave.)	-	Urenco	UK	Conceptual design
Westinghouse eVinci (MMR)	Heat pipe	7-12/2-3.5	TRISO or another encapsulation	5 – 19.75	Not Disclosed	NA800 (Core temperature)	Westinghouse Electric Company, LLC.	USA	Conceptual Design Completed
MMR	HTGR	15/>5	FCM or TRISO graphite/Hexagonal	HALEU 19.75	> 60	Helium 300/630, solar salt stored at 560	USNC (Ultra Safe Nuclear Corporation)	USA	Preliminary design
TCR*	HTGR	~3/	UCO TRISO or UN TRISO FCM	< 19.75 HALEU <20			ORNL	USA	Conceptual design



## ANNEX II.

### EXAMPLE OF FUEL SPECIFICATIONS

Specifications of some coated particle fuel designs are described in this Annex.

TABLE II-1. SPECIFICATION OF US NEW PRODUCTION REACTOR (NPR) FUEL COMPACT

<b>FUEL KERNEL</b>	
Material	UCO
Enrichment (wt.%)	93.15 <sup>+0.15</sup> <sub>-1.00</sub>
Impurities (wt.-ppm)	5000
C/U atomic ratio	0.5
O/U atomic ratio	1.4 – 1.7
Diameter (μm)	195 <sup>+15</sup> <sub>-50</sub>
Density (g/cm <sup>3</sup> )	10.3
<b>COATINGS</b>	
Buffer layer thickness (μm)	90 – 110
Buffer layer density (g/cm <sup>3</sup> )	0.80 – 1.10
IPyC thickness (μm)	40 – 60
IPyC density (g/cm <sup>3</sup> )	1.85 – 1.95
IPyC BAF	1.20
SiC thickness (μm)	35 – 40
SiC density (g/cm <sup>3</sup> )	3.18
OPyC thickness (μm)	30 – 50
OPyC density (g/cm <sup>3</sup> )	1.80 – 1.95
OPyC BAF	Not specified
PPyC <sup>20</sup> thickness (μm)	40 – 60
PPyC density (g/cm <sup>3</sup> )	0.80 – 1.10
<b>FUEL COMPACT</b>	
Length (mm)	49.3 ± 0.5
Diameter (mm)	12.37 – 12.62
Burnable impurities (B, Cd, Eu, Gd, Li, Sm) (ppm EBC <sup>21</sup> )	5
Non-burnable impurities (Na, S, Ca, Yb, Ti, V, Cr, Lu, Mn, Fe, Co, Al, In, Ta, Cs, La, Ce, W, Pr, Nd, Tb, Ho, Er, Tm) (ppm EBC)	1
Total free uranium fraction	6×10 <sup>-5</sup>

\* Data taken from [II-1].

<sup>20</sup> PPyC stands for protective (or overcoating) pyro carbon.

<sup>21</sup> EBC stands for Equivalent Boron Concentration.

TABLE II-2. SPECIFICATION OF US AGR FUEL COMPACT

	Specification of fuels for irradiation tests AGR-5/6/7	Specification of fuels for irradiation test AGR-1
<b>FUEL KERNEL</b>		
Material	UCO	UCO
Enrichment (%)	15.5 ±0.1	19.8±0.1
Diameter (mm)	425 ± 10, also a critical region <sup>22</sup> was defined as < 375 and > 475	350 ± 10, also a critical region was defined as < 300 and > 400
Density (g/cm <sup>3</sup> )	10.4	10.4
Uranium fraction (gU/gU-CO)	0.885	0.87
C/U atomic ratio	0.4 ±0.1	0.5 ±0.2
O/U atomic ratio	1.5 ± 0.2	1.5 ± 0.2
(C + O) / U atomic ratio	2.0	2.0
Individual impurities (wt.-ppm): Li, Na, Al, Cl, Ca, V, Cr, Mn, Fe ©, Co, Ni, Cu, and Zn	100 each	100 each
Process impurities (wt.-ppm): P, S	1500 each	1500 each
Aspect ratio or sphericity (ellipticity)	Not specified, but a critical region was defined as 1.05, it was also indicated the fraction of composite kernels in the critical region to be ≤ 0.10	Not specified, but a critical region was defined as 1.05, it was also indicated the fraction of composite kernels in the critical region to be ≤ 0.10
<b>COATINGS</b>		
Buffer layer thickness (mm)	100 ± 15	100 ± 15
Buffer layer density (g/cm <sup>3</sup> )	1.05 ± 0.10	1.03 ± 0.15
IPyC thickness (mm)	40 ± 4	40 ± 4.
IPyC density (g/cm <sup>3</sup> )	1.90 ± 0.05	1.90 ± 0.05
IPyC BAF	Not provided.	Not provided.
SiC thickness (mm)	35 ± 3	35 ± 3
SiC density (g/cm <sup>3</sup> )	3.19	3.19
SiC aspect ratio	Not specified, but a critical region was defined as 1.14.	Not provided.

<sup>22</sup> How to determine the critical region is not reported.

TABLE II-2. SPECIFICATION OF US AGR FUEL COMPACT

	Specification of fuels for irradiation tests AGR-5/6/7	Specification of fuels for irradiation test AGR-1
OPyC thickness (mm)	40 ± 4	40 ± 4
OPyC density (g/cm <sup>3</sup> )	1.90 ± 0.05	1.90 ± 0.05
OPyC BAF	Not provided.	≤Not provided.
Defective IPyC coating fraction	1.0 × 10 <sup>-4</sup>	2.0 × 10 <sup>-4</sup>
Defective SiC coating fraction	1.0 × 10 <sup>-4</sup>	1.0 × 10 <sup>-4</sup> also another value of 2.0 × 10 <sup>-4</sup> was defined
Defective OPyC defect fraction	1.0 × 10 <sup>-4</sup>	0.01
Missing OPyC layer defect fraction		3.0 × 10 <sup>-4</sup>
FUEL COMPACT		
Mean uranium loading (gU/compact)		
Nominally 40% packing fraction	1.36 ± 0.10	0.905 ± 0.04
Nominally 25% packing fraction	0.90 ± 0.08	
Length (mm)	Not specified, but critical limits were set as 24.4 and 25.3.	Not specified, but a lower critical limit of 25.02 and an upper limit 25.40 were set.
Diameter (mm)	Not specified, but critical limits were set as 12.20 and 12.44.	Not specified, but a lower critical limit of 12.22 and an upper limit of 12.46 were set.
Matrix density (g×cm <sup>-3</sup> )	1.65	Not provided.
Iron (Fe) outside of SiC per compact (mg)	25, also a critical limit of <sup>3</sup> 100 was set.	25, also an upper critical limit of 100 was set.
Transition metals (Cr, Mn, Co, and Ni) outside SiC per compact (mg)	50 each element.	≤ 75 each element
Calcium (Ca) outside SiC per compact (mg)	50	90
Aluminium (Al) Al outside SiC per compact (mg)	50	45
Titanium (Ti) and Vanadium (V) outside SiC per compact (mg)	240	400
Chlorine (Cl) content outside SiC in compact (wt.- ppm)	Not provided	30
Dispersed uranium fraction (DUF) <sup>23</sup> ; (g U <sub>leached</sub> /g U <sub>sample</sub> )	1.0 × 10 <sup>-5</sup>	1.0 × 10 <sup>-4</sup>

<sup>23</sup> In Refs. [II-2, II-3], a term “Heavy metal contamination fraction, g exposed U/g U in compact” is used, and it is believed that it is equivalent to DUF. In addition, these terms somewhat are equivalent to total free uranium fraction, which includes both terms: matrix contamination and particles with defective SiC.

TABLE II-3. SPECIFICATION FOR GERMAN FUEL PEBBLES

FUEL KERNEL	
Material	UO <sub>2</sub>
Enrichment (wt%)	8.0 ± 0.1
Diameter (mm)	480 – 520
Density (g/cm <sup>3</sup> )	10.4
Sphericity	
Fraction of odd-shaped kernels	
COATING LAYERS	
Buffer layer thickness (mm)	72 – 108
Buffer layer density (g/cm <sup>3</sup> )	1.05
IPyC thickness (mm)	30 – 50
IPyC density (g/m <sup>3</sup> )	1.91 ± 0.1
IPyC BAF	1.1
IPyC OPTAF	
SiC thickness (mm)	31 – 39
SiC density (g/cm <sup>3</sup> )	3.18
OPyC thickness (mm)	25 – 45
OPyC density (g/cm <sup>3</sup> )	1.91 ± 0.1
OPyC BAF	1.1
OPyC OAF	
FUEL ELEMENT MATRIX	
Density (g/cm <sup>3</sup> )	1.75±0.02
Ash content (ppm)	
Thermal conductivity, at 1000°C (W/cm·K)	≥ 25
Standard specific corrosion rate (mg/cm <sup>2</sup> ·h)	≤ 1000°C
Standard abrasion rate (mg/cm <sup>2</sup> ·h)	
Crushing strength (kN)	≥ 18
Total free uranium fraction	6 × 10 <sup>-5</sup>

\* Data taken from Ref. [II-1].

TABLE II-4. SPECIFICATION FOR JAPANESE HTTR FUEL COMPACTS

FUEL KERNEL	
Material	UO <sub>2</sub>
Enrichment (wt%)	6
Diameter (mm)	600 ± 55
Density (g/cm <sup>3</sup> )	10.63 ± 0.26
Impurity (ppm) – EBC	< 3.0
COATING LAYERS	
Buffer layer thickness (mm)	60 ± 12
Buffer layer density (g/cm <sup>3</sup> )	1.1 ± 0.1
IPyC thickness (mm)	30 ± 6
IPyC density (g/cm <sup>3</sup> )	1.85 <sup>+0.10</sup> <sub>-0.05</sub>
SiC thickness (mm)	25 <sub>0</sub> <sup>+12</sup>
SiC density (g/cm <sup>3</sup> )	3.2
OPyC thickness (mm)	45 ± 6

TABLE II-4. SPECIFICATION FOR JAPANESE HTR FUEL COMPACTS

OPyC density (g/cm <sup>3</sup> )	1.85 <sup>+0.10</sup> <sub>-0.05</sub>
IPyC/OPyC OAF	1.03
COATED FUEL PARTICLE	
Diameter (mm)	920 <sup>+50</sup> <sub>-30</sub>
Sphericity	Up to 1.2
ANNULAR FUEL COMPACT	
Particle packing factor (vol%)	30 ± 3
Impurity (ppm) – equivalent boron content	5
Outer diameter (mm)	26.0 ± 0.1
Inner diameter (mm)	10.0 ± 0.1
Height (mm)	39.0 ± 0.5
Matrix density (g/cm <sup>3</sup> )	1.70 ± 0.05
Compressive strength (N)	4900
Total free uranium fraction	2×10 <sup>-3</sup>

\* Data taken from Ref. [II-1].

TABLE II-5. SPECIFICATION FOR CHINESE HTR-10 FUEL BEBBLES

FUEL KERNEL	
Material	UO <sub>2</sub>
Diameter (mm)	500 ± 50
Density (g/cm <sup>3</sup> )	10.4
Sphericity	< 1.2
O/U ratio	2.01
Fraction of odd-shaped kernels	5 × 10 <sup>-4</sup>
COATING LAYERS	
Buffer layer thickness (mm)	90 ± 36
Buffer layer density (g/cm <sup>3</sup> )	1.10
IPyC thickness (mm)	40 ± 20
IPyC density (g/cm <sup>3</sup> )	1.9 ± 0.1
SiC thickness (mm)	35 ± 10
SiC density (g/cm <sup>3</sup> )	3.18
OPyC thickness (mm)	40 ± 20
OPyC density (g/cm <sup>3</sup> )	1.9 ± 0.1
IPyC/OPyC OAF	1.03
GRAPHITE MATRIX	
Density (g/cm <sup>3</sup> )	1.70
Total ash (ppm)	300
Li content (ppm)	0.3
Impurity (ppm) – equivalent boron content	3.0
Thermal conductivity (W/cm·K)	0.25 at 1000°C
Corrosion rate (mg/cm <sup>2</sup> ·h)	1.3 at 1000°C in He + 1 vol% H <sub>2</sub> O
Erosion rate (mg/h)	6 per fuel element
Breaking loading (kN)	18
FUEL ELEMENT	
Diameter (mm)	59.6 – 60.2

TABLE II-5. SPECIFICATION FOR CHINESE HTR-10 FUEL BEBBLES

Thickness of fuel free shell (mm)	4.0 – 6.0
Total free uranium fraction	$3 \times 10^{-4}$

\* Data taken from Ref. [II-1].

TABLE II-6. SPECIFICATION FOR KOREAN KAERI FUEL PEBBLES

Properties	Design value	Measured value	Remarks
Kernel			
- Diameter ( $\mu\text{m}$ )	$480 \pm 30$	$483.50 \pm 15$	300–350 particles/batch (PSA*)
- Density ( $\text{g}/\text{cm}^3$ )	$10.65 \pm 0.25$	$10.68 \pm 0.023$	6g of sample weight (Pycnometer)
- U-235 enrich. (wt%)	$4.5 \pm 0.10$	$4.504 \pm 0.004$	chemical analysis (TIMS)
- O/U ratio	$2.00 \pm 0.01$	$2.003 \pm 0.002$	30 mg of sample weight (TG/DTA)
- Total uranium (wt%)	$\geq 87.0$	88.13	cal. Value
- Sphericity (aspect ratio)	$< 1.2$	$\leq 1.04$	average
Coated fuel particle			
- Buffer thickness ( $\mu\text{m}$ )	$95 \pm 45$	$102.91 \pm 30$	CG* (10 particles/batch)
- Buffer density ( $\text{g}/\text{cm}^3$ )	$1.00 \pm 0.10$	$1.052 \pm 0.002$	X-ray (10 particles/batch)
- IPyC thickness ( $\mu\text{m}$ )	$40 \pm 20$	$40.55 \pm 0.53$	CG* (10 particles/batch)
- IPyC density ( $\text{g}/\text{cm}^3$ )	$1.85 \pm 0.20$	$1.91 \pm 0.01$	DC* (10 particles/batch)
- Anisotropic index of IPyC	$\leq 1.03$	$1.0165 \pm 0.003$	OM* (10 particles/batch)
- SiC thickness ( $\mu\text{m}$ )	$35 \pm 10$	$36.08 \pm 0.15$	CG* (10 particles/batch)
- SiC density ( $\text{g}/\text{cm}^3$ )	$\geq 3.18$	$3.182 \pm 0.004$	DC* (10 particles/batch)
- OPyC thickness ( $\mu\text{m}$ )	$40 \pm 20$	$46.3 \pm 3.05$	CG* (10 particles/batch)
- OPyC density ( $\text{g}/\text{cm}^3$ )	$1.85 \pm 0.20$	$1.88 \pm 0.07$	DC* (10 particles/batch)
- Anisotropic index of OPyC	$\leq 1.03$	$1.019 \pm 0.004$	OM* (10 particles/batch)
- Particle dia. (mm)	$0.90 \pm 0.10$	$0.95 \pm 0.011$	PSA* (10 particles/batch)
- Average wt. (g)	0.001392	0.001392	
Fuel compact			
- Compact mass (g)	1.050	$1.028 \pm 0.024$	Average of 14 compacts
- Mean U loading (gU)	0.14	0.135	Average/compact
- Diameter (mm)	$8.0 \pm 0.2$	$7.981 \pm 0.006$	Average of 14 compacts
- Length (mm)	$10.0 \pm 0.5$	$9.995 \pm 0.270$	Average of 14 compacts
- No. of compact (ea)	9(rod1)/5(rod2)	9(rod1)/5(rod2)	
- Packing (volume) fraction (%)	20	$19.703 \pm 0.44$	263 particles/compact
Matrix graphite (M) & structural graphite (G) specimen			
- Diameter (mm)	$8.0 \pm 0.2$	$7.976 \pm 0.004$	Average of 8 specimens
- Length (mm)	$5 \pm 0.2$	$5.028 \pm 0.008$	Average of 8 specimens
- No. of specimens(ea)	8(rod 2)	8(rod 2)	
- Density ( $\text{g}/\text{cm}^3$ )	$1.7 \pm 0.1$	$1.770 \pm 0.004$	Average of 8 specimens

\*CG: Ceramography; DC: Density column; PSA: Particle size analysis; OM: Optical microscopy

\*\* Data provided by KAERI.

## REFERENCES

- [II-1] PETTI, D.A., MAKI, J.T., BUONGIORNO, J., HOBBS, R.R., MILLER, G.K., Key Differences in the Fabrication, Irradiation and Safety Testing of US and German TRISO-coated Particle Fuel and Their Implications on Fuel Performance, INEEL/EXT-02-00300, INL, Idaho Falls (2002).
- [II-2] MARSHALL, D.W., "AGR-5/6/7 Fuel Specification", SPC-1352, INL/MIS-11-21423, INL, Idaho Falls (2017).
- [II-3] BARNES, C.M., AGR-1 Fuel Product Specification and Characterization Guidance, INL/MIS-05-00238-Revision-1, INL, Idaho Falls (2006)



## LIST OF ABBREVIATIONS

ADU	Ammonium diuranate
ADUN	Acid-deficient uranyl nitrate
AGR	Advanced Gas Cooled Reactor
ALARA	As low as reasonably achievable
APT	Atom probe tomography
AVR	Arbeitsgemeinschaft Versuchs Reaktor in Germany
BAF	Bacon Anisotropy Factor
BEC	Backscattered electron composition
BISO	Bi-structure isotopic
BOL	Beginning of life
CNL	Canadian Nuclear Laboratories
CTE	Coefficient of thermal expansion
CVD	Chemical vapour deposition
DFT	Density functional theory
DTF	Design to fail
DLOFC	Depressurized loss-of-forced cooling
EPMA	Electron probe microanalyzer
FB-CVD	Fluidized bed-chemical vapor deposition
FCM fuel	Fully ceramic microencapsulated fuel
FHR	Fluoride Salt-Cooled High-Temperature Reactor
FIMA	Fission per initial metal atom
FP	Fission product
FPD	Full power day
FSV	Fort St. Vrain
GA	General Atom
GCR	Gas Cooled Reactor

Gen IV	Generation IV
GFR	Gas-cooled fast reactor
GT-MHR	Gas Turbine-Modular Helium Reactor
HALEU	High Assay Low Enriched Uranium
HEU	High enriched uranium
HFIR	High Flux Isotope Reactor
HTGR	High temperature gas-cooled reactor
HTTR	High Temperature Test Reactor in Japan
INET	Institute of Nuclear and New Energy Technology
INL	Idaho National Laboratory
IPyC	Inner isotropic pyrocarbon.
JAEA	Japan Atomic Energy Agency (former Japan Atomic Energy Research Institute, JAERI)
JMTR	Japan Materials Testing Reactor
KAERI	Korea Atomic Energy Research Institute
KCMI	Kernel-coating mechanical interaction
LASL	Los Alamos Scientific Laboratory
LEU	Low enriched uranium
LOCA	Loss-of-coolant accident
LWR	Light water reactor
MHTGR	Modular HTGR
MMR	Micro modular reactor
NCC	Numerical calculation case
NGNP	Next Generation Nuclear Plant
NPR	New production Reactor
NSRR	Nuclear Safety Research Reactor
OAF	Optical Anisotropy Factor
OPyC	Outer isotropic pyrocarbon
ORNL	Oak Ridge Nuclear Laboratory

PBMR	Pebble Bed Modular Reactor in South Africa
PIE	Post-irradiation examination
PyC	Isotropic pyrocarbon
PSA	Particl size analyzer
RE	Rare earth
R/B	Release to birth
R&D	Research and development
SEM	Scanning electron microscopy
SiC	Silicon carbide
SMR	Small modular reactor
STEM	Scanning transmission electron microscopy
TD	Theoretical density
TEM	Transmission electron microscopy
THTR	Thorium High Temperature Reactor
TRISO	Tri-structural isotropic
USNC	Ultra Safe Nuclear Corporation
UUNG	Uranium Naturel Graphite Gaz reactor in France
VHTR	Very High Temperature Reactor
XRD	X-Ray Diffraction analysis



## CONTRIBUTORS TO DRAFTING AND REVIEW

Cheon, J-S.	Korea Atomic Energy Research Institute (KAERI), Republic of Korea
Demkowicz, P.	Idaho National Laboratory (INL), United States of America
Fomichenko, P.	National Research Centre “Kurchatov Institute”, Russian Federation
Kim, B.G.	Korea Atomic Energy Research Institute (KAERI), Republic of Korea
Kim, Y.M.	Korea Atomic Energy Research Institute (KAERI), Republic of Korea
Liu, B.	Tsinghua University, China
Nabielek, H.	Research Center Jülich (FZJ), Germany
Onder, N.	Canada Nuclear Laboratories (CNL), Canada
Sim, K.S.	International Atomic Energy Agency (IAEA)

### **Consultants Meetings (virtual)**

27–28 April 2021,

4–17 March 2022.



**IAEA**  
International Atomic Energy Agency

## **CONTACT IAEA PUBLISHING**

Feedback on IAEA publications may be given via the on-line form available at:  
[www.iaea.org/publications/feedback](http://www.iaea.org/publications/feedback)

This form may also be used to report safety issues or environmental queries concerning IAEA publications.

Alternatively, contact IAEA Publishing:

Publishing Section  
International Atomic Energy Agency  
Vienna International Centre, PO Box 100, 1400 Vienna, Austria  
Telephone: +43 1 2600 22529 or 22530  
Email: [sales.publications@iaea.org](mailto:sales.publications@iaea.org)  
[www.iaea.org/publications](http://www.iaea.org/publications)

Priced and unpriced IAEA publications may be ordered directly from the IAEA.

### **ORDERING LOCALLY**

Priced IAEA publications may be purchased from regional distributors and from major local booksellers.